University of Southampton

Faculty of Engineering and Physical Sciences

Aerodynamics and Flight Mechanics Group

Modelling vapour transport in indoor environments for improved detection of explosives using dogs

by

Timothy G. Foat

Thesis for the degree of Doctor of Philosophy

October 19, 2021

University of Southampton

Abstract

Faculty of Engineering and Physical Sciences
Aerodynamics and Flight Mechanics Group

Thesis for the degree of Doctor of Philosophy

Modelling vapour transport in indoor environments for improved detection of explosives using dogs

by Timothy G. Foat

Air movement in indoor spaces can be complex due to large regions with no dominant flow direction and low mean velocities. Therefore, vapour released from an explosive indoors would be expected to result in a high degree of temporal and spatial variability in concentration. To improve canine detection capability, specifically training equipment, training methods and concepts of use, the science of vapour signatures in enclosed spaces needs to be improved.

Large-eddy simulation has been used to study the vapour field in a benchmark test room. The work provides insight into vapour behaviour within indoor spaces and results have been interpreted in relation to vapour detection using dogs. For the test room, it was shown that vapour concentrations reduce rapidly within a short distance from the source. However, the concentration fluctuations, which occur at frequencies that a dog should be able to detect, can be significantly greater than the mean concentration.

Due to the low volatility of many explosives, the vapour they produce will readily partition onto surfaces altering the concentrations in the room. A multi-layer vapour sorption model based on computational fluid dynamics (CFD) was validated. The CFD sorption model and a well-mixed sorption model were applied to the benchmark test room. It was shown, for a moderately high volatility explosive, that absorption had little effect on the well-mixed concentration but could have a significant effect on concentrations in the vicinity of the absorbing surface.

When it is not possible/practical to build a CFD model, eddy diffusion models can be used to rapidly predict the spatially resolved concentration field indoors. However, there is uncertainty over the parameter that governs mixing, the eddy diffusion coefficient, D_e. Work has been carried out to develop a method to predict D_e for mechanically ventilated, isothermal rooms. It was found that D_e is a function of the air flow rate, room volume and number of air supply vents only. This will enable eddy diffusion modelling to be used with more confidence in the future to plan canine training experiments or to interpret detection results.

Contents

List of Figures

List of Tables

Nomenclature

Acronyms

ACR	air change rate.
BCDS	bounded central difference scheme.
CDS	central difference scheme.
CFD	computational fluid dynamics.
CFL	Courant-Friedrichs-Lewy.
CI	confidence intervals.
DES	detached-eddy simulation.
DMNB	dimethyl-dinitrobutane.
DNB	dinitrobenzene.
DNT	dinitrotoluene.
DS	dynamic Smagorinsky-Lilly.
DSTL	Defence Science and Technology Laboratory.
EGDN	ethylene glycol dinitrate.
EH	2-ethylhexanol.
EWT	enhanced wall treatment.
FAC1.3	percentage of points within a factor of 1.3.
FAC2	fraction of points within a factor of two.
FAC5	fraction of points within a factor of five.
FB	fractional bias.
FTIR-ATR	Fourier transform infra-red spectroscopy-attenuated total reflectance.
HDPE	high density polyethylene.
HME	home-made explosive.
HP	hydrogen peroxide.
HVAC	heating, ventilation and air-conditioning.
IED	improvised explosive device.
IMS	ion-mobility spectrometry.

IPA	propan-2-ol.
LDPE	low density polyethylene.
LES	large-eddy simulation.
MB	geometric mean bias.
MIT	Massachusetts Institute of Technology.
MUSCL	monotonic upwind scheme for conservation laws.
NMSE	normalised mean square error.
PDF	probability density function.
PE	polyethylene.
PI	prediction intervals.
PISO	pressure implicit with splitting of operator.
PP	polypropylene.
ppm	parts per million.
ppt	parts per trillion.
PS	polystyrene.
PTFE	polytetrafluoroethylene.
PVC	polyvinyl chloride.
QCM	quartz crystal microbalance.
RANS	Reynolds-averaged Navier-Stokes.
RDX	research department explosive.
RMS	root mean squared.
RNG	renormalization group.
RSM	Reynolds stress model.
SIMPLE	semi-implicit method for pressure linked equations.
SKE	standard k-epsilon.
SST	shear stress transport.
SVOC	semi-volatile organic compound.
TKE	turbulent kinetic energy.
TKEB	turbulent kinetic energy balance model.
TNT	trinitrotoluene.
TVD	total variation diminishing.
UDF	user defined function.
UDM	user defined memory.
UVIC	ultra-violet ion counter.
VG	geometric variance.
VOC	volatile organic compound.

Latin symbols

a	Mass transfer coefficient.
A	Surface area.
$\boldsymbol{A_{ss}}$	The state-space state matrix.
$\boldsymbol{B}$	Diagonal state-space model matrix.
Bi_m	Mass transfer Biot number.
C	Concentration.
$C_{1\epsilon}$	Constant for ϵ transport equation.
$C_{2\epsilon}$	Constant for ϵ transport equation.
$C_{3\epsilon}$	Constant for ϵ transport equation.
C^*	Gas phase concentration in equilibrium with the surface concentration, m.
$C_{ambient}$	Ambient concentration.
C_{cont}	Concentration from a continuous release.
C_{equil}	Equilibrium concentration.
c_ϵ	Constant in turbulent kinetic energy balance model.
C_{finite}	Concentration from a finite duration release.
C_{out}	Concentration at the outlet.
C_p	Concentration in near-wall cell.
C_s	Smagorinsky constant.
C_{solid}	Concentration in the solid.
C_{surf}	Concentration on the surface.
c_{TKEB}	A constant for the TKEB model.
c_v	Von Karman constant.
C_μ	Constant relating to turbulence.
D	Diffusion coefficient.
$D_{effective}$	Effective diffusivity i.e. the sum of molecular and turbulent diffusivity.
d_c	Distance to the closest wall.
d_{layer}	Thickness of the permeation layer.
d_{total}	Total thickness of the permeable solid.
D_e	Eddy diffusion coefficient.
DH	Hydraulic diameter.
D_m	Molecular diffusion coefficient.

D_{solid}	Solid phase diffusion coefficient.
D_t	Turbulent diffusion coefficient.
Ec	Empirical constant (9.793).
E	Energy.
F	Rate of transfer per unit area or flux.
G	LES filter function.
G_b	Production term for k due to mean velocity gradients.
G_k	Production term for k due to buoyancy.
G_ω	Production term for ω.
Gr	Grashof number.
H	Height.
H_{inlet}	Height of inlet.
H_{outlet}	Height of outlet.
$\boldsymbol{I}$	Identity matrix.
k	Turbulent kinetic energy.
k_p	Turbulent kinetic energy in the near-wall cell.
K_{ab}	Partition coefficient for absorption.
K_{ad}	Partition coefficient for adsorption.
K_B	Boltzmann's constant.
K_H	Henry's law constant.
L	Length.
L_{char}	Characteristic length.
$L_{m,sgs}$	Mixing length for the subgrid scales.
L_{source}	Length of source.
L_{ij}	Germano identity variable.
L_s	Thickness of the solid.
$\dot{M}$	Mass emission rate.
M	Instantaneous release mass or mass in room or zone.
M_a	Molecular mass.
MW	Molecular weight.
MW_a	Molecular weight of vapour a.
MW_{ab}	Combination of molecular weight of vapour a and b.
MW_b	Molecular weight of vapour b.
n	Index.
n_{layer}	Number of permeation layers.

N	Number of supply vents.
N_{1ppt}	Number of times 1 ppt threshold is exceeded.
N_A	Avogadro's constant.
P	Gas pressure.
P_0	Vapour pressure.
$P_{0,n}$	Vapour pressure of pure compound n.
P_c	Empirical constant.
Pe	Peclet number.
P_n	Partial pressure of compound n.
Q	Total volumetric air flow rate.
Q_f	Total volumetric fresh air flow rate.
r	Radial distance from the source.
R^2	Coefficient of determination.
Re	Reynolds number.
Ri	Richardson number.
Sc	Schmidt number.
Sc_t	Turbulent Schmidt number.
$Sc_{sg,t}$	Subgrid turbulent Schmidt number.
Sh	Sherwood number.
$\widetilde{S_{ij}}$	Strain rate tensor for the LES resolved scales.
t_{95-5}	The time between the 95th and 5th percentiles concentration crossing a threshold.
t_{end}	Release duration.
t_{lag}	Time constant relating to permeation.
$t_{transitAR}$	Mixing time predicted by jet transit model.
$t_{mixCell}$	Mixing time predicted by the mechanical power model.
t_{ND}	Non-dimensional diffusion time.
$t75_{sorp}$	Time taken to reach 75 % of C_{equil} for the sorption case.
$t75_{noSorp}$	Time taken to reach 75 % of C_{equil} for the no sorption case.
T	Temperature.
Ti	Turbulent intensity.
T_{ij}	Subtest-scale stress tensor.
u	Velocity in the x direction.
u_{max}	Maximum velocity in the x direction.
$\boldsymbol{u_{ss}}$	Source vector for state-space model.

u_0	Inlet velocity.
u^+	Non-dimensional velocity (parallel to the wall).
u_τ	Friction velocity.
u_{turb}	Representative turbulent velocity.
V	Volume.
W	Width.
x	Distance in x direction.
x_0	x-coordinate of release location.
y_0	y-coordinate of release location.
z_0	z-coordinate of release location.
x_n	Mole fraction of compound n in a mixture.
$y_{1/2}$	Distance from wall where $u = 0.5\ u_{max}$.
Y	Species mass fraction.
Y_ω	Dissipation of ω.
Y_k	Dissipation of k.
Y^+_{BWF}	Normalised species mass fraction for the blended wall function.
Y^+_{lam}	Laminar component of Y^+_{EWT}.
Y^+	Normalised species mass fraction.
Y^+_{turb}	Turbulent component of Y^+_{EWT}.
Y_w	Species mass fraction at the wall.
Y_p	Species mass fraction in the centre of the first cell.
y^+	Non-dimensional distance from the wall.
y^+_1	Non-dimensional distance from the wall to the first cell centre.
y^*	Non-dimensional distance from the wall based on TKE.
y^*_c	Non-dimensional distance from the wall at which the species sub-layer ends.

Greek symbols

α^*	Damping coefficient for ω.
β	Thermal expansion coefficient.
Γ	Blending function for enhanced wall treatment.
δ_{ij}	Kronecker delta.

Δ	Local grid scale.
$\widehat{\Delta}$	Test-filter scale.
ϵ	Turbulent dissipation rate.
ζ	Position vector.
η	Kolmogorov length scale.
λ	Air change rate.
λ_f	Fresh air change rate.
$\Lambda_{t,c}$	Integral time scale for concentration.
$\Lambda_{t,u}$	Integral time scale for velocity.
μ	Dynamic viscosity.
μ_t	Turbulent dynamic viscosity.
$\mu_{t,sgs}$	Subgrid scale turbulent viscosity.
ν	Kinematic viscosity.
ρ	Density of air.
σ_k	Turbulent Prandtl number for k.
σ_ϵ	Turbulent Prandtl number for ϵ.
Σ_{v-a}	Atomic diffusion volumes of molecule a.
Σ_{v-b}	Atomic diffusion volumes of molecule b.
τ	Characteristic mixing time.
τ_{ij}	Subgrid scale stress tensor.
ϕ	A time varying variable.
ω	Specific turbulent kinetic energy dissipation rate.
Ω	Computational domain.

Subscripts and accents

$\bar{\phi}$	Time averaged variable.
$\widetilde{\phi}$	LES filtered variable.
$\widehat{\phi}$	Second scale LES filtered variable.
$\phi^{'}$	Fluctuating component.
C_0	Initial, inlet or source condition.
$\boldsymbol{C}$	Vector or matrix property.
u_{RMS}	Root mean square.
$\dot{C}$	Time derivative of variable.

Declaration of Authorship

I, Timothy G. Foat, declare that the thesis entitled *Modelling vapour transport in indoor environments for improved detection of explosives using dogs* and the work presented in the thesis are both my own, and have been generated by me as the result of my own original research. I confirm that:

- This work was done wholly or mainly while in candidature for a research degree at this University.
- Where any part of this thesis has previously been submitted for a degree or any other qualification at this University or any other institution, this has been clearly stated.
- Where I have consulted the published work of others, this is always clearly attributed.
- Where I have quoted from the work of others, the source is always given. With the exception of such quotations, this thesis is entirely my own work.
- I have acknowledged all main sources of help.
- Where the thesis is based on work done by myself jointly with others, I have made clear exactly what was done by others and what I have contributed myself.
- Parts of this work have been published as: (Foat, 2014, 2015, 2017; Foat et al., 2017, 2018, 2020, 2021).

Signed:.....

Date:.....

Acknowledgements

This thesis is dedicated to my wife Sarah and children Evie and Maya. Without their support and understanding I would not have been able to complete this PhD.

I would like to thank my supervisor, Dr. Zheng-Tong Xie, and co-supervisor, Prof. Ian Castro, from the University of Southampton and my colleague, Dr. Simon Parker, for their guidance and encouragement.

I would like to acknowledge the assistance of my employer, Dstl, who provided funding for my PhD and for some of the project work which has formed the basis of my studies. Finally, I would like to recognise the support and facilities provided by the University of Southampton.

Chapter 1

Introduction

Due to the low vapour pressures of many explosives, vapour concentrations can often be measured only by time integrated sampling in controlled environments. Downwind concentrations are often not detectable at all in real time by analytical equipment. Dogs remain the most effective method for the detection of explosives in many situations yet the chemical signature that they sense varies spatially, temporally and chemically and cannot easily be quantified. In order to be able to improve the canine detection capability (specifically training equipment, training methods and concepts of use) the science behind vapour signatures needs to be improved.

Vapour plumes can be highly unsteady and intermittent. Crimaldi and Koseff (2001) for example, reported that at a short distance from a low Reynolds number[1] (less than 2000) plume centreline, the peak concentration could be 500 times the mean concentration at that point for a short period of time. The problem is further complicated in indoor spaces where turbulent, transitional (Li and Nielsen, 2011; van Hooff et al., 2013) and laminar flow can exist (Zhai et al., 2007) and there may not be a dominant flow direction. Improving the understanding of these unsteady phenomena in indoor spaces would be an important step towards understanding canine detection.

The high resolution modelling, e.g. large-eddy simulation (LES), required to accurately simulate unsteady air flow and vapour transport in indoor spaces is time consuming, so faster running models, e.g. eddy diffusion models, also have a place. Coarse models have particular application for drawing more general conclusions or for studying specific scenarios, for example, before a training exercise takes place.

The aims of this PhD research are to:

- Improve the understanding of the fluid dynamics of explosives vapour transport indoors.

[1]The dimensionless Reynolds number, $Re = \frac{\rho\, u\, L_{char}}{\mu}$, where ρ [kg·m^{-3}] is the density of the fluid, u [m·s^{-1}] is the velocity, L_{char} is a characteristic length and μ [kg·s^{-1}·m^{-1}] is the viscosity.

- Provide advice to and tools for detection practitioners to improve their training processes and increase the likelihood of successful detection.

1.1 Detection of explosives

Detection of explosives can be carried out using a number of different physical methods. The main methods are: identification of signature airborne volatile vapours and identification of signature chemicals via surface swabbing[2] with subsequent analysis of the sample. Explosive can also be detected indirectly using techniques such as: x-ray, ground penetrating radar, radio frequency detection and millimetre wave imaging. These techniques look for a signal produced by the system controlling or housing the explosives.

Explosive detection is undertaken in both civilian and military environments. Baggage, cargo, vehicles and people are typically screened at airports, ports and high risk buildings or events. Buildings are also searched prior to particular events (such as political conferences or royal visits) as are the areas through which VIPs may pass. The military screen people and vehicles at check points and a key concern in overseas operations has been the detection of roadside improvised explosive devices (IEDs). A crossover between the military and civilian arena is in the detection of landmines, particularly anti-personnel mines.

Only airborne vapour detection, in both civilian or military environments, is considered in this PhD research.

1.1.1 Vapour detection

Operational vapour detection is conducted for the most part using either electronic equipment or dogs. The methods used within electronic equipment include: ion-mobility spectrometry (IMS) such as the Multi-Mode Threat Detector (MMTD) and the Sabre 5000 (both Smiths Detection Inc., MD, USA), fluorescent polymer sensors such as the FIDO range of detectors (FLIR Detection Inc., OK, USA) and mass spectrometers (such as the two instruments under development by SEDET (Fernandez de la Mora and Fernandez de la Mora, 2013) and Massachusetts Institute of Technology (MIT) Lincoln Laboratory (Aernecke, 2014; Ong et al., 2017). The two mass spectrometry systems are both designed to have very high sensitivity. The SEDET system initially samples the vapours onto a filter, the MIT system provides real-time analysis.

Other vapour detection methods that have been explored include: Schlieren imaging (Bigger, 2008); adsorption on micro-cantilevers (Pinnaduwage et al., 2003, 2004); and

[2] It may also be possible to sample airborne vapour which was subsequently sorbed onto a surface by swabbing.

bio-sensor systems such as the CSIRO CYBERNOSE® which is based on receptor proteins from nematode worms.

1.1.1.1 Vapour detection using dogs

Dogs have been used for centuries for tracking and hunting due to their excellent sense of smell and the ease with which they can be trained (Settles, 2005). Dogs have an olfactory epithelium (within which the olfactory receptor neurons are located) that sits behind the respiratory region of the nose, so that the bulk of the inhaled air does not pass through it. Because of this, the shape of this region has evolved to produce air flow which is optimised for smell alone. The human olfactory epithelium contains considerably fewer olfactory receptor neurons and is located within the main nasal cavity, which is optimised for breathing. Dogs are said to sniff with a frequency of between 4 Hz and 7 Hz (Craven et al., 2010) but do sometimes take longer sniffs at 0.5 Hz (Settles, 2005). This means that they will not be able to differentiate plume structures with frequencies higher than this.

Operational explosives detection dogs work in three main ways: searching an area, objects or people on the lead; searching an area, objects or people off the lead; being presented with samples while off the lead. When searching an area they may either be trained to signal when detecting the target odour or to track towards the odour source.

The ways in which animals locate the source of a chemical signal include:

- Chemotaxis, movement up a mean concentration gradient (Vickers, 2000).
- Sensing of a chemical followed by anemo- or rheotaxis, moving upwind or upstream (Vickers, 2000).
- Sensing the frequency of odour filaments (Weissburg, 2000).
- Eddy chemotaxis, where the instantaneous concentration signature is used instead of the mean signal (Atema, 1996).

The method, or methods, an animal uses depends on its size relative to the size of the structures in the chemical plume and the nature of the plume i.e. whether it is turbulent, intermittent, laminar or diffusional (Weissburg, 2000). Only a subset of these methods may be applicable to an indoor environment where there is often no strong, dominant flow direction.

It has not been determined conclusively which of these methods dogs use, but it has been reported, for example, that wind direction can be detected by differential cooling of a dog's nose (Vickers, 2000), so they may be able to use anemotaxis.

1.2 How vapour becomes available for detection

For vapour to be available for sampling by a dog or a piece of electronic equipment, two processes must occur. The first is the emission of vapour, which in the simplest case, is directly from the solid or liquid explosive through sublimation or evaporation. The second is the transport of this vapour from the explosive into the location where the sampling is taking place. A third set of processes, which can have a significant effect on the concentration of the transported vapour, is the interaction of the vapour with surfaces, specifically: adsorption onto a surface, or absorption into a material[3].

Emission can also occur when the explosive is contained or wrapped in another material. This could be tightly wrapped cling-film (polyvinyl chloride (PVC)), in which case components of the explosive may be able to dissolve into the polymer and then be emitted on the outer side. Another situation is where the explosive is held within a container such as a cardboard box. In this case, the vapour may need to permeate through the cardboard before being available for sampling.

As the emission from an unwrapped explosive is driven by evaporation or sublimation, the vapour source can be considered to be passive, i.e. there is no air movement associated with the emission.

Methods to model these processes (excluding the case where a second material is in direct contact with the explosive) form the basis of this PhD.

1.3 Explosive vapour detection scenarios of interest

1.3.1 Training scenario

There is a requirement to train dogs to detect a range of explosive materials. To do this they need to be trained with the real material to imprint the odour or set of odours into their memory and then be taught to find this material when concealed. To test a dog's ability to detect a particular explosive against a set of inteferent odours, vapour samples are typically presented to the dog in containers, either arranged in a line (Porritt et al., 2015) or on the circumference of a scent wheel.

An example training scenario is shown in Figure 1.1. In this case the dog is presented with a number of containers, one of which contains a small amount of an explosive. The dog should indicate to its handler if it believes that it has found a positive sample. This training was conducted in a large empty room that had no mechanical ventilation

[3] Collectively these processes are referred to as sorption.

Some explosives, in particular some of the modern home-made explosives (HMEs), are very sensitive (i.e. easily detonated). Therefore, the smaller the sample that can be used for training the better. However it is not understood how the vapour plume from a small sample differs to that of a larger sample. Anecdotal evidence suggests that dogs who are trained on small samples may sometimes not be able to detect larger samples.

Figure 1.1: An example training scenario for detection dogs.

1.3.2 Operational or more realistic training scenario

In an operational scenario or a more realistic training scenario, the explosive may be concealed within a room. One example of a possible concealment is shown in Figures 1.2 and 1.3. In this scenario, the explosive is held within a small, partially or fully sealed, box. The vapour from the explosive can permeate through the sides and top of the inner box and also diffuse or advect through openings in this box, if any are present. The vapour can then permeate, diffuse or advect through openings in the outer box. Figure 1.3 shows what may affect the transport of the vapour within a room. Similar effects may be present in other enclosed spaces such as vehicles or cargo containers.

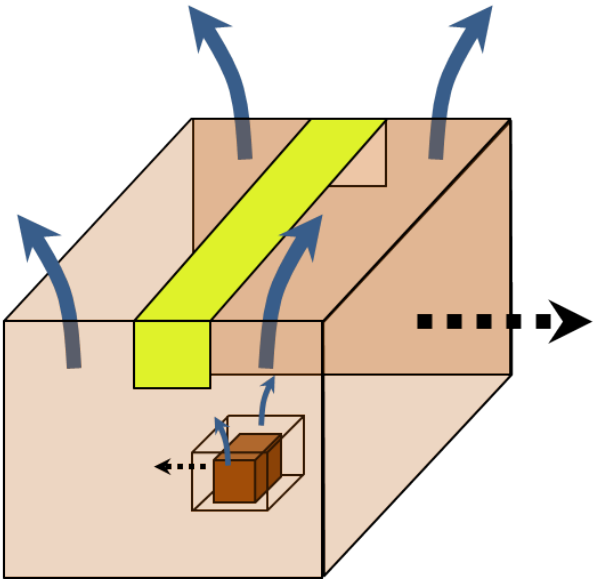

Figure 1.2: Sketch of vapour permeating (black dashed arrows) and advecting or diffusing through holes (blue arrows) from an explosive material, through an inner and outer container. The lime green strip represents sealing tape.

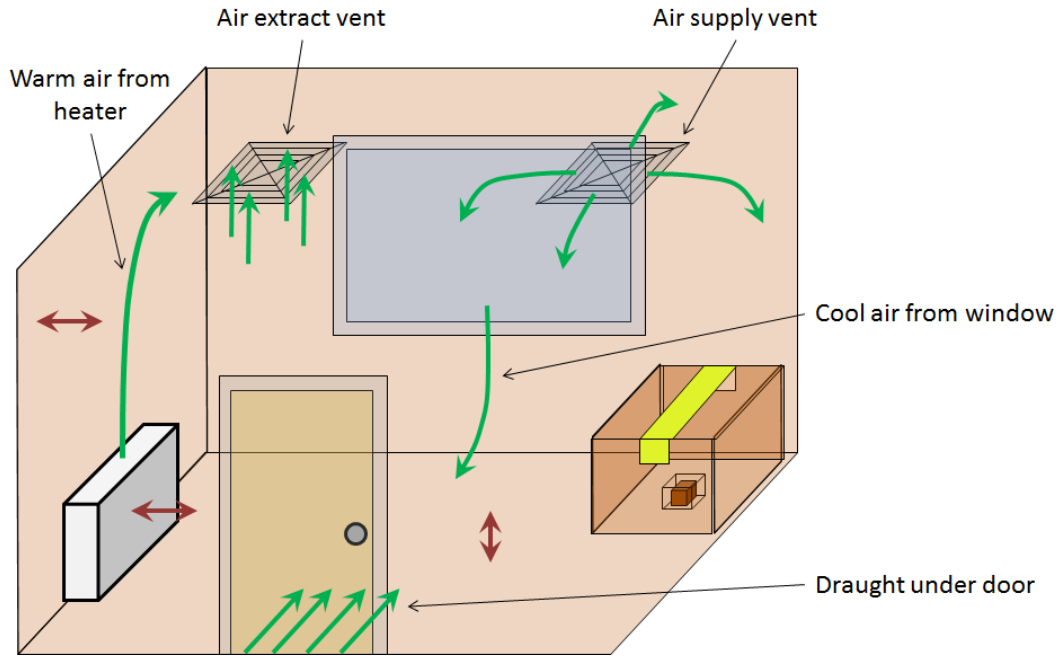

Figure 1.3: Sketch of an explosive concealed in a room. Possible drivers of the flow in the room are included (green arrows) and two-way sorption is indicted by the red arrows. The processes shown in Figure 1.2 would also be occuring.

1.4 Indoor air flows

Indoor airflow is complex because there are typically large regions within a room with no dominant flow direction and very low mean velocities. This complexity can be present for both mechanically and naturally ventilated rooms and is more pronounced when air change rates are small. Indoor flows are thought to contain turbulent, laminar and transition regions (Zhai et al., 2007) and are both unsteady and three dimensional. Nielsen (1992) suggested that at air change rates (ACRs), λ, below $5\,\mathrm{h}^{-1}$ and velocities less than $0.25\,\mathrm{m{\cdot}s}^{-1}$ the flow can be classed as low Reynolds number and is without fully developed turbulence. The ACR of a space, which is an indication of how quickly air is being mixed around a room, can be calculated by the following,

$$\lambda = \frac{Q}{V}, \tag{1.1}$$

where Q [$\mathrm{m^3{\cdot}s^{-1}}$] is the volumetric air flow rate through the room and V [$\mathrm{m^3}$] is the volume of the space. Mechanically ventilated rooms often recirculate some of the air (to reduce heating costs) so the total volume of air being supplied can be split into a fresh air component and a recirculated component. The fresh air change rate, λ_f [$\mathrm{s^{-1}}$], which is an indication of how quickly a room is being ventilated is given by the following,

$$\lambda_f = \frac{Q_f}{V}, \tag{1.2}$$

where Q_f [$\mathrm{m^3{\cdot}s^{-1}}$] is the volumetric flow rate of the fresh air entering the room.

A number of studies have looked at air velocity and turbulence intensity in rooms. Turbulence intensity, Ti [dimensionless], is defined as u_{RMS} / $\overline{u}$, where u_{RMS} is the root mean squared (RMS) velocity and $\overline{u}$ is the time averaged velocity. Finkelstein et al. (1996) carried out measurements of air flows in two different full scale ventilated test rooms (the rooms were furnished and occupied) with 44 different combinations of air distribution and air exchange rates from $4\,\mathrm{h}^{-1}$ to $8\,\mathrm{h}^{-1}$. They took measurements in what was defined as the occupied zone. Mean air velocities (time averaged) from $0.05\,\mathrm{m{\cdot}s}^{-1}$ to $0.6\,\mathrm{m{\cdot}s}^{-1}$ were measured with turbulence intensities of up to 70 % at the lower velocities and not lower than 10 % for all velocities. 90 % of the velocity fluctuations (by energy) were between 0.1 Hz and 2 Hz in the occupied zone. Finkelstein et al. (1996) stated that there could have been regions with higher fluctuation rates within the air jets from the diffusers when these penetrated into the occupied zone. Nielsen (1992) measured air velocities in two small rooms (5.4 m x 3.6 m with a height of 2.4 m or 2.6 m). The rooms had a high wall mounted air supply device and a low level, wall mounted extract.

For empty rooms, the maximum velocity measured in the occupied zone varied from approximately $0.05\,\mathrm{m{\cdot}s^{-1}}$ at an ACR of $2\,\mathrm{h^{-1}}$ to approximately $0.4\,\mathrm{m{\cdot}s^{-1}}$ at an ACR of $8\,\mathrm{h^{-1}}$. Matthews et al. (1989) recorded air velocities in domestic environments and showed that median values, recorded in different rooms and positions within the rooms, varied from $0.015\,\mathrm{m{\cdot}s^{-1}}$ to $0.058\,\mathrm{m{\cdot}s^{-1}}$ when the heating, ventilation and air-conditioning (HVAC) system was off to $0.057\,\mathrm{m{\cdot}s^{-1}}$ to $0.155\,\mathrm{m{\cdot}s^{-1}}$ when it was on. Kovanen et al. (1989) recorded data in a number of buildings, mainly consisting of office spaces. The greater part of the mean velocity distribution data had values less than $0.10\,\mathrm{m{\cdot}s^{-1}}$. They also recorded Ti and found that 90 % of the distribution of values ranged from 15 % to 50 % and showed some dependence on height above the ground. That the latter two studies had lower velocities in general is perhaps indicative of the lower air change rates in those rooms compared to the those assessed by Finkelstein et al. (1996) and Nielsen (1992). This data shows that indoor air flows typically consist of low velocity air movement and high turbulence intensity.

Zhou (1999) took 140 velocity measurements in a number of ventilated spaces and recorded a mean velocity across all measurements of $0.15\,\mathrm{m{\cdot}s^{-1}}$. The integral time scale for velocity was less than 5 s for 90 % of the measurement, the integral length scale was typically less than 0.5 m and the characteristic frequency was between 0.002 Hz and 0.4 Hz. The frequency of the velocity fluctuations were much smaller than the dog sniffing frequencies given in Section 1.1.1.1 (4 Hz to 7 Hz). Therefore, for vapours with Schmidt numbers (Equation 2.34) close to one, the fluctuations must have frequencies that a dog can differentiate.

Some studies give estimates for the Kolmogorov length scale, η, in indoor air flow. These vary from 0.01 m and 0.001 m (Chen and Srebric, 2002), 7.8×10^{-4} m (Knight et al., 2005) or as low as 1×10^{-4} m (Murakami and Kato, 1989).

Limited experimental data is available for highly spatially and temporally resolved species transport in indoor spaces, and even less for the constant concentration releases of interest to this study. Constant concentration sources are of particular interest for explosives detection, as it can often be assumed that the vapour concentration close to an explosive is maintained at the saturation vapour pressure of the material (see Section 2.1 for more details). For constant concentration sources, the flux of vapour can vary depending on the local air flow and turbulence.

Data of lower spatial and temporal resolution is more readily available. Drescher et al. (1995); Cheng et al. (2011); Acevedo-Bolton et al. (2012) studied gaseous point releases, monitored concentrations at a number of locations and related mixing to power input (Drescher et al., 1995) and air change rate (Cheng et al., 2011). Topp (1999) described experiments with evaporation of decane in an indoor environment but only used a single point measurement. Ferri et al. (2009) conducted an experiment using a constant

concentration vapour source and measured high resolution time histories of concentration at a number of locations but did not provide any statistics on the turbulence or concentration fluctuations. Acevedo-Bolton et al. (2012) presented data on an experimental set-up similar to Cheng et al. (2011) but with 15 s time resolution. Hargather et al. (2011) sampled vapour from explosives in cargo containers, but only from a single location. High resolution concentration data from different explosives was produced by Ong et al. (2017) using a mass spectrometer. Ong et al. recorded concentration fluctuations from two explosives with a sampling duration of approximately 1 s at 0.3 m from the source. Yang et al. (2019) recorded vapour concentrations from evaporating ethanol with 2 s resolution and had both strong air flow (a pedestal fan) and no strong air flow conditions. As with Ferri et al. (2009), Yang et al. (2019) did not provide any statistics on the turbulence or concentration fluctuations. Crucially, Yang et al. (2019) commented that concentrations indoors fluctuate rapidly and irregularly with time so that concentration gradients do not always point towards the source.

Even though with all of the complexity described above, indoor dispersion can often be represented by a simple model. The most commonly used simplification is to assume that the variation in concentration across the room or parts of the room is small. This condition is referred to as well-mixed and is achieved when the relative standard deviation for concentration in the room (or part of the room) is 10 % or less (Baughman et al., 1994). For other models it is assumed that the air flow is steady over time periods and length scales of interest, and that it can be prescribed. Another assumption could be that mixing due to large scale laminar and/or turbulent motion in the room is isotropic so transport can be thought of as a diffusion like process.

These simple modelling approaches are frequently used to predict the hazard from airborne material but could also be applied to the transport of vapour from explosives. Also, the models need to be simple when it is not practical to fully survey the environment (e.g. when there is insufficient time to visit a building and carry out measurements or when the building is difficult to access). In such cases it may be impossible to define, with sufficient confidence, the boundary conditions required for more complex techniques such as computational fluid dynamics (CFD) modelling. Another significant advantage of most simple models is the fast speed with which they can be set up and solved in time. Table 1.1 lists the advantages and disadvantages of some of the different simple model approaches for a single enclosed space.

Method	**Advantages**	**Disadvantages**	**Reference**
Well-mixed	Very simple model with only room volume and air change rate required.	No spatial resolution within zone.	Reinke and Keil (2009)
Two-zone	Represents concentrations close-to and far-from the source.	No spatial resolution within each of the zones. Transfer rate between zones required.	Nicas (1996)
Dilution ventilation and mixing factor	Takes account of high concentrations near the source.	No spatial resolution within zone.	Feigley et al. (2002)
Zonal	Provides spatial resolution within zone.	Usually needs flow to be prescribed.	Megri and Haghighat (2007)
Markov chain	Provides spatial resolution. Can account for additional effects such as particle sedimentation.	Needs flow to be prescribed.	Nicas (2001)
Eddy diffusion	Provides spatial resolution. Analytical models available for a number of scenarios.	There is some uncertainty in the value of the eddy diffusion coefficient. May not be accurate close to the source.	Nicas (2009)

Table 1.1: Assessment of different simple modelling methodologies for an enclosed space.

All the methods discussed above, except the eddy diffusion method, do not provide spatial resolution or need the flow to be prescribed. Therefore, the eddy diffusion method is uniquely suited to provide spatial resolution with minimal set up requirements.

If sufficient time and information is available then a higher resolution modelling technique such as CFD modelling can be used. CFD should also be used when information on the local features of the flow are required.

A range of different turbulence models or modelling methodologies are available for CFD and different approaches have been shown to perform well at predicting indoor airflows

in different situations (Zhang et al., 2007). LES is a modelling technique in which the large-eddies are fully resolved and only the small eddies (which are assumed to be isotropic) are modelled. The more commonly used Reynolds-averaged Navier-Stokes (RANS) turbulence models have a disadvantage compared to LES, when fluctuating properties are of interest, as the Navier-Stokes equations in RANS models are time averaged and the effects of turbulence are approximated.

LES has been used previously to predict the transport of passive scalars in indoor environments. van Hooff et al. (2014) for example, compared LES predictions to those from RANS models for scalar transport in a simple enclosure. Endregard et al. (2010) used LES to study the consequences of the releases of a nerve agent in a large building, and Choi and Edwards (2012) included the effects of people movement and the opening of doors. However, none of these included releases from the constant concentration sources, which are of interest to this PhD, or attempted to relate the time varying concentration to vapour or gas detection. In addition, few studies consider extreme values of the concentration distribution, which may be important for vapour detection.

It should be noted that CFD models can also be solved rapidly using techniques such as those employed in the fast fluid dynamics method (Zhu and Chen, 2009; Zuo and Chen, 2010) and the lattice Boltzmann method (Elhadidi and Khalifa, 2013; Khan et al., 2015). However, detailed information about the indoor space is still required for these models so they will not be suitable in all cases.

This PhD explores the use of both eddy diffusion and CFD modelling to study the transport of vapour from explosives in indoor spaces.

1.5 Objectives

It is currently not known how the spatially and temporally resolved concentration field from an explosive (or other area sources) could be exploited for detection. Previous experimental and numerical work has provided information on flow and passive scalar transport in indoor environments but little on how different detection/search strategies could be employed in these environments. This work will use large-eddy simulation to extensively study the turbulence fluctuations and the instantaneous vapour field in a widely studied, isothermal, benchmark test room, considering the effects of the source size and location.

Due to the low volatility of many explosives, the vapour they produce will readily partition onto surfaces altering the concentrations in a room. Vapour transport has previously been modelled in a range of environments, from small emission cells to whole rooms, using both analytical and numerical approaches. These models typically include either a well-mixed air volume or a simple sorption model. This work will be extended by

testing/validating a CFD based multi-layer vapour sorption/permeation model. This will then be used to assess the effect that sorption has on vapour concentrations in an example test room.

Eddy diffusion models are uniquely placed to rapidly predict spatially resolved concentrations for airborne materials in indoor environments. This type of model could be used to support explosive detection training activities or to predict likely concentrations in operational settings. The single parameter that governs mixing in these models is the eddy diffusion coefficient. Some relationships that enable this coefficient to be predicted have been proposed in the literature, but wider applicability of these has not previously been tested. A novel automated CFD tool will be used to calculate the eddy diffusion coefficient in a range of isothermal, mechanically ventilated rooms. Available relationships for the diffusion coefficient will then be tested and modified if required.

In summary the objectives are:

1. To study the turbulence fluctuations and the instantaneous vapour field in a test room and to explore how the spatially and temporally resolved concentration field from an explosive could be exploited for detection.
2. To test/validate a CFD based multi-layer vapour sorption/permeation model and then use it to assess the effect that sorption has on vapour concentrations in an example test room.
3. To demonstrate applicability of models to predict the eddy diffusion coefficient in indoor spaces. This will be done using a novel automated computational fluid dynamics tool.

The PhD has focussed on two common explosives, trinitrotoluene (TNT) which is a medium to low vapour pressure solid explosive and ethylene glycol dinitrate (EGDN) which is a higher vapour pressure liquid.

1.6 Structure of the thesis

Chapter 2 gives background to the methods which have been used to predict the concentration of transported vapour. This includes vapour emission, transport and interaction of the vapour with surfaces.

LES was used in Chapter 3 to demonstrate how complex the vapour signature from an explosive could be in a simple isothermal room. The results of this modelling were interpreted in terms of current theories of chemical location by animals and the capability of detection dogs.

In order to extend the generality of the results in Chapter 3, the simple indoor test room was modelled at a range of air change rates. This study is discussed in Chapter 4.

In Chapter 5 a new spatially resolved sorption/permeation modelling capability was validated using a set of increasingly complex (bespoke) experiments. The effects of vapour sorption were then included in a RANS model of the indoor test room to see whether this affected the concentration predictions.

In Chapter 6 a study to improve on existing relationships to predict the eddy diffusion coefficient in indoor spaces is described. This was carried out using a novel automated CFD tool. The applicability of the relationships for the eddy diffusion coefficient and eddy diffusion modelling more generally was reported on. One of the cases used to test the model was the simple isothermal room used for the CFD modelling in the preceding chapters.

The overall conclusions and recommendation for further work are presented in Chapter 7.

1.7 Publications

Parts of this thesis were presented at international conferences: the Canine S&T workshop in North Carolina, USA (Foat, 2014), the 68th Annual Meeting of the APS Division of Fluid Dynamics, Massachusetts, USA (Foat, 2015), the International Defence and Security Canine Conference, Cirencester, UK (Foat, 2017) and a poster at the DTRA CBD S&T conference (Drodge et al., 2019). Presentations were also given to the Aerodynamics and Flight Mechanics Group at Southampton University (Foat, 2016, 2019).

A paper based on the LES work described in Chapter 3 was published in the Journal of Wind Engineering and Industrial Aerodynamics (Foat et al., 2018). One paper on the automated CFD method used in Chapter 6 and one of the eddy diffusion modelling discussed in the same chapter were published in Building and Environment (Foat et al., 2017, 2020). A paper on the vapour sorption modelling described in Chapter 5 is in press with the International Journal of Heat and Mass Transfer (Foat et al., 2021).

Chapter 2

Background

For vapour to become available for sampling by a dog or a piece of electronic equipment, two processes must occur. The first is the emission of vapour from the solid or liquid explosive. The second is the transport of this vapour from the explosive to the location where the sampling is taking place. A process, which can have a significant effect on the concentration of the transported vapour, is sorption. In this chapter, methods to predict vapour emissions, transport and sorption are discussed.

2.1 Vapour emission

The rate at which vapour is produced by a solid explosive can be affected by a number of processes as represented in Figure 2.1. There are processes that are internal to the explosive, such as diffusion of vapour or permeation of liquid through the solid; equilibrium between the solid/liquid phase and the vapour phase (sublimation and evaporation) and processes that are external to the explosive itself such as the advective or diffusive transport of the vapour away from the material. Any of the internal or external processes could limit the overall vapour production rate and components of different volatiles may be limited by different rates. For explosives where the compound of interest makes up most of the weight of the explosive, e.g. 2,4,6 TNT which may make up greater than 99 % of a block of TNT (see Appendix A.2), it can be assumed that only external processes need to be considered. It should be noted that the volatile compound 2,4 dinitrotoluene (DNT), which is present in TNT, is often the target used for detection of TNT. EGDN is usually present in explosives as a minor component, but here it is only considered to be in its pure form, as was used in the experiments described in Chapter 5.

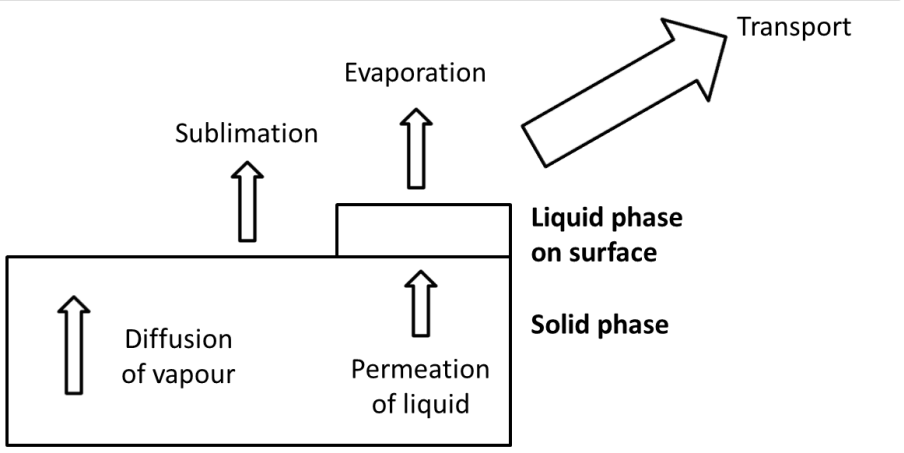

Figure 2.1: The processes that may affect the production of vapour from a solid explosive.

The chemical signature that is produced from an explosive may change with time as the material ages. As it ages, the total mass of volatile components will reduce more than the total mass of less volatile components, particularly those near to the surface. The ageing process may be accelerated at higher temperatures.

Chemical decomposition can also affect the make up of chemicals in the bulk and the vapour phase. This is discussed briefly in Section 2.1.4.

Liu et al. (2013) described a ratio that indicates whether the internal or external mass transfer limits the vapour emission. The ratio is shown below.

$$\frac{Bi_m}{K_{ab}}, \tag{2.1}$$

where Bi_m [dimensionless] is the mass transfer Biot number (defined below) and K_{ab} [dimensionless] is the partition coefficient defined as the equilibrium solid phase concentration divided by the vapour phase concentration adjacent to the surface.

$$Bi_m = \frac{a\, L_s}{D_{solid}}, \tag{2.2}$$

where a [m·s^{-1}] is the convective mass transfer coefficient, L_s [m] is, according to Liu et al. (2013), the thickness of the solid material and D_{solid} [m^2·s^{-1}] is the solid phase molecular diffusion coefficient for the vapour transport in the solid.

When the ratio, $\frac{Bi_m}{K_{ab}}$, is much larger than 1, the vapour emission rate is controlled by diffusion within the solid and when it is close to or smaller than 1, the rate is controlled by external processes, such as local air flows.

The concept of the mass transfer Biot number is based on a balance of fluxes, F [kg·s^{-1}·m^{-2}], within and external to the solid.

For volatile organic compounds (VOCs) Liu et al. (2013) calculated that the ratio is usually much larger than 1 and therefore the emissions are controlled by internal processes. For semi-volatile organic compounds (SVOCs) they showed that the ratio is typically much smaller than one and the rates are therefore controlled by external processes. This, they reported was mainly due to the difference in K_{ab} between the classes of compounds. With SVOCs having significantly larger values for K_{ab}, i.e. the solid phase concentration is much higher than the vapour phase concentration. A SVOC was classed by Weschler and Nazaroff (2008) as an organic compound with an equilibrium vapour pressure between 1×10^{-9} Pa and 10 Pa. This classification puts most explosive compounds in the SVOC group (see Section 2.1.2) with the taggants[1] and other compounds such as 2-ethylhexanol (EH) (a compound present in the explosive C-4) in the VOC group. One exception is undiluted hydrogen peroxide (HP), which has a vapour pressure of approximately 300 Pa at 25 °C (Ewing et al., 2013), putting this explosive in the VOC range. HP is not actually a VOC as it does not contain carbon.

The mass transfer Biot number ratio (Equation 2.1) for three compounds of interest for the detection of explosives was calculated and the results are given in Section 2.1.7.

2.1.1 Constituent components of explosives

In order to calculate the vapour production rate, the first step is to specify what compounds are present in the explosive material.

Unless purified, explosives are typically composed of a number of different compounds. Some explosives, such as C-4, intentionally contain components other than the explosive (research department explosive (RDX) is the explosive in C-4) such as a plasticizer. Some explosive all contain a taggant. The constituent components of explosives can also vary from manufacturer to manufacturer and even from batch to batch. Leggett et al. (1977) presented data for TNT and showed that for eight samples of production grade military TNT, the percentage of impurities by mass varied from 0.2 % to 1.6 %.

Details of the constituent components of TNT are given in Appendix A.2

2.1.2 Vapour pressure

The vapour pressure, P_0 [Pa], or more accurately, equilibrium vapour pressure of a substance is the pressure exerted by the vapour in thermodynamic equilibrium with its condensed phases (solid or liquid) at a given temperature, T [K], in a closed system.

[1] Most explosives that are used industrially or militarily contain a taggant, typically a volatile liquid, which is easier to detect than the explosive itself.

For an ideal gas, the concentration of the vapour that exists above a solid or liquid, C_0 [kg·m^{-3}], can be given in terms of the vapour pressure, P_0, and the molecular weight, MW [kg·mol^{-1}], or the vapour pressure and the molecular mass, M_a [kg].

$$C_0 = \frac{P_0 MW}{R\,T}, \tag{2.3}$$

$$C_0 = \frac{P_0 M_a}{K_B\,T}, \tag{2.4}$$

where K_B is Boltzmann's constant, which is 1.381×10^{-23} J·K^{-1}. The molecular mass is the mass of one molecule which equals $\left(\frac{K_b}{R} MW\right)$ or $\left(\frac{MW}{N_A}\right)$, where N_A [mol^{-1}] is Avogadro's constant.

A number of sources provided empirical data for vapour pressures for explosives or the compounds within explosives e.g. Gongwer (2005); Ostmark et al. (2012); Ewing et al. (2013). Gongwer and Ewing et al. presented vapour pressure data from a range of sources for explosives, associated manufacturing and processing compounds, taggants, and decomposition products. Data from Ewing et al., Ostmark et al. and Gongwer is shown in Figure 2.2 to illustrate the range of vapour pressures for materials of interest at 25 °C and also the variability in some of the data. The spread of the data highlights the variability in this information and shows that there are often no single definitive values for vapour pressure for any one compound at a particular temperature. The data presented by Ostmark et al. also highlighted the temperature dependence of the vapour pressure. A change in temperature from 20 °C to 25 °C results in more than an doubling of P_0 for TNT.

2.1.3 Partial pressure of a compound above a mixture

Section 2.1.2 discussed the vapour pressure of individual compounds. However, as explosives are typically made up of mixtures of compounds, the concentration of vapour of each compound will differ from that of the pure substance. The concentration of each compound in the mixture can be defined by its partial pressure, P_n [Pa]. The partial pressure of all components added together would equal the vapour pressure.

Raoult's law describes how the partial pressure of a compound varies as a function of its mole fraction in a mixture and is given by the following equation. Raoult's law is usually applied to liquid mixtures but can also be applied to solid mixtures (Goldfarb and Suuberg, 2010).

$$P_n = P_{0,n}\,x_n, \tag{2.5}$$

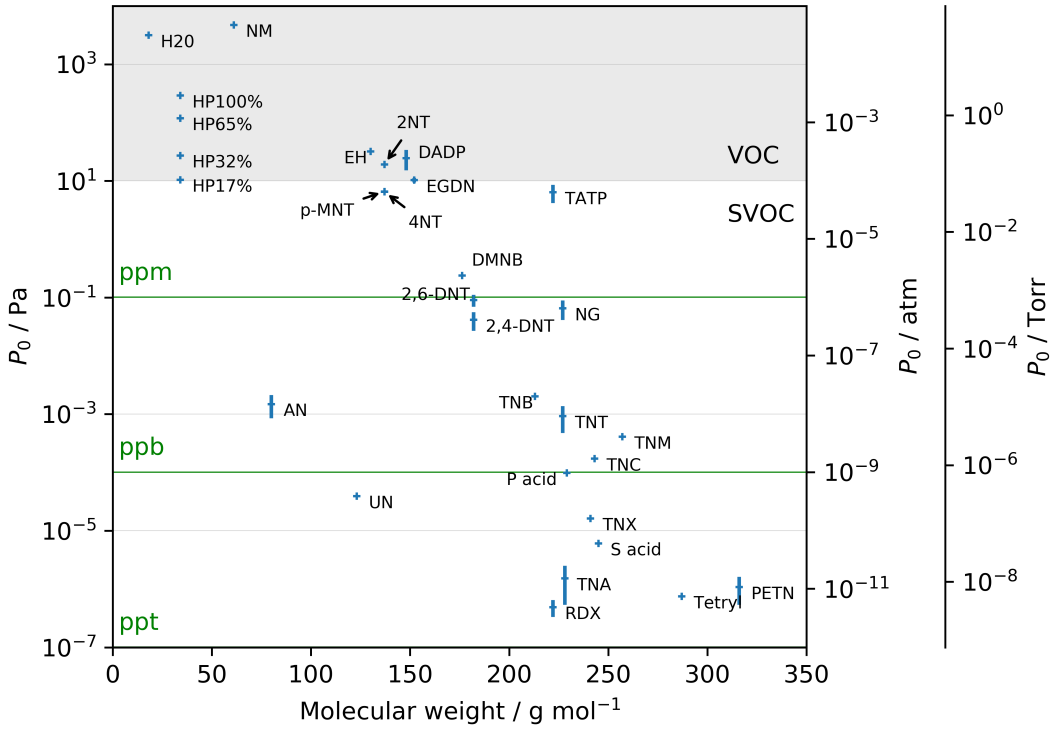

Figure 2.2: Vapour pressures, P_0, for a selection of explosive compounds and associated materials at 25 °C. The error bars represent ± standard deviation. Only one value was available for some of the data, so no error bars are shown in these cases. The meanings of the acronyms is given in the appendix in Table A.1. H20 is water.

where $P_{0,n}$ [Pa] is the vapour pressure of the pure compound, n and x_n is the mole fraction of compound n in the mixture. Raoult's law assumes that the partial pressure scales linearly with mole fraction.

Raoult's law often does not hold as it is based on the assumption that intermolecular forces between unlike molecules are equal to those between similar molecules. Goldfarb and Suuberg (2010) described its applicability for solid mixtures of polyaromatic hydrocarbons and report however that it is a fair approximation for the systems they studied (mole fractions ranged from only 0.33 to 0.5). An alternative to Raoult's law is Henry's law which can be written as

$$P_n = K_H \, x_n, \tag{2.6}$$

where K_H is the Henry's law constant [Pa]. Henry's law constants are typically empirical values which may vary with x_n. As can be seen from Equation 2.5 and 2.6, if the Henry's law constant for a compound equals the vapour pressure of the pure compound then Henry's law becomes equivalent to Raoult's law.

Leggett et al. (1977) presented Henry's law data for 2,4 DNT within TNT for a range of production grade military TNT samples. 2,4 DNT makes up only a small percentage of TNT (e.g. 0.096 % by mol (Leggett et al., 1977)) however the vapour pressure for 2,4-DNT is much higher than that for TNT. The vapour pressure for TNT is 3.51×10^{-4} Pa and 2,4 DNT is 1.53×10^{-2} Pa at 20 °C (Gongwer, 2005). According to Raoult's law, if 2,4 DNT makes up 0.096 % by mole then its partial pressure should be 1.47×10^{-5} Pa. From empirical measurement Leggett showed that the actual partial pressure of 2,4-DNT above the samples he tested was on average 2.86×10^{-3} Pa. Therefore if Raoult's law was used instead of Henry's law the predicted vapour pressure would have been underestimated by a factor of almost 200. The average Henry's law constant at 20 °C for the samples tested by Leggett was 2.78 Pa.

Leggett et al. (1977) postulated that their data indicated that less energy is required to volatilise 2,4 DNT from TNT than from pure 2,4 DNT which suggested that the intermolecular forces are weaker in a TNT matrix.

The same effect was described by Lovestead and Bruno (2010), who presented headspace concentration data for dimethyl-dinitrobutane (DMNB) above C-4. At 20 °C the vapour concentration was 4.46×10^{-3} g·m^{-3} and the C-4 contained between 1.0 % and 1.5 % DMNB[2]. The vapour pressure concentration of pure DMNB according to Gongwer at 20 °C is 9.28×10^{-3} g·m^{-3}. If DMNB made up 1.25 % then its partial pressure would be expected to be 1.16×10^{-4} g·m^{-3}. This means that the actual partial pressure was almost 40 times higher than would have been predicted by Raoult's law.

In summary, care needs to be taken when using vapour pressures measured from pure substances for mixtures, particularly when the component of interest is a small fraction of the total weight.

2.1.4 The effects of ageing on explosives

As stated previously, the chemical signature that is produced from an explosive may change with time as the material ages. As it ages, the total mass of volatile components will reduce more than the total mass of less volatile components, particularly those near to the surface. The ageing process may be accelerated at higher temperatures.

Leggett et al. (1977) presented vapour pressure data for eight samples which had been manufactured using different processes over the preceding 30 years. They showed that there was no discernible relationship between sample age and mole fraction of TNT and 2,4 DNT. This suggests that the 2,4 DNT was not being depleted to a level that could be detected over tens of years. The experiments of Leggett et al. were conducted using

[2]It is not clear whether this is percentage by mole or weight. As the molecular weights of DMNB (176.17 g·mol^{-1}) and the predominant material in C-4, RDX (222.12 g·mol^{-1}) are not too dissimilar the results will not differ greatly either way.

samples taken from larger original samples which were left to reach an equilibrium state in small vials for two weeks. The equilibrium state would mean that there is no further net transfer of vapour from the solid into the air, this would then allow for any regions near the surface of the explosive that had become partially depleted of 2,4 DNT to be replenished.

Trace samples of explosives (10 µg) have been shown to age over reasonably short time periods under outdoor environmental conditions. Clark et al. (2010) and Kunz et al. (2012) showed that the TNT within 10 µg samples of TNT or the explosive composition-B had a half-life (i.e. the time at which half the solid material has been lost) between less than one hour and tens of hours depending on the ambient meteorological conditions and the type of surface on which the material was deposited. RDX in C-4 or composition-B was shown to have a half-life that varied from a few hours to more than 400 h. The degradation was reported to be due to both chemical photo-degradation (due to ultra-violet (UV) radiation) and sublimation. Kunz et al. suggested that the photo-degradation may only act on the outer 2 µm of material (due to the penetration depth of the UV radiation) and that for TNT the breakdown products from the degradation may actually slow the sublimation rate.

This PhD research only considers bulk samples in indoor environments so it is assumed that the effects of ageing will be negligible.

2.1.5 Molecular diffusion coefficients for vapours in air

The molecular diffusion coefficient for a vapour in air, D_m, is important for both predicting the vapour production rate (Gershanik and Zeiri, 2010) and vapour transport when the air movement is very slow.

The molecular diffusion coefficients of explosive vapours in air can be estimated from their molecular weights and other parameters using a number of different methods as described in Poling et al. (2007) and Guo (2002). One method is given in Appendix A.3.

Phelan and Webb (1997) gave measured diffusion coefficients for TNT and DNT in air at 27 °C of $4.5 \times 10^{-6}\,\mathrm{m^2{\cdot}s^{-1}}$ and $4.8 \times 10^{-6}\,\mathrm{m^2{\cdot}s^{-1}}$ respectively. The model given in Appendix A.3 gives diffusivities of $6.7 \times 10^{-6}\,\mathrm{m^2{\cdot}s^{-1}}$ and $7.1 \times 10^{-6}\,\mathrm{m^2{\cdot}s^{-1}}$ for TNT and DNT respectively. Based on this limited data, the model prediction is within a factor of 1.5.

2.1.6 Diffusion through the solid matrix of the explosive.

To calculate the importance of internal and external processes on vapour production, the diffusion coefficient for vapour in the solid, D_{solid}, is required. D_{solid} is also required for some sorption and permeation models (see Section 2.3 and Chapter 5).

To date, only one study (Zhou et al., 2011) has been found on predicting diffusion rates through the solid matrix of the explosive. Ideally more work should be carried out in this area. Zhou et al. (2011) carried out molecular modelling for the migration of 2,4,6 TNT in the fluorine rubber binder of polymer-bonded explosives. The authors reported values at 27 °C of $D_{solid} = 6.8 \times 10^{-12}\,\mathrm{m^2{\cdot}s^{-1}}$, at 67 °C, $D_{solid} = 4.16 \times 10^{-11}\,\mathrm{m^2{\cdot}s^{-1}}$ and at 107 °C, $D_{solid} = 6.08 \times 10^{-11}\,\mathrm{m^2{\cdot}s^{-1}}$. They compared their data to an experimental data set and their predictions were approximately one order of magnitude lower. The empirical data was however for soil as opposed to a rubber.

Tung et al. (1997) used the Fourier transform infra-red spectroscopy-attenuated total reflectance (FTIR-ATR) technique to measure the diffusion of TNT through acrylonitrile butadiene rubber. They gave values for D_{solid} in the order of $10^{-11}\,\mathrm{m^2{\cdot}s^{-1}}$ in the temperature range of 90 °C to 110 °C which is comparable to the data from Zhou et al..

Cragin and Leggett (2003) reported diffusion coefficients for 2,4,6 TNT, 2,4 DNT and 1,3 dinitrobenzene (DNB) in five plastic materials (which were surrogates for landmine casings). The plastics were high density polyethylene (HDPE), low density polyethylene (LDPE), polypropylene (PP), polystyrene (PS) and PVC. The plastic samples were saturated with vapour over six months and vapour loss measured into air and water. The diffusion coefficients for transfer into air were measured at 21.5 °C. Values for D_{solid} for both compounds ranged from $1.1 \times 10^{-14}\,\mathrm{m^2{\cdot}s^{-1}}$ to $3.0 \times 10^{-13}\,\mathrm{m^2{\cdot}s^{-1}}$. These values are significantly lower than those given by Zhou et al. (between 23 and 618 times lower at 27 °C) and Tung et al.. Cragin and Leggett reported that diffusion coefficients in unplasticised materials can be several orders of magnitude lower than in plasticised materials or unplasticised material above their glass transition temperatures. Cragin and Leggett assumed that their materials were either above their glass transition temperature or had plasticisers added. Cragin and Leggett showed that their data was comparable to data for other aromatic compounds in HDPE and LDPE (plastics below their glass transition temperatures). Cragin and Leggett also commented that they thought the diffusion coefficient in the solid was concentration dependent. This was due to their data showing a faster initial rate of mass loss from the solid samples. This effect could, however, just be due to the system equilibrating.

2.1.7 Vapour emission summary

The Biot number ratio has been estimated for three compounds of interest for the detection of explosive, where the compound of interest does not make up the bulk of the solid. These are: EH and DMNB, which are both present in C-4 and 2,4 DNT which is present in TNT; the results are shown in Table 2.1. As stated earlier, for explosives where the compound of interest makes up most of the weight of the explosive (e.g. TNT and pure EGDN) it can be assumed that only the external process need to be considered.

The mass transfer coefficient, a, was calculated using the model of Danberg (2008) (see Section 3.3.2). The friction velocity, required for the Danberg model, was taken from the CFD model described in Chapter 3, using the large source in slow flowing air on the left of the room. The diffusion coefficient in air for the vapours was calculated according to the model in Appendix A.3. The explosive block was assumed to be 0.01 m thick and the ratio in Equation 2.1 was calculated for $L_s = 0.01\,\text{m}$ and an arbitrary 0.001 m (i.e. assuming that most of the concentration gradient was located in a small region close to the surface).

As discussed in Section 2.1.6, data for the solid phase diffusion coefficient for the compounds and solids of interest is not readily available so this parameter was taken to be $1 \times 10^{-13}\,\text{m}^2\cdot\text{s}^{-1}$ based on the average data for 2,4 DNT diffusion through a range of polymers. The vapour phase concentrations were calculated as described in Section 2.1.2. If it is assumed that Raoult's law applies then the partition coefficient, K_{ab}, will be independent of the fraction of EH and DMNB in the explosive. This is because partial pressure will scale by the same fraction. However, data for 2,4 DNT in TNT shows that Henry's law should be used in this case. Henry's law data for 2,4 DNT in TNT at 20 °C (Leggett et al., 1977) was used.

Vapour	L_s	a	Bi_m	$\frac{Bi_m}{K_{ab}}$
	m	$\text{m}\cdot\text{s}^{-1}$		
EH	1×10^{-3}	1×10^{-3}	1×10^{7}	10
EH	1×10^{-2}	1×10^{-3}	1×10^{8}	100
DMNB	1×10^{-3}	1×10^{-3}	1×10^{7}	0.1
DMNB	1×10^{-2}	1×10^{-3}	1×10^{8}	1
2,4 DNT	1×10^{-3}	1×10^{-3}	1×10^{7}	1
2,4 DNT	1×10^{-2}	1×10^{-3}	1×10^{8}	10

Table 2.1: The mass transfer Biot number and Biot number ratio for three compounds and two values of L_s.

The data in Table 2.1 shows that the Biot number ratio is only less than one for DMNB when the concentration gradient is contained in the top 1 mm layer of the explosive. For the more volatile EH, the ratio is greater than 1 in all cases, which agrees with the assessment of Liu et al. (2013), as EH can be classed as a VOC. 2,4 DNT is less volatile than DMNB and has a lower Bi_m but because of the Henry's law effect it has a higher ratio, which is 1 or above for both values of L_s. The solid phase diffusion coefficient was only an estimate and was based on the range of data presented in Section 2.1.6, it could easily be an order of magnitude higher or lower.

Based on this assessment, when there is an air flow over an explosive, the emission of any VOC component of an explosive should be considered to be a process where internal diffusion is the controlling factor. For compounds with vapour pressures close

to 2,4 DNT, particularly when the fraction of that component in the mixture is small (therefore Henry's law may be important), both external and internal processes should be considered.

In order to simplify the modelling in this PhD, only externally limited vapour production is considered. Therefore, only compounds of interest where the compound makes up most of the weight of the explosive i.e. TNT and pure EGDN will be modelled. It will be assumed that concentrations adjacent to the surface of the explosive can be calculated from the vapour pressure of the compound.

2.2 Vapour transport

Vapour can be transported through the air from the source to the detector (dog or electronic equipment) by two physical processes: advection and diffusion. Advection is transport due to a fluid's motion and diffusion is transport from regions of high to low concentration and is a result of random mixing.

As stated earlier, even with all of the complexity of indoor air flow, transport indoors can often be represented by a diffusion model. This approach, called eddy diffusion modelling, can be applied when there is isotropic mixing on a large scale (i.e. room scale) due to laminar and/or turbulent motion. The validity of the eddy diffusion approach has been demonstrated in indoor spaces by Cheng et al. (2011); Drivas et al. (1996); Shao et al. (2017). Eddy diffusion models have been applied to rooms ranging in size from approximately $50\,\mathrm{m}^3$ (Cheng et al., 2011) to over $20\,000\,\mathrm{m}^3$ (Nicas, 2009) and with air change rates from less than $0.2\,\mathrm{h}^{-1}$ (Cheng et al., 2011) to $15\,\mathrm{h}^{-1}$ (Cooper and Horowitz, 1986). They have also been applied to rooms with small non-isotropic flow, for example by Shao et al. (2017).

Eddy diffusion models provide a useful guide to the concentration distributions in the room but cannot easily cover more complex or realistic scenarios and a CFD model is typically required in these cases. CFD modelling, and particularly LES, is uniquely placed to provide detailed information on the unsteady, spatially varying, complex flow and dispersion which occurs in indoor spaces.

2.2.1 Eddy diffusion modelling

A number of analytical models for diffusion in indoor spaces have been derived by, for example, Crank (1979) and Nehorai (1995). These models have application in the study of the transport of vapour from explosives in environments where advection is disordered and simply has the effect of mixing the vapour, in which case D would be the eddy diffusion coefficient, D_e $[\mathrm{m}^2{\cdot}\mathrm{s}^{-1}]$.

Eddy diffusion models have been used to predict spatially resolved exposures to toxic airborne materials in indoor environments, for example see Scheff et al. (1992); Shade and Jayjock (1997); Donovan et al. (2011); Zontek et al. (2019). The method is also described in the American Industrial Hygiene Association (AIHA) book 'Mathematical Models for Estimating Occupational Exposure to Chemicals' (Nicas, 2009) and is one of the tools included in the AIHA IH Mod 2.0 software (Drolet and Armstrong, 2018).

The eddy diffusion coefficient for indoor spaces has been calculated from a number of experimental studies (Nicas, 2009; Cheng et al., 2011; Drivas et al., 1996; Cooper and Horowitz, 1986; Scheff et al., 1992; Shao et al., 2017) and empirical or *a priori* relationships have also been produced for certain situations (Karlsson et al., 1994; Drivas

et al., 1996; Cheng et al., 2011). The experimentally calculated values have been shown to range from a suggested lower limit of $1 \times 10^{-3}\,\mathrm{m^2{\cdot}s^{-1}}$ (Drivas et al., 1996) to as high as $1.9 \times 10^{-1}\,\mathrm{m^2{\cdot}s^{-1}}$ (Nicas, 2009).

Even with this experimental data and the models, there is still a large amount of uncertainty over what D_e should be in different situations. Therefore, part of this PhD research has focussed on improving a model for D_e which was proposed by Karlsson et al. (1994) and used by Drivas et al. (1996) and Shao et al. (2017). This work is reported in Chapter 6.

2.2.2 CFD modelling

CFD modelling is based on the use of numerical methods to solve the Navier-Stokes equations. The Navier-Stokes equations describe the advective and diffusive transport of a fluid. They are derived by equating the rate of change of momentum for a fluid volume to the sum of forces on the volume. Equation 2.7 shows the Navier-Stokes equations for an incompressible fluid in tensor notation.

$$\rho\left[\frac{\partial u_i}{\partial t} + \frac{\partial}{\partial x_j}(u_i u_j)\right] = -\frac{\partial P}{\partial x_i} + \mu\frac{\partial}{\partial x_j}\left(\frac{\partial u_i}{\partial x_j}\right), \tag{2.7}$$

where ρ [$\mathrm{kg{\cdot}m^{-3}}$] is the density, u [$\mathrm{m{\cdot}s^{-1}}$] is the velocity, P [Pa] is the pressure and μ [$\mathrm{kg{\cdot}m^{-1}{\cdot}s^{-1}}$] is the dynamic viscosity.

2.2.2.1 Natural convection

For buoyant flows, an additional buoyancy term can be added to the incompressible, Navier-stokes equation. When the variation in density due to temperature differences is only accounted for in a buoyancy term; this is called the Boussinesq model. When the Navier-Stokes equations with a buoyancy term are non-dimensionalised, the buoyancy force becomes a function of the non-dimensional temperature difference and the following ratio (Jiji, 2009), called the Richardson number, Ri [dimensionless].

$$Ri = \frac{Gr}{Re^2}, \tag{2.8}$$

where Gr [dimensionless] is the Grashof number, given by the following:

$$Gr = \frac{\beta\, g \Delta T\, L_{char}^3}{\nu^2}, \tag{2.9}$$

where β [K^{-1}] is the thermal expansion coefficient (approximately $0.003\,K^{-1}$ for air at room temperature), g is acceleration due to gravity ($9.81\,m{\cdot}s^{-2}$) and ΔT [K] is the temperature difference across a characteristic length L_{char} [m]. The Richardson number can also be used to indicate the stabilising effect of stratification and is often evaluated for atmospheric flows.

The Richardson number describes the relative importance of buoyancy forces and forced convection forces. If this ratio is close to or exceeds 1, then buoyancy forces become important (Mills, 1995).

If the air velocity in a room is in the middle of the range measured by Finkelstein et al. (1996) in ventilated rooms (i.e. $0.325\,m{\cdot}s^{-1}$) and L_{char} is approximated to the cube root of the volume of a ventilation zone (3 m for example), then $Re \approx 7.0 \times 10^4$. Even with a temperature difference of only 1 K across the space and using the same value for L_{char}, $Gr \approx 4 \times 10^9$ and the Richardson number ≈ 0.8. Therefore, in a typical mechanically ventilated space, in which there is a heat source distributed across the space (e.g. people in the room), buoyancy forces could be significant. The relative importance of buoyancy forces would be expected to be even larger in naturally ventilated spaces or spaces with lower ventilation rates than those studied by Finkelstein et al. (1996).

In order to simplify the problems studied in this PhD it will be assumed that the Richardson numbers in the rooms of interest are much less than 1. This would be representative of rooms which are empty of local heat sources or have sufficient mixing to remove temperature gradients.

2.2.2.2 Turbulence modelling

In order to allow for solution of the Navier-Stokes equations in a wide range of problems, the equations can be time averaged. Each time varying property, ϕ, can be broken down into a mean component, $\bar{\phi}$ and a fluctuating component, ϕ' as represented by the following equation, whether ϕ is a scalar or a vector.

$$\phi = \bar{\phi} + \phi' \tag{2.10}$$

If the terms in the Navier-Stokes equations (2.7) are replaced with the mean plus fluctuating components and the equations are time averaged, this results in the RANS equations.

$$\rho\left[\frac{\partial \overline{u_i}}{\partial t} + \frac{\partial}{\partial x_j}(\overline{u_i}\,\overline{u_j})\right] = -\frac{\partial \overline{P}}{\partial x_i} + \mu\frac{\partial}{\partial x_j}\left(\frac{\partial \overline{u_i}}{\partial x_j}\right) - \left(\frac{\partial \overline{u_i' u_j'}}{\partial x_j}\right) \tag{2.11}$$

The extra terms that the RANS equations have over the Navier-Stokes equations are called the Reynolds stresses. Turbulence models are required to represent these Reynolds stresses in order to be able to close the RANS equations. As an alternative to the RANS approach, the Navier-Stokes equations can be filtered to separate the effects of the large and small scale eddies, with the large eddies being resolved directly and the effects of the small eddies being modelled. This approach is called large-eddy simulation and is discussed in Section 2.2.2.3.

A large number of turbulence models are based on the Boussinesq hypothesis (Equation 2.12) where the Reynolds stresses are related to the strain rate through the use of a turbulent viscosity, μ_t [kg·s^{-1}·m^{-1}]. This class of turbulence models is called eddy viscosity models and include the k-ϵ and k-ω models and mixing length models.

An alternative to the eddy viscosity turbulence modelling approach is given by the Reynolds stress model (RSM). The RSM avoids some of the problems eddy viscosity models have by solving transport equations for the six independent Reynolds stresses. This can have the advantage of broader generality, compared to eddy viscosity models, and allows for anisotropy in the turbulence. The main disadvantages of the RSM are the extra computational cost required to solve the additional equations and the need to specify the Reynolds stresses at the inlet. The RSM was compared to eddy viscosity models for the prediction of air flow in an indoor benchmark test-case (Nielsen, 1990) in Chapter 5. In this comparison, the RSM gave no significant advantages so was not pursued any further in this work.

The standard k-ϵ (Launder and Spalding, 1972) and k-ω (Wilcox, 1998) models work by solving transport equations for the turbulent kinetic energy, k [m^2·s^{-2}] (equation 2.13), the turbulent kinetic energy dissipation rate, ϵ [m^2·s^{-3}] (Equation 2.14), or the specific turbulent kinetic energy dissipation rate ω [s^{-1}] (Equation 2.16). The turbulent viscosity, μ_t, is then calculated from k and ϵ (Equation 2.15) or k and ω (Equation 2.17). A variant of the k-ω model, called the k-ω shear stress transport (SST) model (Mentor, 1994) uses a standard k-ω approach in near-wall regions with a k-ϵ model away from the wall.

The k-ω model has an advantage over the k-ϵ model in that ω can be calculated right through the near-wall region, whereas the transport equation for ϵ cannot be solved in this region so ϵ has to be computed algebraically.

$$-\rho\overline{u_i'u_j'} = \mu_t\left(\frac{\partial u_i}{\partial x_j}+\frac{\partial u_j}{\partial x_i}\right)-\frac{2}{3}\left(\rho k+\mu_t\frac{\partial u_k}{\partial x_k}\right)\delta_{ij}, \tag{2.12}$$

$$\frac{\partial}{\partial t}(\rho k)+\frac{\partial}{\partial x_i}(\rho k u_i)=\frac{\partial}{\partial x_j}\left[\left(\mu+\frac{\mu_t}{\sigma_k}\right)\frac{\partial k}{\partial x_j}\right]+G_k+G_b-\rho\epsilon, \tag{2.13}$$

$$\frac{\partial}{\partial t}(\rho\epsilon) + \frac{\partial}{\partial x_i}(\rho\epsilon u_i) = \frac{\partial}{\partial x_j}\left[\left(\mu + \frac{\mu_t}{\sigma_\epsilon}\right)\frac{\partial \epsilon}{\partial x_j}\right] + C_{1\epsilon}\frac{\epsilon}{k}\left(G_k + C_{3\epsilon}G_b\right) - C_{2\epsilon}\rho\frac{\epsilon^2}{k}, \quad (2.14)$$

$$\mu_t = \rho C_\mu \frac{k^2}{\epsilon}, \quad (2.15)$$

$$\frac{\partial}{\partial t}(\rho\omega) + \frac{\partial}{\partial x_i}(\rho\omega u_i) = \frac{\partial}{\partial x_j}\left[\left(\mu + \frac{\mu_t}{\sigma_\omega}\right)\frac{\partial \omega}{\partial x_j}\right] + G_\omega - Y_\omega, \quad (2.16)$$

$$\mu_t = \alpha^* \frac{\rho k}{\omega}, \quad (2.17)$$

where δ_{ij} [dimensionless] is the Kronecker delta, which equals zero if $i \neq j$ or one if $i = j$. G_k [kg·m^{-1}·s^{-3}], G_b [kg·m^{-1}·s^{-3}] and G_ω [kg·m^{-1}·s^{-3}] represent generation of k and ω. $C_{1\epsilon}$, $C_{2\epsilon}$, $C_{3\epsilon}$ and C_μ are constants. σ_k and σ_ϵ are the dimensionless turbulent Prandtl numbers. Y_ω [kg·m^{-3}·s^{-2}] represents the dissipation of ω. In the k-ω model the $\rho\epsilon$ term in Equation 2.13 is replaced with Y_k [kg·m^{-1}·s^{-3}], which represents dissipation of k. The coefficient α^* damps the turbulent viscosity in the k-ω model.

In the near-wall region, non-dimensional velocity (parallel to the wall), u^+, follows a standard profile when plotted against non-dimensional distance from the wall, y^+. $u^+ = \frac{u}{u_\tau}$ and $y^+ = \frac{u_\tau y}{\nu}$ where u_τ [m·s^{-1}] is the friction velocity and y [m] is the distance from the cell centre to the wall. The standard profile has a linear layer called the viscous sub-layer near the wall, i.e. $y^+ \leq 5$, where $u^+ = y^+$, and a logarithmic layer at approximately $y^+ >$60. The region between the viscous sub-layer and logarithmic layer is called the buffer layer. If the first computational cell is placed in the logarithmic region then a wall function can be applied which relates u^+ to y^+ based on a logarithmic relationship. If the first cell is placed in the viscous sub-layer then a linear relationship can be applied. Some CFD software offers a blended wall function to calculate u^+ wherever the first cell is placed.

2.2.2.3 Large-eddy simulation

The principle behind LES is that the large eddies, which contain most of the kinetic energy, are simulated, whereas the smallest eddies, which tend to be more universal in their nature, are modelled. For LES, the Navier-Stokes and continuity equations are filtered to allow for separation of the resolved and modelled eddies.

A filtered variable, represented by an tilde (e.g. $\widetilde{\phi}$), is given by the following,

$$\widetilde{\phi}(\mathbf{x}) = \int_{\mathbf{\Omega}} \phi(\mathbf{x} - \zeta)\mathbf{G}(\mathbf{x}, \zeta)\mathbf{d}\zeta, \quad (2.18)$$

where $\mathbf{x}$ is the location at which $\widetilde{\phi}$ is being calculated, Ω is the computational domain, ζ is a position vector and G is the spatial filter function. A simple filter function is the top-hat, which is given by the following,

$$G(\mathbf{x},\zeta)\begin{cases}\frac{1}{\Delta}, & |\mathbf{x}-\zeta| \leq \frac{\Delta}{2} \\ 0, & \text{otherwise,}\end{cases} \tag{2.19}$$

where Δ is the filter width. Other types of filter exist, including those that operate in the spectral domain.

The filtered Navier-Stokes equations for incompressible flow are the following,

$$\rho\left[\frac{\partial\widetilde{u_i}}{\partial t}+\frac{\partial}{\partial x_j}(\widetilde{u_i}\,\widetilde{u_j})\right]=-\frac{\partial\widetilde{P}}{\partial x_i}+\frac{\partial}{\partial x_j}\left(\mu\frac{\partial\widetilde{u_i}}{\partial x_j}-\tau_{ij}\right) \tag{2.20}$$

The additional term in the filtered Navier-Stokes equation is the subgrid scale stress tensor, τ_{ij} [kg·s^{-2}·m^{-1}] which is defined as the following,

$$\tau_{ij}=\rho\widetilde{u_i u_j}-\rho\widetilde{u_i}\,\widetilde{u_j} \tag{2.21}$$

The subgrid scale stresses are usually modelled using the eddy viscosity approach as employed in a range of turbulence models. The subgrid scale stress tensor is therefore given by the following,

$$\tau_{ij}=-2\mu_{t,sgs}\widetilde{S_{ij}}+\frac{1}{3}\tau_{kk}\delta_{ij}, \tag{2.22}$$

where $\mu_{t,sgs}$ [kg·s^{-1}·m^{-1}] is the subgrid scale turbulent viscosity, $\widetilde{S_{ij}}$ [s^{-1}] is the strain rate tensor. $\widetilde{S_{ij}}$ is given by the following,

$$\widetilde{S_{ij}}=\frac{1}{2}\left(\frac{\partial\widetilde{u_i}}{\partial x_j}+\frac{\partial\widetilde{u_j}}{\partial x_i}\right) \tag{2.23}$$

The subgrid scale turbulent viscosity, $\mu_{t,sgs}$, can be calculated using a subgrid scale model.

2.2.2.4 Subgrid scale models

One of the most widely used subgrid scale models is the Smagorinsky-Lilly model (Smagorinsky, 1963) for which $\mu_{t,sgs}$ is given by the following,

$$\mu_{t,sgs}=\rho L_{m,sgs}^2\left|\widetilde{S}\right|. \tag{2.24}$$

$L_{m,sgs}$ [m] is the mixing length for the subgrid scales, given by the following,

$$L_{m,sgs} = min\left(c_v d_c, C_s \Delta\right), \tag{2.25}$$

where c_v is the Von Karman constant, d_c [m] is the distance to the closest wall, C_s is the Smagorinsky constant and Δ [m] is the local grid scale, given by $\sqrt[3]{V_c}$, where V_c [m^3] is the cell volume. $\left|\widetilde{S}\right|$ [s^{-1}] is given by the following,

$$\left|\widetilde{S}\right| \equiv \sqrt{2\widetilde{S_{ij}}\ \widetilde{S_{ij}}}. \tag{2.26}$$

An improvement to the Smagorinsky-Lilly is the dynamic Smagorinsky-Lilly (DS) model. In this model the Smagorinsky constant is calculated locally during the simulation by applying a second filter scale, $\widehat{\Delta}$, called the test-filter (Germano et al., 1991; Lilly, 1992). The test-filter is typically double the size of the subgrid-filter. The test-filtered Navier-Stokes equation produces a subtest-scale stress tensor, T_{ij} [kg·s^{-2}·m^{-1}].

$$T_{ij} = \rho\widehat{\widetilde{u_i}\widetilde{u_j}} - \rho\widehat{\widetilde{u}_i}\ \widehat{\widetilde{u}_j}. \tag{2.27}$$

T_{ij} and τ_{ij} are modelled in the same way as in the standard Smagorinsky model (cf. Equation 2.22). A hat indicates a test-filtered variable, $\widehat{\phi}$.

$$T_{ij} = -2C_{DS}\,\rho\widehat{\Delta}^2\left|\widehat{\widetilde{S}}\right|\widehat{\widetilde{S_{ij}}} + \frac{1}{3}T_{kk}\delta_{ij} \tag{2.28}$$

and

$$\tau_{ij} = -2C_{DS}\,\rho\Delta^2\left|\widetilde{S}\right|\widetilde{S_{ij}} + \frac{1}{3}\tau_{kk}\delta_{ij}, \tag{2.29}$$

where C_{DS} is the dynamic Smagorinsky model constant. T_{ij} and τ_{ij} are related to each other by the Germano identity (Germano et al., 1991).

$$L_{ij} = T_{ij} - \widehat{\tau_{ij}} = \rho\widehat{\widetilde{u_i}\ \widetilde{u_j}} - \rho\widehat{\widetilde{u}_i}\ \widehat{\widetilde{u}_j}, \tag{2.30}$$

where L_{ij} [kg·s^{-2}·m^{-1}] can be thought of as the stresses between the test-filter scale and the grid-filter scale. L_{ij} can be calculated from the resolved field. Lilly (1992) showed that you can calculate C_{DS} from the following

$$C_{DS} = \frac{(L_{ij} - L_{kk}\delta_{ij}/3)}{M_{ij}M_{ij}}, \tag{2.31}$$

where

$$M_{ij} = -2\left(\widehat{\Delta}^2\rho\left|\widehat{\widetilde{S}}\right|\widehat{\widetilde{S_{ij}}} - \Delta^2\rho\,\widehat{|\widetilde{S}|\widetilde{S}_{ij}}\right). \tag{2.32}$$

It should be noted that C_{DS} is equivalent to the square of the standard Smagorinsky constant, C_S. $\sqrt{C_{DS}}$ is usually bounded and spatially averaged locally to aid stability. In ANSYS® Fluent® (hereon referred to as Fluent) for example, $\sqrt{C_{DS}}$ is clipped at zero and 0.23 and is locally averaged over the test-filter.

The DS model has been shown to perform better in modelling indoor air flows than the standard Smagorinsky model. For example (Davidson and Nielsen, 1996) demonstrated this in a simple test-case room.

2.2.2.5 Species transport

The conservation equation for species transport due to convection and diffusion (without a species source) is given by the following,

$$\rho \left[\frac{\partial Y}{\partial t} + \frac{\partial}{\partial x_i}(u_i Y) \right] = \frac{\partial}{\partial x_j} \left(D \frac{\partial Y}{\partial x_j} \right), \tag{2.33}$$

where Y [kg·kg^{-1}] is the species concentration mass fraction. For a laminar flow, D is the molecular diffusion coefficient, D_m.

The species transport equation can be non-dimensionalised to show that the diffusive terms in the equation are multiplied by one over the dimensionless Schmidt number, Sc, where Sc is given by the following,

$$Sc = \frac{\mu}{\rho\, D}. \tag{2.34}$$

A small Sc means that the diffusion term is important and a large Sc means that diffusion term is small and advective transport is more important. A Schmidt number of close to 1 means that diffusion of a vapour compound in air takes place at a similar rate to the dissipation of momentum and therefore the smallest eddies will be similar in size to the smallest vapour structures (Koehl, 2006).

D_m for EGDN and TNT at 20 °C are $8.5 \times 10^{-6}\,\mathrm{m^2{\cdot}s^{-1}}$ and $6.5 \times 10^{-6}\,\mathrm{m^2{\cdot}s^{-1}}$ respectivley. With $\mu = 1.8 \times 10^{-5}\,\mathrm{kg{\cdot}m^{-1}{\cdot}s^{-1}}$ and $\rho = 1.2\,\mathrm{kg{\cdot}m^{-3}}$ for air at 20 °C, $Sc = 1.8$ for EGDN and 2.3 for TNT.

For a turbulent flow D is given by the following,

$$D = \left(D_m + \frac{\mu_t}{\rho Sc_t} \right), \tag{2.35}$$

where Sc_t is the dimensionless turbulent Schmidt number. Sc_t is defined as

$$Sc_t = \frac{\mu_t}{\rho\, D_t}, \tag{2.36}$$

where D_t [$m^2 \cdot s^{-1}$] is the turbulent diffusivity[3]. The default value for Sc_t in Fluent is 0.7. By defining Sc_t, the only unknown in Equation 2.35 is μ_t and this is calculated by the turbulence model (e.g. Equation 2.15). Studies have shown (Tominaga and Stathopoulos, 2007) that the optimum value for Sc_t ranges from 0.2 to 1.3 depending on the class of problem being solved. Another review of Sc_t is given by van Hooff et al. (2014).

For large-eddy simulations in Fluent the subgrid scale species flux is calculated using Equation 2.35 but with the turbulent viscosity calculated by the subgrid scale model. Therefore, a subgrid turbulent Schmidt number, $Sc_{sg,t}$, is required. This number can be set to a fixed value or it can be calculated dynamically. Fluent's dynamic scalar flux model uses a similar approach to that used for the dynamic Smagorinsky model to calculate $Sc_{sg,t}$ and clips the variable at 0.1 and 10. Some details and an application of the dynamic scalar flux model are given in Liu and Barth (2002).

Tominaga and Stathopoulos (2007) reported that $Sc_{sg,t} = 0.5$ has been broadly used for LES modelling. However, Boppana et al. (2012) (turbulent channel flow) used 0.9 and Xie and Castro (2009) (outdoor dispersion) used 1.0.

2.2.3 CFD modelling of indoor air flow and indoor dispersion

CFD has been used for many years to study air flows and transport of species in indoor environments. The first CFD modelling of indoor airflows took place around the 1970s where Nielsen (1973) modelled a simple room with slot ventilation. Two reviews of the application of CFD to ventilation were conducted by Li and Nielsen (2011) and Nielsen (2015). A number of papers (e.g. Chen (1995); Zhang et al. (2007)) have compared the suitability of different turbulence modelling methods to different classes of indoor air flow problem.

Zhang et al. (2007) compared a wide range of turbulence models (from zero equation to LES) for a range of indoor airflow experimental data sets (natural ventilation, mixed ventilation, forced ventilation) using Fluent V6.2. The LES model provided the most detail in the flow solution for the forced convection case but the authors questioned its accuracy. They commented that the forced convection case had a low turbulence level but was not laminar and that the k-ω SST model never switched to the k-ω model due to the low turbulence levels throughout the domain. For the mixed ventilation case, the k-ω SST model performed the worst and under-predicted the turbulent kinetic energy k by 50 %. LES models took 100 to 1000 times longer to solve than the RANS models. Renormalization group (RNG) k-ϵ and $\overline{v^2}$-f models performed best for: accuracy, computing efficiency and robustness (for the RANS models). Overall, Zhang et al. (2007)

[3]The turbulent diffusion coefficient, D_t, is a measured of the rate of small scale turbulent mixing, whereas the eddy diffusion coefficient, D_e, relates to larger scale mixing due to both turbulent and laminar motion.

stated that one turbulence model may perform well in one geometry but less well in another. The LES model used was the dynamic Smagorinsky model.

A widely used validation data set for air flow in a mechanically ventilated room was described by Nielsen (1990). A number of studies have modelled the flow using either a two dimensional RANS approach (for example Chen (1995, 1996); Rong and Nielsen (2008); Le Dreau et al. (2012); Pulat and Nielsen (2015); Thysen (2015)) or three dimensional RANS approach (for example Nielsen et al. (2010); Cortes and Nielsen (2010); Susin et al. (2009); Mazzaro et al. (2010)). The studies all showed significant variation in results when applying different turbulence models (e.g. a change in the overall pattern of the streamlines) and other features such as an under-prediction of turbulence intensity. A smaller number of papers discuss application of LES (e.g. Zhang and Chen (2000); Davidson and Nielsen (1996); Muller and Davidson (2000); Voigt (2001); Han et al. (2019)). Of these, some used a coarse mesh (Davidson and Nielsen, 1996), while others used periodic boundary conditions on the side walls (Voigt, 2001). The study by Davidson and Nielsen (1996) used the dynamic Smagorinsky model having concluded that the standard Smagorinsky model was inadequate due to the need to optimise C_s. The Muller and Davidson (2000) study compared two different alternatives to the Germano et al. (1991) subgrid scale model. Lattice Boltzmann methods have also been used with some success (Elhadidi and Khalifa, 2013; Han et al., 2019).

Nielsen et al. (2010) discussed attempts to model the Nielsen (1990) isothermal, mechanically ventilated benchmark test-case and commented that different flow patterns have been predicted when using a range of turbulence models. Nielsen et al. (2010) commented that it is possible that these patterns were all present in his experiment but they were not there when measurements were taken. Nielsen et al. (2010) also commented on the possible three-dimensionality of the flow.

LES was first applied to indoor air flows in the 1990s (Davidson and Nielsen, 1996; Murakami et al., 1995) and, as stated previously, even these early studies concluded that the standard Smagorinsky subgrid scale model was inadequate so a dynamic model is required. More recent studies of indoor air flows using LES have been reported by Choi and Edwards (2008); Abdilghanie et al. (2009); Endregard et al. (2010); Choi and Edwards (2012); van Hooff et al. (2014).

CFD has been used widely to predict gas/vapour dispersion indoors (for example Gan and Awbi (1994); Foat et al. (2017); Yang and Chen (2001); Murakami et al. (2003); Deng and Kim (2007); Zhang and Zhang (2007); Wang et al. (2012); Sorensen and Weschler (2002)). Some studies used the Nielsen (1990) test-case (e.g. Nielsen (1981); Topp (1999); Sorensen and Weschler (2002)). A comparison of the ability of different CFD codes and turbulence models to predict the dispersion of hydrogen gas in a garage was given by Venetsanos et al. (2000). The collaborators used ten different commercial CFD codes with eight different turbulence models including two using LES and the

remainder using RANS models. Some of these studies include vapour sorption and or emission and these are discussed in more details in Section 2.3.

As discussed in the introduction, LES has been used to predict gas/vapour transport indoors. van Hooff et al. (2014) for example compared LES predictions (using the dynamic Smagorinsky model) to those from RANS for scalar transport in a slot ventilated enclosure with Re $\approx$ 2500 (based on the inlet height and velocity). They concluded that the RANS predictions were within a factor of two of the LES predictions because convective mass fluxes dominated in their domain. Endregard et al. (2010) used LES to study the consequences of the releases of a nerve agent in a large building and Choi and Edwards (2012) included the effects of people movement and door opening. As mentioned above, two collaborators used LES to predict hydrogen dispersion in a garage (Venetsanos et al., 2000). However, none of these studies include scalar releases from constant concentration sources or attempt to relate the time varying concentration to vapour or gas detection and few studies consider extreme concentrations.

Indoor air flow has also been studied using hybrid RANS and LES, i.e. detached-eddy simulation (DES) models. DES models use LES in the separated flow regions and a RANS model in the near-wall regions to avoid the stringent mesh requirements of LES. DES was used by Wang and Chen (2010) and they reported good results for their $\overline{v^2}$-f DES model for mixed convection and buoyancy driven indoor flows. However, DES suffers the same low accuracy problem in the near wall region as RANS model. It also receives criticism on the treatment of the LES/RANS interface. Given that high accuracy in the near wall region is required in the current research, DES was not considered.

Surprisingly little published research exists that describes the modelling of the transport of vapour from explosives at the room scale. One of the few studies found was by Hobbs and Conde (1993) who modelled RDX transport in a screening portal.

2.2.4 Vapour transport summary

CFD modelling has been shown to be an effective tool for the prediction of indoor airflows with different approaches being suitable for different problems. It has also been shown that LES can accurately predict scalar transport. However, there are very few published studies on the LES modelling of vapour from the constant concentration sources, which are of interest for explosive detection.

Eddy diffusion models can provide a useful guide to the concentration distributions in a room, but there is still a large amount of uncertainty over what D_e should be in different situations.

This PhD research aims to address these gaps.

2.3 Vapour sorption

A vapour can coexist alongside either its liquid or solid phase. The partition coefficient describes the ratio of concentrations in the solid or liquid phase and the vapour phase. A number of authors (Guo, 2002; Goss and Schwarzenbach, 1998) have shown that the partition coefficient increases as the vapour pressure of the material of interest decreases. Most of the materials of interest to explosive detection have low to very low vapour pressures suggesting that they should have large partition coefficients. Therefore, for a particular airborne concentration, there should exist a much higher concentration on or in a surface. For this reason, it is important that sorption is considered in a transport model for low or medium volatility material.

A description of the sorption processes is given below as is some sorption data relevant to vapour from explosives.

Sorption can be approximated by two or three sub-processes as shown in Figure 2.3. First the vapour has to move from the bulk air region, where the concentration is $C_{ambient}$ [kg·m^{-3}], to close to the surface, where the concentration is C^* [kg·m^{-3}]. This process will be governed by either molecular or turbulent diffusion, or a combination of the two, and can be described by a mass transfer coefficient, a [m·s^{-1}].

The surface concentration, C_{surf} [kg·m^{-2}], is related to C^* by a sorption isotherm which contains a partition coefficient K. K has different units depending on the isotherm model used.

Three example isotherms are described in Murakami et al. (2003). The simplest linear relationship, the Henry-type isotherm, applies when the concentration of the sorbing substance is low. The Langmuir type isotherm describes a rate that reduces as the adsorption saturation point is approached.

After partitioning, the material can move into or through the surface (absorption) resulting in a concentration in the solid, C_{solid} [kg·m^{-3}]. This third process can be described by the solid phase diffusion coefficient, D_{solid} [m^2·s^{-1}]. Absorption will not occur if the material is impermeable. Crystalline substances such as metals and inorganic materials typically have insufficient intermolecular spacing to allow diffusion of organic compounds (Cussler, 2009). All these processes can occur in both directions.

2.3.1 Analytical transport models which include vapour sorption or emission

Many mathematical models have been produced to predict the transport of vapour from sources of both SVOCs and VOCs. Analytical models can be used to predict vapour concentrations such as the model developed by Griffy (1992) who applied it to a block

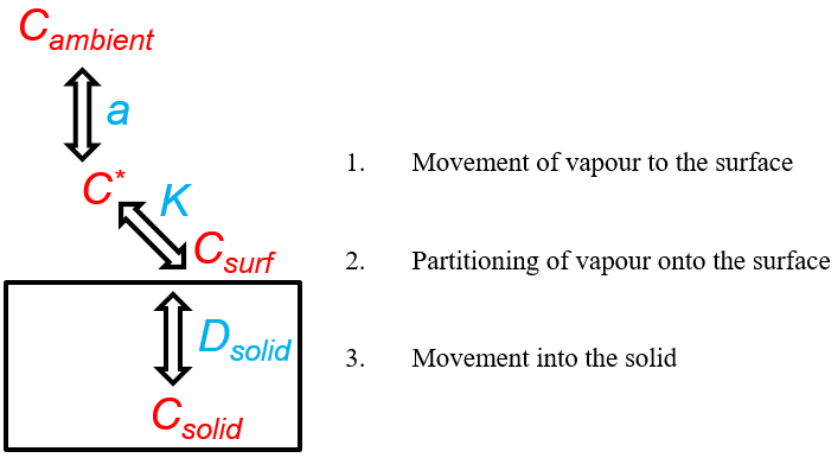

Figure 2.3: The three sorption sub-processes.

of TNT in a small room (18 m^3) and included sorption of TNT vapour onto the walls of the room. This type of model may have many applications but does not provide any information on the spatial distribution of the vapour concentrations. More advanced analytical or numerical models which include sorption (as well as many other processes) have been produced by Jørgensen et al. (2000); Guo (2013); Little et al. (2012); Shi and Zhao (2014); Xiong et al. (2012); Singer et al. (2004, 2005). These studies have also ignored the spatial variation in concentrations, most likely because they are considering exposure to SVOCs over long time periods (e.g. hundreds of days) and/or for moving subjects.

Spatial resolution can be critical as vapour concentrations may reduce by orders of magnitude within very short distances from the source (see Chapter 3) therefore, spatially averaged concentrations are not representative of the entire space. This information is of interest in explosives detection applications when the detector may be sampling from either high or low concentration regions.

2.3.2 Vapour sorption and emission modelling using CFD

CFD has been used to model systems with vapour emission and/or sorption ranging in size from emission cells with volumes of a few litres or less (Mao et al., 2016; Clausen et al., 2010) and a dog's nose (Lawson et al., 2012), to room scale (Yang and Chen, 2001; Murakami et al., 2003; Deng and Kim, 2007; Zhang and Zhang, 2007; Wang et al., 2012; Sorensen and Weschler, 2002). Sorption has been considered using a range of different approaches. Mao et al. (2016) and Clausen et al. (2010) used a linear adsorption isotherm and Murakami et al. (2003) applied three different adsorption isotherm models (linear, Langmuir and Polanyi Dubinin-Radushkevich) across a two-dimensional representation of a room (4.5 m x 3.0 m). Lawson et al. (2012) modelled odourant vapour transport in

a dog's nasal cavity. They used a simplified one-way sorption model (i.e. no desorption) to represent partitioning into and diffusion through the mucus layer. The work of Mao et al. (2016) was specifically focussed on SVOCs and they were able to accurately predict chamber output concentrations compared to experimental data for experiments that ran for tens of days. Room scale CFD modelling with a VOC emission model that contains a partition coefficient was conducted by Deng and Kim (2007). However, they did not consider sorption of the VOC onto the walls of the room. A one-way (laminar) sorption model was used with the Nielsen (1990) test-case by Sorensen and Weschler (2002) along with a constant (surface) emission rate model.

Studies have considered both laminar (Mao et al., 2016; Clausen et al., 2010) and turbulent flows (Murakami et al., 2003). However, even in the work of Murakami et al. (2003), where the air flow in the room was turbulent, the mesh was refined in the near-wall region to place the first cell in the viscous sub-layer. This meant that a simple Fick's law model (Equation 2.37) could be used represent vapour transport between the wall-adjacent cell and the wall.

Fick's first law states that the rate of transfer of a diffusing substance is proportional to the concentration gradient.

$$F = -D\frac{dC}{dx}, \tag{2.37}$$

where D [$m^2 \cdot s^{-1}$] is the diffusion coefficient of the diffusing substance, C [$kg \cdot m^{-3}$] is its concentration and x [m] is the coordinate axis in the direction of the transfer.

Nally et al. (2009) developed sorption models for CFD based on the work of Singer et al. (2005) and Karlsson and Huber (1996). The Nally et al. model includes transport to the surface, partitioning onto the surface and transfer into and out of the embedded layer (i.e. the three processes shown in Figure 2.3). They used a linear isotherm for partitioning. Transfer into and out of the embedded layer was governed by two empirically defined rates, k_1 and k_2 both with units of [h^{-1}] (Singer et al., 2005). The Nally et al. (2009) model also included a turbulent wall function so that the viscous sub-layer did not need to be fully resolved.

In summary, there is a limited capability for modelling tools which can predict spatially resolved, laminar and turbulent vapour transport including the effects of sorption and desorption. Only the Nally et al. (2009) model included absorption into a multilayer material and a turbulent wall function and this model had only a simplistic representation for the embedded layer. The models that have been validated and applied within this PhD build on the capability of the Nally et al. (2009) model.

2.3.3 Sorption data

For a linear isotherm, K is the ratio of C_{surf} or C_{solid} to the airborne concentration, for adsorption and absorption respectively. For absorption, K will be presented in dimensionless form as K_{ab}, where K_{ab} is given by the following,

$$K_{ab} = \frac{C_{solid}}{C^*}. \tag{2.38}$$

The same convention will be applied to the adsorption isotherm K_{ad}, which has units of [m].

$$K_{ad} = \frac{C_{surf}}{C^*}. \tag{2.39}$$

Griffy (1992) gave a saturation surface concentration for TNT of $1 \times 10^{-6}\,\mathrm{kg{\cdot}m^{-2}}$ (equivalent, according to Griffy, to a mono-layer of TNT molecules). If this was combined with the vapour pressure concentration of TNT at 25 °C, $7 \times 10^{-8}\,\mathrm{kg{\cdot}m^{-3}}$, $K_{ad} = 14\,\mathrm{m}$.

Cragin and Leggett (2003) gave K_{ab} for DNB, TNT and DNT for five different types of plastic (landmine surrogates). The values ranged from 1.1×10^3 to 3.0×10^4 for DNB, 1.3×10^3 to 5.4×10^4 for DNT and 1.5×10^4 to 2.9×10^5 for TNT. For $K_{ab} = 2.9 \times 10^5$ the vapour concentrations would be 2.9×10^5 times less than the equilibrium solid phase concentration at 21.5 °C. Partition coefficients are more commonly provided for a water-air interface (Phelan and Webb, 1997)

It has been postulated (Weschler and Nazaroff, 2008) that both impenetrable and penetrable indoor surfaces have water and organic films at their surfaces and so compounds with large partition coefficients could be considered to partition mainly into these films. It can be assumed therefore that a partition coefficient that represents equilibrium between the air and a surface made up of organic compounds, can be used to represent equilibrium between the air and surfaces in a room. The coefficient that best represents this transfer is the octanol-air partition coefficient (Weschler and Nazaroff, 2008).

Muralidharan et al. (2003) and Pinnaduwage et al. (2004) discussed sorption of TNT onto micro-cantilevers. Pinnaduwage et al. (2004) showed that TNT forms 'islands' on their silicon dioxide coated surface rather than a uniform layer (monolayer or otherwise). They referred to the study by Mu et al. (2003) during which an amorphous layer of TNT was formed but suggest that the different deposition modes were due to the presence or absence of water vapour (present in their experiment but not in the Mu et al. experiment). They did not reach a sorption limit during their short experiments with the mass deposited still apparently increasing beyond a surface concentration of $1 \times 10^{-4}\,\mathrm{kg{\cdot}m^{-2}}$ for their 500 s loading. This is considerably higher than the $1 \times 10^{-6}\,\mathrm{kg{\cdot}m^{-2}}$ figure given by Griffy (1992).

This literature search has shown that there is limited sorption data for vapours from explosives. Therefore, more work needs to be conducted to find suitable representative data or experiments need to be carried out to generate the data. Some new sorption data was generated to support this PhD and is discussed in Chapter 5.

2.3.4 Vapour sorption summary

It is important that sorption is considered in a transport model for low or medium volatility material. Many analytical models which include vapour sorption have been developed, but they assume the zone/room is well-mixed. For explosive detection applications, spatial resolution is critical as vapour concentrations may reduce by orders of magnitude within very short distances from the source. Among the available spatially resolved models all have a simplistic representation of how the vapour permeates into the surface.

2.4 Summary

Published theories, methodologies and research in the areas of vapour emission, transport and sorption have been discussed and critically reviewed.

Explosives can consist of complex mixtures of compounds and the rate at which these compounds produce vapour can be limited by processes which are either internal or external. Most compounds of interest have low vapour pressures and can be classed as SVOCs. To simplify the modelling in this PhD research, only bulk samples in indoor environments will be considered so it is assumed that the effects of ageing will be negligible. Only externally limited vapour production will be considered. Therefore, only explosives where the compound of interest makes up most of the weight of the explosive e.g. TNT and EGDN will be modelled. It will be assumed that concentrations adjacent to the surface of the explosive can be calculated from the vapour pressure of the compound.

Both high-resolution CFD modelling and coarser approaches such as eddy diffusion modelling can be used to provide information about the vapour field in indoor spaces. Although eddy diffusion modelling cannot provide the detail that a CFD model can, it has an advantage that it can provide information on likely concentrations when it is not practical to fully survey the environment of interest. Another significant advantage of most simple models is the speed with which they can be set up and solved. The biggest weakness of the eddy diffusion modelling approach is currently the uncertainty over the eddy diffusion coefficient, D_e.

RANS CFD and to a lesser extent LES have been used to study gas dispersion indoors. However, none of the LES models include scalar releases from the constant concentration sources, which are of interest for explosive detection. They also do not attempt to relate the time varying concentration to vapour or gas detection and few studies consider extreme concentrations.

Most of the materials of interest to explosive detection have low vapour pressures suggesting that they should have large partition coefficients. Therefore, it is important that sorption is considered in a transport model. However, there is currently a limited capability for modelling tools which can predict spatially resolved, laminar and turbulent vapour transport including the effects of sorption and desorption.

Chapter 3

Large-eddy simulation of an indoor species transport test-case

3.1 Introduction

In order to demonstrate how complex the vapour signature from an explosive could be in an indoor space, a CFD model has been built of a widely used benchmark test-case for air flow in an isothermal mechanically ventilated room (Nielsen, 1990). The results of this model were interpreted in terms of current theories of chemical location by animals and the capability of detection dogs.

Attempts by others to model the Nielsen test-case are discussed in Section 2.2.3. The test-case has been used to predict the spatially and temporally varying vapour concentration from constant concentration area sources located on the floor of the room. As the time varying concentration field is required, a LES approach has been used.

As stated previously, RANS CFD and to a lesser extent LES have been used to study gas dispersion indoor. However, none of the LES models include scalar releases from the constant concentration sources, which are of interest for explosive detection. They also do not attempt to relate the time varying concentration to vapour or gas detection.

This test-case was used because it is well documented and allows for validation of the mean velocity and RMS velocity, although clearly it is not representative of all rooms. Even in this simple room the flow is unsteady and complex, but the simple geometry allows the fluid dynamics of plumes from constant concentration area sources to be studied in detail. Methods developed in this work could be applied to more complex rooms in the future. Constant concentration vapour sources were located on the floor, to the left of the room where the flow is slower and to the right where the flow was faster and steadier. Two different size sources were defined at each location. These are described in more detail in Section 3.2.1.

Figure 3.1 shows the room geometry, with dimensions $L = 9$ m, $H = W = 3$ m, inlet slot height, $H_{inlet} = 0.168$ m and outlet slot height, $H_{outlet} = 0.48$ m. The test-case was created for the testing of two-dimensional CFD codes (Nielsen, 1990), with the assumption that with $W \gg H$, the flow would be two-dimensional. However, laser-Doppler anemometer data is provided from a scale model experiment with $W = H$ (Restivo, 1979). The mean inlet velocity, $u_0 = 0.455\,\mathrm{m{\cdot}s^{-1}}$ and the temperature = 20 °C. For this room, the air change rate, λ, was $10.2\,\mathrm{h^{-1}}$. Based on a kinematic viscosity, $\nu = 1.53 \times 10^{-5}\,\mathrm{m^2{\cdot}s^{-1}}$ (air density, $\rho = 1.20\,\mathrm{kg{\cdot}m^{-3}}$), the inlet Reynolds number, Re, was 5000, with H_{inlet} as the characteristic dimension. A brief discussion on the most suitable characteristic length for Re is given in Chapter 4.

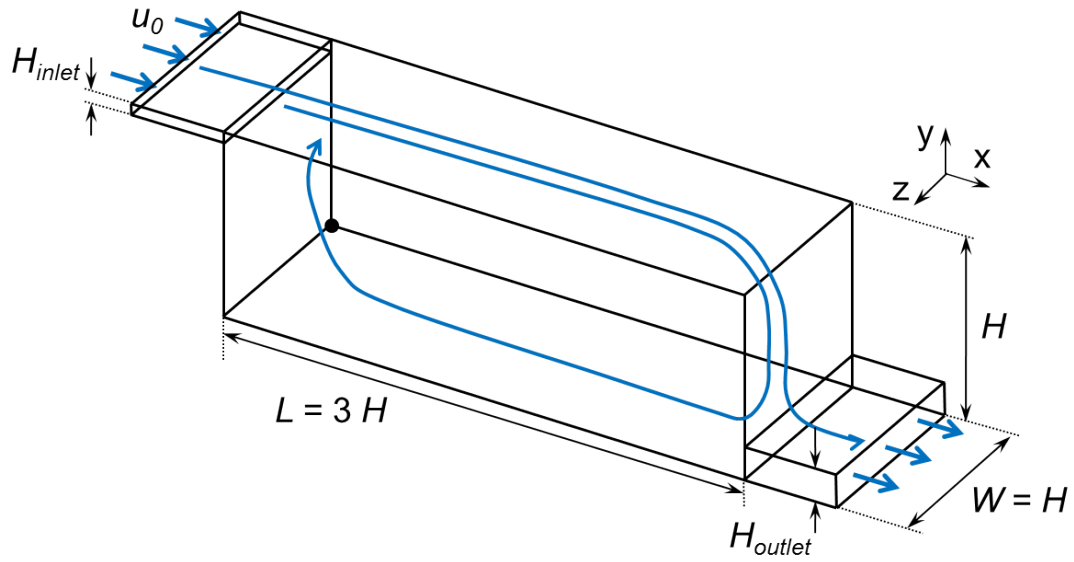

Figure 3.1: The Nielsen benchmark test-case. The blue arrows indicate the mean flow direction and the black dot is located at axis origin. For the current modelling both the inlet and outlet channels were $10H_{inlet}$ long.

The bulk of the work in chapter has been published in Foat et al. (2018).

3.2 Methodology

In this work Fluent V15.0 was used to model the flow and vapour transport with a LES approach (see Section 2.2.2.3), using a structured mesh produced in Gambit V2.4 (ANSYS Inc., Pennsylvania, USA). The vapour was modelled as a passive scalar (see Section 2.2.2.5). The dynamic Smagorinsky subgrid scale model (see Section 2.2.2.4), typically applied to indoor airflows (Davidson and Nielsen, 1996; van Hooff et al., 2014), was used. Fluent's dynamic scalar flux model (see Section 2.2.2.5), as used in a number of LES scalar dispersion studies (van Hooff et al., 2014; Liu and Barth, 2002), was used to

calculate the subgrid turbulent Schmidt number, $Sc_{sg,t}$. For information, the predicted volume average $Sc_{sg,t}$ across the domain was 1.0.

A comparison between the Smagorinsky and dynamic Smagorinsky model in a simple indoor geometry was carried out by Abdilghanie et al. (2009). They showed that the two models gave similar results (mean and RMS velocities) in the middle of the domain, away from the inlet, with the results deviating nearer to the inlet where the ratio of modelled to resolved turbulent kinetic energy (TKE) was higher. They do not state which model performed best.

The flow was initialised using results from a steady k-ϵ RNG turbulence model. The LES model was run using a time step, $\Delta t = 0.01$ s and non-dimensional time step, $\Delta t/\tau$, (where $\tau = 1 \ / \ \lambda_f = 353$ s) was 2.83×10^{-5}.

Second-order temporal discretisation with an implicit solver was used as employed in most indoor LES models (van Hooff et al. (2014); Endregard et al. (2010)). The pressure implicit with splitting of operator (PISO) scheme was used for the pressure-velocity coupling. A second-order central difference scheme (CDS) was used for the convection terms of the momentum transport equations. The CDS was chosen for the discretisation due to the improved accuracy it should provide over the more dissipative bounded central difference scheme (BCDS), however, a CDS is susceptible to instability[1]. The species transport equations were initially also solved using a CDS. No instability was observed in the flow field but it was apparent in the species field in the form of intermittency that appeared to be non-physical. The species transport was therefore re-run using the Fluent BCDS and this removed the spurious intermittency. It is believed that the species transport became unstable, whereas the momentum transport did not, due to the presence of large concentration gradients.

The Fluent BCDS is based on a normalised variable diagram approach (Leonard, 1991). The variables of interest are normalised using the upwind and downwind values. Following this, different discretisation schemes can be plotted as linear relationships between the two normalised variables. Fluent uses a pure CDS or a blended second-order upwind scheme depending on the value of the two normalised variables. The schemes also applies a convection boundedness criterion (Gaskell and Lau, 1988) so that a first-order upwind scheme is applied if these conditions are exceeded.

The flow was run until mean velocities stabilised (2τ in this case) and then it was averaged for at least 4τ. It may be that 4τ was insufficient for higher order statistics, such as the RMS velocity, to fully stabilise, so it is recommended that the convergence of higher order statistics of interest are monitored in future work. The constant concentration area vapour sources were turned on once the flow was developed and the species

[1] A CDS should be stable if the cell Peclet number ($Pe, = uL \ / \ D_{\text{effective}}$, where u is the flow velocity in the cell, L is the cube root of the cell volume and $D_{effective}$ is the effective diffusivity i.e. the sum of molecular and turbulent diffusivity) is less than 2.

field was then initialised for at least 4τ and averaged for 10τ. It was found that the long averaging period, compared to the velocity field, was required due to the additional unsteadiness of the vapour field.

In order to generate realistic and representative turbulence in the domain, LES models usually require the specification of fluctuating boundary conditions at any inlets. This can be done in a number of ways including:

- Explicit representation of the upstream geometry.
- A precursor simulation from which conditions are saved and then applied to the actual simulation.
- The use of periodic boundary conditions whereby turbulence is allowed to develop within the domain.
- Synthetic generation of turbulence.

Two reviews of the different methodologies were given by Xie and Castro (2008); Tabor and Baba-Ahmadi (2010).

The most widely used method for indoor air flow (van Hooff et al., 2014; Abdilghanie et al., 2009) is the vortex method which is implemented in Fluent according to Mathey et al. (2006). In the vortex method, perturbations are added to a plane which is normal to the streamwise direction via a fluctuating two dimensional vorticity field. The size of the vortex and the amount of vorticity are calculated from k and ϵ. The fluctuations in this plane are then used to calculate the streamwise fluctuations.

A number of people have studied the effect of inlet boundary conditions for air flow in simple indoor geometries with both RANS modelling and LES (Said et al., 1993; Joubert et al., 1996; Jiang, 2007; Abdilghanie et al., 2009; van Hooff and Blocken, 2017). Abdilghanie et al. (2009) showed that changing the inlet boundary in their LES model from laminar to turbulent had a significant effect on the flow, but a further increase in Ti, had much less effect. van Hooff and Blocken (2017) showed that increasing Ti had a significant effect on both the flow and species transport in their RANS model of a low-Reynolds number scenario. Said et al. (1993); Joubert et al. (1996); Jiang (2007) reported either a negligible effect from a change in Ti, or that the effect was contained in a region close to the inlet. van Hooff and Blocken (2017) suggested that the effect of a change in Ti might depend on whether the flow being studied contains fully developed turbulence or not and this seems to correspond with the other studies described above.

The velocity, TKE and dissipation rate profiles at the inlet were taken from a precursor steady k-ϵ RNG model in which the flow was allowed to develop in a channel which was h high, H wide and 30 h long. The mean inlet velocity for the precursor model, u_0, was set to that defined by Nielsen (1990). The hydraulic diameter for the precursor

model, DH, used to define the integral length scale at the inlet, was calculated using an equation for rectangular ducts (van Hooff et al., 2014), $DH = 4Wh_{inlet} \ / \ 2(W + h_{inlet}) = 0.318$ m. The TKE decayed rapidly in the inlet channel so a high inlet Ti (47 %) was required to achieve even a moderate Ti at the end of the inlet channel, i.e. at the entrance to the main volume of the domain. A normalised RMS velocity, $u_{RMS} \ / \ u_0$, (the parameter reported by Nielsen (1990)) = 4.6 %, was achieved at the end of the inlet channel, i.e. the centre of the opening at the entrance to the main volume of the domain, while a value of 8.4 % was reported by Nielsen (1990).

A simulation was also run with a laminar inflow, i.e. the vortex method was turned off. The results of this comparison are shown in Appendix B, in Figures B.3 and B.4. Changing to laminar inflow had little effect of the air flow in the room beyond a distance of approximately $x \ / \ H = 1$ from the end of the inlet channel. This suggests that the flow in the domain contains fully developed turbulence so is not sensitive to turbulence levels at the inlet. The presence of fully developed turbulence in the room is explored in Chapter 4.

The model was originally run without the precursor simulation, i.e. with flat (constant) velocity, TKE and dissipation rate profiles applied directly to the start of the inlet channel. However, this type of profile was incompatible with the way Fluent applies the vortex method and resulted in asymmetric flow conditions being created at the inlet. The results from this simulation are discussed briefly in Section 3.3.1.

All walls were given no-slip boundary conditions.

A fully structured hexahedral mesh with 5.4 million cells was produced initially. An image of the mesh on the vertical centre plane and a horizontal plane at a distance of $h_{inlet} \ / \ 2$ from the floor is shown in Figure 3.2. There were 20 cells across the inlet height and the largest cell dimension in the domain was 0.03 m. The initial mesh was refined (i.e concentrated) near the source locations and also around the shear layer of the wall jet. Nearly all of the top and left/right walls ($x \ / \ H = 0$ and 3) had a y_1^+ (where y_1^+ is the non-dimensional distance from the wall of the first cell centre) across them of less than 5, so the first cell centres should be in the viscous sub-layer. The near wall mesh on the sides ($z \ / \ H = 0$ and 1) was slightly coarser, with y_1^+ as high as 13 near the inlet, putting the cell centroid in the buffer layer. Most of the mesh on the bottom wall had $y_1^+ < 2.5$ and the source regions had a y_1^+ of 1.0 and 1.7 for the left and right sources respectively. The aspect ratio of the cells, both $x \ / \ y$ and $z \ / \ y$, at the sources was 3.5. The largest aspect ratio for the near-wall cells on the floor (both $x \ / \ y$ and $z \ / \ y$) was 13. This occurred at approximately $x \ / \ H = 1.5$ for $x \ / \ y$, and half way between the centre of the room and side walls for $z \ / \ y$.

The ratio of subgrid scale TKE to total TKE can be used to give an indication of the amount of turbulence that is being resolved, as opposed to modelled, in a LES simulation (Pope, 2004). Abdilghanie et al. (2009) reported that their LES mesh was well resolved

with a TKE ratio of less than 5 % across most of their domain. The volume weighted average ratio of subgrid scale TKE to total TKE in this model was 1.5 %, showing that the mesh size was sufficiently small to resolve 98.5 % of the TKE. The mesh dependency is discussed in Section 3.2.2.

The time step and mesh size resulted in a Courant-Friedrichs-Lewy (CFL) number of $\leq$ 0.5 across the bulk of the domain with a few small regions having a slightly larger CFL number but still well below 1.

The upper frequency cut-off (1 / ($2\Delta t$)) was 50 Hz, but as the CFL number was ≤ 0.5, the relative coarseness of the mesh further reduces the maximum frequencies that can be resolved to $\leq$ 25 Hz. However, this is still well above the typical room turbulence and dog sniffing frequencies given in Section 1.4. The sensitivity of the results to a change in the time step size is discussed in Section 3.2.2.

See Section 4.3 for a discussion on the cut-off frequency close to the left source.

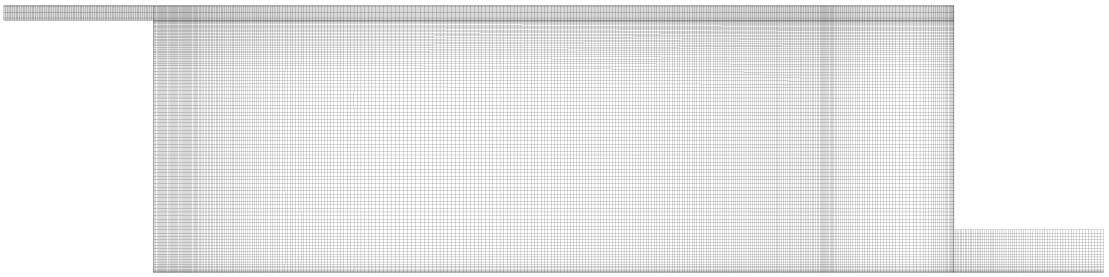

(a)

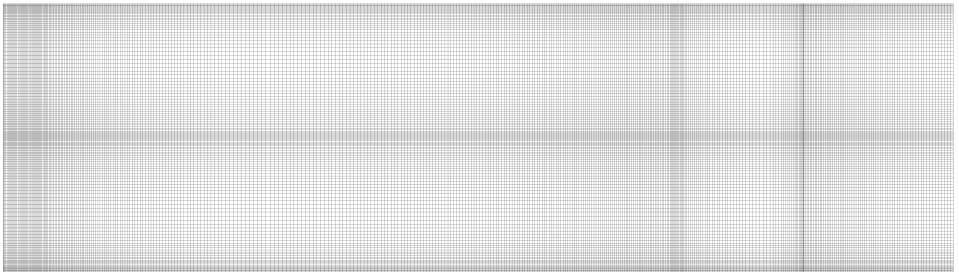

(b)

Figure 3.2: The original, un-refined CFD mesh shown on the vertical (x-y) centre plane, (a); and a horizontal (x-z) plane h_{inlet} / 2 from the bottom wall, (b). The dimensions are given in Figure 3.1. To better see the detail in the images, please view the electronic version of the thesis.

3.2.1 The vapour source and monitoring locations

This chapter focuses on vapour released from TNT explosive. A volatile material can be viewed as a vapour generator with the production rate being a function of physicochemical factors (e.g. vapour pressure and molecular vapour-air diffusion coefficient), scenario details (source size, ambient conditions, local air flow and ventilation) or internal processes such as the diffusion of a vapourising compound through the solid (see Section 2.1 for more details).

The CFD models used to study the vapour transport are based on passive scalar transport and it is assumed that the concentrations can be scaled linearly to represent different target vapours. Processes such as vapour sorption onto surfaces, which may make the scaling non-linear, have not been included here but are included in the modelling in Chapter 5. The movement of a dog and handler in the room has not been accounted for and it is expected that this movement would produce additional unsteadiness and increased local mixing. The effect that people movement has on mixing is reported on by Mora and Gadgil (2002); Keil (2015); Mingotti et al. (2020) and is discussed briefly in Section 6.1.

Two sets of large and small vapour sources were modelled representing an explosive fully exposed on the floor of the room. The large and small sources were defined as squares with side length, d, of 0.144 m and 0.048 m respectively. The areas, A, of the large and small sources were $0.0207\,\mathrm{m}^2$ and $0.002\,30\,\mathrm{m}^2$ respectively, therefore, the large source was nine times the area of the small source. The source face represents the surface of the explosive and was set with a constant species concentration, c_0. This creates a vapour source based on the assumption that, close to the surface of the explosive, there is a continuous reservoir of vapour at the saturation vapour pressure concentration. This assumption is a reasonable one when the flow over the explosive is weak, but, too high a flow could deplete this reservoir faster than it is replenished from the bulk explosive. For semi-volatile organic compounds SVOCs the vapour production rate should only be limited by processes external to the solid. The same is also true for materials where the compound of interest makes up the bulk of the mass of the solid (such as TNT). See Section 2.1 for more details.

Both sets of sources were centred in the z direction with the centre for one at $x = 0.350$ m and the other at $x = 7.572$ m (Figure 3.3). This placed the left sources in a small recirculation region where the mean velocity was small and in the positive x-direction (see Figure 3.8). The right sources were in a faster flowing region with flow in the negative x-direction. The area around the left source location is perhaps more representative of typical mechanically or naturally ventilated rooms which would not be expected to have strong directional flow near the floor.

Figure 3.3 shows the locations of the monitor points and lines used to report vapour concentrations. Vertical lines VR2 and VR3 were used to show how the concentration profiles evolve downwind of the source. As the flow direction near the left source varies it was not possible to define a downwind direction so additional vertical monitor lines for the left source were not used.

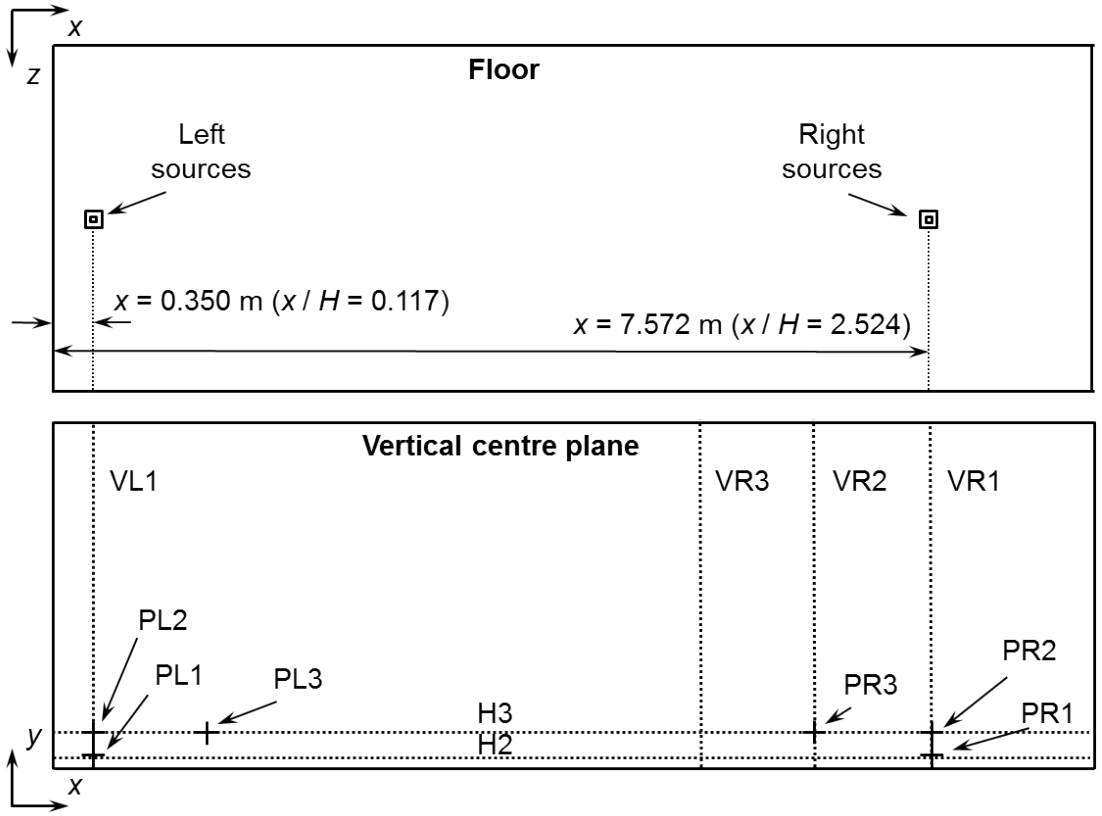

Figure 3.3: The locations of the sources, monitor lines and monitor points on the floor (upper) and the vertical centre plane (lower). Lines VL1 and VR1 are centred on the left and rights sources respectively. Lines VR2 and VR3 are offset from VR1 by 1 m and 2 m respectively. Lines H3 and H2 are 0.3 m and 0.084 m above the ground respectively. There is an additional horizontal line, H1, at $y = 0.01$ m which is not shown here. Points PL1 and PL2 are 0.1 m and 0.3 m above the centre of the left sources and PR1 and PR2 are at the same heights above the right sources. Points PL3 and PR3 are at $y = 0.3$ m and are offset from the centre of the sources in the x-direction by 1 m. All points and lines are on the vertical centre plane.

The vapour diffusion coefficient was set to $5.6 \times 10^{-6}\,\mathrm{m^2{\cdot}s^{-1}}$ which is representative of the diffusion of TNT vapour in air under ambient conditions (Gershanik and Zeiri, 2010). The corresponding Schmidt number, Sc, was set to 2.7. The volatility of TNT at 20 °C is $3.2 \times 10^{-8}\,\mathrm{kg{\cdot}m^{-3}}$ (or 3.4 ppb, volume/volume) (Ostmark et al., 2012).

3.2.2 Mesh and model sensitivities

To assess the mesh dependence of the model, separate adaptions were made to study the effect on both the flow field and the vapour flux from the source.

As the ratio of the estimated subgrid scale TKE and total TKE was already small across most of the domain, the mesh was only refined in the inlet channel and the start of the shear layer (see Figure 3.4) when testing the effect of the mesh on the flow field. For the refined mesh, Δt was reduced to 0.005 s to maintain the same maximum CFL number in the inlet region. The refinement of the mesh in the inlet channel and shear layer had little effect on the velocity and RMS velocity profiles, as shown in the appendix in Figures B.1 and B.2, so this refinement was not used for subsequent modelling.

Figure 3.4: Mesh refinement (show on the vertical centre plane) at the inlet and shear layer. For reference, the inlet channel height, h_{inlet}, is 0.168 m and the channels is $10h_{inlet}$ long. To better see the detail in the images, please view electronic version of the thesis.

Two localised adaptions of the fully structured mesh at the left and right source locations were performed to assess the dependence of the vapour flux predictions on the mesh. The mesh was refined in a cuboid (0.60 m x 0.6 m x 0.6 m in the x, y and z directions respectively) centred on the sources to produce the first adaption and then refined again in a smaller region (0.3 m x 0.3 m x 0.3 m in the x, y and z directions respectively), see Figure 3.5.

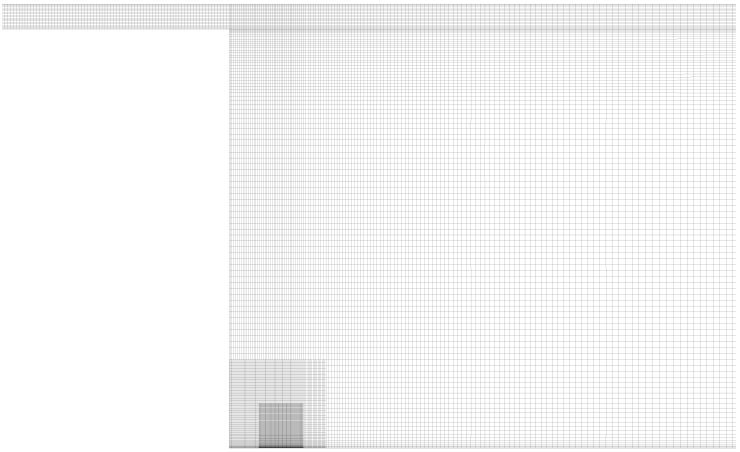

(a)

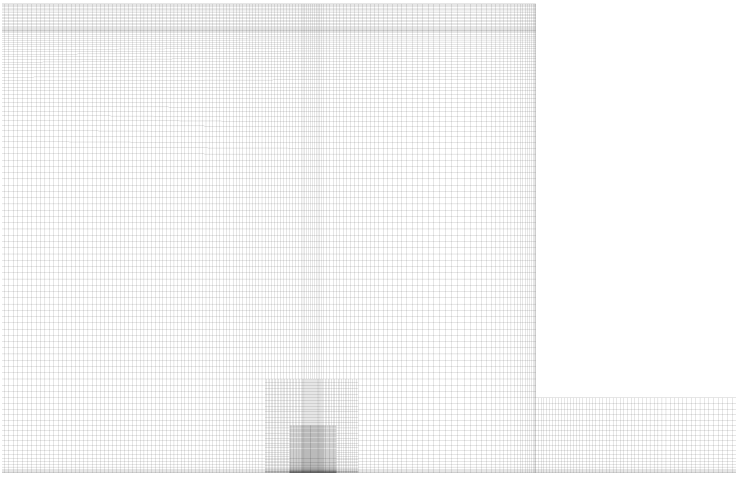

(b)

Figure 3.5: The second refined mesh at the left source (a); and the right source, (b) both shown on the vertical centre plane. For reference, the inlet channel height, H_{inlet}, is 0.168 m and the outlet channel height, H_{outlet}, is 0.48 m. To better see the detail in the images, please view the electronic version of the thesis.

Considering only the convective component, the vapour flux, F, given by Equation 3.1 was compared for each mesh.

$$F = \frac{\int \overline{u}\,\overline{c}\rho\, dA_{outlet}}{A}, \tag{3.1}$$

where $\overline{c}$ is the time average concentration, A_{outlet} is the area of the domain outlet and A is the area of the source. Equation 3.1 should approximate the flux at the source with a good accuracy (when averaged over a sufficiently long period), given that the turbulent

flux is usually small compared to the streamwise convective component (van Hooff et al., 2014).

For both source locations there was a small change in the vapour flux as the mesh was refined but this was never more than an 8 % difference (compared to the initial mesh) for the left sources and never more than a 2 % difference for the right sources. The overall patterns in the mean and RMS vapour fields were qualitatively similar for all three meshes, as were the mean and RMS velocities. Boppana et al. (2010) showed that reducing y_1^+ from 2.1 to 1.1 at their constant concentration vapour source had little effect on the local mean concentration when normalised to the vapour flux, for their vapour, naphthalene ($Sc = 2.3$).

As the variation in flux for the right sources was small and the initial mesh had a y_1^+ within the range used by Boppana et al., the initial mesh was used for modelling the right sources. As the variation in flux for the left source was larger, the mesh with one refinement was used for subsequent modelling. This meant that y_1^+ at the left and right sources was 0.3 and 1.7 respectively.

Using the mesh with one refinement at the left source, the time step, Δt, was reduced from 0.01 s to 0.005 s and the normalised mean velocity and normalised RMS velocity profiles were compared. There was only a small change in the normalised mean velocity and normalised RMS velocity profiles (see Figures B.5 and B.6 in the appendix). With the reduction in Δt, the time-averaged flux from the small and large left sources changed by +4 % and +3 % respectively. The concentration and RMS concentration fields were similar for both time step sizes (see Figures B.7, B.8, B.9 and B.10 in the appendix), as were probability histograms of relative instantaneous concentrations (see Figures B.11 and B.12 in the appendix). As the results show only a small time step size dependency, $\Delta t = 0.01$ s was used.

As discussed previously, changing the inflow conditions from turbulent to laminar flow had little effect on the flow apart from close to the inlet.

3.3 Results and discussions

3.3.1 Validation of the flow field

Time-averaged velocity vectors on the vertical plane at the centre of the domain are shown in Figure 3.6.

The flow is dominated by a large primary recirculation with secondary recirculation regions in the lower left (small x and small y) and upper right (large x and large y) corners of the vertical plane.

Figure 3.6 shows that TKE, created in the shear layer produced by the wall jet, decays as the jet moves along the top wall and down into the room.

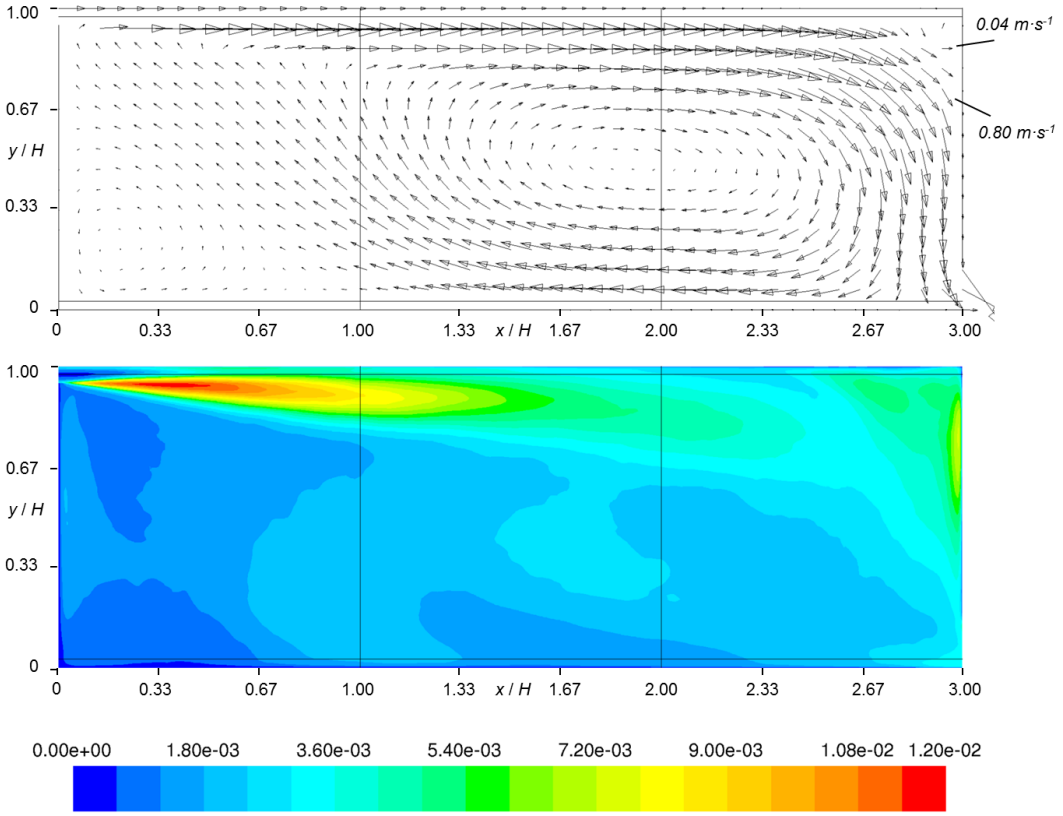

Figure 3.6: Mean velocity vectors (upper) and contours of resolved TKE [$m^2 \cdot s^{-2}$] (lower), on the vertical centre plane. The vertical lines are at x / H = 1 and 2 and the horizontal lines are at a distance of H_{inlet} / 2 from the top wall and the bottom wall. Vectors are plotted on a regular grid of points and some example vectors are annotated.

The time-averaged velocity, $\overline{u}$, and u_{RMS}, both normalised against u_0, were compared to the data of Nielsen (1990) and the results are shown in Figures 3.7 and 3.8. The figures show data over vertical lines on the centre plane at x / H = 1 and 2 and on horizontal lines on the centre plane at a distance of H_{inlet} / 2 from the top and bottom surfaces (as shown in Figure 3.6).

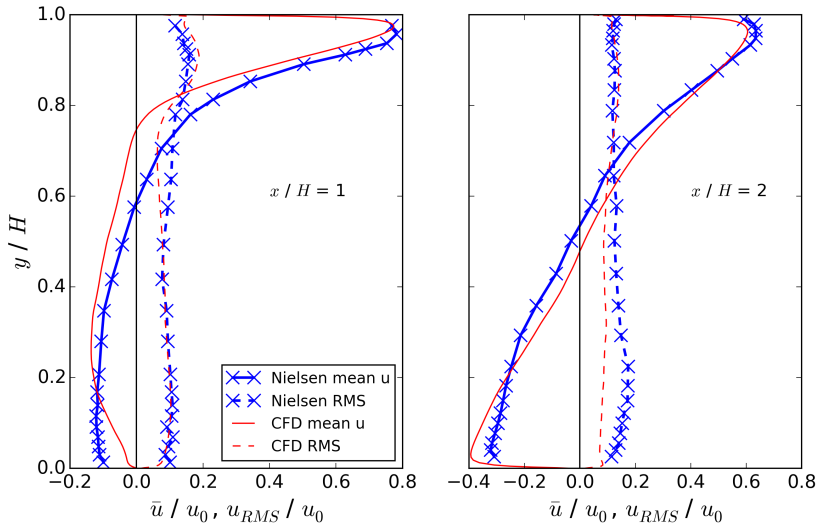

Figure 3.7: $\overline{u}$ / u_0 and u_{RMS} / u_0 against y / H on vertical lines on the centre plane at x / $H = 1$ (left graph) and x / $H = 2$ (right graph).

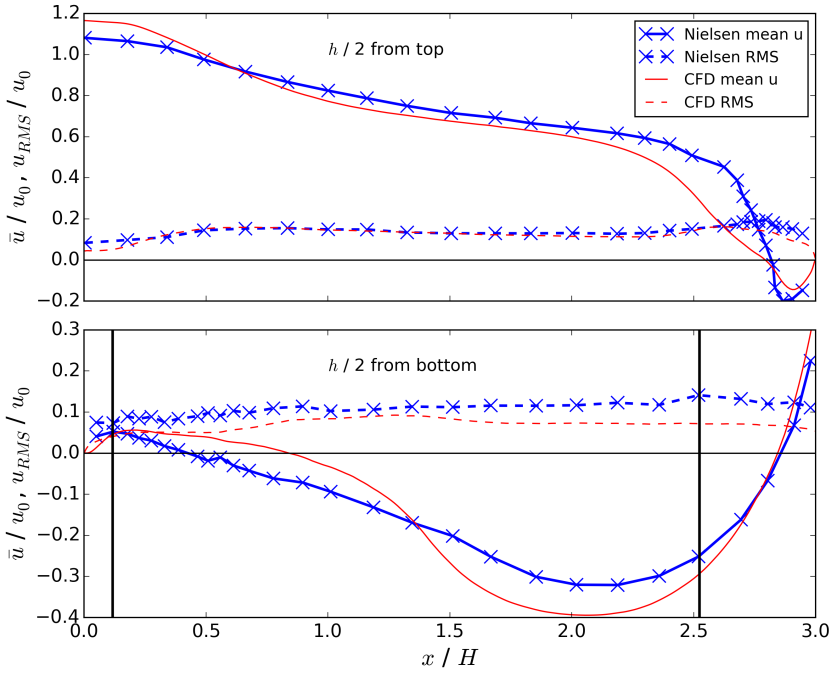

Figure 3.8: $\overline{u}$ / u_0 and u_{RMS} / u_0 against x / H on horizontal lines on the centre plane at a distance of H_{inlet} / 2 from the top wall (upper graph) and H_{inlet} / 2 from the bottom wall (lower graph). The vertical lines show the locations of the source centres.

The mean and RMS velocity profiles are broadly similar to those reported by, for example, Susin et al. (2009); Thysen (2015); Zhang and Chen (2000). Interestingly the

velocity prediction in the present study at x / $H = 1$ are similar to those of Davidson and Nielsen (1996), who used a considerably coarser mesh. The main discrepancies between the LES model and the experiment are: the velocity profile near the floor, in particular the point of separation and the peak negative velocity; and the under-prediction of the RMS velocity near the floor. Regarding the former, some previous modelling studies (Thysen, 2015; Davidson and Nielsen, 1996) have shown a better fit to the mean velocity data near the floor. However, a similar point of separation to that shown in the current modelling, was reported by Pedersen and Meyer (2000), who carried out particle image velocimetry measurements in a scale model.

The under-prediction of the RMS velocity near the floor is a feature that, to the author's knowledge, has not been predicted accurately in any published studies. Zhang and Chen (2000) stated that coarse mesh resolution may have been the cause of their errors in the LES prediction of the fluctuating velocity. However, the finer mesh used in the present study has not significantly altered the effectiveness of the model.

The model performance has been assessed using a number of metrics as described by Hanna et al. (2004) and used for velocities and turbulence predictions by Tominaga (2015) and van Hooff et al. (2017). These are: the fraction of points within a factor of two (FAC2), percentage of points within a factor of 1.3 (FAC1.3), the fractional bias (FB) and normalised mean square error (NMSE). The FB is a measure of the systematic error which would be expected to be seen as a consistent over- or underestimate. The NMSE is a measure of how scattered the data is. Each assessment used 106 data points. The results are presented in Table 3.1, alongside the ideal values for each metric for a perfect model.

	$\overline{u}/u_0$	u_{RMS}/u_0	Ideal value
FAC2	0.75	0.95	1
FAC1.3	0.53	0.51	1
FB	0.14	0.22	0
NMSE	0.26	0.11	0

Table 3.1: Model performance metrics for $\overline{u}$ / u_0 and u_{RMS} / u_0.

The metrics show that the model has performed well in predicting both the mean and RMS velocities, with more than 50 % of predictions within a factor of 1.3 of the experimental data.

It is of interest to note that the turbulence intensity, Ti, was very high across the domain, as is typical of indoor air flows. The median Ti on the vertical line at x / $H = 1$ was 77 % and on the horizontal line, at a distance of h / 2 from the bottom wall, it was 85 %. These values are similar to the upper Ti limit from the measurement study of

Finkelstein et al. (1996) and slightly higher than the upper range of those measured by Kovanen et al. (1989).

When the model was run without the precursor simulation, i.e. with flat (constant) velocity, TKE and dissipation rate profiles applied directly to the start of the inlet channel, an asymmetry in the flow was created at the inlet. This was due to an incompatibility with the flat velocity profile and the way Fluent applies the vortex method. The asymmetry was sufficiently strong to produce circulation in the horizontal plane between x / H = 0 and 1. Interestingly the velocity profiles from this model, on the horizontal line at H_{inlet} / 2 from the bottom wall, better matched the experimental data than the model discussed above.

Nielsen (1990) reported some three-dimensionality in the measured flow and a similar asymmetric circulation region was seen in a steady k-ω solution (Nielsen et al., 2010). It is known that symmetric geometries can produce asymmetric flows (Cherdron et al., 1978) and that room airflows can have multiple stable solutions (Li and Nielsen, 2011; Pulat and Nielsen, 2015). Therefore, the accidental asymmetry applied when the model was run without the precursor simulation may have resulted in a fortuitous replication of the flow condition that was actually present when the measurements were taken.

3.3.2 Vapour flux

In order to predict the vapour flux from an explosive in a room, empirical models are available. For laminar flow, the mass transfer from a constant concentration source can be represented by the following Sherwood number (Sh) relationship (Incropera and De Witt, 1990).

$$Sh = 0.664 Re^{\frac{1}{2}} Sc^{\frac{1}{3}} \tag{3.2}$$

The Sherwood number is defined as

$$Sh = \frac{a L_{char}}{D}, \tag{3.3}$$

where L_{char} [m] is a characteristic length. The vapour flux, F, can then be calculated using Equations 3.2, 3.3 and the following,

$$F = a \left(C_0 - C_{ambient} \right), \tag{3.4}$$

where $C_{ambient}$ [kg·m^{-3}] is the ambient concentration.

An assumption in Equation 3.2 is that the velocity boundary layer and the concentration boundary layer both begin at the leading edge of the plate. For indoor air flows it is often

difficult to define the length of a boundary layer due to the point of flow attachment being unclear. Also, the subliming explosive could be located at any point in that boundary layer. An alternative relationship, which should have more applicability for the type of problem being considered here, was given by Danberg (2008) for Couette flow[2] over a circular or rectangular source. The equation for the rectangular source is given by the following.

$$Sh = 0.796 \left(\frac{u_\tau L_{source}}{\nu} \right)^{\frac{2}{3}} Sc^{\frac{1}{3}}, \tag{3.5}$$

where u_τ [m·s^{-1}] is the friction velocity, L_{source} [m] is the length across the source and ν [m^2·s^{-1}] is the kinematic viscosity. The friction velocity is given by the following:

$$u_\tau = \sqrt{\frac{\tau_w}{\rho}}, \tag{3.6}$$

where τ_w [kg·m^{-1}·s^{-2}] is the wall shear stress.

Danberg compared his model (for a circular source) to data for droplet evaporation in a wind tunnel for three temperatures. The slope of the line fitted to the experimental data was 13 % larger than or 3 % smaller than that of the model depending on whether he excluded possible outliers.

The CFD predicted vapour fluxes, F, for the large and small sources at both locations for TNT are given in Table 3.2 alongside prediction using the Danberg (2008) model. The ratio of the two predictions is also given.

	Small left	**Large left**	**Small right**	**Large right**
CFD flux /ng·m^{-2}·s^{-1}	37.1	25.7	71.4	49.9
Danberg flux /ng·m^{-2}·s^{-1}	28.4	19.5	54.9	38.1
Ratio CFD:Danberg	1.3	1.3	1.3	1.3

Table 3.2: Vapour fluxes predicted by the CFD model compared to that of the Danberg (2008) model.

For both source locations, the vapour flux, F, from the large source was 0.7 times that from the small source. Therefore, the mass emission rate, $\dot{M}$, from the large sources was 6.3 times that from the small source (the large source has nine times the surface area of the small source). The fluxes, F, from the right sources were 1.9 times those from the left sources (for both sizes). The CFD predictions are very close to those of the Danberg model for all sources. It should be noted that the Danberg model was developed for a steady two-dimensional flow with a constant friction velocity in space and time. This provides some additional confidence in the accuracy of the CFD vapour model.

[2]Couette flow is drag induced flow between parallel plates where the velocity profile between the plates is linear.

3.3.3 Vapour concentrations

Figure 3.9 shows contours of time-averaged concentration, $\overline{c}$, normalised by c_0, on the vertical centre plane, for the left and right large sources. For the left source, there is a small, high concentration region to the right of the release location due to the mean flow in that area being in the positive x direction. The vapour is then carried up and round in a clockwise direction. There is a gradient in the mean concentration field towards the lower left of the domain where the source is located. However, this gradient is very weak on the right side of the room. For the right source the high concentration region stays close to the floor and there is a gradient in from the lower left of the room to the lower right. Similarly to the left source, the concentration gradients are weak in large parts of the room.

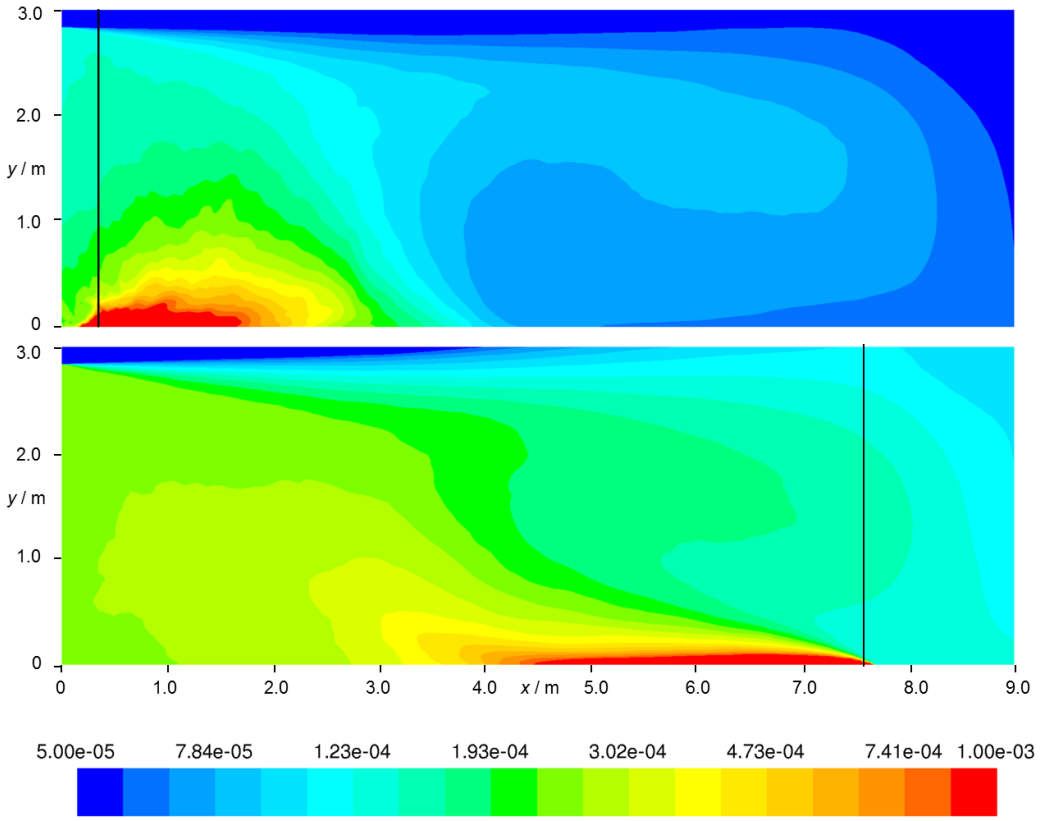

Figure 3.9: Normalised mean concentrations ($\overline{c}$ / c_0) for the large left source (upper) and the large right source (lower) on the vertical centre plane. The concentrations are shown on a log scale and are not clipped to the range. The vertical lines are positioned at the centres of the sources.

Figures 3.10 and 3.11 show graphs of normalised mean concentration on vertical lines above the sources and downwind from the right source, and horizontal lines at various heights (Figure 3.3 shows the locations of the lines). Lines VL1 and VR1 show how the mean concentration reduced rapidly over a short distance from the source. Within

approximately 0.1 m or less from the sources in the vertical direction the concentrations have reduced by more than three or four orders of magnitude. For horizontal distances from the left sources (Figure 3.11) greater than 4.5 m, $\bar{c}$ / c_0 is almost constant at approximately 6.7×10^{-4} for the large source and a factor of 6.3 less for the small source, irrespective of the height of the horizontal line. For the right sources the downstream concentration decay in the horizontal direction is rapid. However, concentrations do not quite reach the background levels seen upwind of the source by the time the vapour plume reaches $x = 0$ m. The mean concentration profile flattens with increasing vertical or horizontal distance from the source.

For a source of TNT, the background concentrations in the room would be approximately 0.22 parts per trillion (ppt) and 0.036 ppt for the left large and small source respectively and 0.44 ppt and 0.070 ppt for the right large and small source respectively.

As would be expected from their relative vapour fluxes, the time-averaged concentrations from the large sources were consistently 6.3 times that from the small sources (calculated along the lines in both the horizontal and vertical directions), apart from very close to the source.

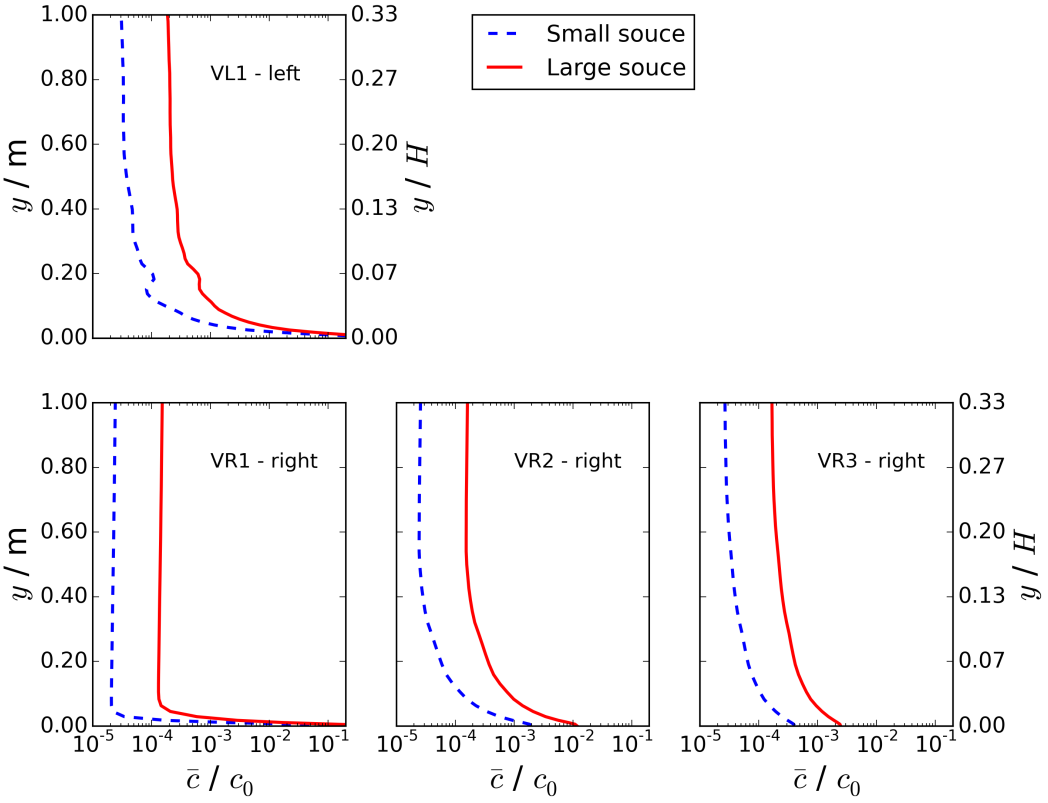

Figure 3.10: $\bar{c}$ / c_0 along vertical lines VL1, VR1, VR2 and VR3. The upper graph shows releases from the left sources and the lower graphs the right sources. Only data up to $y = 1.0$ m (or y / $H = 0.33$) is shown.

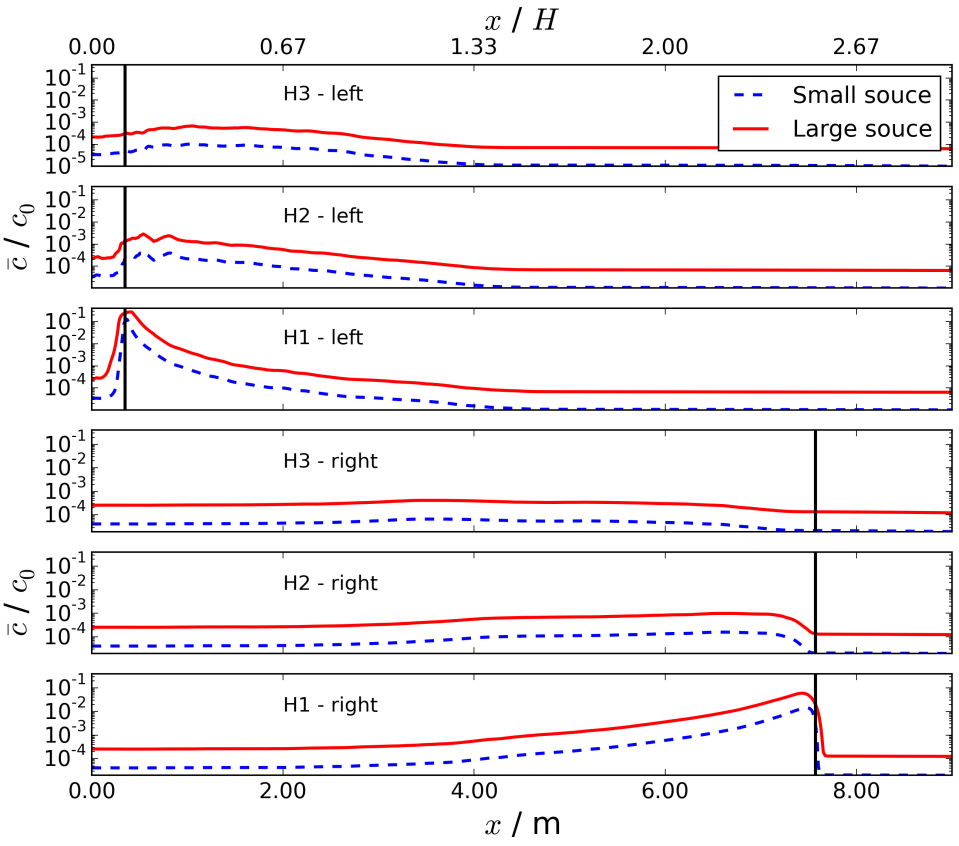

Figure 3.11: $\overline{c}$ / c_0 along horizontal lines H3, H2 and H1. The upper three graphs show releases from the left sources and the lower three graphs the right sources. The vertical black lines indicate the location of the centre of the sources.

To illustrate the intensity of the fluctuating concentration (as would be used in eddy chemotaxis), Figures 3.12 and 3.13 show the RMS of the fluctuating concentration relative to the local mean concentration, c_{RMS} / $\overline{c}$.

There is little difference between c_{RMS} / $\overline{c}$ for the two source sizes apart from in the near-source region and a small region to the left of the left sources on line H1. This shows that generally the intensity of the relative concentration fluctuations is not sensitive to the source size for these two sizes. For the right sources there is a clear gradient in the upwind direction leading to the source. This is similar to that of a ground level source in an atmospheric boundary layer flow (Fackrell and Robins, 1982; Xie et al., 2007; Boppana et al., 2012). For the left sources, the pattern of the gradient is complex but there is a clear gradient upwind of the left source (on the left of the room). The results for the right source can be compared quantitatively to published data from wind tunnel and LES studies of ground level passive scalar releases in a fully turbulent boundary layer. On the horizontal line 0.01 m above the floor, H1, c_{RMS} / $\overline{c}$ peaks between 1.4 and 1.8 (downwind of the source) which is larger but within a factor of four of the published data (0.8 (Xie et al., 2007), 0.5 (Fackrell and Robins, 1982), 0.5 Boppana

et al. (2012)). It should be noted that the boundary layer in the scenario studied here is unlikely to be fully developed.

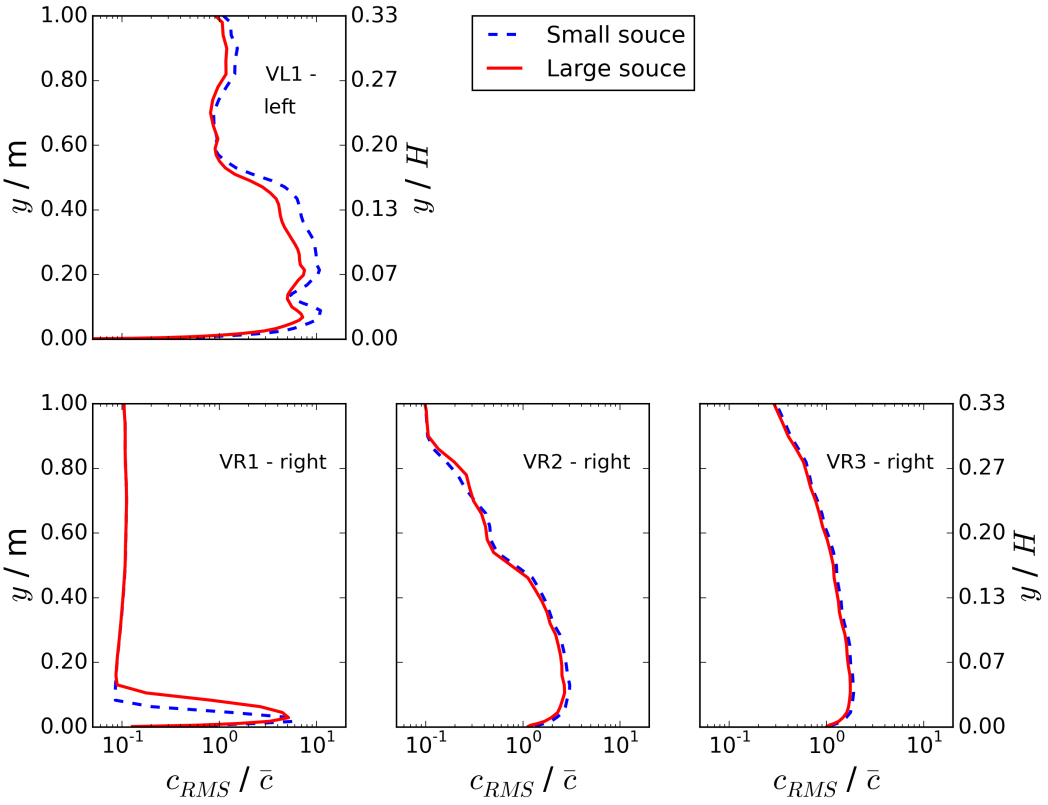

Figure 3.12: c_{RMS} / $\overline{c}$ along vertical lines VL1, VR1, VR2 and VR3. Note that $\overline{c}$ is the local time-averaged concentration, which changes with height. The upper graph shows releases from the left sources and the lower graphs the right sources. Only data up to $y = 1.0$ m (or y / $H = 0.33$) is shown.

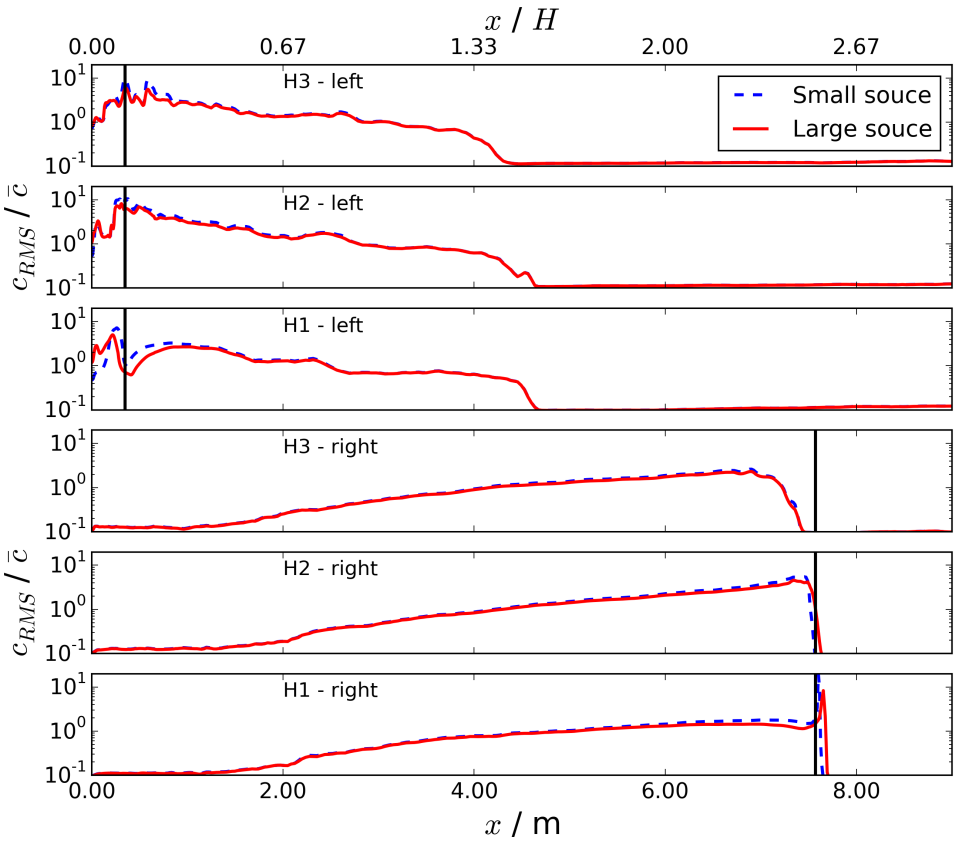

Figure 3.13: c_{RMS} / $\overline{c}$ along horizontal lines H3, H2 and H1. Note that $\overline{c}$ is the local time-averaged concentration, which changes with horizontal distance. The upper three graphs show releases from the left sources and the lower three graphs the right sources. The vertical black lines indicate the location of the centre of the sources.

Time histories of relative instantaneous concentrations, c / $\overline{c}$, are shown for the left and right large source in Figures 3.14 and 3.15. From these graphs it is clear to see how the vapour structures are very different on two sides of the room. This is partly due to the relative location of the monitor points in the plumes from the two sources. As can be seen in Figure 3.9, the flow on the right of the room has caused the plume there to stay lower to the ground compared to the left side. This means that even monitor PR1 is located out of the (time averaged) plume. The occasional peaks in the concentration time history at PR1 must be due to the unsteady air flow occasionally lifting the plume off the ground. Animations of the instantaneous concentration field show that these types of event do happen. Monitor PR2 is sitting well away from the plume so only sees background concentrations. Monitor PR3 is located on the edge of the (time averaged) plume so displays a more varying concentration time history.

There are some similarities in the time histories at PL1 and PL2, which suggests that the vapour structures must be at least 0.2 m in size (the separation between the two

points in 0.2 m). All the three monitors for the left source are more clearly within the plume than the right monitors.

Peak instantaneous concentrations for the left source reach approximately two orders of magnitude above the mean, whereas at the right source, peaks are a little over one order of magnitude above the mean.

From a visual examination of the instantaneous concentrations time histories, the frequency of the concentration fluctuations was of the order of approximately 1 Hz or slower.

The integral time scale for velocity, $\Lambda_{t,u}$ was calculated (using the first zero-crossing point on an autocorrelation function) at monitor points located between 0.1 m to 0.5 m above the left source and the values were between 13.4 s and 20.5 s. The integral time scales for the concentration fluctuations, $\Lambda_{t,c}$, were smaller, 3.5 s to 14.6 s, and broadly increased as the height above the source increased. Integral velocity time scales are close to, but larger than, those reported by Zhou (1999) for ventilated spaces.

The Kolmogorov length scale, η, was estimated for the room. The Reynolds number was calculated using the average velocity across the middle region on the room along x / $H = 1$, and H was used as the characteristic length. This gives $Re = 7200$, which is slightly larger than the inlet Re. Using Equation 3.7, $\eta = 4$ mm, which is within the range of values given by Chen and Srebric (2002) for indoor air flow.

$$\frac{L_{char}}{\eta} = Re^{3/4} \tag{3.7}$$

Using the friction velocity on the floor (the average value at the left and right sources was $0.01\,\mathrm{m{\cdot}s^{-1}}$) as the characteristic turbulent velocity, the frequency of the smallest scales of turbulence was approximately 2.5 Hz.

The integral time scales for concentration are more than one order of magnitude greater than the dog sniffing time scales, 0.14 s to 0.25 s (based on sniffing frequencies reported by Craven et al. (2010)). The sniffing frequencies are also higher than frequency of the smallest scale turbulence.

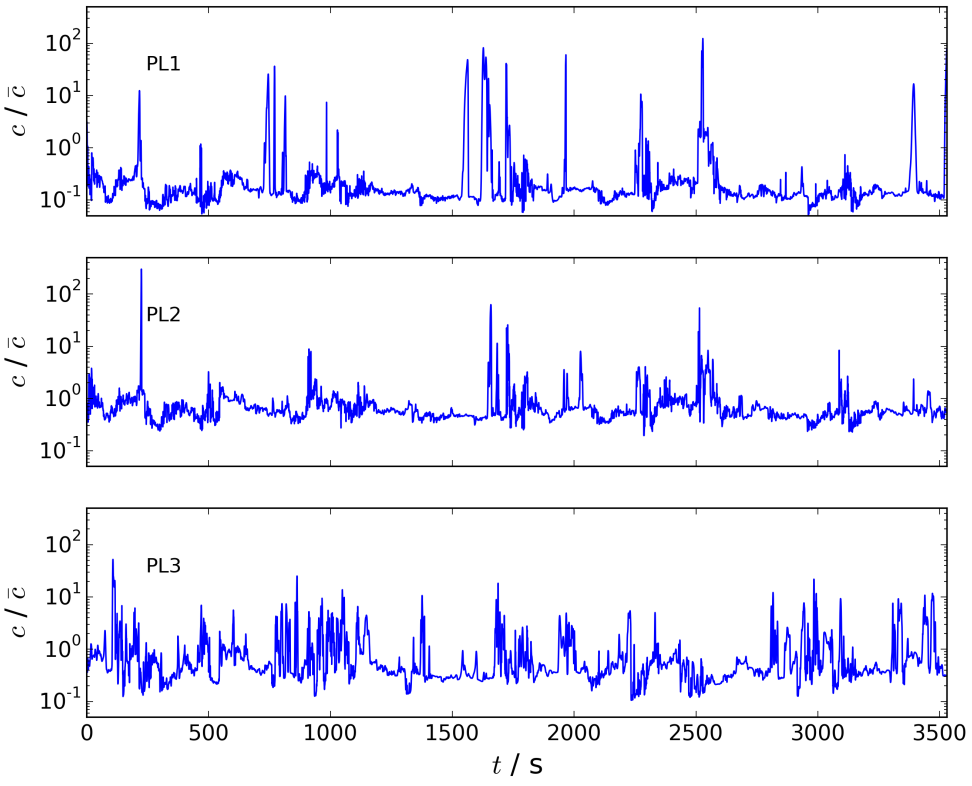

Figure 3.14: Time histories of relative instantaneous concentrations, c / $\bar{c}$, for the left large source at points PL1, PL2 and PL3.

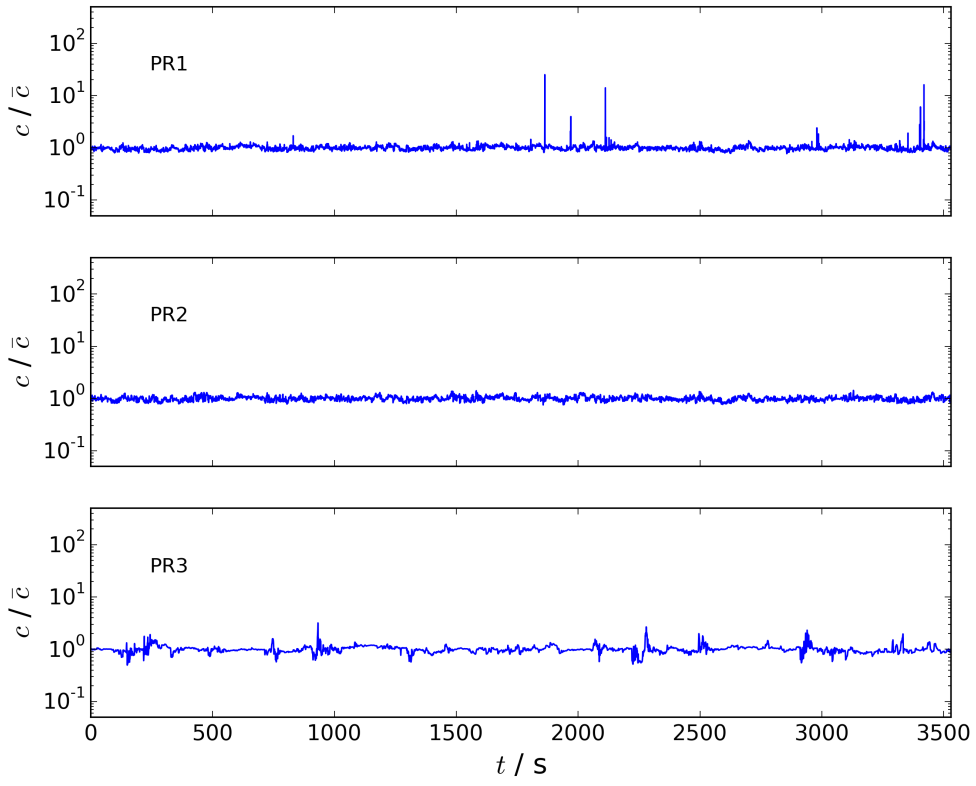

Figure 3.15: Time histories of relative instantaneous concentrations, c / $\overline{c}$, for the right large source at points PR1, PR2 and PR3.

Probability histograms of relative instantaneous concentrations, c / $\overline{c}$, are shown in Figures 3.16 and 3.17 for four locations. The 99th percentile value for c / $\overline{c}$, C_{99th}, C_{99th}, is given on each graph. For the left sources the largest value of C_{99th} was 28.1, which was for the large source at point PL1 (see Figure 3.17). It should be noted that similar results were produced in models with Δt = 0.01 s or 0.005 s. At point PL3, C_{99th} was approximately nine for both sources sizes. C_{99th} was 1.1 and 1.6 for both the small and large sources at PR1 and PR3 respectively.

The instantaneous concentration time histories show that higher c / $\overline{c}$ peaks exist but for less than 1 % of the time.

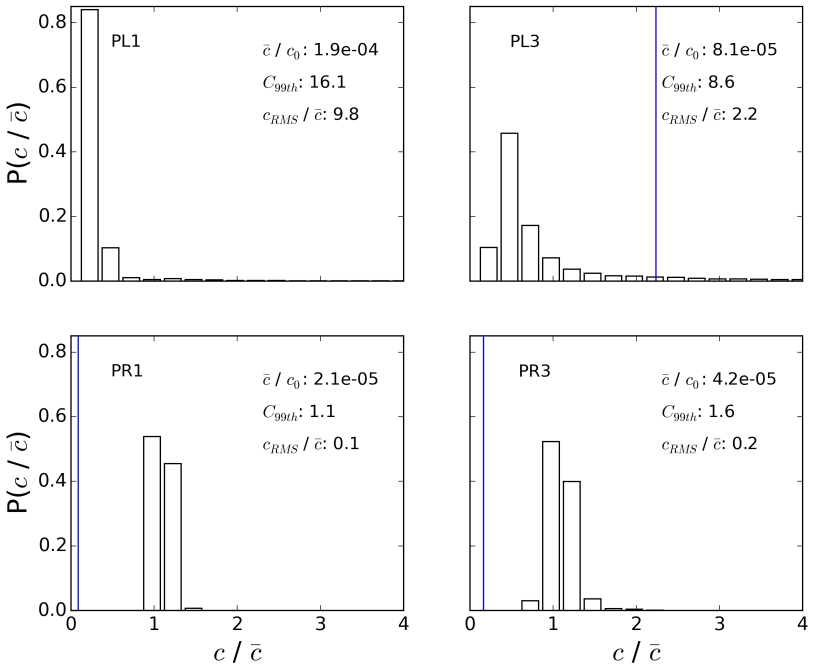

Figure 3.16: The probability distributions of c / $\overline{c}$ for the small sources at points PL1, PL3, PR1 and PR3. The upper graphs show releases from the left sources and the lower graphs the right sources. The vertical line shows c_{RMS} / $\overline{c}$. The bin width = 0.25.

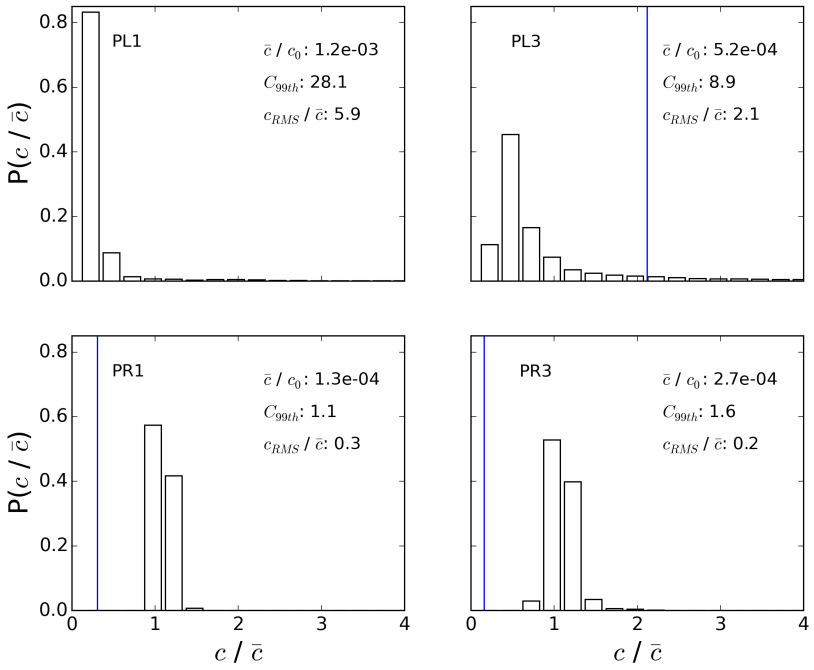

Figure 3.17: The probability distributions of c / $\bar{c}$ for the large source at points PL1, PL3, PR1 and PR3. The upper graphs show releases from the left sources and the lower graphs the right sources. The vertical line shows c_{RMS} / $\bar{c}$. The bin width = 0.25.

As with the concentration time histories, at both locations the probability distributions of c / $\bar{c}$ are very similar for the small and large sources.

3.3.4 Relating the fluctuating concentrations to canine limits of detection

In order to assess how frequently the vapour concentration exceeds the limit of detection of a dog at various locations, the vapour field has been scaled to represent that which would be produced if the sources were TNT (with c_0 = 3.4 ppb at 20 °C). It has been assumed that the dog has a 1 ppt limit of detection for TNT. Dogs are reported to have limits of detection of 1 ppt to 2 ppt (Walker et al., 2006) but may be significantly lower (Nicklin, 2015). Time series of the scaled concentrations at points PL1 and PL3 for the small left source, with the 1 ppt threshold are shown in Figure 3.18. Information on the number of times this threshold is exceeded, N_{1ppt}, over 3530 s at the monitor points PL1, PL3, PR1 and PR3 is given in Table 3.3 for both the large and small left sources. Also shown in the table are the percent of time spent above this threshold along with the maximum and median duration for the individual peaks.

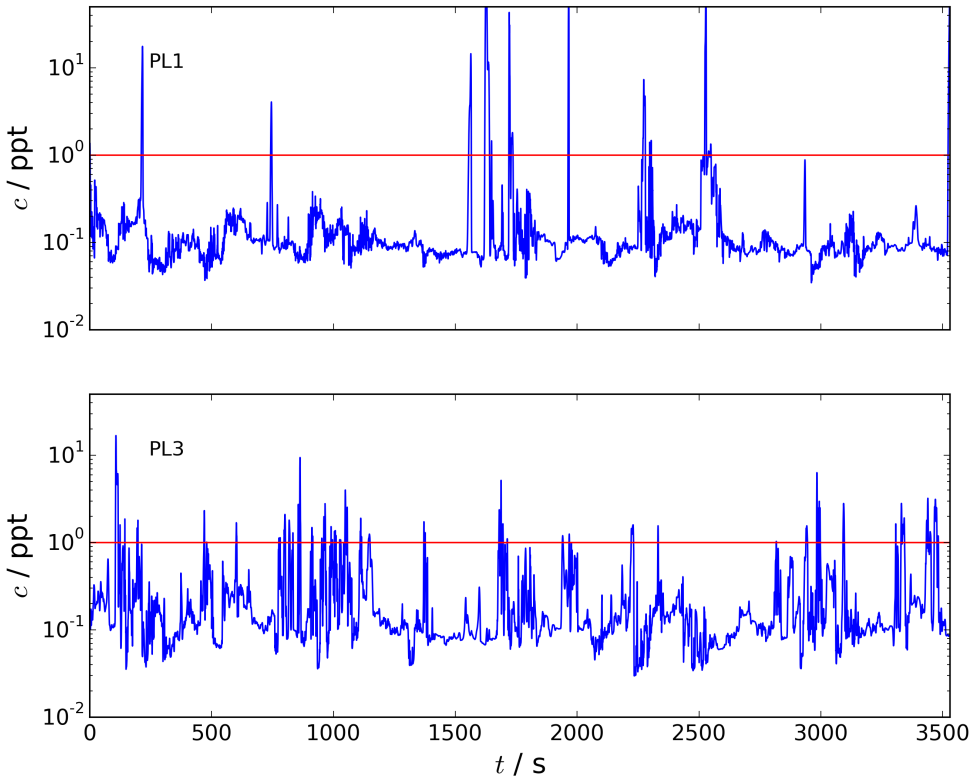

Figure 3.18: Time series of the scaled concentrations at points PL1 and PL3 for the small left source, with the 1 ppt threshold shown as a red line.

Source size	Location	N_{1ppt}	Percent of time /%	Maximum duration /s	Median duration /s
Small	PL1	16	2.9	20.0	5.5
Small	PL3	58	5.0	11.7	2.0
Small	PR1	0	0	0	0
Small	PR3	0	0	0	0
Large	PL1	126	18.7	66.5	1.8
Large	PL3	151	37.1	66.6	4.7
Large	PR1	10	0.1	0.9	0.3
Large	PR3	81	14.4	93.3	2.7

Table 3.3: Information on how frequently a 1 ppt threshold was exceeded over a period of 3530 s.

As expected, the threshold was crossed considerably more frequently for the large sources compared to the small sources. This is because $\dot{M}$ for the large source was 6.3 times that

from the small sources. When the threshold was exceeded, it was typically exceeded for approximately two seconds or longer. There are no exceedance events for the the right small source due to the location of the monitors relative to the plume. For the right large source, the room background concentration has been increased sufficiently for PR1 to register a small number of exceedance events.

3.4 Relating the results to chemical location techniques and the detection of vapour using dogs

The following discussion is based on the specific geometry and flow studied. Therefore, the conclusions cannot necessarily be applied to other types of room. However, the same principles should apply in appropriate cases. As stated previously, the first objective of this PhD is to investigate the unsteady flow present in a test room and the extent to which it can produce complex vapour fields that could either help or hinder vapour detection. One of the aims is provide advice to and tools for detection practitioners to improve their training processes and increase the likelihood of successful detection

Depending on the limit of detection of the dog and the source of the vapour, the animal may not be aware of the vapour until it enters the high concentration region, immediately adjacent to the source, due to the diluting effect of the supplied fresh air. This would be particularly relevant for low volatility materials such as most explosives. Based on a dog's sampling frequency, up to 7 Hz (Craven et al., 2010), it should be able to detect the concentration fluctuations. The instantaneous concentrations could be greater than 28 times the mean when sampling 0.1 m from the source and greater than 8 times at more than 1 m from the source. This effect was reduced for the right source as the flow there was less unsteady than at the left source. These peak concentrations were only present for 1 % of the time and the peaks were typically more than a minute apart. Therefore, a dog may need to remain stationary or to continue to search within a region in order to come across them.

Assuming that a dog can detect the vapour, consideration should be made for how it could then track to the source location. For both release locations there was a mean concentration gradient (in both the vertical and horizontal directions) leading towards the source. Therefore, chemotaxis may be a suitable method to track towards a vapour source in these cases. It should be noted that the unsteady nature of the vapour field means that a dog would need to be stationary and sampling the air for an unreasonably long period of time (of the order of τ, i.e. 353 s) to be able to sense (and then utilise) the time-averaged concentration field. This point should also be of interest to those designing autonomous sensor systems for operation indoors. It may be that dogs or autonomous systems could use eddy chemotaxis due to the relatively low frequency of the concentration fluctuations. Due to the way air circulates in rooms it is possible that

the source of an odour could lay downwind of the location where a dog first detects a signal. As a result, anemotaxis would also not be expected to work in all cases. All sources produced a relative RMS concentration field in which magnitudes decreased with distance from the source. However, the horizontal gradient was mainly contained within the left of the room for the left sources. To find the source of vapour the dog may have to employ a structured (e.g. the spiral search pattern of Ferri et al. (2009)) or random search pattern to enable it to move into the high concentration/gradient region near the source.

As mentioned earlier, the movement of a dog and handler in the room has not been accounted for in the modelling but it is expected that this movement would produce additional local unsteadiness and increase local mixing.

The large vapour sources, with nine times the surface area of the small sources, only produced concentrations 6.3 times higher. This was because the flux, F, from the large sources was 0.7 times that of the small sources. This has implications for the use of source materials in training exercises; increasing the surface area of the source may not increase the vapour concentration in the room proportionally.

The RMS concentration and the instantaneous concentration (not shown in this thesis) relative to the local time-averaged concentration were almost indistinguishable between the two sources, except very close to the source. Fackrell and Robins (1982) saw a similar effect for ground level sources in their wind tunnel study. They pointed out that the key ratio was the local turbulence integral length scale to the source diameter. When the local integral length scale is smaller than the source, the relative RMS concentration should be independent of source size. The implication of this is that small sources of explosive could produce the same relative RMS and relative instantaneous concentration as a large source. However, this would only apply when both sources are larger than the local integral length scale and within certain size constraints.

3.5 LES modelling conclusions and recommendations

A LES CFD model of vapour transport from a constant concentration area source in a mechanically ventilated room has been used to illustrate the capability of LES to simulate the complexity of indoor vapour fields and to assess how they relate to detection using dogs.

The following conclusions relate to the set-up of the model and its validity:

- The predicted turbulence statistics up to the 2nd order moment are generally in agreement with experimental data (Nielsen, 1990) (FAC2 of 0.75 and 0.95 and

FAC1.3 of 0.53 and 0.51 for mean and RMS velocity respectively). Other studies (e.g. Thysen (2015); Davidson and Nielsen (1996)) have captured certain flow features better than achieved here, but the use of LES has enabled the fluctuating velocity field to be predicted more accurately than in studies using a RANS approach.

- There are some uncertainties over the experimental data (Nielsen, 1990), for example, it was not reported what the conditions upstream of the inlet were. However, the modelled flow was shown to be not particularly sensitive to the level of turbulence applied at the inlet.

- There is some question over the two-dimensionality of the flow (Thysen, 2015; Nielsen et al., 2010; Voigt, 2005) and Nielsen et al. (2010) stated that it is possible that different flow patterns were present in the experiment but were not captured in the reported data. This means that there may be more than one correct solution for the flow, as can be the case for room airflows, where the flow can switch between different stable modes (Li and Nielsen, 2011; Nielsen et al., 2010).

- Regarding the model set-up, there are a considerable number of components in a LES model that can be selected by the user. While great effort has been made to assess the sensitivity to the key ones, it is not practical to assess them all. For example, it is not known whether a finer mesh across the domain with a second-order central difference scheme applied to the species transport equations would improve the accuracy of the peak concentration predictions. However, best practice, based on previously reported studies, was used to define the modelling approach.

The following conclusions relate to the concentration field and detection:

- The predicted scalar flux and intensity of concentration fluctuations were compared against analytical models and wind tunnel and LES data in the literature with success.

- Due to the low volatility of some compounds of interest and the diluting effect of the fresh air in the room, the time averaged vapour concentrations present in the bulk of the room may be extremely low, whereas the peak concentration can be much greater than the mean.

- Near the source the concentration fluctuates significantly but the amplitude of these fluctuations was shown to be dependent on the location of the source, and the local turbulent flow field.

- It was shown that instantaneous concentrations of approximately 28 times the mean were predicted 0.1 m away, and greater than 8 times the mean more than 1

m away for the large and small left sources. These peaks were present for 1 % of the time.

- The vapour field did not scale linearly with the surface area of the source, for the modelled source sizes. This is perhaps not surprising given the very low speed of airflow in the room and the relatively large area size of the sources.
- The source size did not have a significant effect on the instantaneous and RMS concentrations, relative to the local mean concentration, apart from close to the source. Therefore, ten times the surface area of the source material would not produce ten times the vapour, but may produce the same relative RMS and relative instantaneous concentration field.
- Based on the ways in which animals are known to use air- or water-borne chemicals to locate a source, it is not clear whether there is sufficient information present in large parts of the room for dogs to be able to achieve this after they have detected the vapour.
  - It may be necessary to use a structured or random search pattern that enables a detection dog to encounter sufficiently high concentrations or gradients (in the mean or RMS field) close to the source.
- A dog should be able to differentiate the concentration fluctuations, as the integral time scales for concentration were well above reported dog sniffing time scales.
- The above conclusions are based on a simple indoor scenario and although the findings cannot be directly extrapolated to others types of room, the same principles should apply in appropriate cases.

It is recommended that:

- The modelling methods developed in this chapter are applied to a range of room types, including various mechanical ventilation configurations, naturally ventilated room and various room shapes. This should be done to see whether the findings can be applied more generally.
- Work is undertaken to reduce the simulation time. Generating the time-averaged flow solution took approximately one week on 60 compute cores. An initialised and time-averaged species solution could take could take one month on 60 cores.
  - Using the results of the current simulations it may be possible to use the standard Smagorinsky instead of the dynamics model (the volume averaged value for $\sqrt{C_{DS}}$ in the current model was 0.14) and achieve similar results.
  - It may also be possible to reduce the mesh resolution near some of the walls, away from the source regions, without having a negative effect on the results.

– The model may run more quickly in a different CFD code such as OpenFOAM®.

In the following chapter the same test room is modelled at a range of ACRs to try to make the findings more generic. Sorption is included in the model in Chapter 5 and in Chapter 6 the same vapour transport scenario is simulated using an eddy diffusion model.

Chapter 4

The effect of air change rate on the concentration fluctuations

4.1 Introduction

To extend the generality of the conclusions from Chapter 3, the Nielsen (1990) test-case was run with species transport for a range of air change rates. The air change rates included were: $10.2\,\mathrm{h}^{-1}$, $7.5\,\mathrm{h}^{-1}$, $5.0\,\mathrm{h}^{-1}$, $2.5\,\mathrm{h}^{-1}$, $0.5\,\mathrm{h}^{-1}$. This range went from the reasonably high condition specified in the original experiment (Nielsen, 1990), down to a rate which is more typical of a residential building (Murray and Burmaster, 1995).

4.2 Methodology

The room geometry and model set-up were the same as those described in Chapter 3. The only changes were the inlet velocity, u_0, and the time step size, Δt. Δt was increased as u_0 was decreased to keep the CFL approximately the same for all models (i.e. a maximum of less than 1).

As the velocity was reduced from that in the previously validated model it was assumed that the solution would remain valid as the non-dimensional grid sizes (e.g. y_1^+) would be reduced.

The inlet velocity and Re for the different air change rates are shown in Table 4.1. Most studies of the Nielsen (1990) test-case, or similar test cases, use the inlet height, H_{inlet}, as the characteristic length for Re. Kandzia and Mueller (2016) discussed the use of a Reynolds number calculated using the square root of the inlet area. They showed that this is a better indicator of Reynolds number independence as it is indicative of the total momentum flux into the room. For completeness, both Reynolds numbers are given, but

only the inlet hight Re is given in the remainder of the chapter as this is used in the majority of the relevant studies.

λ $/\mathrm{h}^{-1}$	u_0 $/\mathrm{m{\cdot}s}^{-1}$	Re inlet height	Re inlet area
10.2	0.455	5000	21100
7.5	0.335	3680	15500
5.0	0.223	2450	10400
2.5	0.112	1230	5180
0.5	0.022	245	1040

Table 4.1: Model conditions for the air change rate study. Re is calculated from both H_{inlet} and the square root of the inlet area.

For a similar shape geometry, van Hooff et al. (2012a) showed that the flow along the top of their domain was in transition to turbulence from an inlet height Reynolds number of approximately 1750, up to at least 2500. Nielsen (1990) stated that the flow in the geometry had fully developed turbulence at an inlet height $Re = 5000$ and the data indicated that there was some transition below this Reynolds number. Nielsen et al. (2000) reported on experiments in a scale model of similar shape to that studied here that the flow was laminar for inlet height $Re = 211$ and transitional for Reynolds number of approximately 1000. A study by Nielsen (1988, 2015), looked at isothermal air flow in a full-scale room with five different air supply devices. Nielsen stated that air change rates above $2\,\mathrm{h}^{-1}$ to $5\,\mathrm{h}^{-1}$ (depending on the air supply devices used) were required to achieve fully developed turbulence in at least some parts of the room. Davidson et al. (2000) carried out LES modelling of a similar room with an inlet height $Re = 600$ and reported that a transitional flow was found. Topp et al. (2000) carried out experiments in a full scale room with a similar design and their results indicated that the flow was turbulent for Re >500. In a room with isothermal flow, Kandzia and Mueller (2016) suggested that the flow only became Reynolds number independent, and therefore fully turbulent, at an inlet height Reynolds numbers greater than approximately 20000 or inlet area Reynolds numbers of 45000. A number of other factors could influence whether the flow is laminar or turbulent, such as: the shape of the room, the presence of furniture or people and thermal gradients.

Therefore, based on the previous work it was expected that the applied range of inlet conditions should create fully turbulent, laminar and transitional flows.

4.3 Results and discussions

4.3.1 The flow field

Contours and vectors of time averaged, normalised, velocity ($\overline{u}$ / u_0) on the vertical centre plane are shown in Figures 4.1 and 4.2. The data for $7.5\,\mathrm{h}^{-1}$ is not included in this and subsequent figures, as it is similar to that shown for $10.2\,\mathrm{h}^{-1}$ and $5\,\mathrm{h}^{-1}$.

The overall pattern of the contours are very similar for ACRs from $10.2\,\mathrm{h}^{-1}$ and $2.5\,\mathrm{h}^{-1}$, with a small reduction in the normalised velocity of the jet as it moves from the ceiling to the side-wall, as the ACR reduces. The separation point on the floor moves slightly towards the middle of the room as the ACR reduces. For an ACR $= 0.5\,\mathrm{h}^{-1}$ the contours are very different, the wall jet mixes much less as it moves across the ceiling and the separation point on the floor occurs much earlier. This suggests that the flow in the room is laminar when the ACR $= 0.5\,\mathrm{h}^{-1}$ and the inlet height Re = 245.

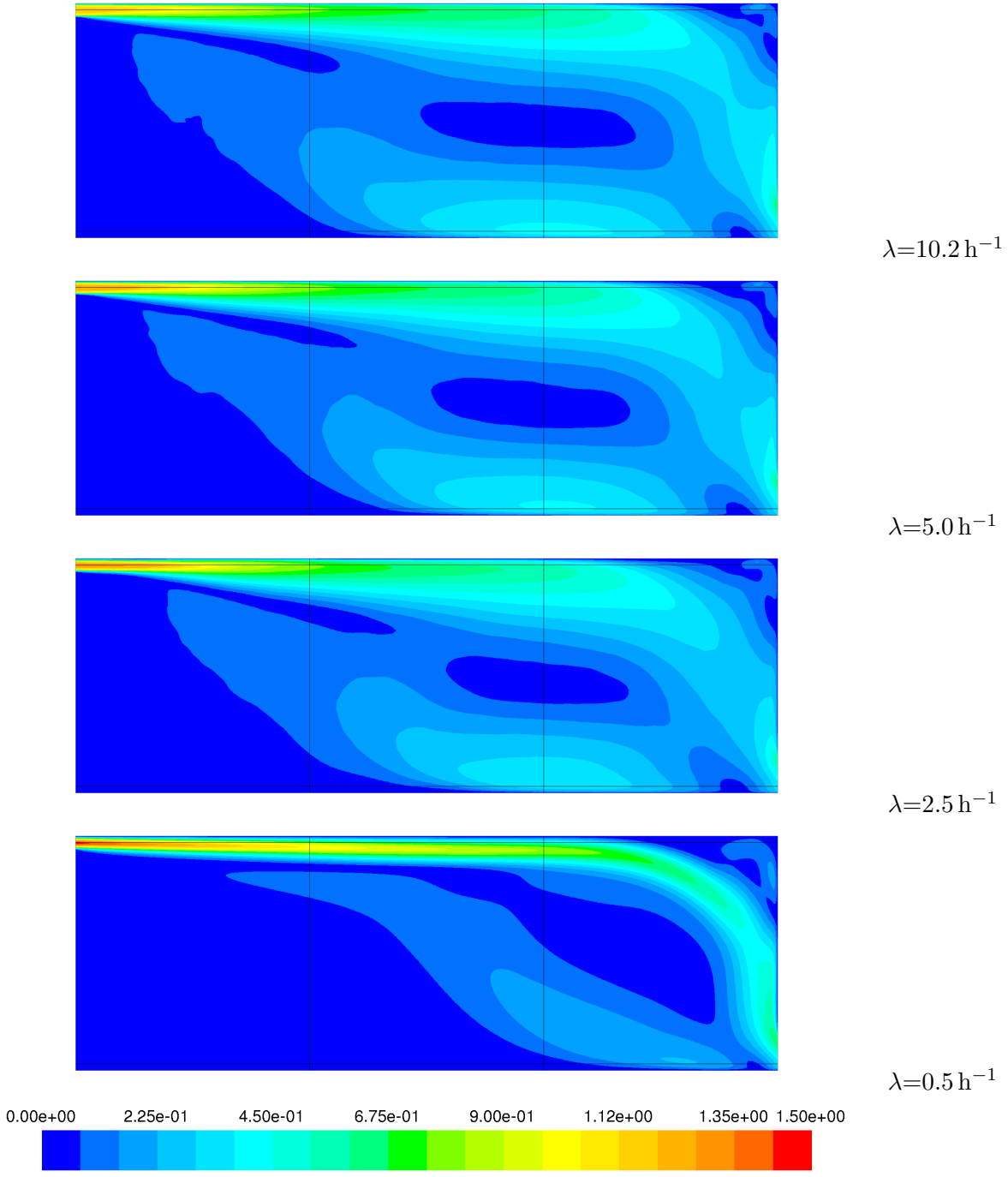

Figure 4.1: Contours of normalised mean velocity ($\overline{u}$ / u_0) for four different air change rates, on the vertical centre plane.

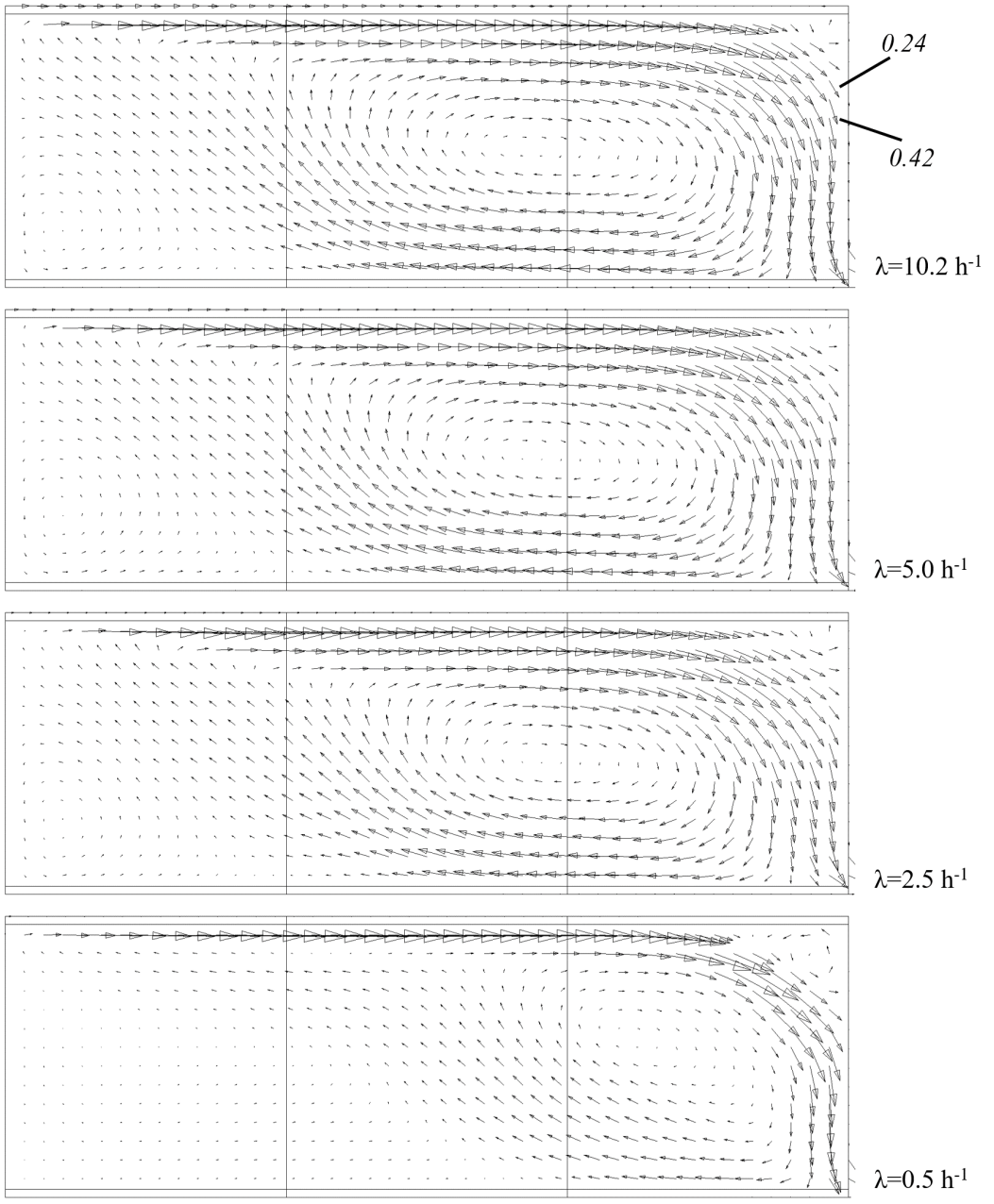

Figure 4.2: Vectors of normalised mean velocity ($\overline{u}$ / u_0) for four different air change rates, on the vertical centre plane.

The flow along the top wall of the room can be considered to be a plane wall jet, albeit one with a reasonably small aspect ratio of H/H_{inlet} = 17.9. It has been shown that plane wall jets show similar profiles within the characteristic decay region (x/H_{inlet} >7). An empirical relationship for the non-dimensional velocity in a turbulent plane wall jet was given by Rajaratnam (1976) and a theoretical relationship for a laminar plane wall jet was given by Glauert (1956).

Non-dimensional velocity profiles for four of the different cases, at $x\ /\ H = 2$, are shown in Figure 4.3 in comparison with the turbulent and laminar profiles of Rajaratnam (1976) and Glauert (1956), respectively. u_{max} is the maximum velocity in the jet and $y_{1/2}$ is the distance from the wall at which u has decayed to 0.5 u_{max}.

The profiles for the cases with an ACR of $\geq 2.5\,\mathrm{h}^{-1}$ quite closely follow the theory for a turbulent wall, whereas the profile for the ACR $= 0.5\,\mathrm{h}^{-1}$ case clearly follows the theoretical laminar profile.

For the cases with an ACR of $\geq 2.5\,\mathrm{h}^{-1}$, the location of the maximum velocity moves towards the wall as the ACR increases. Even with the highest Re (5000), the profile does not quite match that of the Rajaratnam (1976). A similar trend (movement of the maximum velocity towards the wall as the ACR increases) was seen by van Hooff et al. (2012b) when carrying out experiments in a comparable geometry to the Nielsen test-case with inlet Reynolds numbers varying from 1000 to 2500. This change with Re (i.e. movement of the point of maximum velocity towards the wall) is most likely an indication that the flow from the inlet should be considered transitional in the Re range studied. Another important effect, as discussed by van Hooff et al. (2012b), is that the wall at the end of the room forces the flow to separate from the top wall and the result of this is to move the maximum velocity point away from the wall.

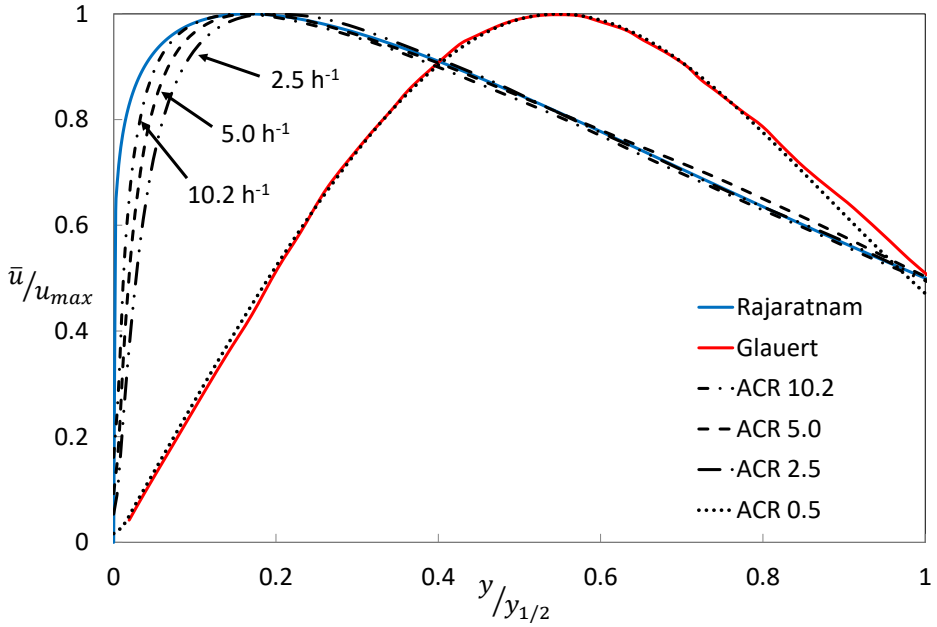

Figure 4.3: Non-dimensional velocity profiles for the wall jet for the four CFD cases, compared to the empirical model for a turbulent wall jet (Rajaratnam, 1976) and the theoretical model for a laminar wall jet (Glauert, 1956).

Figure 4.4 shows contours of normalised total (i.e. resolved and subgrid scale) TKE. Again, the overall patterns are similar for the higher ACRs but there is very little TKE present when ACR $= 0.5\,\mathrm{h}^{-1}$. A small amount of TKE is generated in the $0.5\,\mathrm{h}^{-1}$ ACR model when the jet reaches the far wall.

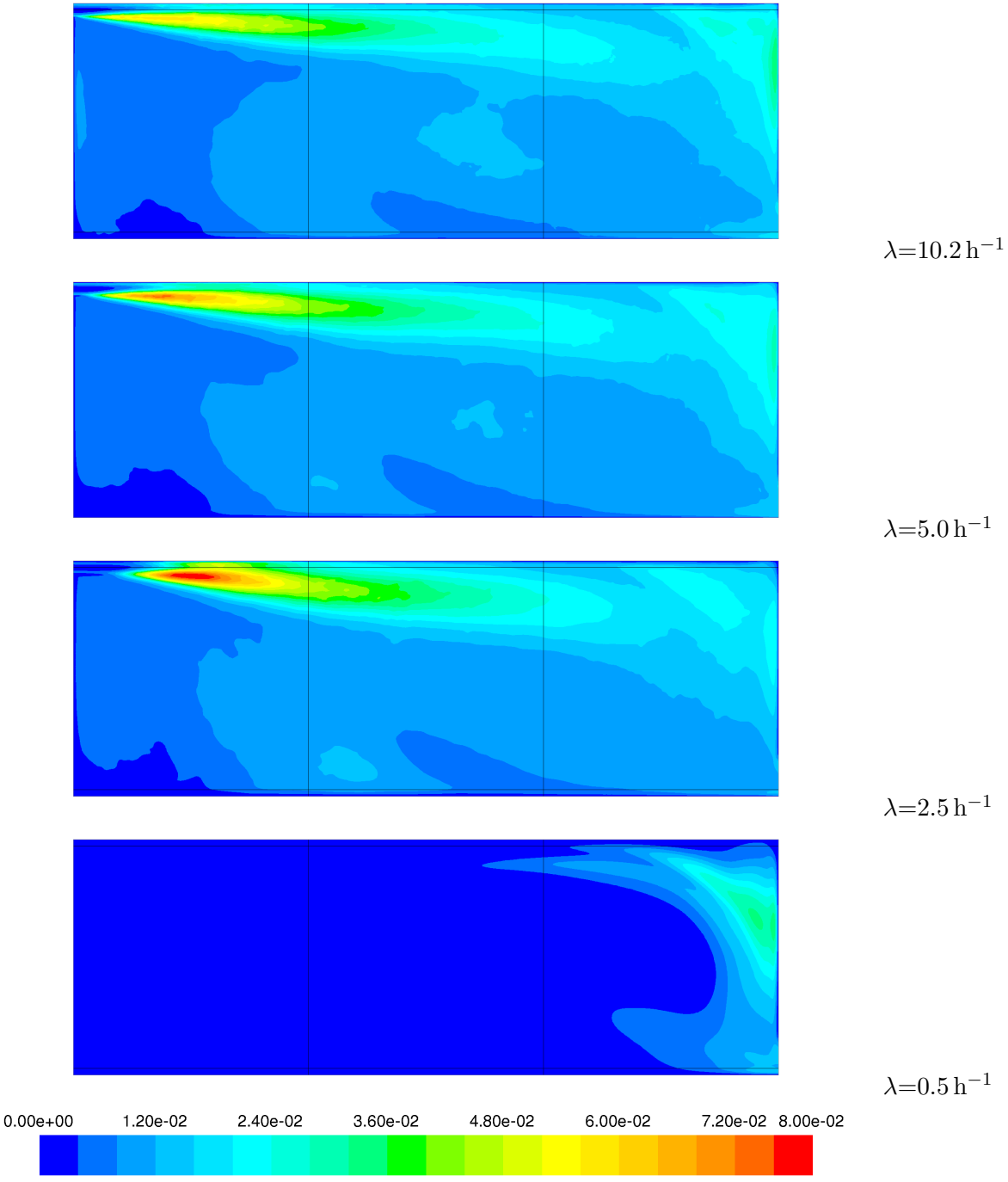

Figure 4.4: Contours and vectors of normalised total TKE (TKE / u_0^2) for four different air change rates, on the vertical centre plane.

Normalised energy spectra (where E is the energy) for the five ACRs are shown in Figure 4.5, for the u velocity at point PL1, i.e. 0.1 m above the centre of the left source. As stated previously, Δt was increased as u_0 was decreased to keep the CFL approximately the same for all models. Therefore, the upper frequency cut-off (1 / ($2\Delta t$)) decreases as the ACR decreases. For the 0.5 h^{-1} model this cut-off was 2.5 Hz. The CFL number at PL1 was approximately 0.03 for the models with ACR from 10.2 h^{-1} to 2.5 h^{-1} but

dropped to 0.002 for the $0.5\,h^{-1}$ model. This was because, proportionally, less of the flow reaches the lower left-hand corner of the room in that model. Therefore, the relative coarseness of the mesh further reduced the maximum frequencies that can be resolved. This cut-off is 4.7×10^{-3} Hz for the $0.5\,h^{-1}$ model and 0.32 Hz and above for the other models.

The cut-off frequency for the $10.2\,h^{-1}$ model, close to the left source, was approximately 1.5 Hz. In the bulk of the domain the CFL number was higher so the cut-off frequency was ≤ 25 Hz. Therefore, this should be suitable to capture most of the velocity/vapour fluctuations based the range of frequencies seen in typical rooms (0.002 Hz to 2 Hz, see Section 1.4)

For an ACR of $10.2\,h^{-1}$, the smallest eddy size (the Kolmogorov scale) was about 2 mm, while its frequency was approximately 2.5 Hz (see Section 3.3.3). This means the resolution of the LES is reasonable. Reducing the ACR (and consequently the velocity), increases the smallest eddy size and reduces the corresponding frequency.

It can be seen that the energy in the higher frequencies increases as the ACR (or Re) increases. The -5/3 slope indicates that the inertial subrange was resolved in the models with an ACR $\geq 2.5\,h^{-1}$. The graph confirms that the flow near the floor of the room is laminar in the ACR $= 0.5\,h^{-1}$ model as there is very little energy in the flow apart from at the lowest frequencies.

That there is laminar flow for ACR $= 0.5\,h^{-1}$ (Re inlet height = 245, Re inlet area = 1040) and turbulent flow for ACR $\geq 2.5\,h^{-1}$ (Re inlet height $\geq$ 1230, Re inlet area = 5180) is consistent with most of the published data discussed in Section 4.2. Only the data of Kandzia and Mueller (2016) showed transition happening at a higher Reynolds number (Re inlet area = 45000). However, in the Kandzia and Mueller (2016) study, the presence of fully developed turbulent flow was only indicated by measuring the velocity at one location in the room and the authors themselves stated that Reynolds numbers effects are not easy to track in a complex flow field.

Without conducting an extensive study it is not possible to say whether the air change rate, or Re based on the inlet height or area, or even Re based on a characteristic room dimension is the best indicator of whether the air flow in a room is turbulent. It is recommended that further modelling or experimental work is carried out to find an optimum metric.

A survey of air change rate data for US residential buildings has been compiled by Murray and Burmaster (1995). They compiled data from 2844 single and multiple family residential units. The median air change rate across all buildings was $0.51\,h^{-1}$. Therefore, based on a simple assumption that ACR provides an indication of whether room air flow is turbulent and accepting that other factors identified above could have

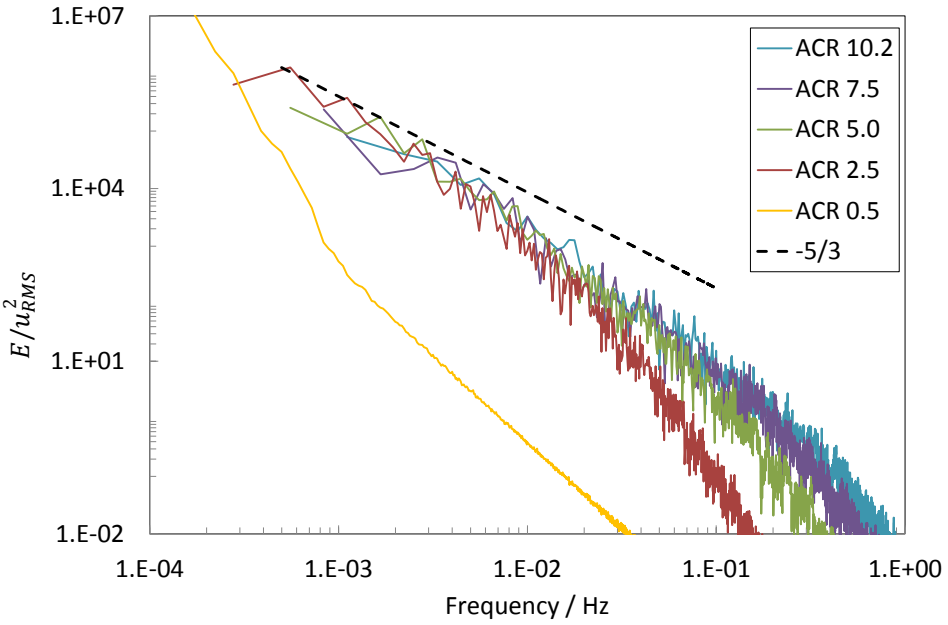

Figure 4.5: Normalised energy spectra from the u velocity at point PL1 for the five ACRs.

an effect, it is possible that a large proportion of residential buildings primarily have laminar air flow.

This implies that the findings for the ACR $= 0.5\,\mathrm{h}^{-1}$ room may apply in these rooms as well. This also means that the air flow in these rooms could be modelled using an unsteady laminar model instead of LES. Laminar models have been used before for predicting indoor air flow, for example Posner et al. (2003) showed that a laminar model accurately predicted air flow in their room with an inlet $Re = 1600$ (they do not document whether Re is based on the inlet area or length). Davidson et al. (2000) used an unsteady 2D laminar model (alongside a LES model) to predict the flow in a Nielsen (1990) test-case like room (inlet height $Re = 600$) but showed that the laminar model was not able to predict even the main flow features in the room. One explanation for the poor performance might have been the coarseness of their mesh; they used only 0.3 million cells in their full 3D model vs. more than 5 million cells used in the models for this PhD.

It should be noted that the ACR is not the only parameter which indicates whether room air flow is laminar or turbulent. Other effects, such as buoyancy and people movement, could be sources of turbulence.

Given the uncertainty over whether the air flow in a room is laminar or not and the possible poor performance of the laminar model reported by Davidson et al. (2000), it is recommended that LES with a dynamic Smagorinsky subgrid scale model is used for this type of problem, if time and computer resources allow.

4.3.2 The vapour flux

As the ACR in the room reduces, so does the friction velocity at the source and this results in a decrease in the vapour flux according to the mass transfer model of Danberg (2008) (Equation 3.5), this effect is shown in Figure 4.6 for the large sources. The figure includes data from a model with $\lambda = 0.25\,\mathrm{h}^{-1}$ as well as the models with λ from $0.5\,\mathrm{h}^{-1}$ to $\lambda = 10.2\,\mathrm{h}^{-1}$. The figure shows a solid line which represents the Danberg (2008) model (Equation 3.5). For $u_\tau \geq 7.3 \times 10^{-4}\,\mathrm{m{\cdot}s^{-1}}$, the CFD data follows the change in rate predicted by the Danberg model with an over-prediction of only a factor of between 1.4 and 1.2.

The dashed line in Figure 4.6 shows the diffusion-limited vapour flux model of Gershanik and Zeiri (2010). Gershanik and Zeiri (2010) showed that under certain conditions, the sublimation rate of an explosive can effectively be described by a diffusion-in-air limited rate. For the case of vapour production from a flat disc, Gershanik and Zeiri (2010, 2012) showed that the following is true for samples of explosives with diameters up to 6 mm.

The concentration, C, around a sphere with radius R, with a fixed surface concentration in an unbounded space, when time, $t = \infty$ is given by the following (Gershanik and Zeiri, 2010),

$$C = C_0 \frac{R}{r}, \tag{4.1}$$

where r is the radial distance from the sphere. Equation 4.1 can be differentiated with respect to r to give the following (Gershanik and Zeiri, 2010),

$$\frac{dC}{dr} = -C_0 \frac{R}{r^2} \tag{4.2}$$

Inserting Equation 4.2 into Fick's first law, Equation 2.37, when $r = R$, gives the diffusion limited sublimation or evaporative flux, F from a sphere or a hemisphere on a perfectly reflecting surface. This is a modified form of the equation given in Gershanik and Zeiri (2010).

$$F = \frac{D_m\, C_0}{R} \tag{4.3}$$

Gershanik and Zeiri (2010) also gave an equation for sublimation or evaporation rate from a disc with radius R, and it has been modified here to give F in terms of C_0 rather than P_0.

$$F = \frac{4 D_m\, C_0}{\pi R}, \tag{4.4}$$

The dashed line in Figure 4.6 is calculated using Equations 4.4 and 3.4, with R calculated for a disc with the same surface area as the square source used in the LES model.

Interestingly, as noted by Gershanik and Zeiri (2010), when R approaches infinity, F approaches zero. The concentration gradient from an infinite flat plate is indeed zero when $t = \infty$ (Crank, 1979). Also, integrating either Equation 4.3 or 4.4 shows that the mass emission rate is proportional to the radius of the source, not the surface area.

Gershanik and Zeiri (2010) commented on the steady-state assumption of their model and showed how this condition would be reached very quickly with small hemispherical TNT particles. Some additional discussion on the Gershanik and Zeiri (2010) model including the time taken to reach a steady-state condition are given in Appendix A.4 along with some sublimation flux data for TNT.

The CFD data confirms, for the first time (to the best of our knowledge), that when u_τ reaches a certain lower threshold, $3 \times 10^{-4}\,\mathrm{m{\cdot}s^{-1}}$ in this case, the flux becomes limited by the rate of molecular diffusion as opposed to the friction velocity. This suggests that as the flow reduces to a certain point, transport due to molecular diffusion becomes dominant over that due to advection. This transition point can be calculated using the following equation, which comes from a combination of Equations 3.5 and 4.4.

$$u_\tau = \frac{4.77\sqrt{D_m}\,\nu}{L_{source}}. \tag{4.5}$$

4.3.3 The concentration field

For the rooms with turbulent flow, the friction velocity at the floor reduces approximately linearly with the ACR and therefore the Sherwood number reduces at approximately $\mathrm{ACR}^{2/3}$, according to Equation 3.5. This results in an increase in concentration across the room as the ACR is reduced, i.e. the flux reduces at a slower rate than the fresh air rate, Q_f. This effect can be seen in Figure 4.7. The pattern of the concentration contours is similar for ACRs from $10.2\,\mathrm{h^{-1}}$ to $2.5\,\mathrm{h^{-1}}$, but there is an increase in the background concentration as the ACR reduces.

For the laminar case, the high concentration region around the source extends quite far to the right of the source due to the location of the separation point on the floor and the reduced mixing in the room. This clearly shows that the concentration does not follow a simple relationship with the air change rate.

Relative instantaneous concentration (c / $\overline{c}$) time histories at point PL1 (see Figure 3.3), which is 0.1 m above the centre of the left source, for four ACRs are shown in Figure 4.8. The relative instantaneous concentration is plotted against t normalised by the

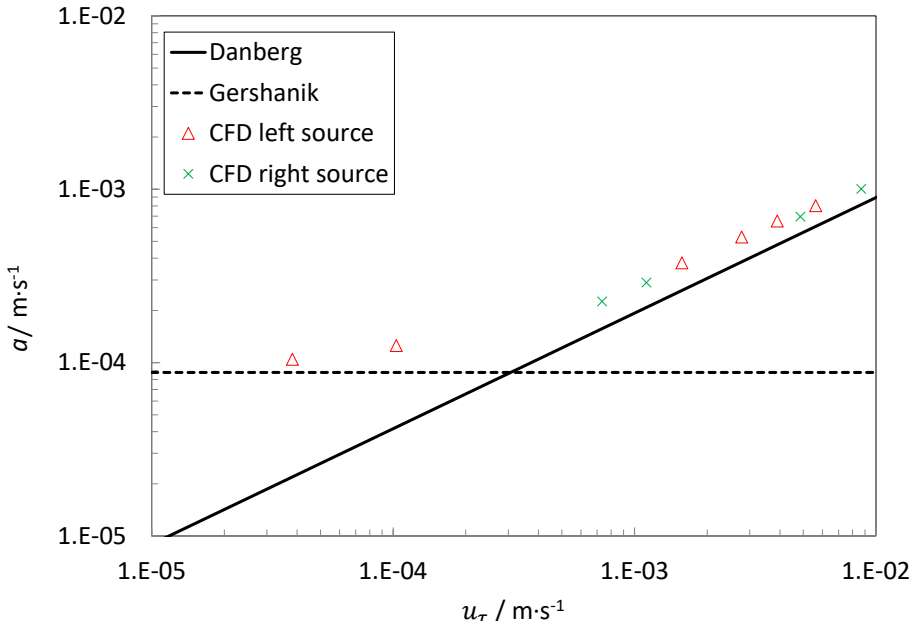

Figure 4.6: Mass transfer coefficients against friction velocities for the left and right large sources at six air change rates. The solid and dashed lines show the mass transfer coefficient as predicted by the Danberg (2008) (friction velocity controlled) and Gershanik and Zeiri (2010) (diffusion-limited) models respectively.

characteristic mixing time, $\tau = 1 \,/\, \lambda$. Probability distributions of relative instantaneous concentration for the four ACRs at points PL1, PL2 and PL3 are shown in Figure 4.9.

A broadly similar pattern is shown for ACR = $10.2\,\mathrm{h}^{-1}$ to $2.5\,\mathrm{h}^{-1}$, with the data for ACR = $0.5\,\mathrm{h}^{-1}$ looking very different. Both figures 4.8 and 4.9 show that there are no significant concentration fluctuations at PL1 for ACR = $0.5\,\mathrm{h}^{-1}$, as indicated by the small values for $c_{RMS} \,/\, \overline{c}$ and C_{99th} (C_{99th} is the 99th percentile value for $c \,/\, \overline{c}$). At PL2 and PL3 there are some fluctuations, but these are smaller than at the other ACRs.

The time histories for the higher ACR cases in Figure 4.8 have similar features. As τ is longer for lower ACRs, the duration of the high concentration fluctuations will be longer too. This means that there might be an optimum air change rate for sampling, when the concentration fluctuations are high and of long duration (i.e. the lowest air change rate which produces turbulent flow). Similarly though, there would also be long periods of low concentration.

The integral time scale for concentration, $\Lambda_{t,c}$, was calculated (using the first zero-crossing point on an autocorrelation function) at monitor locations PL1 and PL3, i.e. 0.1 m and 0.3 m above the left source (See Figure 3.3 for monitor locations), for each ACR model. The results are shown in Table 4.2.

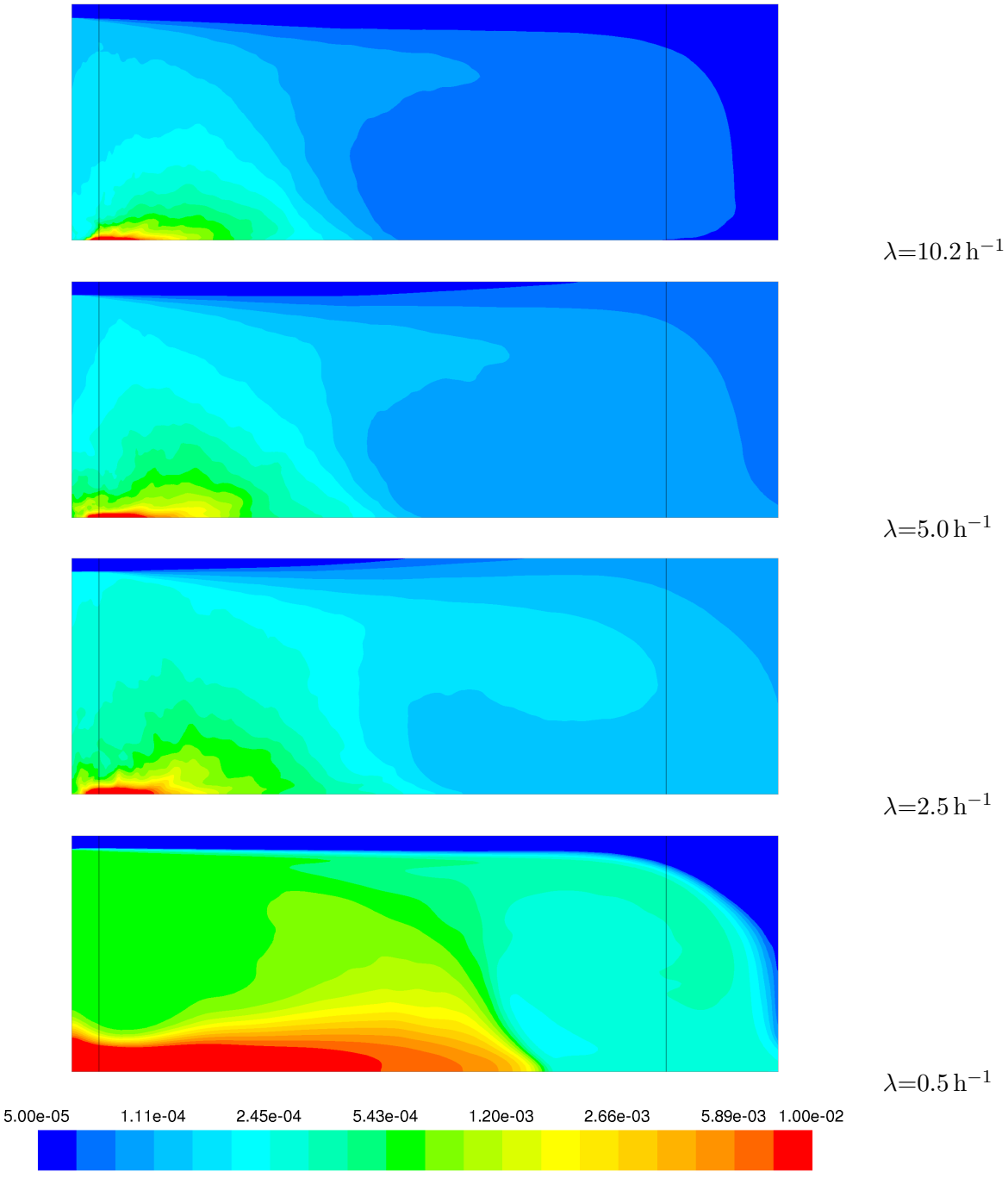

Figure 4.7: Normalised mean concentrations ($\overline{c}$ / c_0) for four different air change rates. For the large left source on the vertical centre plane. The concentrations are shown on a log scale and are not clipped to the range. The vertical lines are positioned at the centres of the left and right sources.

ACR	PL1		PL2	
$/\mathrm{h}^{-1}$	$\Lambda_{t,c}/s$	$\Lambda_{t,c}$ / τ	$\Lambda_{t,c}/s$	$\Lambda_{t,u}$ / τ
10.2	3.5	0.010	4.3	0.012
7.5	4.5	0.009	7.5	0.016
5.0	7.3	0.010	28.1	0.039
2.5	45.4	0.032	18.0	0.013
0.5	2607.2	0.362	2573.7	0.357

Table 4.2: Integral time scales for concentration at PL1 and PL3.

There was a general increase in $\Lambda_{t,c}$ as the ACR reduced from $10.2\,\mathrm{h}^{-1}$ to $2.5\,\mathrm{h}^{-1}$. For the $0.5\,\mathrm{h}^{-1}$ model, the time scales were considerably longer, at >2000 s.

$\Lambda_{t,c}$ is also shown in Table 4.2 normalised by τ. Some of the $\Lambda_{t,c}$ / τ values for each location are similar, e.g. for $10.2\,\mathrm{h}^{-1}$, $7.5\,\mathrm{h}^{-1}$ and $5.0\,\mathrm{h}^{-1}$ at PL1 and for $10.2\,\mathrm{h}^{-1}$, $7.5\,\mathrm{h}^{-1}$ and $2.5\,\mathrm{h}^{-1}$ at PL3, but this requires further exploration to see if a more general relationship between the room and turbulence time scales can be found.

The integral time scales for concentration, at all air change rates, are more than one order of magnitude greater than the dog sniffing time scales, 0.25 s to 0.14 s (based on sniffing frequencies reported by Craven et al. (2010)).

It is worth noting here that the local effective air change rate (calculated from local concentration decay curves) can differ from the whole room air change rate, λ. In the Nielsen test room the flow pattern means that the lower left corner of the room was less well ventilated than the rest of the room. This effect was most significant in the $0.5\,\mathrm{h}^{-1}$ model as the flow separated from the floor at around x / $H = 6$ and as there was less mixing with the laminar wall jet along the top wall.

As with the LES model in Chapter 3, the concentration fields here were averaged for 10τ. However, for the $0.5\,\mathrm{h}^{-1}$ model the average concentration was still changing after 10τ so this model was averaged for 20τ. This was required due to the lower effective air change rate in the lower left corner of the room.

The effective air change rate effect is further discussed in Section 5.4, where it is shown that the effective air change rate in the lower right corner of the room was $8.0\,\mathrm{h}^{-1}$ when the whole room air change rate was $10.2\,\mathrm{h}^{-1}$.

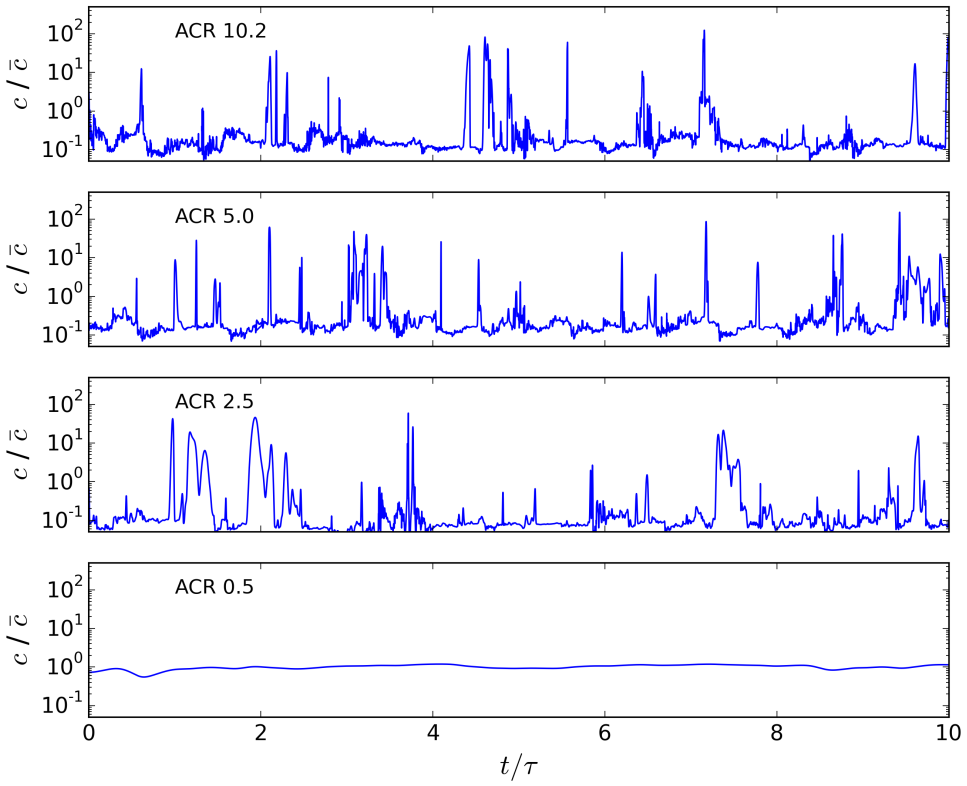

Figure 4.8: Time histories of relative instantaneous concentrations (c / $\bar{c}$) for four different air change rates, for the left large sources at point PL1. t is normalised by τ.

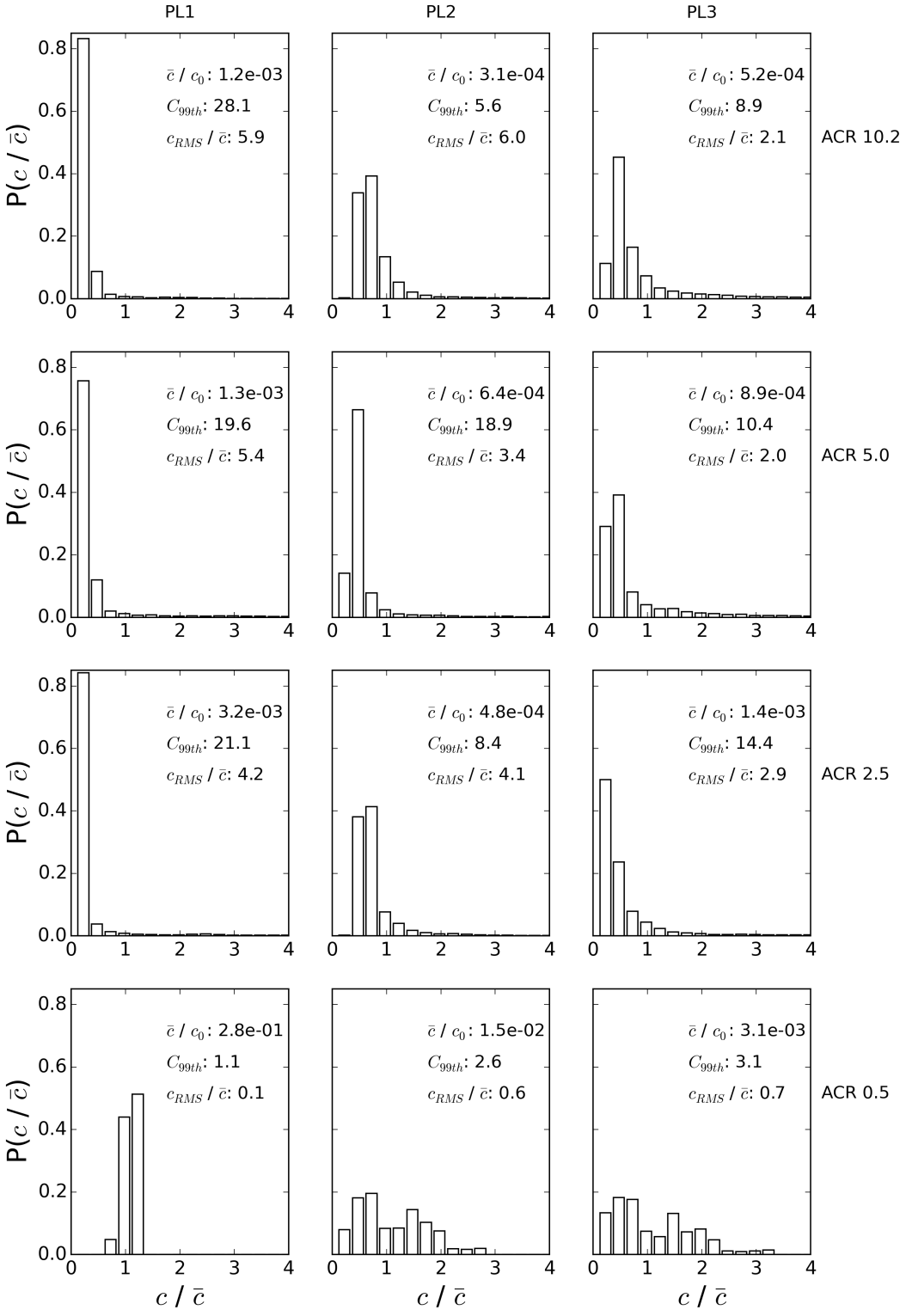

Figure 4.9: The probability of c / $\bar{c}$ for the large left sources at points PL1, PL2 and PL3 for four different air change rates. The bin width = 0.25.

As was shown in the previous chapter, when the air change rate was high, large concentration fluctuations were present in the room. 28 times the mean was recorded at 0.1 m and greater than 8 times the mean at more than 1 m from the source. The analysis in this chapter has shown that large concentration fluctuations are also present at lower ACRs, i.e. 14 times the mean at more than 1 m from the source for ACR = $2.5\,\mathrm{h}^{-1}$.

When the air flow in the room becomes laminar (below an ACR of $2.5\,\mathrm{h}^{-1}$ and an inlet height Re of 1230 in this case) the fluctuations at PL1 are no longer present or are much reduced. That no high frequency fluctuations exist in a laminar flow is to be expected, however, it was not known whether lower frequency meandering of the vapour plume could produce periods of high concentration. Figure 4.10 shows relative instantaneous concentration time histories at four heights above the centre of the large left source for ACR = $0.5\,\mathrm{h}^{-1}$. This shows that low frequency events are present in the room but they are slow, with a period of approximately 0.4τ (2800 s) or greater. This corresponds with the integral time scales for concentration for the $0.5\,\mathrm{h}^{-1}$ case (Table 4.2).

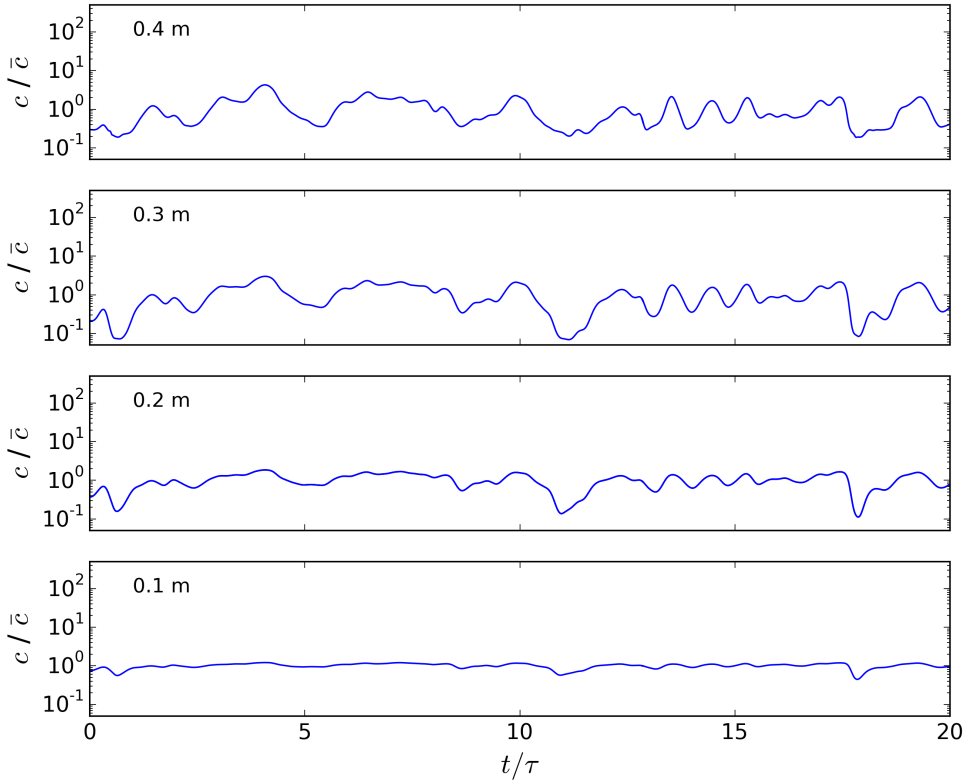

Figure 4.10: Time histories of relative instantaneous concentrations ($c\,/\,\bar{c}$) for an air change rate of $0.5\,\mathrm{h}^{-1}$, at four heights (0.1 m, 0.2 m, 0.3 m and 0.4 m) above the centre of the large left source. t is normalised by τ.

As the time averaged concentration across the room generally increased as the ACR decreased, a dog is more likely to be able to detect the vapour in large parts of the room

for lower ACRs, assuming that detectability is a function of concentration only and not other parameters, e.g. concentration gradient. However, this increase in time averaged concentration was not as large as the short duration peaks in concentration close to the source for the turbulent cases.

For the laminar case, the high concentration region around the source is much larger with a strong gradient leading towards the source.

4.4 Conclusions and recommendations on the effect of the air change rate

Vapour transport in the Nielsen test room (Nielsen, 1990) has been studied at a number of different air change rates, from $0.5\,\mathrm{h}^{-1}$ to $10.2\,\mathrm{h}^{-1}$. The following conclusions have been made:

- In agreement with previously published work, the air flow in the room was turbulent for Reynolds number ≥ 1230, based on the height of the inlet. At an inlet height Reynolds number of 1230, Re based on the inlet area was 5180 and the room ACR was $2.5\,\mathrm{h}^{-1}$. The air flow was laminar when the inlet height $Re = 245$. Without further work it is difficult to conclude which of these three parameters (Re based on inlet height, Re based on inlet area or air change rate) is the best indicator of turbulent flow in a room in general.
- Apart from a few minor variations, the air flow in the room appeared to be Reynolds number independent for Re ≥ 1230.
- For the first time, it was shown that two simple models, one based on a diffusion limit and the other on the friction velocity, can be used to predict the vapour flux from a constant concentration vapour source. The transition point between the models was shown to occur when $u_\tau = \frac{4.77\sqrt{D_m}\,\nu}{L_{source}}$, for the room and range of flow conditions studied here.
- The LES data showed that concentration fluctuations in the $10.2\,\mathrm{h}^{-1}$ ACR model were similar to those in the ACR $= 2.5\,\mathrm{h}^{-1}$ model. When the flow became laminar at $0.5\,\mathrm{h}^{-1}$, these fluctuations were no longer present.
  - For the turbulent flows (ACRs $\geq 2.5\,\mathrm{h}^{-1}$) it was shown that instantaneous concentrations of greater than 20 times the mean were predicted 0.1 m away from the large left source, and greater than 8 times the mean more than 1 m away.
  - It was also shown that fluctuations in the concentration did occur in the laminar model but were very slow, with a period of 0.4τ (2800 s) or greater.

- Despite the reduction in the vapour flux, the time averaged concentrations in the room increased as the ACR decreased.
  - The highest time averaged room concentrations were present when the air flow was laminar.
  - For the turbulent cases, the increase in time averaged concentration with the reduction in ACR was not as large as the short duration peaks in concentration close to the source. Therefore, this increase may not be significant if dogs are able to exploit the fluctuating concentrations.
- For the simple room modelled (and assuming that detectability is a function of concentration only) a dog is perhaps more likely to be able to detect the vapour when the air flow is laminar as higher concentrations build up near the source. However, if a dog was searching in a room with turbulent air flow for long enough they may chance upon one of the fluctuating high concentration peaks which could be a factor of 20 higher than the local time averaged concentration.
- Dog handlers should be advised to spend more time searching a room if the air flow is turbulent, whereas a single pass around the room may suffice if the air flow is laminar. Without information indicating otherwise, they could assume that air flow in the room is laminar if the air change rate is below $0.5\,\mathrm{h}^{-1}$.
- A large proportion of residential buildings have low air change rates. Therefore, based on a simple assumption that ACR provides an indication of whether room air flow is turbulent (accepting that other factors could have an effect), it is possible that a large proportion of residential buildings primarily have laminar air flow.
  - This implies that the findings for the ACR $= 0.5\,\mathrm{h}^{-1}$ room may apply in these rooms as well.

It is recommended that:

- Given the uncertainty over whether the air flow in a room is laminar or not it is recommended that LES with a dynamic Smagorinsky subgrid scale model is used for this type of problem, if time and computer resources allow.
- The methods developed in this chapter should be applied to a range of room types, including various mechanical ventilation configurations, naturally ventilated room and various room shapes. This should be done to see whether the findings can be applied more generally.
- Further modelling or experimental work should be carried out to find the optimum indicator for turbulent air flow in the Nielsen test room. This could be extended to include a broad variety of rooms (shape/size), with isothermal and non-isothermal conditions, with and without furniture etc. and with different air supply devices.

- The room and turbulence time scales are explored further to see whether a more general relationship between them can be found.

In the following chapter the effect of vapour sorption on concentrations in the Nielsen test room (Nielsen, 1990) is considered.

Chapter 5

CFD modelling of vapour sorption

5.1 Introduction

Most of the materials of interest to explosive detection have low to very low vapour pressures indicating that they will have large partition coefficients. Therefore, the effect of vapour sorption onto or into surfaces could be significant. In Section 2.3 it was discussed that many analytical models which include vapour sorption have been developed, and that they assume the zone/room is well-mixed. For explosive detection applications, spatial resolution is critical as vapour concentrations may reduce by orders of magnitude within very short distances from the source, as shown in Chapter 3. Among the available spatially resolved models all have a simplistic representation of how the vapour permeates into the surface and only the Nally et al. (2009) model included sorption into a multilayer material and a turbulent wall function.

To improve on this situation, a new spatially resolved sorption and permeation model has been validated using a set of increasingly complex bespoke experiments. The model is based on partitioning followed by diffusion and is more physically representative than the sink-diffusion model of Jørgensen et al. (2000) or the three-layer models of Singer et al. (2005) and Nally et al. (2009). Zhang et al. (2016) commented that it might not be possible to measure the input parameters for the Jørgensen et al. model directly. The input parameters for the new model, solid phase diffusion coefficient, D_{solid} [$m^2 \cdot s^{-1}$], and the dimensionless partition coefficient, K_{ab}, can be measured easily using a standard permeation experiment, such as that described in Section 5.3.2.1. The Singer et al. (2005), Nally et al. (2009) and Jørgensen et al. (2000) models do not require the depth of the permeable solid to be specified, which could be an advantage in some situations.

The model was written as a set of user defined functions (UDFs) for ANSYS Fluent by a third party[1], based on the framework of Nally et al. (2009).

The validation experiments used the SVOC explosive (pure) EGDN for the vapour sources. This was chosen as its relatively high vapour pressure (see Figure 2.2) makes detection easier. Also, as it is a pure substance it can be assumed that only processes external to the material need to be taken into account when considering vapour production. See Section 2.1 for more details on vapour emission.

The new model includes: a linear isotherm to represent absorption, diffusion through internal layers and desorption on the other side of the solid if required. It uses either a standard or a blended wall function to account for the effects of near-wall turbulence so can be applied whether the near-wall cell is in the viscous region or the log-law region. The model also includes a simple linear mass transfer model.

Following validation, the model was used to assess the effect of sorption on vapour concentrations in the Nielsen test room (Nielsen, 1990).

A paper which describes the model validation work and its application to some simple scenarios is in press (Foat et al., 2021).

5.2 Sorption/permeation model theory

The sorption/permeation model was implemented as illustrated in Figures 5.1 and 5.2, based on the framework originally developed by Nally et al. (2009). The vapour is transported from the near-wall cell, where the concentration is C_p, to a point close to the wall where the concentration, C^*, is in equilibrium with the surface concentration, C_{surf}, or solid phase concentration, C_{solid}. The flux between C_p and C^* is governed by the mass transfer coefficient, a, and the difference in concentration. C^* is related to C_{surf} or C_{solid} by a partition coefficient, K_{ad} or K_{ab}.

For the absorption or permeation model, there is a flux between layers in the solid which is governed by the solid phase diffusion coefficient, D_{solid}, and the concentration gradient. For permeation through a material, the vapour can return to the gas phase from the outer side of the permeable material using the same processes as applied when it entered the solid phase, but in reverse.

[1] Graham Macpherson, Dougal Ranford and Samuel Tabor of Frazer-Nash Consultancy Ltd. through a contract with Riskaware Ltd.

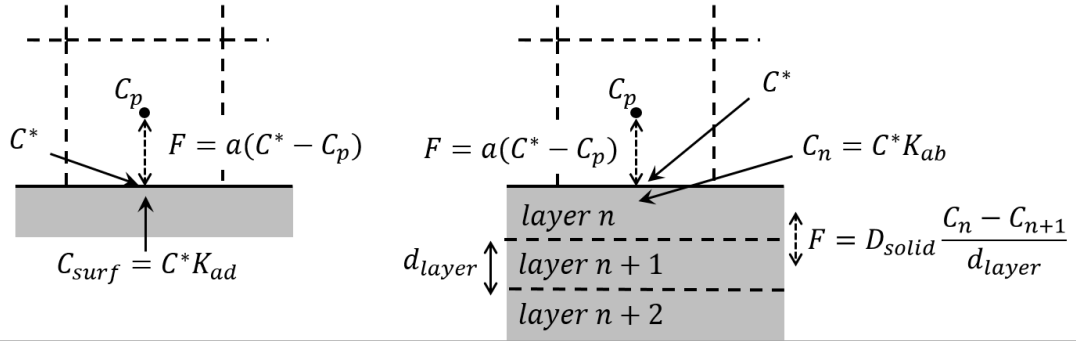

Figure 5.1: Diagram showing the implementation of the adsorption (left) and absorption/permeation model (right).

The basis of the sorption/permeation UDFs is a wall function to model transfer of vapour between the near-wall cell and the surface or solid. The model has three wall treatment options which can be specified depending on the near-wall mesh and the local physics. These are used to calculate the mass transfer coefficient and subsequently the vapour flux.

The three models are: the standard wall function, blended wall function and a simple linear model (referred to as Fick's law in the model). Both the standard wall function and the blended wall function apply a linear model when the non-dimensional near-wall cell height, y^* (see Equation 5.1), is within the species sub-layer and a logarithmic model when it is outside the sub-layer. Moving away from the wall, the location at which the species sub-layer ends is referred to as y_c^*. This location marks the transition from laminar region of the species boundary layer to the turbulent region. The difference in the standard and blended wall functions is that the blended model applies a smooth transition between the two regions, whereas the standard wall function applies an abrupt change. The simple linear model is applied when the flow in the whole of the domain is laminar, or there is no air movement (i.e. molecular diffusion only).

Only the blended wall function and the linear model were used in this work.

The non-dimensional near-wall cell height, y^*, is given by the following.

$$y^* \equiv \frac{\rho C_\mu^{1/4} k_p^{1/2} y_1}{\mu}, \tag{5.1}$$

where C_μ is a constant (0.09), k_p [$\mathrm{m^2 \cdot s^{-2}}$] is the turbulent kinetic energy in the near-wall cell and y_1 is the distance from the wall to the centroid of the near-wall cell and μ is the dynamic viscosity.

The normalised species mass fraction, Y^+ [dimensionless], is defined as

$$Y^+ \equiv \frac{(Y_w - Y_p)\rho C_\mu^{1/4} k_p^{1/2}}{F}, \tag{5.2}$$

where Y_w [kg·kg^{-1}] is the species mass fraction at the wall, Y_p [kg·kg^{-1}] is the mass fraction at the centroid of the first cell and F is the flux [kg·m^{-2}·s^{-1}] between these two locations. The law-of-the-wall for the normalised species mass fraction is given by the following for the standard wall function.

$$Y^+ = \begin{cases} Sc\, y^* & (y^* < y_c^*) \\ Sc_t \left[\frac{1}{c_v} \ln(Ec\, y^*) + P_c\right] & (y^* \geq y_c^*), \end{cases} \tag{5.3}$$

where c_v is the von Karman constant, Ec is an empirical constant (9.793) and P_c is another empirical constant which is given by the following (Jayatilleke, 1966).

$$P_c = 9.24 \left[\left(\frac{Sc}{Sc_t}\right)^{3/4} - 1\right] \left[1 + 0.28 \exp(-0.007 Sc/Sc_t)\right]. \tag{5.4}$$

Moving from the wall, the end of the species sub-layer can be found by solving for y_c^* in the following equation,

$$Sc_t \left[\frac{1}{c_v} \ln(Ec\, y_c^*) + P_c\right] = Sc\, y_c^*. \tag{5.5}$$

For vapours with Sc close to one, y_c^* will occur at a similar location to the end of the viscous sub-layer. For Sc >1, y_c^* will occur before the viscous sub-layer ends.

The species mass transfer coefficient between the near-wall cell and the wall, a, is given by the following,

$$a = \frac{F}{C^* - C_p} = \frac{F}{(Y_w - Y_p)\rho}. \tag{5.6}$$

Equations 5.2, 5.3 and 5.6 can be rearranged to give equations for the species mass transfer coefficient depending on y^* for the standard wall function.

$$a = \begin{cases} \frac{C_\mu^{1/4} k_p^{1/2}}{Sc\, y^*} & (y^* < y_c^*) \\ \frac{C_\mu^{1/4} k_p^{1/2}}{Sc_t \left[\frac{1}{c_v} \ln(E\, y^*) + P_c\right]} & (y^* \geq y_c^*). \end{cases} \tag{5.7}$$

The species flux between the near-wall cell and the wall can then be calculated by

$$F = a(C^* - C_p). \tag{5.8}$$

The blended wall function of Kader (1981) is used. The blending function, Γ [dimensionless] is given by the following,

$$\Gamma = -\frac{0.01(Sc\, y^*)^4}{1 + 5Sc^3 y^*}. \tag{5.9}$$

The normalised species mass fraction for the blended wall function, Y^+_{BWF} [dimensionless], is given by the following,

$$Y^+_{BWF} = \exp(\Gamma)Y^+_{lam} + \exp(1/\Gamma)Y^+_{turb}, \tag{5.10}$$

where the equation for Y^+_{lam} [dimensionless] and Y^+_{turb} [dimensionless] are taken from the $(y^* < y^*_c)$ and $(y^* > y^*_c)$ parts of Equation 5.3 respectively. The mass transfer coefficient between the near-wall cell and the wall is then given by

$$a = \frac{C_\mu^{1/4} k_p^{1/2}}{Y^+_{BWF}}. \tag{5.11}$$

For the simple linear model the mass transfer coefficient between the near-wall cell and the wall is given by,

$$a = \frac{D_m}{y_1}. \tag{5.12}$$

After the mass transfer coefficient, a, is estimated, C^* is calculated from the concentration on the surface or in the solid using an isotherm model. The UDF allows a number of different isotherms to be specified but only a linear isotherm was used in this PhD (see Equations 2.38 and 2.39) as this has been shown to be broadly applicable for low vapour concentrations.

If required, the concentrations in the permeation layers of the solid are calculated using an implicit second-order finite difference method to solve Fick's second law of diffusion in one-dimension, Equation 6.1. C^* is then re-calculated from the new surface or solid concentration.

This whole process (adsorption or absorption) is iterated until a converged solution is reached as shown in Figure 5.2 and it is repeated each time step. Vapour concentration on the surface or concentration in each permeation layer in the solid (at the current and previous time step) are then stored in user defined memory (UDM) relating to each near-wall cell.

The model can become unstable when iterating over C^* and C_{surf} or C_{solid} when K_{ad} or K_{ab} are very large (i.e. for low volatility explosives such as TNT) because the model uses an explicit method. Stability can be improved by adjusting an under-relaxation factor and increasing the number of UDF iterations. Even with a small under-relaxation factor, it is often necessary to use small time steps. This problem can be particularly apparent when the simulation is being started, i.e. when there is zero concentration on the surface. In the future, adaptive time-stepping could be used to automatically increase Δt as the simulation progresses. Alternatively, it may be possible to use an implicit scheme rather than the current explicit scheme.

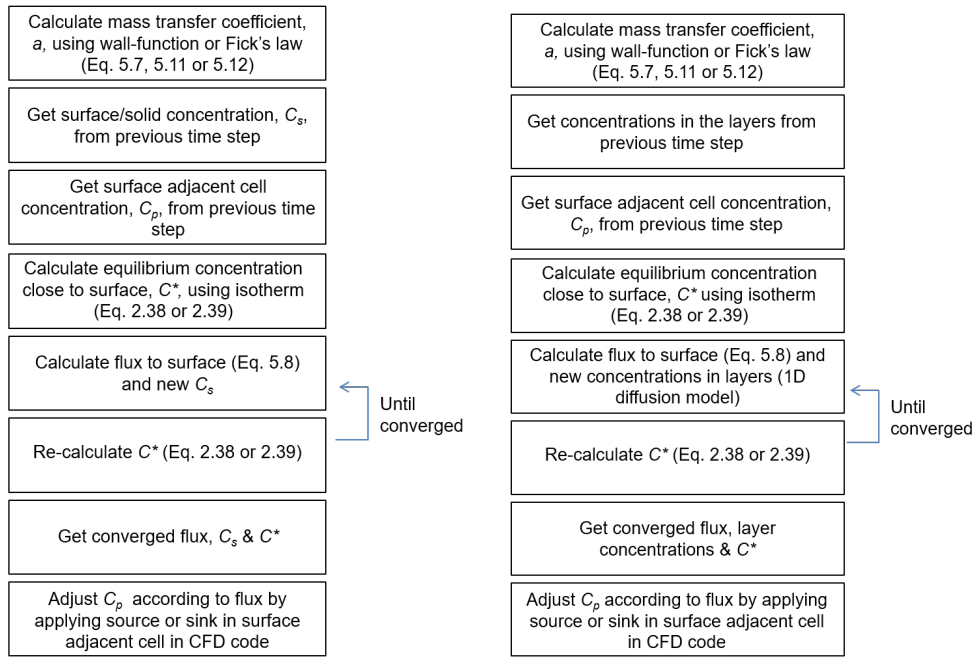

Figure 5.2: Flow charts for the adsorption model (a) and absorption and permeation model (b).

This new model uses an equilibrium isotherm, as do all the models discussed in Section 2.3. This means it is assumed that equilibrium between C^* and C_{surf} or C_{solid} occurs instantaneously. This is a suitable assumption when model time steps are large, but may not be applicable for very small time steps. The model also only allows for 1-dimensional diffusion in the solid so will not be applicable when lateral diffusion is important.

5.3 Model validation

The vapour sorption/desorption and permeation model was validated using three test cases of increasing complexity, these were:

- Flow of vapour through a chamber with permeable walls.
- Permeation of a vapour into, followed by flow through, a chamber with permeable walls.
- Permeation of vapour through a cardboard box into a room.

These experiments were planned by the author in conjunction with a team of Dstl chemists. The experiments were conducted by the chemists. A list of the people involved in the experiments (and modelling) is given in Foat et al. (2021).

The methods used and the comparison between the model predictions and the experimental data are given in the following sections.

5.3.1 Air flow and vapour transport

The air flow and vapour transport was modelled using Fluent V15.0. A single model was also run in Fluent V18.0 and there was negligible difference between the results. Both laminar and turbulent flow models were run. For the turbulent flow model the k-ω shear-stress transport (SST) turbulence model (see Mentor (1994) and Section 2.2.2.2) was used.

For all models, the flow was solved first as steady-state, was then held in steady-state while the vapour transport was solved transiently. The vapour was modelled as a passive scalar with $Sc_t = 0.7$ (the molecular Schmidt number, Sc for EGDN is 1.8 at 20 °C and 1.7 35 °C).

A coupled solver was used for the pressure-velocity coupling. A second-order scheme was used for the pressure terms and a second-order upwind scheme for the convection terms in the momentum equation. The species, k and ω convection terms were solved using a first-order upwind scheme and a first-order implicit scheme was used for the transient species transport[2].

Test models were re-run using second-order discretisation for the species convection terms and a second-order implicit scheme for the temporal discretisation. This had little effect on the concentration predictions, which was due to the high resolution in space and time applied in the model.

5.3.2 Validation set-up

5.3.2.1 Flow of vapour through a chamber with permeable walls

The first experiment consisted of a cylindrical polytetrafluoroethylene (PTFE) chamber (0.2 m long, 0.08 m inner diameter, 0.01 m wall thickness) into which EGDN vapour, at a concentration, $C_{in} = 8.8 \times 10^{-7}\,\mathrm{kg{\cdot}m^{-3}}$, was supplied (see Figure 5.4 (a)). The EGDN vapour was generated using a temperature controlled KIN-TEK, C0395 vapour generator (KIN-TEK Analytical, Inc., Texas, USA) and mixed with dry nitrogen. The flow rate through the PTFE chamber was $1.7 \times 10^{-6}\,\mathrm{m^3{\cdot}s^{-1}}$ at a temperature of 35 °C. The velocity through the narrow inlet tube was $0.1\,\mathrm{m{\cdot}s^{-1}}$ and the average velocity across the full diameter of the chamber was $3.5 \times 10^{-4}\,\mathrm{m{\cdot}s^{-1}}$. This gave a Reynolds number of

[2]Previous work has shown that first-order schemes can give reasonable results for indoor air flows, therefore, this was used as a starting condition for the validation modelling.

less than 2. The PTFE chamber was held in a temperature-controlled box (LABCOLD™ RPDF0012D, Labcold, Hampshire, UK).

The vapour concentration at the outlet of the chamber was monitored over 5 h by periodically taking 1 min gas samples, of approximately 0.1 L, using Tenax™ air sampling tubes. The sample tubes were analysed by thermal desorption gas chromatography mass spectrometry (Agilent 7890A GC, 5975C MSD, Agilent, California, USA). The experiment was repeated twice with triplicate measurements taken at each sample time.

In between experimental replicates, the surfaces of the chamber were cleaned with a combination of propan-2-ol (IPA) and acetone to remove EGDN residues. The chamber was then dried at a temperature of 50 °C for at least two hours before being cooled, reassembled and stabilised at experimental temperatures. During temperature stabilisation the chamber was flushed with dry nitrogen gas. Chamber outputs were measured prior to recommencing experimentation to ensure that there was no residual EGDN remaining within the chamber.

The permeation properties for EGDN through PTFE at 35 °C were measured using a Micro-Chamber/Thermal Extractor™ (μ-CTE™) system with a permeation accessory (Markes International, Llantrisant, UK). The permeation accessory holds a thin layer of the material under investigation with the vapour source placed in a well below. The air flow over the top of the accessory is controlled by the Micro-Chamber and vapour samples are collected onto Tenax™ air sampling tubes. The solid phase diffusion coefficient D_{solid} can then be calculated from the lag time, t_{lag}, a time constant relating to the point at which a constant permeation rate is achieved, given by the following (Crank, 1979).

$$t_{lag} = d_{total}^2 / 6 D_{solid}, \tag{5.13}$$

where d_{total} is the total thickness of the permeable solid.

The partition coefficient (or solubility), K_{ab}, can then be calculated from the equilibrium permeation rate using Fick's first law (Equation 2.37) and 2.38. The permeation data produced is shown in Table 5.1.

The molecular diffusion coefficient for EGDN was calculated using a method based on atomic diffusion volumes (see Poling et al. (2007) and Section A.3) and this data is shown in Table 5.1.

	D_m /m^2·s^{-1}	D_{solid} /m^2·s^{-1}	K_{ab}
EGDN	9.3×10^{-6}		
PTFE		7.5×10^{-14}	1.2×10^3

Table 5.1: Vapour parameters for EGDN permeation used in the first validation experiment at 35 °C.

It should be noted that there is some uncertainty or variability in the measured permeation rates through polymers. For example, permeation rates were calculated from two sets of experiment and differed by a factor of 1.7.

A 2-dimensional axi-symmetric, laminar CFD model of the PTFE chamber was produced. The laminar wall function option, Equation 5.12, was specified in the UDF. The mesh (shown in Figure 5.3) consisted of unstructured triangles, with a maximum cell edge length of 5 mm. The time step, Δt, for the vapour transport was set to 0.05 s for the first 2 s and was then increased to 0.1 s. With these settings it had been shown in a similar model that the concentration prediction changed negligibly following a reduction in the cell size or Δt. The inlet had a constant concentration boundary condition. The PTFE walls of the chamber were defined as permeable boundaries, with values of D_{solid} and K_{ab} specified. The concentration on the outer wall was fixed at zero.

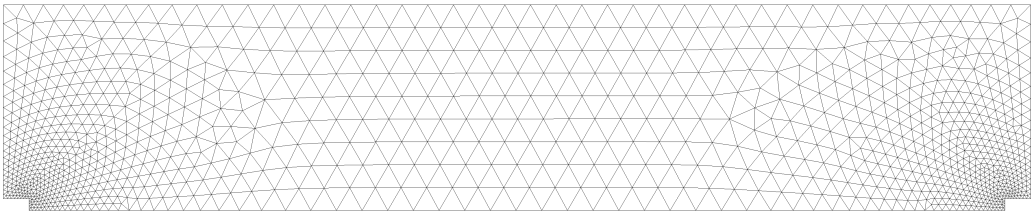

Figure 5.3: The 2D axi-symmetric mesh in the PTFE chamber for the 1st validation experiment. The indentations on the lower left and lower right are where the air supply and extract tubes, as seen in Figure 5.4, extend into the chamber.

The vapour permeation is sensitive to the thickness of the individual permeation layers, d_{layer}. d_{layer} was defined by specifying the total thickness of the solid, d_{total}, and the number of layers, n_{layer} ($d_{layer} = d_{total}$ / n_{layer}). The models were run with different values for n_{layer} to find the point at which the models were no longer sensitive to d_{layer}. The results are most sensitive to d_{layer} at the very early stage of the simulation. As the equilibrium flux is approached, the sensitivity decreases.

The results of this model converged once d_{layer} for the walls of the PTFE chamber reached 1×10^{-5} m. As Fluent limits the number of UDMs to 500, there is a limit to the number of permeation layers which can be defined. In this case n_{layer} was set to 100 and therefore the total thickness, d_{total}, was 1 mm. The d_{total} specified was much smaller than the actual wall thickness of the PTFE chamber walls (10 mm). However, t_{lag} for even a 1 mm thick sheet of PTFE at 35 °C is 620 h, i.e. significantly longer than the duration of the experiment (5 h). In other words, during the experiment, the vapour will have been able to permeate only a small distance into the PTFE. Therefore, the outer region of the PTFE walls played little part in the permeation process. The results here were shown to be insensitive to an increase in n_{layer} (for a fixed d_{total}). Therefore,

a thick permeable material can be represented in the model by a thinner material if the duration of the simulation is short compared to the lag time.

5.3.2.2 Permeation of a vapour into and through a chamber with permeable walls

The second experiment consisted of the same PTFE tube as used in the previous experiment, through which dry nitrogen at 30 °C was pumped at a nominal flow rate of 0.1 L·min^{-1}. The tube was either lined with corrugated cardboard (see Figure 5.4 (b)) or was left unlined i.e. the PTFE surface of the tube was exposed. The corrugated cardboard (single-wall corrugated cardboard, Postpack Ltd., Lincolnshire, UK) was 2.9×10^{-3} m thick or 0.5×10^{-3} m thick when the three layers, of which it consisted, were compressed together.

A source of EGDN vapour (10 % w/w (weight per weight) of EGDN on an inert material, Kieselguhr) was placed in a Markes permeation accessory which was sealed with a 130 µm thick film of polyethylene (PE). The permeation accessory was made of Silcosteel®, an amorphous silicon coated steel, which was shown (data is not reported here) to adsorb a negligible amount of the vapour at 30 °C.

The EGDN was placed within the permeation accessory and was held at 30 °C for 1 h to allow the flux out of the permeation accessory to equilibrate before being placed in the PFTE chamber.

The EGDN vapour concentration was measured at the outlet of the chamber (using the same method as for the previous experiment) periodically over a period of 4 h for the unlined chamber and for 24 h for the cardboard lined chamber. Three repeat experiments were conducted with triplicate measurements taken at each sample time. Each sample was collected for 1 min.

The permeation properties for EGDN through PTFE, PE and cardboard were measured using the same method as described previously. The volatility and molecular diffusion coefficient were calculated using data from the review paper of Ewing et al. (2013) and the atomic diffusion volume method Poling et al. (2007). All these parameters are given in Table 5.2.

	C_0 /kg·m^{-3}	D_m /m^2·s^{-1}	D_{solid} /m^2·s^{-1}	K_{ab}
EGDN	9.7×10^{-4}	9.0×10^{-6}		
PTFE			5.0×10^{-14}	1.4×10^3
PE			2.5×10^{-12}	1.9×10^3
Card			2.0×10^{-11}	1.7×10^3

Table 5.2: Vapour parameters for EGDN permeation used in the second validation experiment at 30 °C.

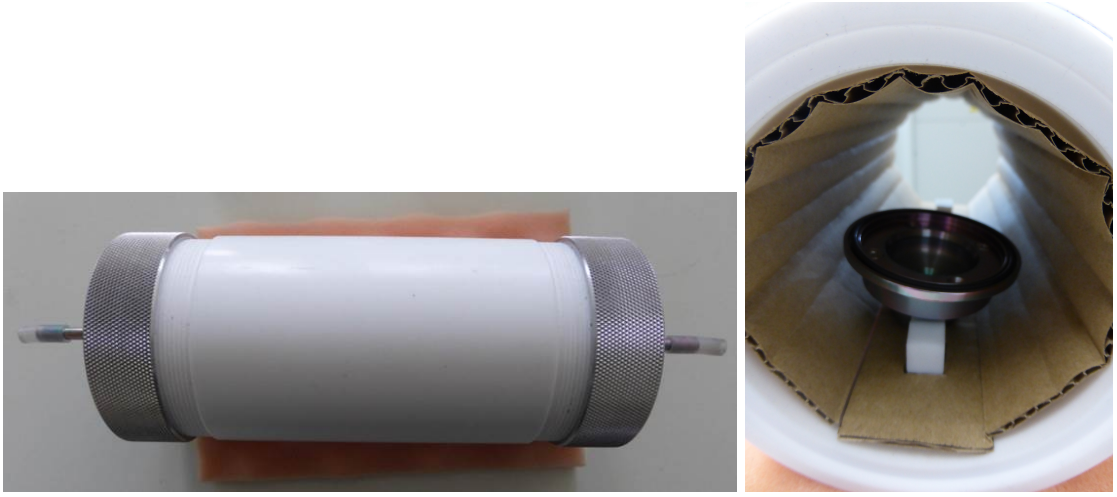

(a) (b)

Figure 5.4: The PTFE chamber. (a) the outside of the PTFE chamber as used in the first and second validation experiments. (b) the inside of the chamber with the cardboard lining and the PE sealed permeation accessory as used in the second validation experiments.

The average flow rate for the unlined experiments was 1.6×10^{-6} m^3·s^{-1} (0.094 L·min^{-1}) and for the cardboard lined experiments it was (1.3×10^{-6} m^3·s^{-1} (0.079 L·min^{-1}).

The chamber was represented using a laminar model. The laminar wall function option (Equation 5.12) was selected in the UDF along with the permeation model for PE, PTFE and cardboard.

The mesh (show in Figure 5.5) used mainly unstructured tetrahedrons and only a symmetric half of the geometry was modelled. 1 mm hexahedral cells were applied to the inside of the permeation accessory. The maximum cell edge length in the chamber was 5 mm (as specified in the first validation experiment model). The time step size was kept at a constant 0.05 s for the unlined chamber and 0.03 s for the cardboard lined chamber. The slight reduction in Δt for the cardboard lined chamber model compared to the unlined chamber model was due to an instability in the UDF when a larger Δt

was used. This was likely caused by the larger partition coefficient for cardboard compared to PTFE (see Table 5.2), as discussed in Section 5.2. It should be noted that all models were shown to be insensitive to a further reduction in Δt. The mesh around the permeation accessory was shown to be sufficiently well resolved to correctly predict the vapour flux through the PE film, i.e. a reduction in the size of the cells around the accessory did not affect the flux.

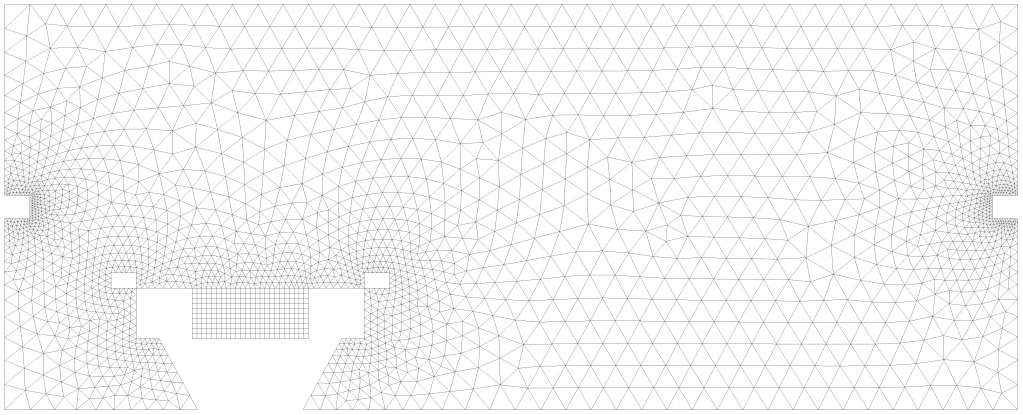

Figure 5.5: The mesh on the symmetry plane in the PTFE chamber for the 2nd validation experiment. Air enters on the left and leaves on the right. The inside of the permeation accessory in meshed with hexahedral cells. To better see the detail in the image, please view the electronic version of the thesis.

As with the model for the 1st validation experiment, the PTFE walls of the chamber were defined as permeable boundaries, with values of D_{solid} and K_{ab} specified. The concentration on the outer wall was fixed at zero. The cardboard was included in the model by simply applying the cardboard permeation parameters to the walls of the chamber in place of the PTFE parameters. The thickness of the cardboard in the UDF was set to represent the three layer of the corrugated cardboard compressed together (0.5×10^{-3} m). This means that the air voids within the cardboard were ignored as diffusion through these spaces should be much faster than it would be through the cardboard.

The model was initialised to represent the set-up process used in the experiment, i.e. the flux out of the permeation accessory was allowed to equilibrate before it was placed in the chamber. The model was run for 30 min for the flux to equilibrate, then the vapour concentration within the chamber, but not within the permeation accessory, was set to zero.

The number of permeation layers, n_{layer}, for the PE film on the permeation accessory ($d_{total} = 130 \times 10^{-6}$ m) was set to 20, therefore $d_{layer} = 6.5 \times 10^{-6}$ m. The results converged with d_{layer} for the cardboard and PTFE set to 2.5×10^{-6} m and 5×10^{-6} m respectively, (n_{layer} was equal to 200 for both materials). This was because the material

with the higher solid phase diffusion coefficient required a thinner d_{layer}. For the cardboard $d_{total} = 0.5 \times 10^{-3}$ m. For the PTFE, the actual wall thickness was 10×10^{-3} m but d_{total} was set to 1×10^{-3} m, as in the model for the first validation experiment (see Section 5.3.2.1).

5.3.2.3 Permeation of vapour through a cardboard box into a room

For the third set of experiments EGDN was held within the same Silcosteel® permeation accessory as used in the second experiment. The container was sealed with a 130 µm thick PE film and the container was placed in a cardboard box (0.2 m x 0.2 m x 0.2 m = 8 L), see Figure 5.6. The cardboard box was made of single-wall corrugated cardboard (Pressel brand from Staples, Birmingham, UK). The box was closed and the joints were sealed using impermeable metal tape. The box was positioned at the end of a laboratory bench and an AM08 Dyson Cool Pedestal Fan (Dyson, Wiltshire, UK) was located at the other end of the bench. The purpose of the fan was to blow a controlled and predictable air flow over the box and to reduce the effect of people moving around the laboratory and disturbing the air. Vapour concentration measurements were taken at locations around the outside of the box at 1 h, 3 h and 5 h after the experiment started by sampling onto Tenax™ tubes. Background measurements were also taken both near the fan and downwind from the box. The locations of the concentration monitors are shown in Figure 5.7. At the end of the experiment (5 h), the vapour from within the box was measured by extracting $1\,\mathrm{L{\cdot}min^{-1}}$ for 10 min onto a Tenax™ tube.

Two repeats experiments were conducted and the average temperature in the laboratory during the experiments was 20 °C.

The permeation properties for EGDN through PE and cardboard were measured using the same method as described previously. It was assumed that permeation through cardboard was a linear function of the thickness (i.e. the solubility and diffusion coefficient were independent of the thickness). The volatility and molecular diffusion coefficient were calculated using data from from the review paper of Ewing et al. (2013) and the atomic diffusion volumes method (Poling et al., 2007). The partition coefficient for adsorption of EGDN vapour onto the tin-foil table covering, K_{ad}, was approximated using a model for SVOCs adsorption onto stainless steel (Liang and Xu, 2014). Adsorption onto the Silcosteel® permeation accessory at 20 °C was measured using a bespoke experimental set-up (not described here as work was conducted outside of this PhD). All these parameters are given in Table 5.3.

As with the set-up of the previous model, the thickness of the cardboard in the permeation model was set to represent the three layers of the corrugated cardboard compressed together.

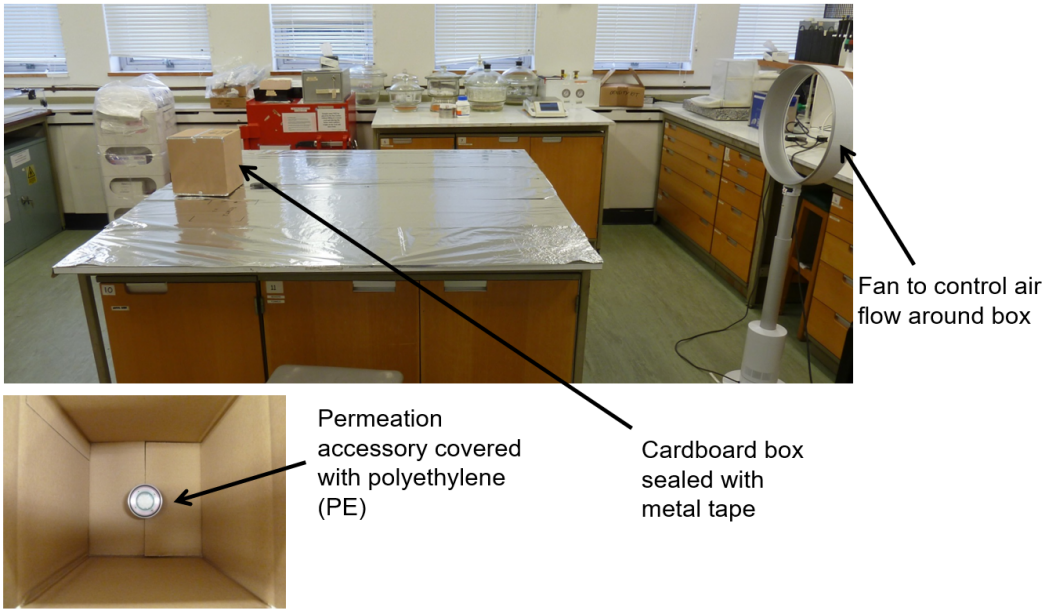

Figure 5.6: The set-up for the permeation of vapour through a cardboard box experiment.

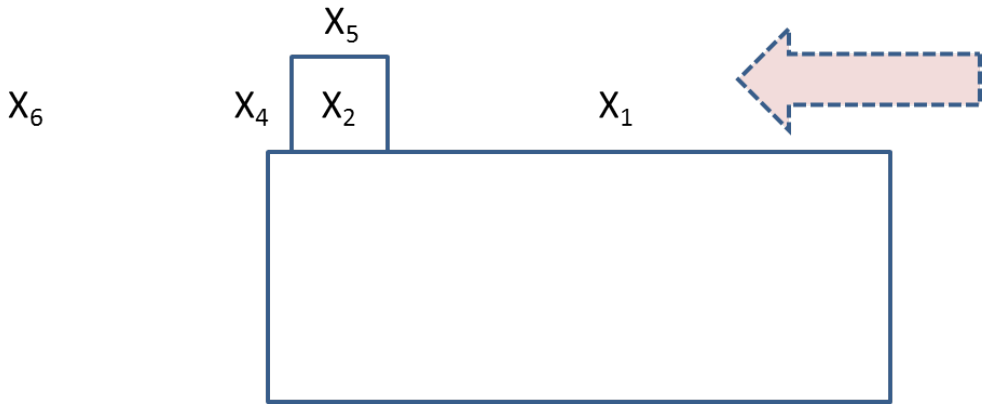

Figure 5.7: The location of the concentration monitors for the cardboard experiment, shown in elevation view. X_3 was on the opposite side of the box to X_2. X_2, X_3, X_4 and X_5 were positioned in the centre of a side, 1 cm away from the box. X_6 was 0.5 m downwind from the rear face of the box and X_1 was 0.5 m upwind from the front face.

The number of permeation layers, n_{layer}, for the PE film on the permeation accessory was 5. n_{layer} for the PE film was increased to 20 but this had very little effect on the results. For the cardboard d_{layer} was set to 5×10^{-6} m. Previous tests had shown that permeation through the cardboard became independent of d_{layer} well before it reached this thickness.

The model was run with solubilities multiplied by a factor of 1/2 and 2 to represent the

uncertainty in the input data (as described in Section 5.3.2.1). To give an upper concentration limit, the solubility in PE was doubled to double the flux from the permeation accessory. The solubility in cardboard was halved to reduce the amount of vapour which was lost in this layer. The inverse was done in both the PE and cardboard to give the lower concentration limit.

	C_0 /kg·m^{-3}	D_m /m^2·s^{-1}	D_{solid} /m^2·s^{-1}	K_{ab}	K_{ad} /m
EGDN	4.1×10^{-4}	8.5×10^{-6}			
PE			1.5×10^{-12}	2.6×10^{3}	
Card			1.8×10^{-11}	1.5×10^{3}	
Tin-foil					1.6
Permeation accessory					0.56

Table 5.3: Vapour parameters for EGDN permeation used in the cardboard box in room model at 20 °C.

A k-ω SST turbulence model and the blended wall function options in the UDF (Equation 5.11) were used in the CFD. Sorption through the PE film covering the permeation accessory and sorption onto the accessory were modelled by using the laminar wall function option (Equation 5.12). The mesh (shown in Figures 5.8 and 5.9) was a hybrid tetrahedral and hexahedral mesh, only a symmetric half of the room was modelled.

In order to simplify the modelling process, only the fan, the box containing the explosive and the bench on which the box sat were included in the model. The other furniture and equipment in the laboratory were expected to have a small effect on the air flow around the box, but might affect the vapour concentration due to sorption effects. It was not practical to characterise the sorption properties of all the furniture and equipment, so their effect was included in the model by defining a high sorption rate on the wall of the laboratory ($K_{ad} = 100$) and by setting the inlet vapour concentration (at the fan) to that measured during the experiment (at location X_1, see Figure 5.7). It is expected that sorption at the wall of the room would have a limited effect on the concentrations measured close to the box.

Air velocities were measured in the laboratory at a number of locations using a TSI VelociCalc® model 9515 (Minnesota, USA) to determine the air movement generated by the fan. A velocity profile was then specified on the fan in the model in order to approximately reproduce the measured profile. The maximum velocity 0.1 m in front of the fan was 0.9 m·s^{-1}, this decayed to 0.3 m·s^{-1} at the axis of the fan. The air velocity was also measured close to the sides and top of the box. 1 cm from the side of the box it varied from approximately 0 m·s^{-1} to 0.2 m·s^{-1} and on the top it varied from approximately 0.2 m·s^{-1} to 0.6 m·s^{-1}.

The permeation accessory was meshed using the same approach as used in the second validation experiment model. The mesh on the outside of the box was kept sufficiently fine to achieve an area-weighted average y_1^+ of 2.3. Compared to a coarser mesh the flow was only altered slightly in this model. A further mesh refinement had no significant effects on the flow. The effect of the further refinement on the EGDN concentrations was less than or equal to the difference due to the uncertainty in the sorption/permeation parameters. The time step size was 0.2 s. It was shown that there was no significant change in the concentrations recorded at the sample locations with a smaller time step size ($\Delta t = 0.1$ s).

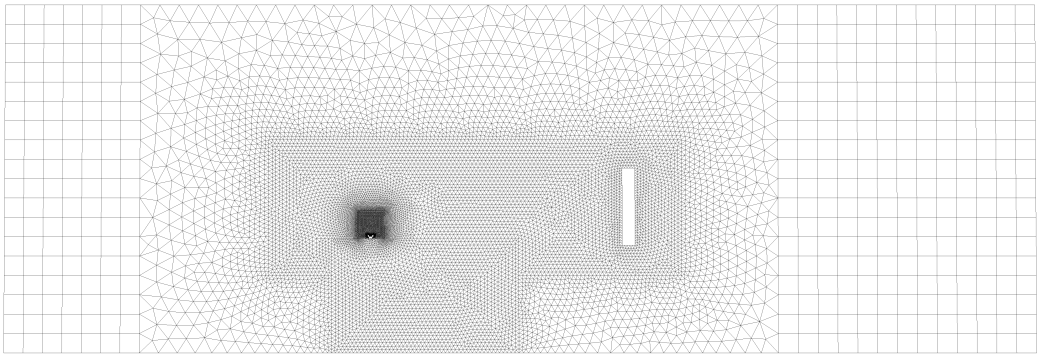

Figure 5.8: The mesh on the symmetry plane in the 3rd validation experiment. The densely meshed region is the cardboard box containing the explosive. The fan can be seen to the right of the image. To better see the detail in the image, please view the electronic version of the thesis.

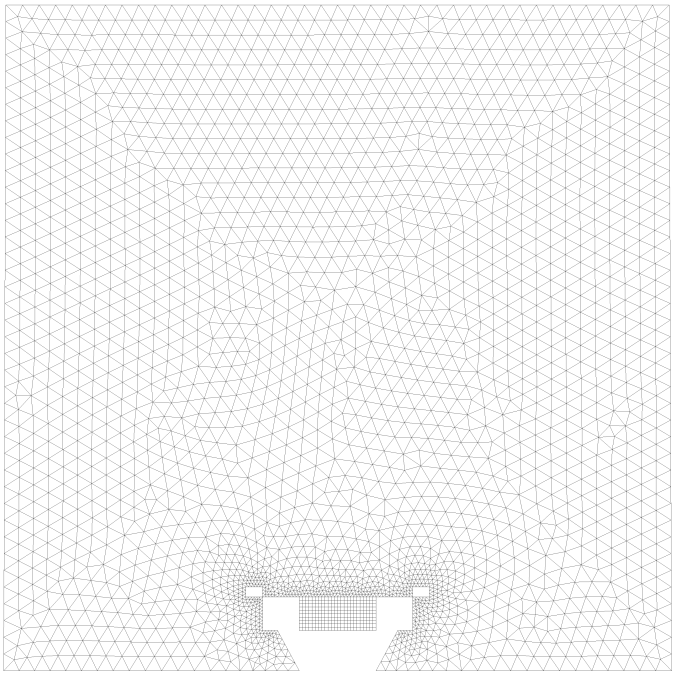

Figure 5.9: The mesh on the symmetry plane showing the permeation cell inside the box in the 3rd validation experiment. To better see the detail in the image, please view the electronic version of the thesis.

A different validation study using a cardboard box is discussed in Foat et al. (2021). This study is not reported here as the modelling was carried out by a colleague (under my supervision, using the methods developed here). The conclusions from that study were as follows.

The CFD predictions for concentrations around the boxes were within an order of magnitude of the experimental data and in most cases they were either within the experimental error bar ranges or were within a factor of two. The CFD model over-predicted the concentration of vapour present in the cardboard box at the end of the experiment. A possible explanation for the over-prediction in the box containing the vapour source was believed to be the inefficiency in the sampling method used. The models can be considered fit-for-purpose for predicting concentrations around cardboard boxes, but can be expected to over-predict concentrations within the box.

5.3.3 Validation results

5.3.3.1 Flow of vapour through a chamber with permeable walls

The outlet concentration, C_{out}, from the PTFE chamber for the first validation experiment is shown in Figure 5.10. The model performed well and numerical data is within the range of experimental data at most time points.

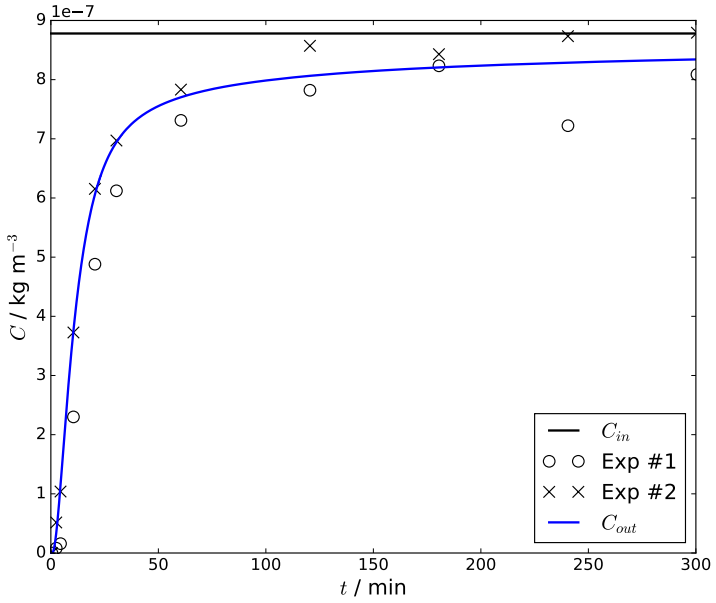

Figure 5.10: Outlet concentration, C_{out}, from the PTFE chamber for the 1st validation experiment.

For future modelling, consideration should be given to the values of d_{layer}, n_{layer} and d_{total}. Ideally d_{total} should be set to the actual thickness of the material, but where this is not possible, a smaller value can be used as long as t_{lag} remains long compared to the duration of the simulation. Model convergence was reached in this case when d_{layer} reached 1×10^{-5} m. However, this value is likely to be dependent on D_{solid}, with thinner layers required for vapours with larger solid phase diffusion coefficients.

The results above have shown that the new permeation model can give accurate results for this type of scenario (laminar flow through a chamber with permeable walls) when suitable parameters are chosen.

5.3.3.2 Permeation of a vapour into and through a chamber with permeable walls

The results from the unlined PTFE chamber are given in Figure 5.11 and the cardboard lined chamber data is in Figure 5.12. The CFD performed well in following both the trend and the magnitude of the experimental data. At 240 min for the unlined chamber and 300 min for the lined chamber, the CFD is within a factor of 1.5 and 1.7 of the maximum experimental data point respectively. It is not known what caused the drop in the measured concentrations in the cardboard lined chamber at around 50 min (see Figure 5.12) and this effect was not reproduced in the model. The model showed approximately the same relative reduction in concentration between the unlined and lined chamber experiments.

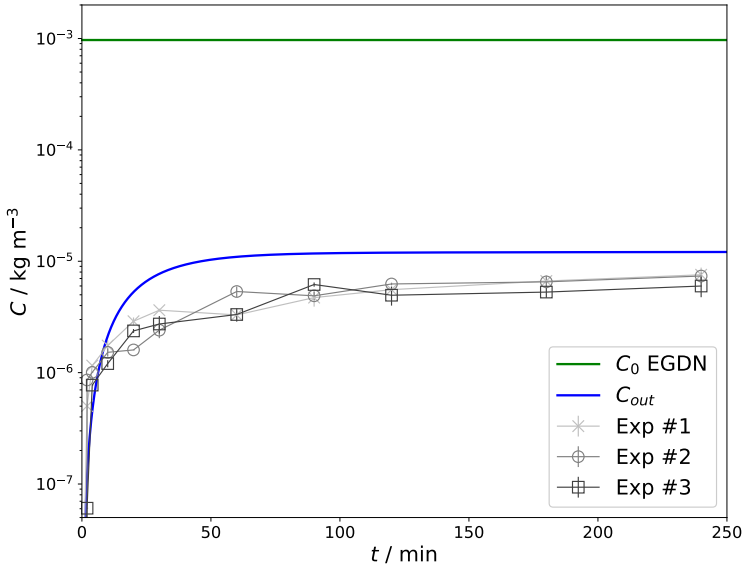

Figure 5.11: Outlet concentration, C_{out}, from the unlined chamber. The error bars on the experimental data indicate one standard deviation from three replicate measurements. The green line shows the EGDN volatility.

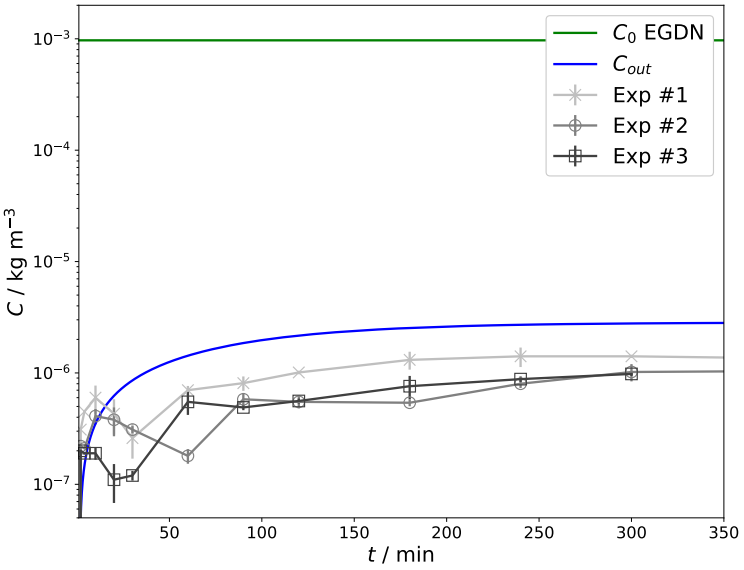

Figure 5.12: Outlet concentration, C_{out}, from the cardboard lined chamber. The error bars on the experimental data indicate one standard deviation from three replicate measurements. The green line shows the EGDN volatility. Only CFD data up to 5 h is shown.

The correlation between the model data and the experimental data is not as good as that shown in the first validation experiment. However, the set-up in this experiment was more complex, as it includes permeation of vapour into the chamber as opposed to the constant concentration in-flow in the experiment. There was also a very large range of concentrations in the domain in this experiment, from the saturation vapour pressure concentration inside the permeation cell to concentrations a couple of orders of magnitude lower than this at the outlet.

The quality of the CFD predictions support the assumption made when modelling the cardboard, i.e. that the diffusion through the air voids in the cardboard can be ignored.

It is felt that this model is fit-for-purpose based on the correlation of the CFD data with the experimental data. However, it should be recognised that, for this type of set-up at least, the CFD has consistently over-predicted the experimental data.

5.3.3.3 Permeation of vapour through a cardboard box into a room

EGDN vapour concentrations, including uncertainty ranges, at the monitor locations around the box are shown in Figure 5.13.

The predicted concentrations are within the range of measurements at a number of points but slightly over- or under-predicted in other locations. If the uncertainty curves

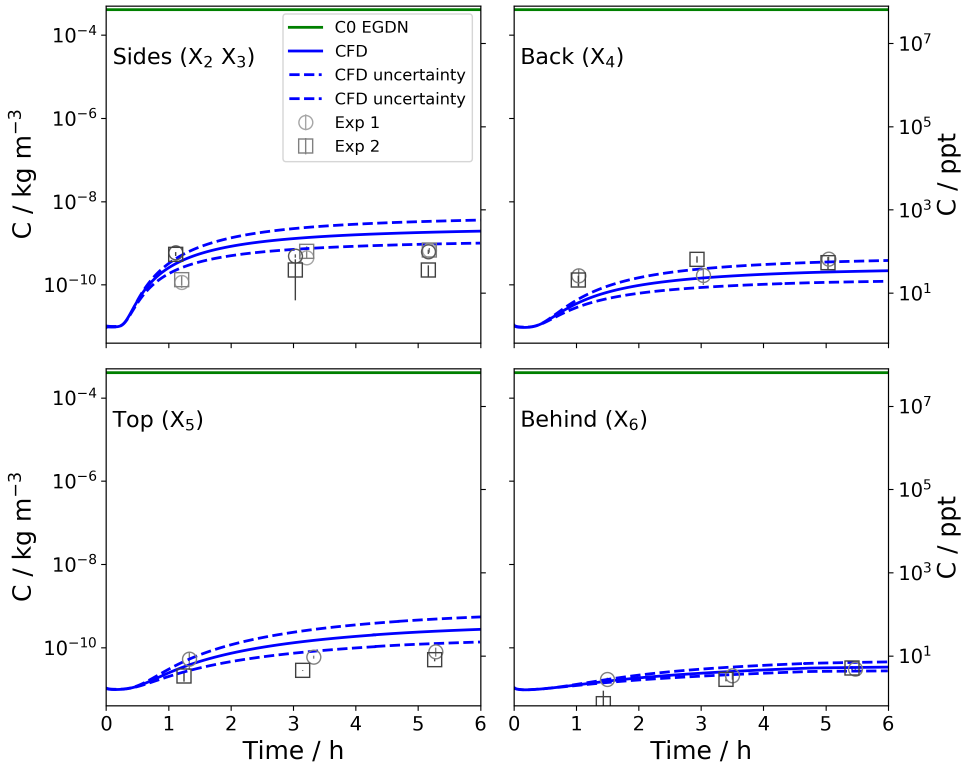

Figure 5.13: Vapour concentrations measured at different location around the cardboard box in the cardboard box in room experiment. The error bars indicate one standard deviation from two replicate measurements. The dashed blue lines show the upper and lower uncertainty ranges. The green line (at the very top of the graph) shows the EGDN volatility.

are included then the CFD predictions are within a factor of approximately 2 at all locations. It should be noted that the background vapour concentrations were specified in the model rather than simulated (as described in Section 5.3.2.3).

Both the measured and predicted concentrations are lower at the back of the box than the side. The CFD model shows that this is likely due to the slightly slower flow across the side faces compared to the back face. The flow separates at the front corners of the box and does not reattach. The increased flow at the back of the box dilutes the permeating vapour more quickly than it does on the side of the box.

The measured concentration at the top of the box was lower still, but this same effect was not shown in the model i.e. the predicted concentration at the back was similar to that on the top. The top concentration is, again, mainly influenced by the air velocity at this location; the concentrations on the inside faces of the box are similar on the side, top and back faces. Therefore, it is possible that the CFD has slightly under-predicted the air velocity close to the top face, i.e. the CFD predicts less dilution of the vapour leaving the top face.

The average vapour concentration inside the box after 5 h was calculated from the experimental data assuming the box was well-mixed, during the sampling period. In the experiment the box volume was 8 L, the sample flow rate was 1 L·min^{-1} and the sample duration was 10 min. Assuming the box is well-mixed, the concentration in the box after 10 min can be calculated using the following (Reinke and Keil, 2009).

$$C = C_0 \exp(-\lambda t) \tag{5.14}$$

This showed that only 71 % of the vapour in the box was sampled after 10 min. Therefore, the average concentration in the box was 3.1×10^{-8} kg·m^{-3}. The average concentration from the CFD was 5.0×10^{-7} kg·m^{-3}, i.e. a factor of 17 higher.

The main reason for the difference in these values is believed to be the inefficiency in the sampling method used in the experiment. A Tenax™ sample tube was inserted into the box and 10 L of gas was extracted. As the gas sample was drawn into the sample tube, fresh air would be drawn into the box and the most likely route for this air would be through the holes created for the insertion of this tube (the rest of the box was sealed using impermeable metal tape). Therefore, it is possible that there was a short circuit with fresh air being sampled in preference to the air from the bottom of the box, where the concentration was higher. The measurement could be improved by taking a larger volume gas sample to increase the likelihood of removing all the vapour within the box and by inserting the Tenax™ tube further into the box, to reduce the likelihood of a short circuit occurring.

It is recommended that either a CFD model is built to represent the vapour sampling process used to extract the vapour from the box to see whether the in-box concentration over-prediction can be fully explained or experiments are conducted using different sampling approaches.

Considering the complexity of the experimental set-up and the approximation of the flow around the box, it is felt that this model is fit-for-purpose, to predict vapour concentrations around the outside of the box. The model should be used with caution when predicting in-box concentration until the difference between the model and experimental data has been explained.

5.3.4 Validation discussion

The vapour sorption and permeation CFD modelling capability has been shown to perform well in a number of scenarios. The CFD model generally over-predicts concentration. Some of the model deficiencies could be due to limitation in the model and uncertainties in the input data, with non-linearity of the permeation through cardboard being one of the possible causes.

The CFD model significantly over-predicted the concentration of vapour present in the box at the end of the cardboard box experiment. A possible explanation for the over-prediction in the box containing the vapour source was given in Section 5.3.3.3.

The vapour permeation is sensitive to the thickness of the individual permeation layers, d_{layer}, and the sensitivity is strongest at the early stages of the simulation. It was shown that a thick permeable material can be represented in the model by a thinner material if the duration of the simulation is short compared to the lag time. This means that it is possible to specify thinner layers than would otherwise be possible (due to Fluent's limitation on the total number of UDMs).

The results for the simulations which included cardboard support the assumption that diffusion through the air voids in corrugated cardboard can be ignored. Therefore, the thickness of the cardboard in the UDF can be set to that of the three layers of the corrugated cardboard when compressed together.

Recognising the limitations described above, the vapour sorption modelling capability can now reliably be used for scenario modelling when the setting consists of cardboard boxes or simple set-ups like the PTFE chamber experiment. Therefore, it could be used for some of the simple operational or training scenarios described in Section 1.3.

All the validation work reported here is for EGDN vapour only. Confidence in the capability would be improved if the validation could be extended to include a range of SVOCs and packaging materials.

5.4 Vapour sorption in an isothermal mechanically ventilated room

The validated vapour sorption methodology was used to see how the inclusion of vapour sorption in the Nielsen test-case (Nielsen, 1990) (discussed in Chapter 3) affects the vapour concentration in the room. The model was implemented using steady RANS to permit longer time periods to be studied than would have been practical using a large-eddy simulation.

Both a CFD and an analytical well-mixed model of the room were built. The CFD model allowed for the spatial variation in concentration to be studied. Some of the model sensitivities could be more easily assessed in the analytical model.

As limited data was available on the permeation properties of explosives vapours, it was assumed that the walls of the room were constructed from thick cardboard. Although it is unlikely that a room would be constructed with cardboard, this can be considered to represent a highly absorbing surface such as bare plaster or certain wallpapers. Both sorption of EGDN and TNT at 20 °C was considered. EGDN represents a semi-volatile

material with a vapour pressure which puts it at the top of the SVOC group (see Section 2.1.2). TNT represents a lower vapour pressure SVOC. Initial CFD simulations showed that the CFD model required very small time steps when modelling absorption of TNT, due to its large partition coefficient. Therefore, TNT was only studied in the analytical well-mixed model.

The permeation properties for EGDN through cardboard, were measured using the same method as described earlier in the chapter. The permeation properties for TNT were extrapolated from data measured at 35 °C and 50 °C. The volatility and molecular diffusion coefficient were calculated using data from from the review paper of Ewing et al. (2013) and Equation A.1 respectively or from Gershanik and Zeiri (2012). All of these parameters are given in Table 5.4.

	C_0	D_m	D_{solid}	K_{ab}
	$kg{\cdot}m^{-3}$	$m^2{\cdot}s^{-1}$	$m^2{\cdot}s^{-1}$	
EGDN	4.1×10^{-4}	8.5×10^{-6}		
TNT	3.2×10^{-8}	5.6×10^{-6}		
EGDN and Cardboard			1.8×10^{-11}	1.5×10^{3}
TNT and Cardboard			4.4×10^{-15}	3.6×10^{6}

Table 5.4: Vapour parameters used in the mechanically ventilated room model at 20 °C.

5.4.1 Methodology

5.4.1.1 CFD

A number of RANS simulations were run to see which turbulence model performed best at predicting the flow. This was done by comparing predicted velocities to those measured by (Nielsen, 1990). The models considered were: the standard, realisable and RNG k-ϵ models (Launder and Spalding (1972), Shih et al. (1995) and (Orszag et al., 1993) respectively), the k-ω SST model (Mentor, 1994) and the Reynolds stress model (Launder et al., 1975). All models apart from k-ω SST used ANSYS Fluent's enhanced wall treatment (EWT) option[3]. The EWT applies a blended wall function (Kader, 1981) for the velocity and two-layer models (Wolfshtein (1969) model in viscous affected region) for ϵ and μ_t. Some additional details on the turbulence models are given in Section 2.2.2.2.

The inlet velocity and length scale were the same as specified in Section 3.2 but they were defined at the inlet to the domain rather than using the precursor model used previously. Ti was set to 20 % due to the large decay of TKE in the inlet channel, and

[3]This option is not available for the k-ω SST model as ω is automatically calculated throughout the domain and a low Reynolds number adjustment is automatically applied for μ_t in viscous affected region.

to achieve an acceptable level of Ti at the end of the inlet channel, i.e. at the entrance to the main volume of the domain.

As with the validation modelling in Section 5.3, a coupled solver was used for the pressure-velocity coupling. A second-order scheme was used for the pressure terms and a second-order upwind scheme for the momentum convection terms. The convection terms in the k, ϵ and ω equations were solved using a first-order upwind scheme. For the subsequent species transport modelling, the species convection terms were solved using a first-order upwind scheme and a first-order implicit scheme was used for the unsteady term.

The standard k-epsilon (SKE) gave the best results when comparing the velocity and RMS velocity to that of Nielsen (1990). The results achieved were comparable or better than those from other 3D RANS studies of the Nielsen test-case, i.e. Susin et al. (2009); Mazzaro et al. (2010). The improvement over some published studies is most likely due to the higher mesh resolution used here. Susin et al. (2009) and Mazzaro et al. (2010) used a few hundred thousand cells, whereas this model had 5.4 million.

To compare the velocity prediction to the experimental data, the RMS velocity was calculated from the TKE using the following relationship (Susin et al., 2009; Thysen, 2015).

$$u_{RMS} = \sqrt{k}/1.1 \tag{5.15}$$

This equation is based on the assumption that the flow can be considered to be a two-dimensional wall jet, in which case $\overline{v'^2} \propto 0.6\overline{u'^2}$ and $\overline{w'^2} \propto 0.8\overline{u'^2}$ (Nielsen, 1990). Therefore, this relationship only really applies in the wall jet region, i.e. close to the top of the room. However, both Susin et al. (2009) and Thysen (2015) applied it across the whole of the room.

The velocity, u, and u_{RMS}, both normalised against u_0, are compared to the data of Nielsen (1990) in Figures 5.14 and 5.15. Table 5.5 shows error metrics calculated for the RANS model. Also shown in the table is the LES data for the test case taken from Table 3.1 in Chapter 3.

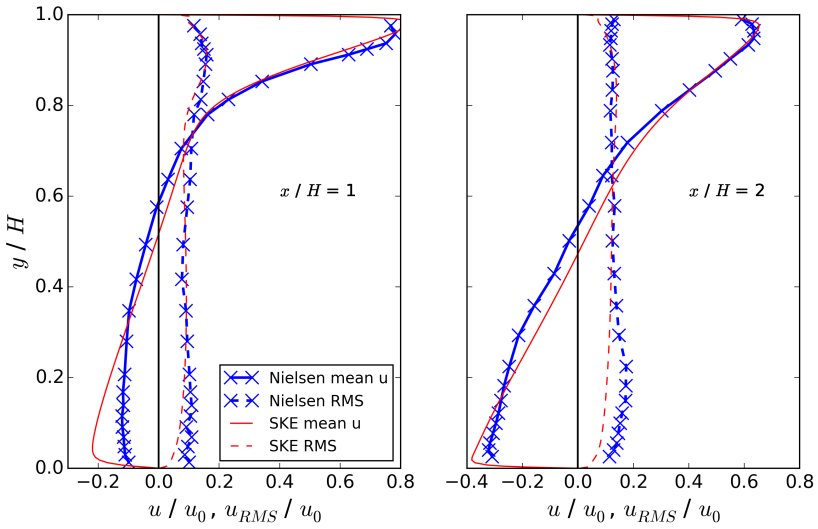

Figure 5.14: $\overline{u}$ / u_0 and u_{RMS} / u_0 against y / H on vertical lines on the centre plane at x / $H = 1$ (left graph) and x / $H = 2$ (right graph).

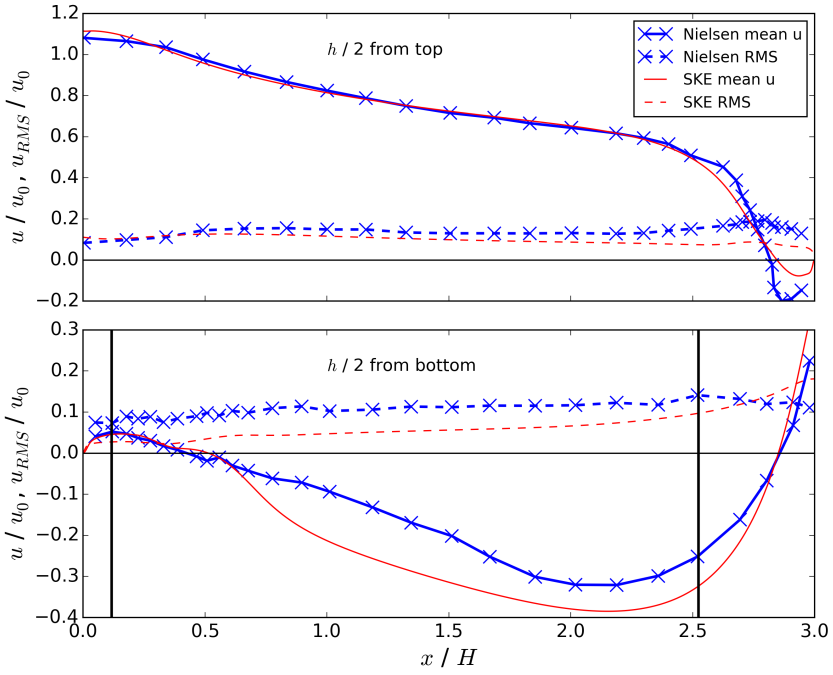

Figure 5.15: $\overline{u}$ / u_0 and u_{RMS} / u_0 against x / H on horizontal lines on the centre plane at a distance of h_{inlet} / 2 from the top wall (upper graph) and h_{inlet} / 2 from the bottom wall (lower graph). The vertical lines show the locations of the source centres.

The SKE model has performed well. According to the error metrics in Table 5.5 the mean velocity predictions are closer to the experimental data than the previous LES model.

However, the RANS model has performed worse at predicting the RMS velocity. The RANS models has more accurately predicted the point of separation near the bottom of the room but over-predicted the velocity along the rest of the line at h_{inlet} / 2 from the bottom wall. As a result of the RANS model forcing a steady solution to an unsteady problem, the solution included a circulation in the horizontal plane between x / $H = 0$ and 1. The same feature was discussed in Section 3.3.1 in relation to the LES modelling. Interestingly, the LES model with horizontal circulation also improved the correlation between the model and the experimental data on the line at h_{inlet} / 2 from the bottom wall.

	$\overline{u}/u_0$		u_{RMS}/u_0		Ideal value
	LES	RANS	LES	RANS	
FAC2	0.75	0.89	0.95	0.72	1
FAC1.3	0.53	0.63	0.51	0.37	1
FB	0.14	0.08	0.22	0.34	0
NMSE	0.26	0.13	0.11	0.22	0

Table 5.5: Model performance metrics for $\overline{u}$ / u_0 and u_{RMS} / u_0 for the LES and RANS models. Each assessment used 106 data points.

For the species transport modelling, the large left source region as described in Chapter 3 was used for the vapour source. All other walls (i.e. walls, floor and ceiling) were defined as absorbing surfaces. The flow was solved first as steady-state and then the transient species transport was modelled on the steady flow field. The vapour source was initialised at $t = 0$ s.

The absorption into the cardboard walls was represented using the permeation model described previously. As mentioned in Section 5.3.3.1, the maximum number of permeation layers, n_{layer}, is limited and the permeation is sensitive to the thickness of the layers, d_{layer}. Therefore, it is not possible to explicitly represent the full thickness of a 'standard' room wall. This issue can be circumvented if the time period being studied is relatively short as the vapour does not have time to permeate very far into the solid, in which case, a thinner wall can be modelled. An exploration of the model sensitivity to d_{layer} and n_{layer} is described below.

For the absorbing surface, d_{total} was set to 6.5×10^{-3} m with $n_{layer} = 100$ (i.e. $d_{layer} = 6.5 \times 10^{-5}$ m) in both the CFD and the initial analytical models. These values mean that $t_{lag} = 111$ h, which is approximately 50 times longer than the planned CFD simulation time (120 min). CFD models were also run with $n_{layer} = 200$ (i.e. $d_{layer} = 3.3 \times 10^{-5}$ m) with no significant effect on the predicted concentrations.

Some of the analytical models were run for longer time periods to check the model sensitivity to d_{total} and n_{layer} for these cases. The predicted concentrations for TNT and EGDN were insensitive to an increase in these parameters when $t \leq 1 \times 10^4$ min

(167 h). For longer simulations, when $t = 1 \times 10^5$ min (1670 h), d_{total} had to be increased to 3 x 6.5×10^{-3} m, with $n_{layer} = 300$, to give a solution which was independent of d_{total} and n_{layer}. When a vapour with D_{solid} equal to ten times that of EGDN was modelled, d_{total} had to be increased to 1.9×10^{-2} m with $n_{layer} = 300$ to produce independent results at $t = 1 \times 10^4$ min.

The vapour concentrations for sorption and no sorption cases were monitored at 16 locations close to the source. The 16 locations consisted of four rows of four points. The first row of points was 0.01 m above the floor, the second 0.1 m above the floor, the third 0.5 m and the fourth 1 m. The four columns of points were 0.01 m, 0.1 m, 0.5 m and 1.0 m away from the right-hand edge (i.e. larger x coordinate) of the large source. The array of monitor locations is shown in Figures 5.16. The points are referred to as point-rc, where r refers to the row number and c the column number.

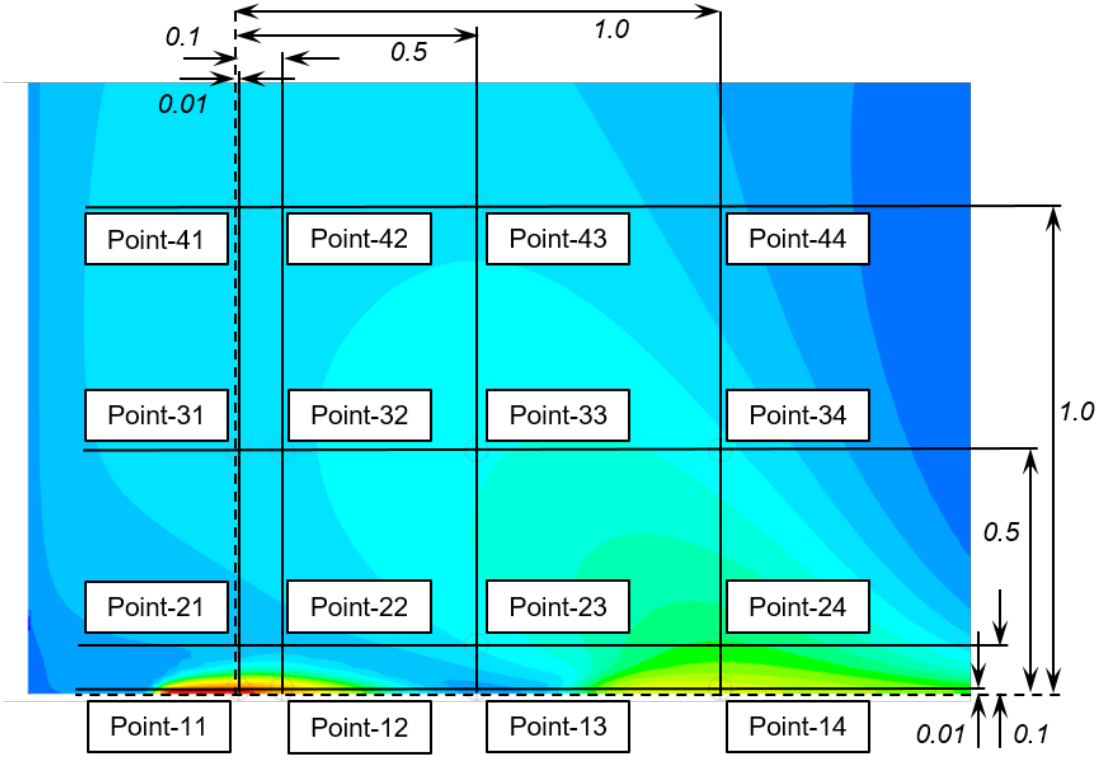

Figure 5.16: The sixteen monitor points used in the CFD model. Dimensions are given in m. The dashed lines indicate the right-hand edge of the source and ground level. The monitor points are on the intersections of the solid lines.

5.4.1.2 Well-mixed model

The analytical well-mixed model used a state-space approach (i.e. a systems of coupled first-order differential equations, which are used to characterise dynamic systems) and the models were built based on the methods in Parker and Bowman (2011) and Parker et al. (2014a). The models were solved using software previously developed by Dr. Parker

which employs the methods described in Parker et al. (2014b). One key advantage of the Parker et al. (2014b) state-space method is that it allows for direction modelling of the concentration at the required time point without having to use a time-stepping method.

The vapour flow in the room and the movement of vapour through the permeation layers (all with units of kg·s^{-1}) are shown in Figure 5.17. The vapour flow into the room from zone zero (outside of the model) into zone one (the room) is represented by Q_{10} and the flow out of the room (zone one) is represented by Q_{01}. The vapour source term is represented by $\dot{M}_1$ [kg·s^{-1}]. The concentration in each zone is represented by $C_n = M_n$ / V_n, where n is the zone index, M is the total mass of vapour in the zone and V is the zone volume.

The rate at which vapour mass is transferred from the room (zone 1) to the first permeation layer (zone 2) is given by aAC_1 (see Equation 5.8), where a is the mass transfer coefficient and A is the surface area of the absorbent material. The rate of transfer back from the first permeation layer to the room is $aAC* = aAC_2$ / K_{ab}. The rate of transfer between permeation layers is given by Fick's first law. The concentration in the outer zone is fixed to zero in the model.

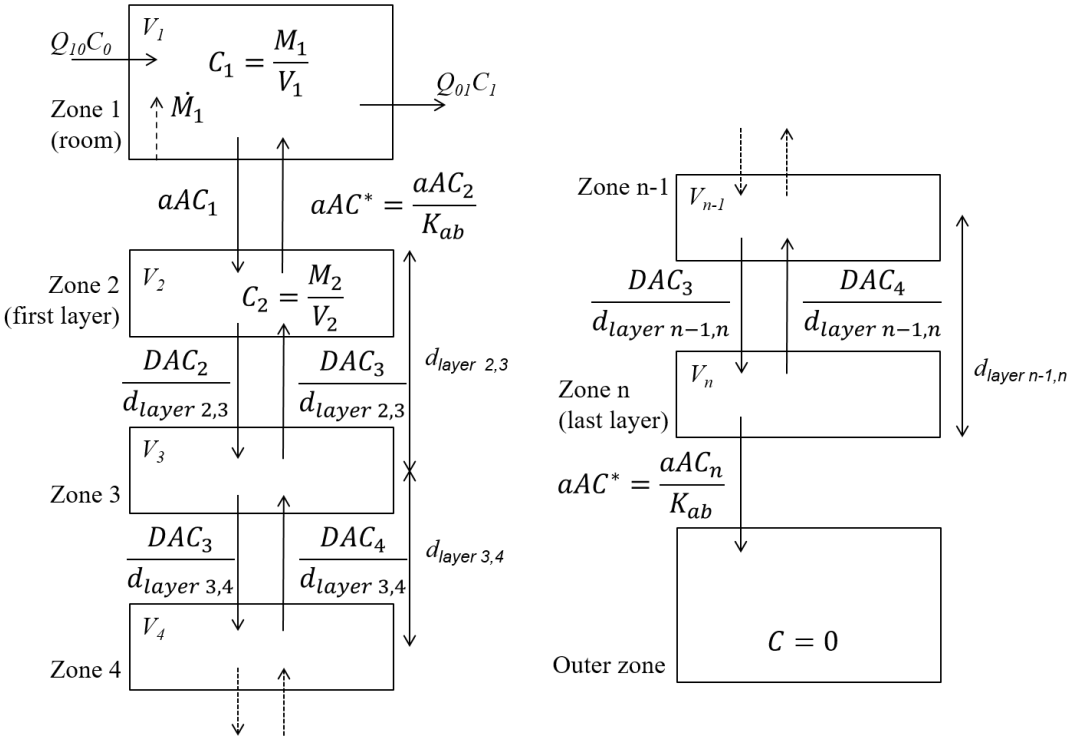

Figure 5.17: Vapour absorption model from a single well-mixed room. Flows between each zone are shown. The room and the top three absorption layers are shown on the left, the last two layers and outer zone are shown on the right. Zone 1 and the outer zone are air spaces, all other zones are solids.

For the well-mixed model the vapour emission rate in zone 1, $\dot{M}_1$, for EGDN was taken from the CFD model and was $1.44 \times 10^{-8}\,\mathrm{kg{\cdot}s^{-1}}$. For TNT, $\dot{M}_1$ was calculated using Equation 3.5 and was $4.05 \times 10^{-13}\,\mathrm{kg{\cdot}s^{-1}}$. The mass transfer coefficient, a, was taken from the EGDN CFD model, as calculated by the vapour sorption/permeation UDF. The area weighted average value for a over all the absorbing surfaces was $3.4 \times 10^{-3}\,\mathrm{m{\cdot}s^{-1}}$. It was assumed that a for TNT was the same as that for EGDN. This is a reasonable assumption as Sc for both vapours are similar. The volume of the room, V, was $81\,\mathrm{m^3}$ and the surface area of the absorbing material, A, was $124\,\mathrm{m^2}$.

The matrix equations for the state-space model are shown in Appendix C.

To build confidence in the state-space approach, the predictions from a state-space model were compared to those from a CFD model for a simple geometry where mixing of the vapour was maximised through the use of a high air change rate and a large molecular diffusion coefficient. The geometry was a 1 m cube which was meshed with only 8800 cells so that it could easily be run for long simulation times. The CFD predicted similar concentrations to the state-space model. There was only 2 % difference in prediction of C / C_{equil} for times larger than approximately 25 min. The details of the models and the results of the comparison are given in Appendix D.

5.4.2 Results and discussion

5.4.2.1 Well-mixed analytical model results

The EGDN and TNT concentration predictions from the well-mixed analytical model are shown in Figures 5.18 and 5.19 for two durations. The graphs show concentrations normalised by the equilibrium concentration, C_{equil} [$\mathrm{kg{\cdot}m^{-3}}$], where C_{equil} is given by $\dot{M}/Q$. The no sorption curve is the same for EGDN and TNT when normalised against C_{equil}.

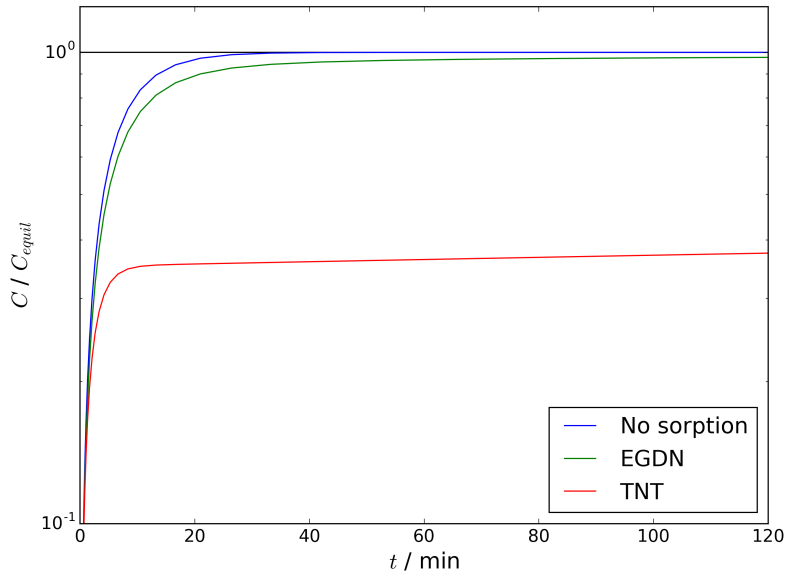

Figure 5.18: C / C_{equil} for EGDN, TNT and the no sorption case calculated using the well-mixed model. The horizontal black line shows C_{equil}.

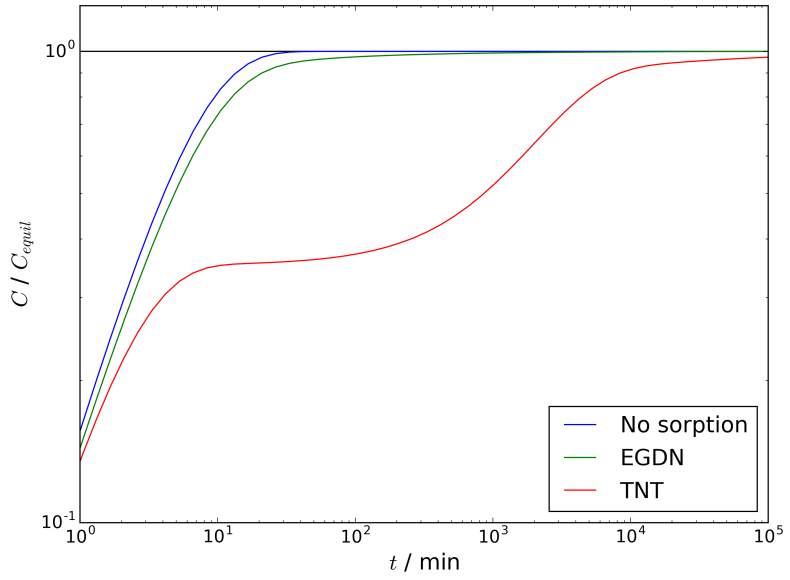

Figure 5.19: C / C_{equil} for EGDN, TNT and the no sorption case calculated using the well-mixed model. The horizontal black line shows C_{equil}. Time is shown on a logarithmic axis.

For the no sorption case, C is given by the following equation for concentration from a continuous release in a well-mixed room (Reinke and Keil, 2009).

$$C = \frac{\dot{M}}{Q}\left[1 - \exp\left(-\lambda t\right)\right]. \tag{5.16}$$

The results, Figures 5.18 and 5.19, show that for a well-mixed room, the absorbing effects of EGDN have only a small effect on the room concentrations, whereas the absorbing effects of TNT have a significant effect. At 132 min, the EGDN concentration is 98 % of the no sorption equilibrium concentration, whereas at the same time, the TNT concentration is 38 % of C_{equil}. The log-log plot in Figure 5.19 (1×10^5 min $\approx$ 70 days) shows that the TNT concentration approaches C_{equil} at $\approx$ 7 days (1×10^4 min).

The same data is also plotted as (1 - C / C_{equil}) in Figure 5.20 as this makes it easier to see the time scales for the model. For the no sorption case the straight line, when plotted with a logarithmic y-axis, shows that there is a constant rate of decrease, which, in this case, is given by $\exp\left(-\lambda t\right)$, with the rate constant, $\lambda = 10.2\,\mathrm{h}^{-1}$. Therefore, the time scale for the decrease is $1/\lambda = 353$ s. For the sorption cases, there are clearly a range of time scales. However, at least for the EGDN case, the concentration initially (t <20 min) changes at a rate which is similar to the no sorption case, i.e. one related to the room air change rate.

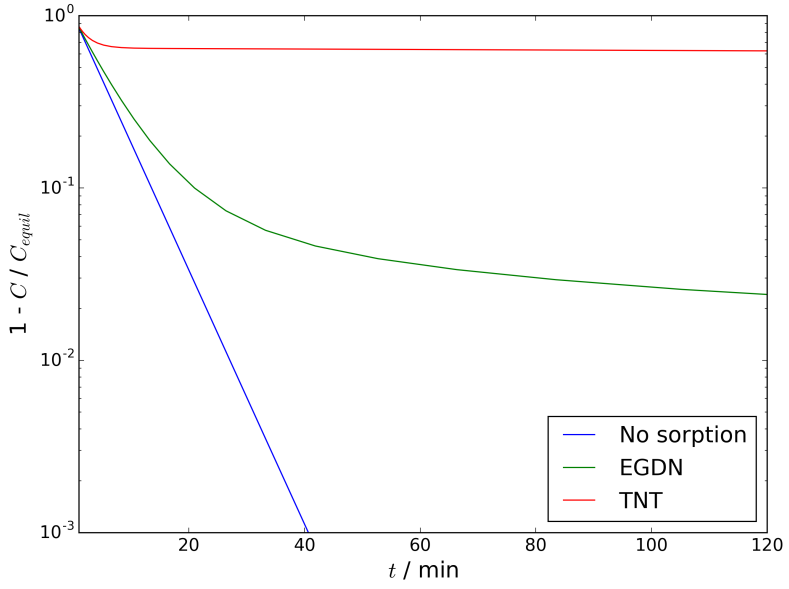

Figure 5.20: 1 - C / C_{equil} for EGDN, TNT and the no sorption case calculated using the well-mixed model.

The effect of changing the flow rate, Q, the solid phase diffusion coefficient, D_{solid}, and the partition coefficient, K_{ab}, are shown in Figures 5.21 to 5.23 for EGDN. In all graphs

the original values, Q, D_{solid} and K_{ab} were multiplied by a factor of 10 or 1/10. It was assumed that changing Q did not affect the mass transfer coefficient. The lower left graph in Figure 5.21 also shows three black lines, which are Equation 5.16 plotted for the three flow rates.

The three sets of graphs show that changing Q has most effect on the concentration early in the simulation (compared to changing D_{solid} or K_{ab}). Changing D_{solid} or K_{ab} has a negligible effect on concentrations during the first few minutes. Changing D_{solid} or K_{ab} affects the rate of change of concentration at intermediate times and none of the parameters appear to have much effect on the rate of change at later times.

For the range of values tested, the concentration was most sensitive to a change of Q. A higher flow rate resulted in equilibrium concentrations being approached much more quickly. It should be noted that a factor of ten change in Q is an extreme change from a room ventilation perspective. Whereas a factor of ten change in D_{solid} or K_{ab} is a reasonably small change when compared to the range of values given for EGDN and TNT in Table 5.4.

Part of the effect of changing Q is to change C_{equil}, i.e. a decrease in Q results in a higher C_{equil}, therefore the target concentration is higher. It was assumed here that changing Q did not affect the mass transfer coefficient. In reality, decreasing Q would result in a smaller mass transfer coefficient which would further compound the effect that Q has on the room concentrations. A similar effect (higher air change rates resulting in increased emission but lower equilibrium concentrations) was shown by Clausen et al. (2010) for emission cells.

The lower left graph in Figure 5.21 further confirms that the initial rate of change in concentration is governed by the room air change rate.

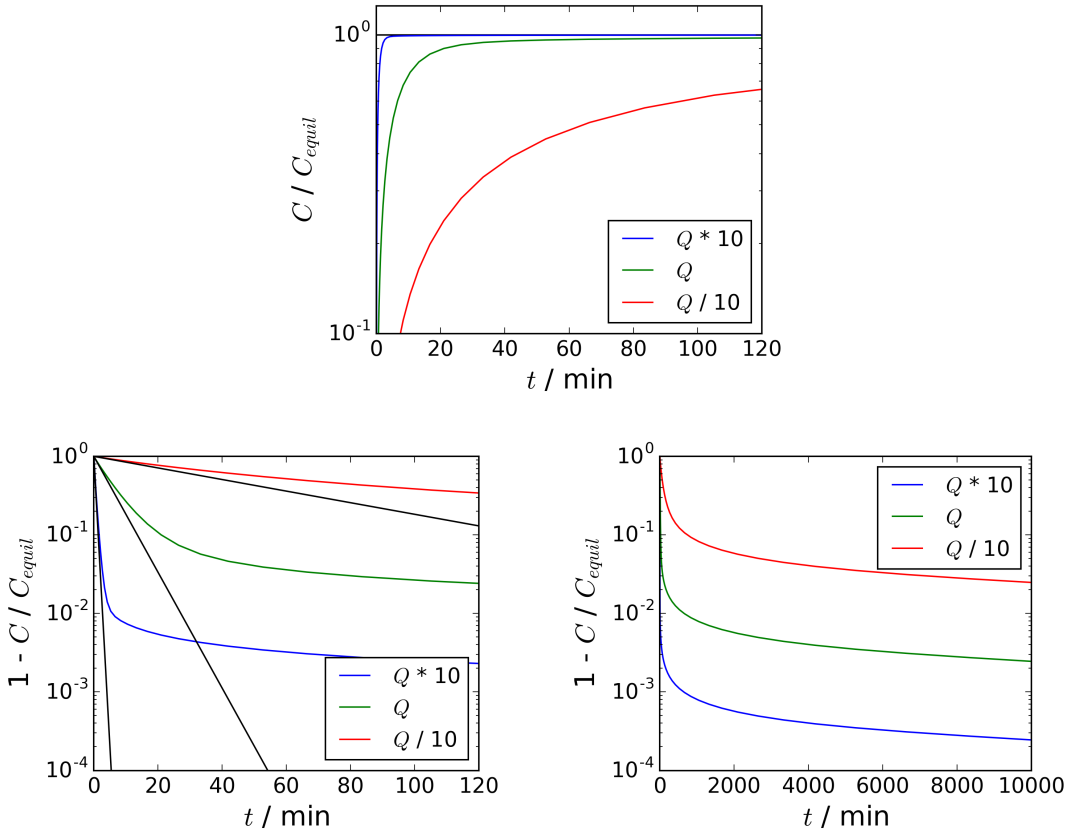

Figure 5.21: C / C_{equil} (upper) and 1 - C / C_{equil} for EGDN. Shown for three different flow rates, where $Q = 0.2295\,\mathrm{m^3{\cdot}s^{-1}}$ and with two different maximum times (lower). The three black lines on the lower left graph shows Equation 5.16 plotted for the three flow rates.

Changing D_{solid} or K_{ab} does not appear to change the slope of the curves, on a log scale, after approximately 100 min, but does change the point at which the curves transitions out of the phase which is controlled by the room air change rate.

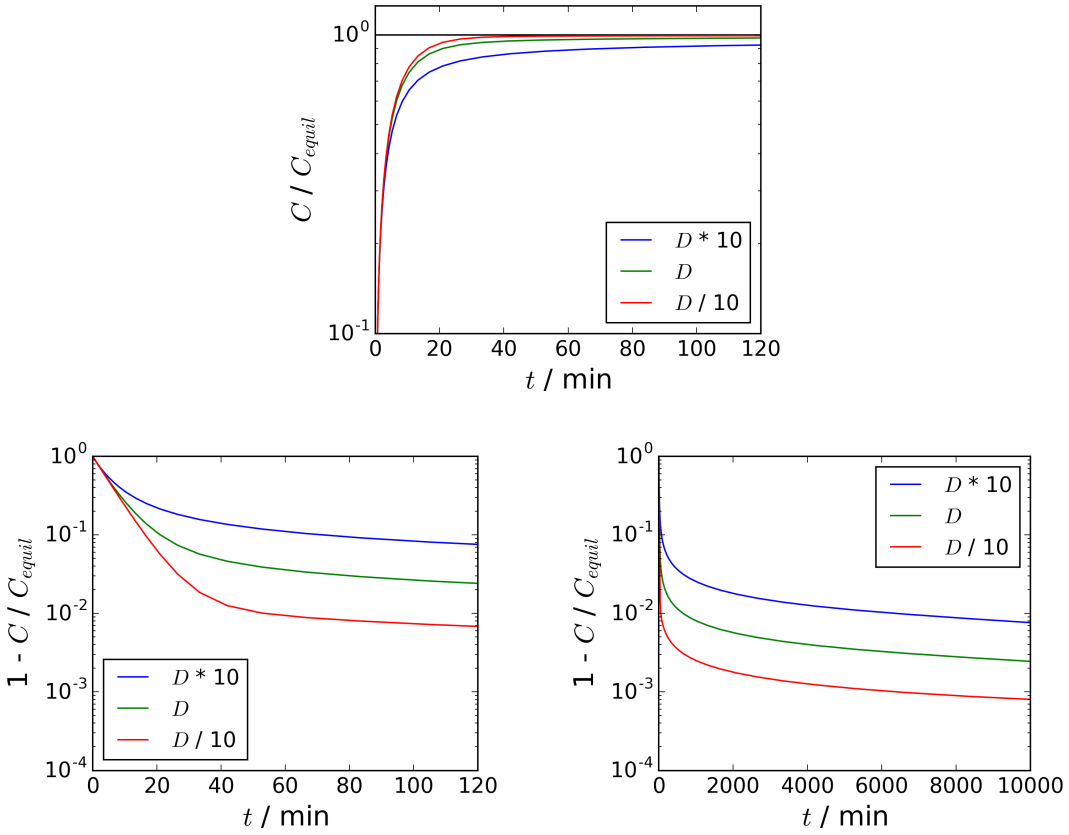

Figure 5.22: C / C_{equil} (upper) and 1 - C / C_{equil} for EGDN. Shown for three different solid phase diffusion coefficients, where $D_{solid} = 1.8 \times 10^{-11}\,\mathrm{m^2{\cdot}s^{-1}}$ and with two different maximum times (lower).

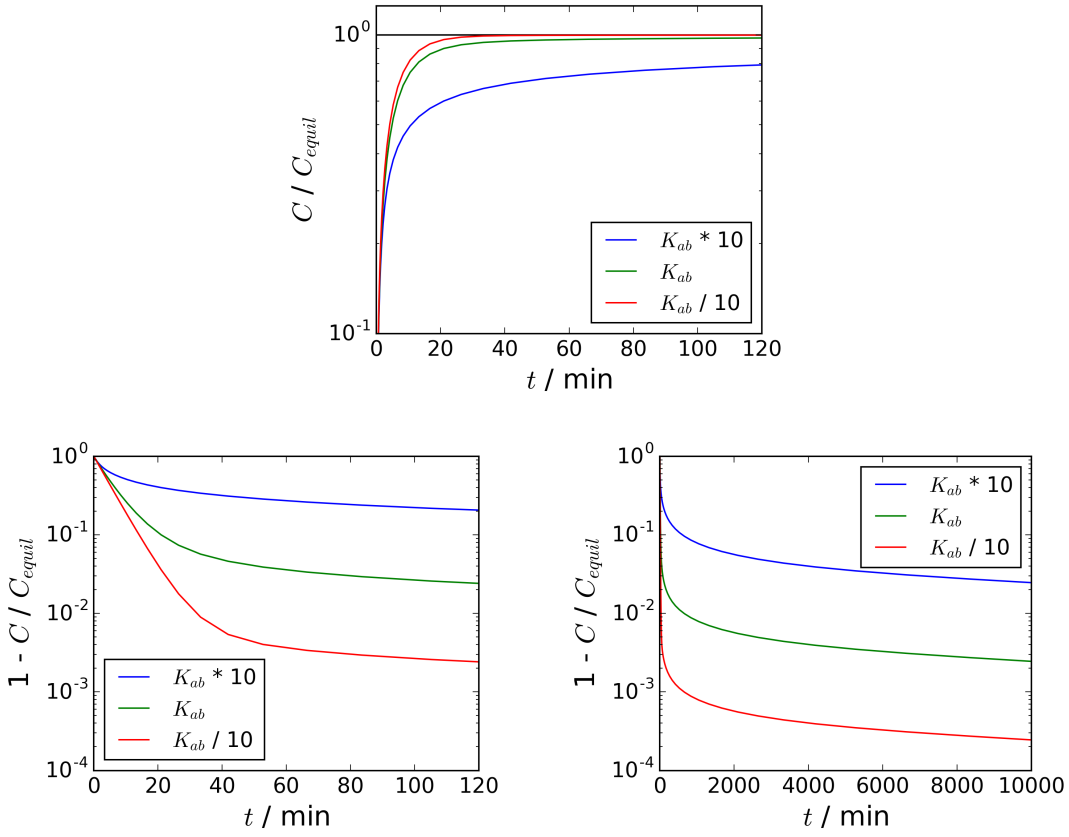

Figure 5.23: C / C_{equil} (upper) and 1 - C / C_{equil} for EGDN for three different partition coefficients, where $K_{ab} = 1.5 \times 10^3$ and with two different maximum times (lower).

The well-mixed analytical model has allowed the general dynamics of the system to be explored in a way which was not practical using CFD. The CFD, however, allows the spatial variation in concentration within the room to be examined.

5.4.2.2 CFD model results

EGDN vapour concentration contour plots from the CFD model of the Nielsen test room for the sorption and no sorption cases are shown in Figures 5.24 and 5.25. The figures show concentrations on the vertical centre plane and a horizontal plane 0.01 m above the floor at 7200 s after the start of the vapour release.

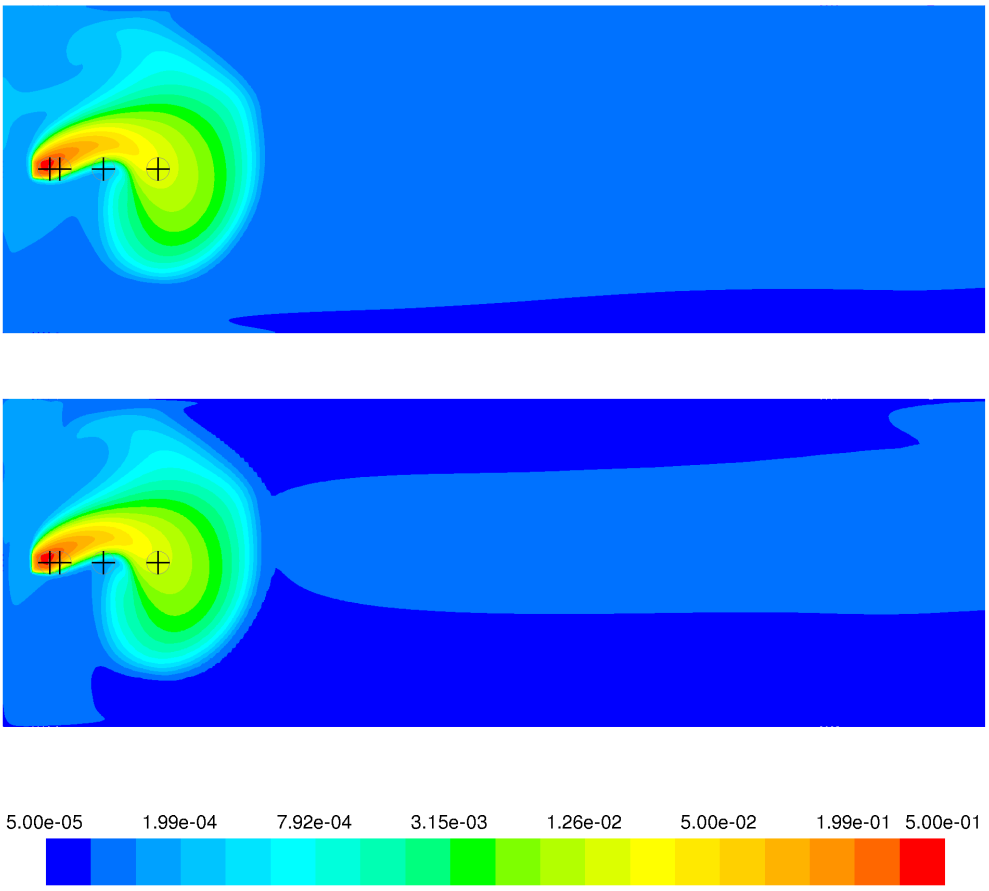

Figure 5.24: Normalised mean concentrations (C / C_0) on a horizontal plane 0.01 m above the floor at 7200 s. Contours for the no sorption case are shown (upper) and the EGDN sorption case (lower) are shown. The concentrations are shown on a log scale and are not clipped to the range.

The horizontal contour plots show the circulation in the horizontal plane which was present in the model. This means that the plume from the source did not travel directly from point-11 to point-14 (see Figure 5.16 for locations of the monitor points) and the outcome of this is that point-13 has a lower concentration than point-14. The vertical contour plots look quite different to those from the LES model in Chapter 3 (e.g. Figure 3.9), this is partly because the LES results are for an equilibrium condition, whereas these graphs are for a time point at 7200 s after the start of the release.

The difference in vapour concentration between the sorption and no sorption cases can be most clearly seen in the horizontal plane, which was only 0.01 m above an absorbing surface. Whereas the difference is less pronounced on the vertical planes.

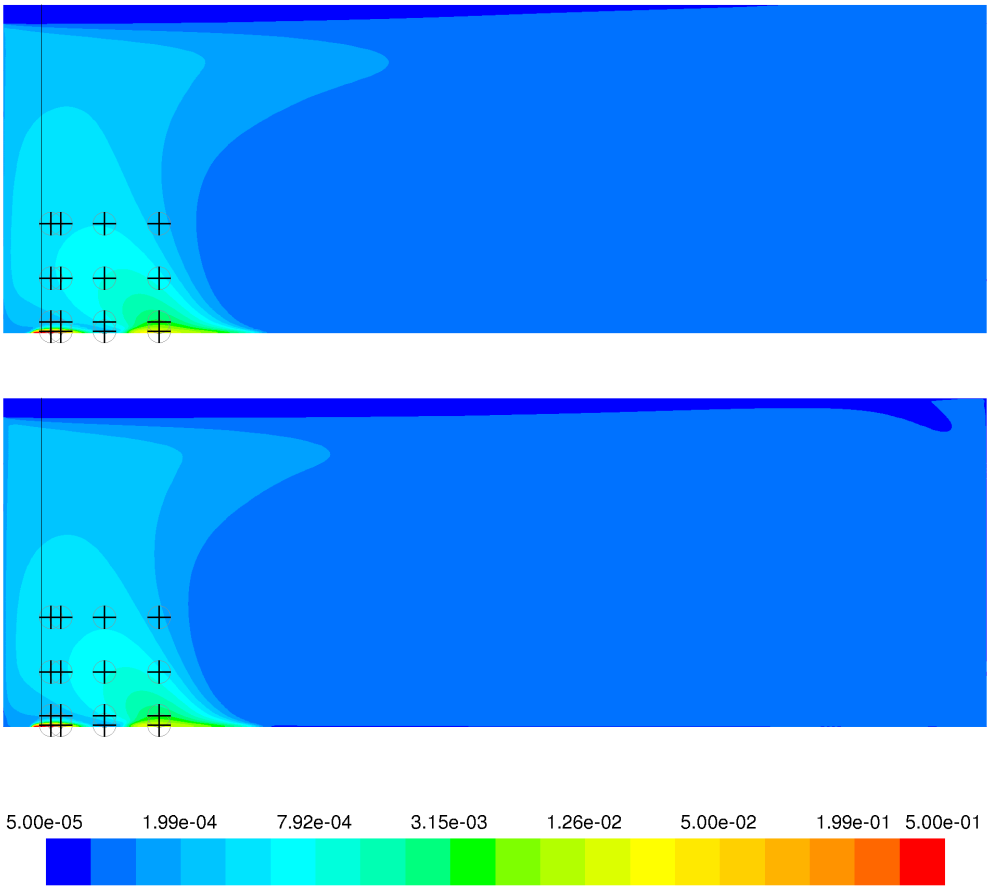

Figure 5.25: Normalised mean concentrations (C / C_0) on the vertical centre plane at 7200 s. Contours for the no sorption case are shown (upper) and the EGDN sorption case (lower) are shown. The concentrations are shown on a log scale and are not clipped to the range. The vertical line is positioned at the centres of the sources.

Normalised concentrations, (C / C_{equil}), for the no sorption case are shown at the 16 monitor location in the left-hand graph in Figure 5.26. All monitor locations reached 99 % of their equilibrium concentration within just over 2000 s (33.6 min). Locations close to the source, i.e. point-11 and point-12 reached the same threshold in 33 s and 177 s respectively.

The right-hand graph in Figure 5.26 shows (1 - C / C_{equil}). This clearly shows that after approximately 20 min, the concentrations all increase at the same rate. By fitting an exponential curve to the these, the rate was found to be 8.0 h^{-1} (the room air change rate = 10.2 h^{-1}). This value, referred to here as the effective air change rate (see section 4.3 for more discussion on the effective air change rate), is lower than the room air change rate, λ. This indicates that the region of the room where the monitor points are located is less well ventilated than the room as a whole. The rate, 8.0 h^{-1}, is equivalent to a flow rate of 0.18 $m^3 \cdot s^{-1}$, assuming that the rate applied across the whole room.

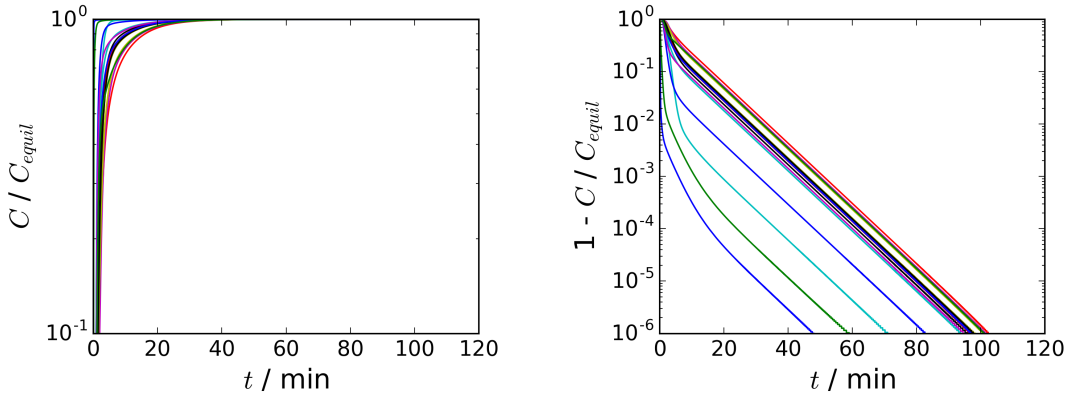

Figure 5.26: CFD predictions for C / C_{equil} (left) and 1 - C / C_{equil} (right) for the no sorption case. Data is shown for the 16 monitor points in the CFD model. Each line corresponds with 1 monitor point.

Figure 5.27 shows (C / C_{equil}) and (1 - C / C_{equil}) for the absorbing EGDN case. For this data, C_{equil} was taken from the no sorption data for each location. These graphs show that, even after 120 min, the concentration is still some way off C_{equil} at some locations. The (1 - C / C_{equil}) graph shows that the concentration at most locations initially increases with a rate which is close to that from the no sorption CFD case, i.e. $8.0\,\mathrm{h}^{-1}$. The rate then reduces in a similar way as it did in the well-mixed model (e.g. see Figure 5.20).

Figure 5.27 is evidently different from Figure 5.26, suggesting that the sorption effect for EGDN is significant when spatially resolved concentrations are modelled. This is because the sorption effect in the near source region is strong at the early stage of the simulation.

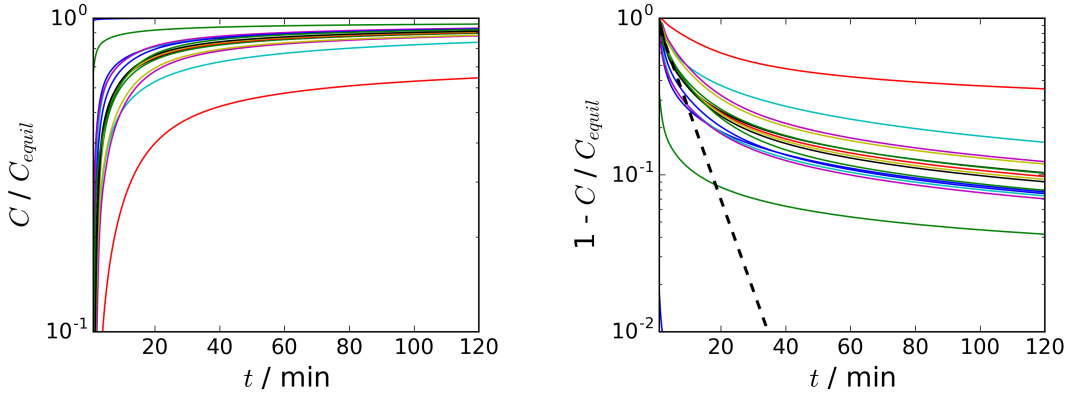

Figure 5.27: CFD predictions for C / C_{equil} (left) and 1 - C / C_{equil} (right) for EGDN sorption. Data is shown for the 16 monitor points in the CFD model. Each curve corresponds with 1 monitor point. The straight black line on the right-hand graph shows Equation 5.16 plotted with the rate = $8.0\,\mathrm{h}^{-1}$.

The input parameters in the CFD model were varied in a similar way as they were in the well-mixed model. Figures 5.28 to 5.30 show the effect of varying Q, D_{solid} and K. When Q was varied, this altered the flow locally so it was difficult to directly compare concentrations at one point to that at another. Therefore, data was averaged across all 16 points. When varying either K or D_{solid}, the same effect was seen at all points so just data from point-22 is shown in Figures 5.29 and 5.30. When varying the flow rate, Q was only changed by a factor of two as reducing it by a factor of ten might have resulted in the flow becoming laminar. Increasing the flow by a factor of ten would have required a refined mesh, so this case was not considered either.

Reducing Q by a factor of two reduced the rate at which C_{equil} was approached as was shown by the well-mixed model. As shown in the C / C_{equil} graphs, changing D_{solid} by a factor of ten had a slightly larger effect on the CFD data than it did on the well-mixed model data. The same was true when K was changed. This may be because all the monitor points considered in the CFD model are relatively near the absorbing surface.

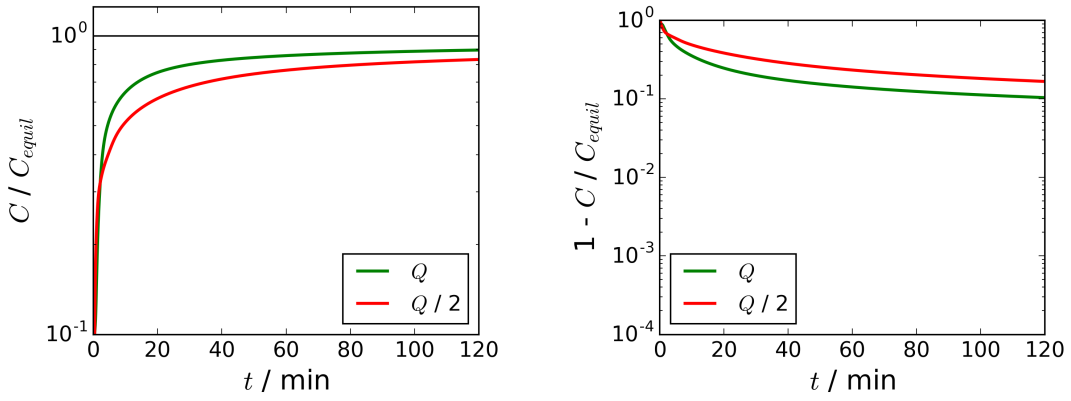

Figure 5.28: CFD predictions for C / C_{equil} (left) and 1 - C / C_{equil} (right) for two different flow rates, where $Q = 0.2295\,\mathrm{m^3{\cdot}s^{-1}}$. Data is the average across all 16 monitor points.

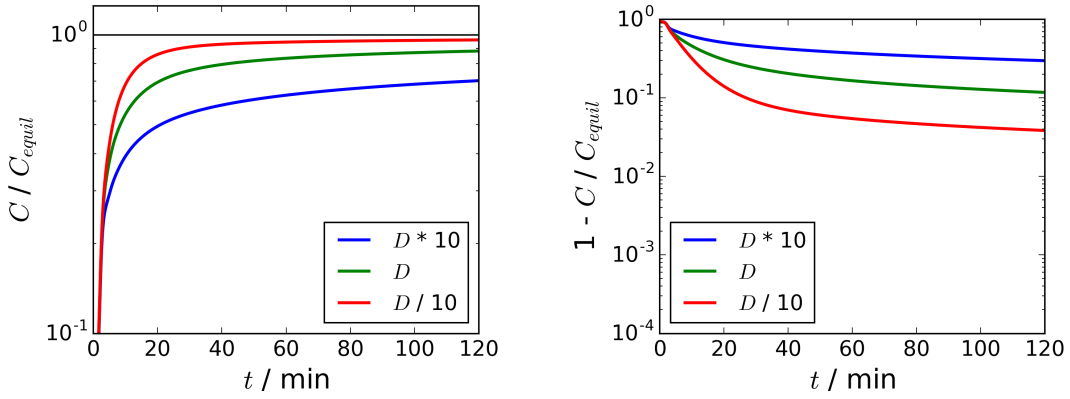

Figure 5.29: CFD predictions for C / C_{equil} (left) and 1 - C / C_{equil} (right) for three solid phase diffusion coefficients, where $D = 1.8 \times 10^{-11}$ m^2·s^{-1}. Data is shown for point-22.

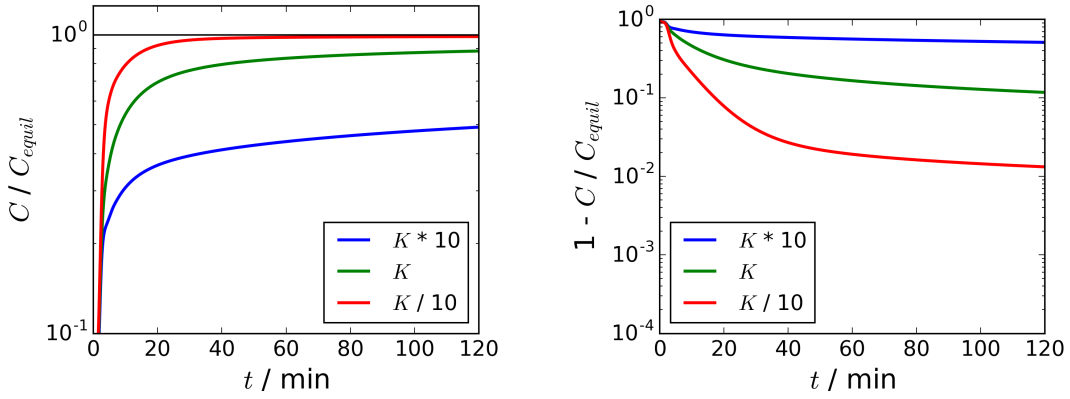

Figure 5.30: CFD predictions for C / C_{equil} (left) and 1 - C / C_{equil} (right) for three different partition coefficients, where $K_{ab} = 1.5 \times 10^3$. Data is shown for point-22.

To highlight the effect that absorption of EGDN could have in an experiment, some additional calculations have been performed. The ratio of the time it takes to reach 75 % of C_{equil} for the EGDN sorption case ($t75_{sorp}$ [s]) and no sorption case ($t75_{noSorp}$ [s]) was calculated at each of the 16 monitor locations. The results from this are shown in Figure 5.31.

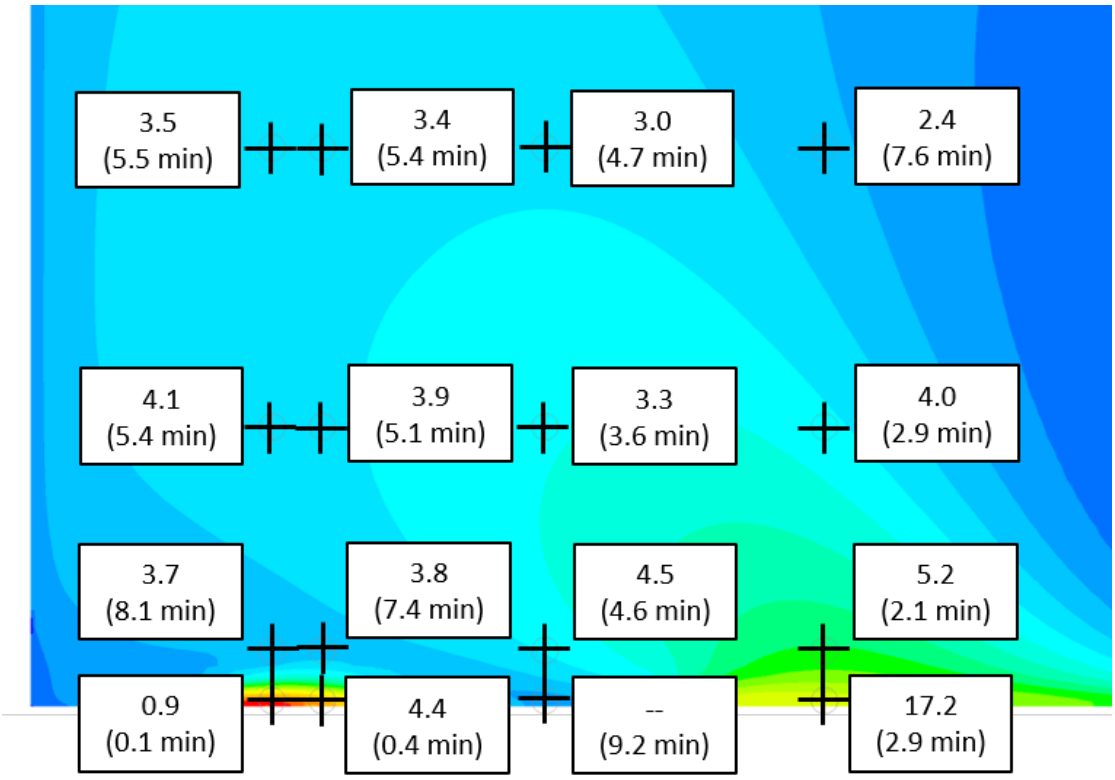

Figure 5.31: Ratio of time taken to reach 75 % of the no sorption equilibrium concentration in the sorption and no sorption models, i.e. $t75_{sorp}$ / ($t75_{noSorp}$). The numbers in brackets show $t75_{noSorp}$. The '–' indicates that the threshold was not reached at that location within 120 min. The contours are from Figure 5.25 and the coordinates and names for the monitor points are shown in Figure 5.16.

Generally the lower the concentration the longer the time it takes to reach 75 % of C_{equil}. Therefore, at the closest point to the source (point-11), the value is reached in only 0.1 min, whereas it can take as long as 9.2 min (point-13). Vapour sorption had a significant effect on the time to reach 75 % of the equilibrium in all locations apart from the closest point to the source. The effect is higher nearer to the floor, with the concentration at point-14 taking 17.2 times longer to reach the equilibrium concentration than the no sorption case. Even at 1 m above the floor, the concentrations taken between 2.4 and 3.5 times longer to reach C_{equil}, compared to the no sorption case. All but one location (point-13) (see Figure 5.16 for location of the monitor points) reached 75 % of C_{equil} in under 50 min.

The ratio of the times at point-11 (0.01 m distance from the right-hand edge of the source and 0.01 m above the floor) was 0.9, i.e. it took less time to reach 75 % of the equilibrium concentration in the sorption case. There are two possible causes of this. The first is that the time step, Δt, was 0.01 s in the sorption model but only 1 s in the no sorption model. This could have resulted in insufficient time resolution at the start of the simulation and therefore an under-prediction of the rate of increase in concentration.

The second is that the loss of vapour to the absorbing surfaces around the source early in the simulation would have locally lowered the concentration in the air. This would have increased the local concentration gradient and could therefore have increased the flux from the source.

5.4.3 Summary on vapour sorption in an isothermal mechanically ventilated room

In summary, it is hard to generalise to other types of room, or vapour-surface pairs, due to the complexity of the room air flow and the sorption processes. However, some useful conclusions can made for the first time in relation to vapour of relevance to explosives detection.

It has been shown that the absorption of EGDN in the test room had little effect on well-mixed concentrations but could have a significant effect on concentrations close to the absorbing surface within the first hour after the explosive is placed in the room. The difference between well-mixed models and CFD models in relation to vapour emission and sorption has been alluded to by Sorensen and Weschler (2002) and Mao et al. (2018) but has not been shown as directly as it has been here.

TNT absorption had a greater effect on the well-mixed concentration, and for the case examined, would take more than 1000 h to reach the equilibrium concentration.

As has been reported previously for emission cells (Clausen et al., 2010), CFD and well-mixed modelling has shown that decreasing Q or increasing K or D_{solid} will result in the concentration taking longer to reach an equilibrium. For both the CFD and well-mixed models the concentrations generally increase at the room air change rate or the effective air change rate in the early stages of the simulation.

As is shown in Figure 2.2 many explosives have a vapour pressure lower than EGDN and a significant number have a vapour pressure lower than TNT. Therefore, as is typically considered for SVOC transport in relation to health effects, vapour sorption should be included in most transport modelling related to explosive detection. For the more volatile materials, such as EGDN, it may be safe to ignore sorption effects if the explosive has been left in place for a significant time or only concentrations away from absorbing surfaces are of interest. The well-mixed modelling approach could be used to carry out an initial assessment of the effect of sorption for a specific scenario of interest.

5.5 Conclusions and recommendations on the effect of vapour sorption

Most of the materials of interest to explosive detection have low to very low vapour pressures indicating that they will have large partition coefficients. Therefore, the effect of vapour sorption onto or into surfaces could be significant. To address this a new spatially resolved sorption and permeation model has been validated and then applied to vapour transport in a test-case. The conclusions of this work are the following.

- A CFD based multi-layer sorption and permeation model has been validated using three experiments of increasing complexity. The model used a blended wall function or a simple Fick's law model to represent near-wall transport and a linear isotherm.
- It has been shown that the CFD capability can now be used to study the operational and training scenarios described in Section 1.3.
- However, the capability has some limitations.
  - The permeation is sensitive to the thickness of the individual permeation layers, d_{layer}, and the sensitivity is strongest at the early stages of the simulation.
  - Based on the validation cases studied, the CFD model generally over-predicts concentrations.
  - The UDF can become unstable if very large or small partition coefficients are used. This problem can be particularly apparent when the simulation is being started, i.e. when there is zero concentration on the surface. It may be possible to use adaptive time-stepping to automatically increase Δt as the simulation progresses. Alternatively, it may be possible to use an implicit scheme rather than the current explicit scheme.
- It was shown that a thick permeable material can be represented in the model by a thinner material if the duration of the simulation is short compared to the lag time.
- The results for the simulations which included cardboard, support the assumption that the diffusion through the air voids in corrugated cardboard can be ignored.

The effect of vapour sorption on airborne concentrations in the Nielsen test-case has been studied using the validated CFD model and a well-mixed model. It is hard to generalise to other types of room, or vapour-surface pairs, due to the complexity of the room air flow and the sorption processes. However, some useful conclusions can made for the first time in relation to vapour of relevance to explosives detection:

- It has been shown that absorption of EGDN in the test room had little effect on well-mixed concentration but could have a significant effect on concentrations close to the absorbing surface within the first hour. The difference between well-mixed models and CFD models in relation to vapour emission and sorption has been alluded to by Sorensen and Weschler (2002) and Mao et al. (2018) but has not been shown as directly as it has been here.
- TNT absorption had a greater effect on the well-mixed concentration, and for the case examined, would take more than 1000 h to reach the equilibrium concentration.
- As has been reported previously for emission cells (Clausen et al., 2010), CFD and well-mixed modelling has shown that decreasing Q or increasing K or D_{solid} will result in the concentration taking longer to reach an equilibrium.
- For both the CFD and well-mixed model the concentrations generally increase at the room air change rate or the effective air change rate in the early stages.
- When planning training scenarios for detection dogs, vapour sorption should be considered for most explosives. The CFD sorption and permeation model could be used to model the specific scenario if the required input parameters are available.

It is recommended that:

- The permeation model is extended to include 3D diffusion. This may give more accurate results in some situations but might require non-isotropic diffusion coefficients to the measured.
- A CFD model is built to represent the vapour sampling process used in the cardboard box validation experiment. This should be done to see whether the in-box concentration over-prediction can be fully explained.
- Models are run to show how long a detectable vapour concentration remains in a room once the explosive has been removed.

Chapter 6

Eddy diffusion modelling

6.1 Introduction

Even with all of the complexity of indoor air flow, advective transport indoors can often be represented by a diffusion model. This approach, called eddy diffusion modelling, can be applied when there is isotropic mixing on a large scale (i.e. room scale) due to laminar and/or turbulent motion. It is also often not practical to fully survey the environment in which detection activities take place. In these cases it will be impossible to define the boundary conditions required for techniques such as computational fluid dynamics.

As discussed in Section 2.2, the validity of the eddy diffusion approach has been demonstrated in indoor spaces by a number of people e.g. Cheng et al. (2011); Drivas et al. (1996); Shao et al. (2017). The single parameter that governs mixing in these models is the eddy diffusion coefficient, D_e. Some relationships that enable this coefficient to be predicted have been proposed in the literature, but wider applicability of these has not previously been tested. In this chapter a novel automated computational fluid dynamics tool was used to calculate the eddy diffusion coefficient in a range of isothermal, mechanically ventilated rooms. Available models for the diffusion coefficient were then tested. A requirement for this type of assessment is supported by both Jayjock et al. (2007) and Nicas (2009).

Parts of this chapter have been published in Foat et al. (2017) and Foat et al. (2020).

6.2 Background and theory

Fick's second law (below) can be derived from Fick's first law, Equation 2.37.

$$\frac{\partial C}{\partial t} = -D\left(\frac{\partial^2 C}{\partial x^2} + \frac{\partial^2 C}{\partial y^2} + \frac{\partial^2 C}{\partial z^2}\right), \tag{6.1}$$

The solution to Equation 6.1 for an instantaneous point source in an infinite volume is given by the following (Crank, 1979). Here D is replaced by D_e.

$$C(r,t) = \frac{M}{8(\pi\, D_e\, t)^{\frac{3}{2}}} \exp\left(\frac{-r^2}{4D_e\, t}\right), \tag{6.2}$$

where M [kg] is the mass of material released at time $t = 0$ at a point in space and r is the radial distance from the source. Drivas et al. (1996) and Cheng et al. (2011) presented equations for the concentrations within a space where the air is being extracted and replenished with clean air. Both simply apply an exponential decay to the diffusion equation.

$$\exp(-\lambda_f\, t), \tag{6.3}$$

where λ_f [s^{-1}] is the fresh air change rate.

The containing effects of the walls of a room can be included by adding sets of image sources. Taking advantage of the superposition principle for linear systems of equations, the solutions from the main source and all the image sources can be combined (Crank, 1979; Fischer et al., 1979). The following equation gives the concentration C in a room of length, L [m], width, W [m], and height, H [m], for an instantaneous point source (Drivas et al., 1996).

$$C(x,y,z,t) = \frac{M\, \exp(-\lambda_f\, t)}{8(\pi\, D_e\, t)^{\frac{3}{2}}} r_x r_y r_z, \tag{6.4}$$

where the wall reflection terms r_x, r_y and r_z are given by the following (Drivas et al., 1996):

$$r_x = \sum_{n=-\infty}^{\infty}\left[\exp\left(\frac{-(x+2nL-x_0)^2}{4D_e\, t}\right) + \exp\left(\frac{-(x+2nL+x_0)^2}{4D_e\, t}\right)\right], \tag{6.5}$$

$$r_y = \sum_{n=-\infty}^{\infty}\left[\exp\left(\frac{-(y+2nW-y_0)^2}{4D_e\, t}\right) + \exp\left(\frac{-(y+2nW+y_0)^2}{4D_e\, t}\right)\right], \tag{6.6}$$

$$r_z = \sum_{n=-\infty}^{\infty} \left[\exp\left(\frac{-(z + 2nH - z_0)^2}{4D_e\, t} \right) + \exp\left(\frac{-(z + 2nH + z_0)^2}{4D_e\, t} \right) \right], \tag{6.7}$$

where x_0, y_0 and z_0 are the release coordinates and the summation is over the image sources. As can be seen, x, y and z correspond with L, W and H respectively. Rather than an infinite sum, only a small number of image sources are required to give a sufficiently accurate solution when the non-dimensional diffusion time, t_{ND}, is small.

$$t_{ND} = \frac{t\, D_e}{L_{diff}^2}, \tag{6.8}$$

where L_{diff} [m] is the distance over which the material is diffusing e.g. the length of the room. Cheng et al. (2011) used six image sources and Nehorai (1995) used only one.

The eddy diffusion coefficient for indoor spaces has been calculated from a number of experimental studies, see Table 6.1. The experimentally calculated values have been shown to range from a suggested lower limit of $1 \times 10^{-3}\,\mathrm{m{\cdot}s^{-2}}$ (Drivas et al., 1996) to as high as $1.9 \times 10^{-1}\,\mathrm{m{\cdot}s^{-2}}$ (Nicas, 2009). Although the upper value of $1.9 \times 10^{-1}\,\mathrm{m{\cdot}s^{-2}}$ may be spurious as this was recorded in a room with a very low air change rate. This wide range makes it difficult to directly apply the experimentally derived diffusion coefficients to cases were D_e is not known.

Ventilation	λ /h^{-1}	**Room volume** /m^3	D_e, **brackets indicate median** /$m^2 \cdot s^{-1}$	**Source**
Natural	0.17 - 1.2	158 or 59	1.1×10^{-3} - 6.9×10^{-2}	Cheng et al. (2011)
Natural	2.08	59	6.8×10^{-3}	Cheng et al. (2011)
Natural	5.4	59	1.3×10^{-2}	Cheng et al. (2011)
Mechanical	10.6	1315	1.8×10^{-3} - 3.8×10^{-3} (2.7×10^{-3})	Scheff et al. (1992)
Mechanical	0.3	8155	1.9×10^{-1}	Nicas (2009)
Mechanical	11	2492	1.7×10^{-3} - 2.2×10^{-2}	Nicas (2009)
Mechanical	5	12233	1.7×10^{-3} - 1.3×10^{-2}	Nicas (2009)
Mechanical	5.7	21804	1.4×10^{-3} - 1.5×10^{-2} (4.7×10^{-3})	Nicas (2009)
Mechanical	8.2	8184	1.4×10^{-4} - 1.7×10^{-1} (5.1×10^{-3})	Nicas (2009)
Natural*	—	1064	2.8×10^{-3} - 6.6×10^{-1}	Demou et al. (2009)
Mechanical	15	195	4.0×10^{-2}	Cooper and Horowitz (1986)

Table 6.1: Empirically derived eddy diffusion coefficients for naturally and mechanically ventilated rooms. It is not known whether the air change rates refer to the fresh air rate or the total rate. *The room was naturally ventilated but had a high ventilation rate for a short duration near to the emission source.

Empirical or *a priori* relationships for D_e have been produced for certain situations (Cheng et al., 2011; Drivas et al., 1996; Karlsson et al., 1994).

The Karlsson et al. (1994) relationship is based on a turbulent kinetic energy balance model (TKEB).

$$\frac{\partial\left(\frac{u_{turb}^2}{2}\right)}{\partial t} = \text{Mech} + \text{Buoy} - \text{Diss} + F_4 = 0, \tag{6.9}$$

where the term on the left is the rate of change of turbulent kinetic energy (u_{turb} [m·s^{-1}] is a representative turbulent velocity). There are four terms on the right: Mech represents TKE produced by the air flow, Buoy represents TKE production by buoyancy, Diss is the dissipation of TKE and F_4 is the pressure and transport term. Karlsson et al. integrated Equation 6.9 over the room volume and stated that the volume average of the total rate of change of TKE in the system and F_4 were zero.

This relationship can be simplified to the following for isothermal rooms (Drivas et al., 1996). In this equation the first term is the mechanical production of TKE and the second is the dissipation.

$$\frac{\lambda u_0^2}{2} - \frac{c_\epsilon\, u_{turb}^3}{L_{char}} = 0, \tag{6.10}$$

where u_0 is the velocity at the inlet and c_ϵ is a constant. The dissipation term, as it is written here, is typically thought to apply in high Reynolds number flows with L_{char} referring to the integral length scale, the largest eddies in the flow. Karlsson et al. gave $c_\epsilon = 0.032$. Using Equation 6.11, which gives a relationship between D_e, u_{turb} and L_{char} (also typically referring to the integral length scale), an equation for D_e, as a function of measurable parameters, can be derived (Karlsson et al., 1994; Drivas et al., 1996).

$$D_e = c_v\, u_{turb}\, L_{char}, \tag{6.11}$$

$$D_e = \sqrt[3]{\frac{\lambda\, u_0^2\, c_v^3\, L_{char}^4}{2c_\epsilon}}, \tag{6.12}$$

where c_v is the von Karman constant ($c_v = 0.4$ has been used here). Drivas et al. (1996) did not give Equation 6.12 directly and they also assumed that both c_v and c_ϵ were equal to 0.4 (without providing a rationale).

Shao et al. (2017) demonstrated the validity of the TKEB relationship (Drivas et al., 1996) up to an air change rate of 2.9 h^{-1} for a single bespoke test chamber when they set L_{char} to the room height.

Drivas et al. (1996) and Shao et al. (2017) assumed that L_{char} was equal to H, which, it will be proposed here, should not be the case.

Cheng et al. (2011) gave an empirical relationship for D_e (Equation 6.13), which was based on two naturally ventilated residential rooms with air change rates of up to $5.4\,\mathrm{h}^{-1}$.

$$\frac{D_e}{V^{2/3}} = 0.52\lambda + 8.61 \times 10^{-5}\,\frac{1}{\mathrm{s}}, \tag{6.13}$$

where V is the room volume. Cheng et al. (2011) also considered that D_e might be related to λ alone (i.e. not V), but this approach resulted in a room specific relationship for D_e.

The TKEB relationship follows a $\lambda^{\frac{1}{3}}$ and a $L^{\frac{4}{3}}$ trend whereas the Cheng relationship is a function of λ and L^2. Based on the empirical data in Table 6.1, the Cheng et al. relationship appears not to be suitable for larger spaces. A moderately large indoor space (20 m x 20 m x 4 m high) with $\lambda = 4\,\mathrm{h}^{-1}$ would have $D_e = 0.09\,\mathrm{m}^2{\cdot}\mathrm{s}^{-1}$ according to Equation 6.13. This value would be higher than all but one of the empirical data points given in Table 6.1. If L was set to the room height, a more reasonable value for D_e is produced, $0.01\,\mathrm{m}^2{\cdot}\mathrm{s}^{-1}$. If the TKEB relationship was applied to the same large indoor space with u_0 based on the two example supply grilles used in Foat et al. (2017) ($u_0 = 0.76\,\mathrm{m}{\cdot}\mathrm{s}^{-1}$) and L_{char} equal to the room height. This gives $D_e = 0.55\,\mathrm{m}^2{\cdot}\mathrm{s}^{-1}$, which again looks like an over-prediction based on the data in Table 6.1.

There remains some uncertainty in the application of the Karlsson et al. (1994) TKEB relationship and the Cheng et al. (2011) relationship to rooms with large volumes. There is also a large spread in the available experimentally derived diffusion coefficients. The use of eddy diffusion models to study vapour transport in indoor spaces would benefit from an assessment of the general applicability of different approachs to calculate D_e. This view is supported by both Jayjock et al. (2007) and Nicas (2009).

None of the relationships introduced above include the effect of people (or dog) movement on the eddy diffusion coefficient. The effect of people movement on mixing time (the time taken for a room to become well-mixed) was described by Mora and Gadgil (2002). They showed that mixing times due to movement of single person could be comparable to that from the mechanical ventilation. Mingotti et al. (2020) carried out a series of water tank experiments with a moving cylinder and showed how D_e could be related to the velocity and size of the cylinder and the size of the 'corridor' along which it was moved. They concluded that mixing due to a single person moving along a corridor could be 1 to 10 times higher than mixing from the ventilation alone. Keil (2015) looked into how the movement of a robotic arm close to a vapour affected D_e. He showed how movement and therefore mixing near the source created a more symmetrical diffusion pattern. This meant that is was then possible to use a diffusion model for the dispersion.

People or dog movement effects are not included in the work described here, but it is recommended that they are considered in the future.

The objective of the work in this chapter is to use CFD to calculate D_e in a large number of rooms and to compare these calculated values to those from the relationships discussed previously. This was done in order to determine which, if any, of the relationships are valid over a wide range of room sizes and ventilation conditions.

6.3 Methodology

A novel automated CFD method was used to produce models for scalar transport from an instantaneous release in 250 different isothermal, mechanically ventilated rooms. The eddy diffusion model given in Equation 6.4 was then fitted to the CFD scalar concentration predictions to give a value of D_e for each room. The relationship between the eddy diffusion coefficient and the room geometry and ventilation parameters were then compared to the existing relationships given in Section 6.2.

Before running the automated CFD study the modelling method was developed/validated against an experimental test-case.

6.3.1 CFD validation

The validation experiment was conducted, prior to this PhD research, in 2005 in a meeting room which was 13.0 m long, 7.0 m wide and 2.6 m high with a small cut out in one corner. The room volume was $237\,\mathrm{m}^3$, the floor aspect ratio was 1.9 and H / (floor area)$^{1/2}$ = 0.27. The room had mixing ventilation with the air supplied through eight diffusers and extracted through four. All ceiling diffusers were square, four-way diffusers (effective area of each diffuser = $0.0446\,\mathrm{m}^2$). In the model, the effective air discharge area for the inlet was used, as opposed to the open area to ensure that the correct momentum was applied (Srebric and Chen, 2002). Also in the model, the air was set to enter the room with an angle of 30° to the horizontal. In the experiment, the total air flow rate was $1.0\,\mathrm{m}^3{\cdot}\mathrm{s}^{-1}$ and the recirculation fraction was 0.56, making $\lambda_f = 6.8\,\mathrm{h}^{-1}$ and $\lambda = 15.4\,\mathrm{h}^{-1}$.

A tracer gas was released in the corner of the room (1 m high and 1 m from each wall) through a spherical diffuser (a device designed to reduce the momentum of a jet of gas). The gas was 2 % propylene in nitrogen and $0.04\,\mathrm{m}^3$ of propylene was released at (a nominally) constant rate over a period of 180 s. The gas concentration was monitored in the test room using seven ultra-violet ion counters (UVICs), Mk. II, photo-ionisation detectors (ARID, 2004). Six of the UVICs were 0.65 m above the ground with one at 1.95 m height. Figure 6.1 shows the meeting room and the layout used in the experiment.

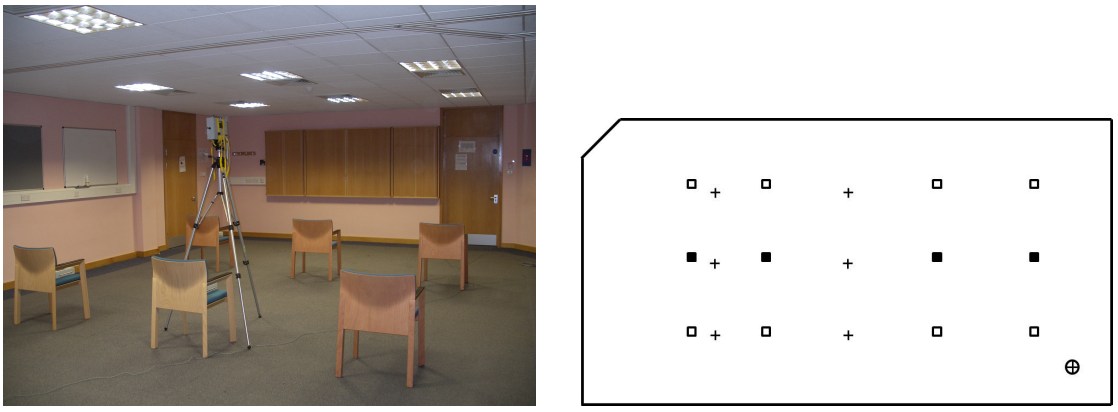

Figure 6.1: The meeting room used for the validation experiment. The photograph show the chairs on which the UVICs were placed and the UVIC at 1.95 m height. The schematic shows a plan view of the layout used in the experiment. The open squares indicate the supply vents, the filled squares the extract vents, the crosses indicate the UVIC locations and the circle with a cross shows the tracer gas release location.

IconCFD version 3.3.9 (ICON[1], United Kingdom) was used[2] to produce a cut-cell mesh for the room (iconHexMesh (ICON, 2017)) and to solve the flow and scalar transport (iconSimpleFoam and iconSpeciesFoam (ICON, 2017)). It was assumed that the flow was steady and turbulent. The supply diffusers were given fixed volume flow rates and the extracts were pressure outlets. All walls were given no-slip boundary conditions. The flow field was solved for 7000 iterations to produce a converged solution. The scalar transport was then solved transiently using the steady-state flow solution. The k-ω SST turbulence model was used and the turbulent Schmidt number, Sc_t, was set to 0.7. The semi-implicit method for pressure linked equations (SIMPLE) scheme (Patankar and Spalding, 1972) was used for the pressure-velocity coupling, a second-order bounded monotonic upwind scheme for conservation laws (MUSCL) scheme[3] (Van Leer, 1979) was used for the momentum transport terms and a first-order upwind scheme was used for all scalar terms. A first-order implicit scheme was used for the transient scalar transport. Previous work has shown that first-order schemes can give reasonable results for indoor air flows, therefore, this was used as a starting condition for the validation modelling. There is a discussion on the use of first-order schemes in Section 6.4.4.

The validation model had a base mesh (refinement level zero) of 0.1 m with the mesh on the supply and extract vents at refinement levels three and two respectively. The mesh on the wall, ceiling and floor was at refinement level one. The non-dimensional distance

[1]The IconCFD software is an open source based CFD product which makes use of openFOAM® technology.

[2]These CFD validation models were run by Joe Drodge (Defence Science and Technology Laboratory (DSTL)) under the instruction of the author using a model template that the author had produced and a procedure they had developed for the initial demonstration of the automated CFD process discussed in Section 6.3.2.1.

[3]The MUSCL scheme is a total variation diminishing (TVD) scheme. A TVD scheme is one where the total variation of the discrete solution should stay constant or diminish with time.

from the wall of the first cell centre, y_1^+, was less than 500 on all walls apart from in the fast flowing air leaving the inlets. The size of the mesh is within the limits for coarse CFD as defined by Wang and Zhai (2012). The mesh on a vertical plane through an extract and two supplies is shown in Figure 6.2. The time step size, Δt, was 1.0 s. The method used to assess the performance of the models is given below. The model was tested for mesh and time step sensitivity. Model sensitivities (to mesh size, Δt and Sc_t) were also considered as part of the automated CFD study (Section 6.3.5).

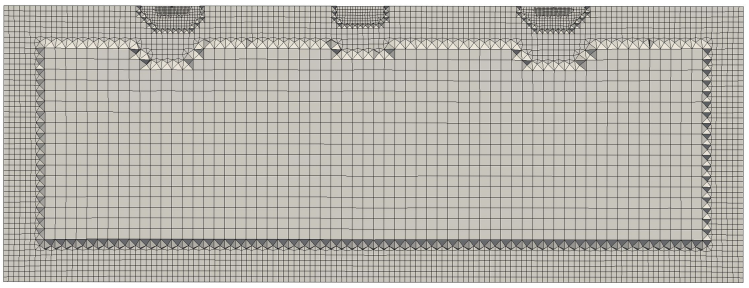

Figure 6.2: The mesh used for the meeting room model shown on a vertical plane through two supply vents and an extract vent. An extract is shown in the middle of the image with supply vents either side.

For the validation, predictions from the model were compared to data at each of the seven UVIC locations and quality metrics were calculated (see below) The minimum, average and maximum concentrations for all the locations are shown in Figure 6.3. It should be noted that the comparison shown in the graph does not directly compare the concentration at one location in the CFD model with the same location in the experiment but represents some statistical characteristics of the concentration field. However, model performance metrics were calculated by comparing data at each corresponding location.

The CFD does not capture some of the unsteadiness in the concentration, as would be expected when using a steady RANS approach. However, the model captures the trends well.

The model performance was assessed by calculating the geometric mean bias (MB) and geometric variance (VG), as defined by Hanna et al. (2004). Data points were included in the assessment when the measured concentration was greater than $1\,\mathrm{mg{\cdot}m^{-3}}$. This was approximately the lowest concentration at which the UVICs were calibrated. The ideal value for both metrics is 1. The MB and VG were used here instead of the FB and NMSE used is Section 3.3.1. This was because the linear measures would be overly influenced by the relatively high and low concentrations measured in the experiment.

MB, which indicates the bias, was 0.95, therefore the model only slightly over-predicted the experiment (by a factor of 1.05, based on the geometric means). VG, which indicates the scatter, was 1.01, therefore the model data was similarly distributed to the experimental data.

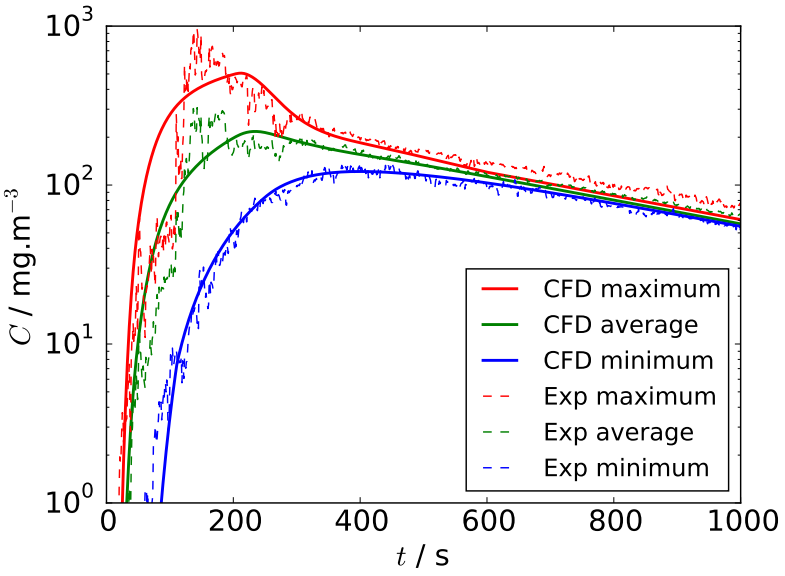

Figure 6.3: Maximum, average and minimum tracer concentrations across seven measurement locations from two experiments compared to predictions from the CFD model.

6.3.2 Scenario for the automated CFD study

The approximately 250 isothermal, mechanically ventilated rooms modelled were all cuboid in shape and contained no furniture. They were served by mixing ventilation with no recirculation, via supply and extract vents (square four-way diffuser) located in the ceiling. The room volume and shape, the air change rate and vent layout were varied across the parameter space shown in Table 6.2.

The automated CFD method used a Sobol sequence experimental design (Sobol, 1967) to produce models which effectively covered the range of the parameters given in Table 6.2. The Sobol sequence is a space filling algorithm which populates the n-dimensional parameter space by selecting the next point from the most sparsely populated region. A schematic diagram of the automated process[4] is shown in Figure 6.4.

[4]The code for the automated CFD tool was written by James Nally (DSTL) around a concept and process that the author developed.

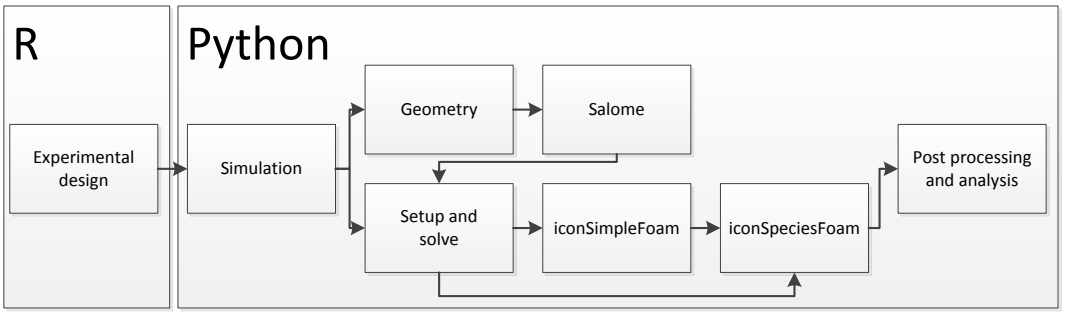

Figure 6.4: Diagrammatic representation of the automated process.

Parameters	Symbol	Ranges
Room volume	V	$50\,\mathrm{m}^3$ - $5000\,\mathrm{m}^3$
Floor aspect ratio	L / W	1 - 3
Height / (floor area)$^{1/2}$	H / $(LW)^{1/2}$	0.1 - 1.5
Air change rate	λ	$0.5\,\mathrm{h}^{-1}$ - $20\,\mathrm{h}^{-1}$
Release location		Centre, corner or mid-point

Table 6.2: Experimental design space. The number of points within each range was determined by Sobol sequence experimental design (Sobol, 1967).

The room height was limited to a minimum of 2.5 m, taken as a lower bound for standard rooms. The floor aspect ratio and height / (floor area)$^{1/2}$ were chosen to represent a broad but realistic range of rooms. The smallest room volume, $50\,\mathrm{m}^3$, could represent a small hotel room or meeting room. The largest volume was set to $5000\,\mathrm{m}^3$ as it was felt that rooms larger than this are more likely to be of a more bespoke design and would not have standard ceiling mounted mixing ventilation. The minimum and maximum air change rates were set to $0.5\,\mathrm{h}^{-1}$ and $20\,\mathrm{h}^{-1}$ to cover a broad range of total air change rates for occupied spaces.

Supply grilles were based on Trox ADT 4-way diffusers (Trox, 2018). A (0.15 m)^2 diffuser, designed for a flow rate of $0.03\,\mathrm{m}^3{\cdot}\mathrm{s}^{-1}$, was chosen for rooms with a total flow rate up to $0.3\,\mathrm{m}^3{\cdot}\mathrm{s}^{-1}$, limiting the number of small diffusers in the room to ten. A (0.375 m)^2 diffuser, designed for a flow rate of $0.16\,\mathrm{m}^3{\cdot}\mathrm{s}^{-1}$, was chosen for rooms with a total flow rate between $0.3\,\mathrm{m}^3{\cdot}\mathrm{s}^{-1}$ and $1.6\,\mathrm{m}^3{\cdot}\mathrm{s}^{-1}$. A (0.6 m)^2 diffuser was specified for rooms with higher flow rates. The number of supply vents in the room was calculated based on the throw and guidance given in Awbi (2003) which states that "the throw should ideally be equal to the distance from a wall or half the distance to the next adjacent diffuser".

Three sizes of extract grille were used: (0.4 m)^2 and (0.6 m)^2 and 0.6 m x 1.2 m. The smallest grilles were used for total room flow rates less than $5\,\mathrm{m}^3{\cdot}\mathrm{s}^{-1}$, the middle size

was specified for flow rates between $5\,m^3{\cdot}s^{-1}$ and $10\,m^3{\cdot}s^{-1}$ and the largest size for flows above $10\,m^3{\cdot}s^{-1}$. The number of vents was chosen so that the mean velocity through the grille was approximately $4\,m{\cdot}s^{-1}$ (ASHRAE, 2001).

Supply and extract vents were distributed across the ceiling in rows with a row of extracts between rows of supplies. The total number of supply and extract rows was determined based on the width of the room as set out in Table 6.3.

Width lower /m	Width upper /m	Number of rows
0	12.5	3
12.5	25.0	5
25.0	42.5	7
42.5	>42.5	9

Table 6.3: Limits for determining the total number of vent rows (supply + extract) within a room.

The rows were uniformly spaced across the room and vents were uniformly spaced in each row. Cases were not considered if the ratio of number of extracts to number of supplies was less than 0.1. Six example room plan views are shown in Figure 6.5.

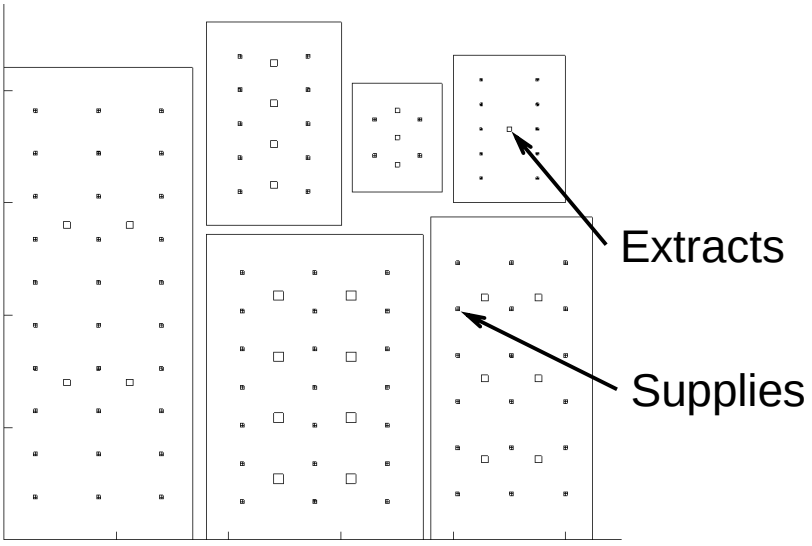

Figure 6.5: Plan views of six example rooms showing the supply and extract vent layouts. The supply vents are shaded, the extracts are open squares. The tick marks on the axes are spaced at 10 m intervals.

The scenario modelled was an instantaneous release of material from one of three locations: the centre of the room (centred in length, width and height), one corner of the room (1 m in from both walls and centred in height), mid-point (mid-way between the centre of the room and one corner and centred in height).

6.3.2.1 Initial demonstration of the automation process

Before being used for the eddy diffusion modelling study, the power of the new automation process was demonstrated by studying pollutant mixing times in a similar set of mechanically ventilated, isothermal rooms, but with the pollutant entering the room via the ventilation system supply vents. Full details of this work are given in Foat et al. (2017).

In this initial study, three analytical mixing time models, including a novel jet transit based approach, were selected for comparison with CFD predictions in a range of cuboidal rooms. The jet transit approach to pollutant mixing times uses the time it takes for a jet of air to move from a ceiling diffuser to a horizontal plane of interest in the room. The two other mixing models were the mechanical power model of Drescher et al. (1995) and a simple characteristic time model where the characteristic time, $\tau = 1 / \lambda$. Three different mixing time metrics were calculated from the CFD for comparison with the analytical models, one of the metric, t_{95-5}, is described below.

If the range of concentrations within the room is described by a distribution, then a useful measure of mixing is given by the difference between the time when only the highest concentrations (the 95th percentile value) have crossed a threshold concentration and when all but the lowest (the 5th percentile value) have. This time is referred to as t_{95-5} [s] and is indicative of the time between the first people and the last people in a room being exposed to a threshold concentration. The threshold was a function of the maximum concentration reached in a well-mixed model of the same room.

For this study the pollutant was released into each room via the ventilation system for a short duration and the release mass was calculated as a function of a single toxic threshold. The CFD method was validated using a similar trial data set to that described in Section 6.3.1 but with tracer entering the room via the ventilation system. The results of the validation are shown in Figure E.1 in Appendix E.

The results of the study showed that the mixing time metrics, t_{95-5}, was best represented by the characteristic time model and the relation is given by Equation 6.14.

$$t_{95-5} = 0.121\tau \tag{6.14}$$

The key graphs from this study are shown in Figure E.2 in Appendix E.

6.3.3 Automated CFD method

Salome V6.5.0 (Open Cascade, France), an open source integration platform for numerical simulation, was used to generate the STL surfaces of the geometries. IconCFD V3.3.9 (ICON, United Kingdom) was used for the meshing (iconHexMesh (ICON, 2017))

and the CFD solutions (iconSimpleFoam and iconSpeciesFoam (ICON, 2017)). The automated CFD used the same model settings and meshing approach as applied in the validation modelling (see Section 6.3.1). This included a second-order MUSCL scheme for the momentum transport terms, a first-order upwind scheme for all scalar terms and a first-order implicit scheme for the transient scalar transport. The first-order schemes were chosen as these had been shown to give accurate results in the validation modelling and to improve convergence in the automated study

6.3.4 Fitting the eddy diffusion model to the CFD data

The eddy diffusion model, Equation 6.4 (with five image sources), was fitted to the CFD data by minimising VG, to a value of 1, by varying D_e.

For each CFD model the optimum eddy diffusion coefficient was calculated independently over three planes at heights of 0.5 m, 1.0 m and 1.5 m. These planes were chosen to cover the occupied zone. On each plane, data from 20 locations was used at times with 10 s intervals up to 1500 s after the start of the release. It was confirmed that the results did not change significantly with an increase in the number of locations used or a decrease in the size of the time intervals. Any location within 2 m of the release location was not included, as close to the source the concentration field was more strongly affected by local flow features. Any data point with a concentration below $1 \times 10^{-20}\,\mathrm{kg{\cdot}m^{-3}}$ was excluded to avoid the VG calculations being skewed by large differences between the CFD and eddy diffusion models at these very low values. A single VG value was calculated for each plane for each CFD model i.e. it incorporated equally weighted data from all locations on that plane and all time points.

The model fitting was performed using a Python script[5], the SciPy optimize.minimize function and the L-BFGS-B algorithm (Byrd et al., 1995).

A subset of the automated models were used to test the sensitivity of the D_e calculations to the mesh, time step and Sc_t.

The input data from the automated CFD study together with the D_e values for the fitted eddy diffusion model are given in the supplementary material for Foat et al. (2020).

An improvement to the three planes approach used here would be to use a sub-set of data from across the entire CFD domain. This would be particularly beneficial for tall rooms, as with the current approach, any changes in the eddy diffusion coefficient above 1.5 m are not being captured directly.

[5]The code I developed to fit the eddy diffusion model to the output from the automated CFD, was optimised by Joe Drodge (DSTL).

6.3.5 Mesh, time step and turbulent Schmidt number sensitivity

A subset (10) of the 250 CFD models were re-run with three different base mesh sizes (0.079 m, 0.100 m, 0.126 m), three Δt values (0.5 s, 1.0 s, 2.0 s) and three Sc_t values (0.5, 0.7, 0.9) with D_e calculated for each model. MB was calculated for the predicted D_e for each parameter change, with the original model as a reference. The results of the sensitivity study are given in Table 6.4.

Fixed parameters	Compared parameters	MB
$Sc_t = 0.7$, Mesh = 0.1 m	$\Delta t = 2.0$ s vs. 1.0 s	1.06
	$\Delta t = 0.5$ s vs. 1.0 s	1.24
$Sc_t = 0.7$, $\Delta t = 1.0$ s	Mesh = 0.126 vs 0.100 m	1.11
	Mesh = 0.079 vs. 0.100 m	1.02
$\Delta t = 1.0$ s, Mesh = 0.1 m,	$Sc_t = 0.9$ vs. 0.7	1.07
	$Sc_t = 0.5$ vs. 0.7	0.94

Table 6.4: Results of the CFD model sensitivity test.

With a base mesh size of 0.1 m the MB for D_e with $\Delta t = 2.0$ s compared to $\Delta t = 1.0$ s was 1.06, i.e. the geometric mean D_e for $\Delta t = 1.0$ s was 106 % of that for $\Delta t = 2.0$ s. For $\Delta t = 0.5$ s compared to $\Delta t = 1.0$ s, MB was 1.24, i.e. the geometric mean D_e for $\Delta t = 1.0$ s was 124 % of that for $\Delta t = 0.5$ s. Therefore, the results did show some time step dependence but due to the spread in the calculated D_e values (almost two orders of magnitude) and the quality of the validation shown previously (where Δt of 1.0 s was used), a Δt of 1.0 s was deemed acceptable for the automated study. There was also a mesh size dependence but this was small between the 0.1 m and 0.079 m meshes. Therefore, the 0.1 m base mesh was deemed acceptable for the automated study. The geometric mean D_e decreased as Sc_t increased, as would be expected. A range of value for Sc_t has been used in different studies, such as 0.2 to 1.3 reported by Tominaga and Stathopoulos (2007). However, $Sc_t = 0.7$ has a wide applicability (van Hooff et al., 2014) and was used successfully in the validation exercise, therefore, this was deemed the most suitable value for the automated study.

6.4 Results and discussion

The results from fitting the eddy diffusion model to the automated CFD data are given in the following figures. Initially only data for the centre release location is shown. Figure 6.6 shows four possible methods for the eddy diffusion coefficient. The four methods are: a simple correlation of D_e with the air change rate, λ, the Cheng et al. (2011) empirical relationship (Equation 6.13) and the TKEB relationship (Equation 6.12) with two different definitions of the characteristic length, L_{char}. For each method

a linear regression line (least squares), with an intercept of zero, has been fitted with the equation of the line and the coefficient of determination, R^2, value shown. R^2 was calculated according to Eisenhauer (2003).

As shown at the start of the chapter the characteristic length scale, L_{char}, in the TKEB relationship is used in both the dissipation rate term in Equation 6.10 and in Equation 6.11. In both cases it is usually assumed to refer to the integral length scale. The integral length scale in a room could be a function of the dimensions of the inlet and the jet of air produced there, or the dimensions of the room. If L_{char} was related to H then, according to Equation 6.12, taller rooms will tend to have higher values of D_e which seems counter-intuitive. In a taller room more of the mixing energy introduced at ceiling mounted inlets would have been dissipated by the time the air reaches the occupied zone. Therefore, it is proposed here that it should be related to the inlet when being used to calculate the eddy diffusion coefficient. To assess which is the best definition for L_{char}, results have been plotted for the TKEB relationship with L_{char} equal to the room height or the square root of the inlet area, A.

If L_{char} is set to the square root of A, then Equation 6.12 can be simplified to Equation 6.15.

$$D_e = c_{TKEB} \frac{Q}{\sqrt[3]{V\,N^2}}, \tag{6.15}$$

where c_{TKEB} is a constant which equals $(c_v \sqrt[3]{1/2c_\epsilon})$, Q is the total volume flow rate into the room and N is the number of supply vents. For the values of c_v and c_ϵ used in this work, $c_{TKEB} = 1$.

From the results shown in Figure 6.6, the best method for calculating D_e, based on R^2, is the TKEB relationship with the characteristic length set to $\sqrt{A}$, where $R^2 = 0.957$. The TKEB relationship with $L_{char} = H$ performs significantly worse with an R^2 of 0.825. Shao et al. (2017) used the TKEB relationship with $L_{char} = H$ and got only a small over-prediction compared to their experimental data. The small difference is possibly due to the low height of their room (2 m) and relatively large effective inlet area ($0.232\,m^2$).

The Cheng et al. (2011) relationship shows a small R^2 value (0.836), meaning that their relationship does not apply well to this data set. However, the rooms examined by Cheng et al. were naturally ventilated through open windows, whereas the rooms modelled here were mechanically ventilated with ceiling located supply and extract.

The air change rate relationship performs reasonably well with $R^2 = 0.929$, but there is a large spread of data at higher air change rates. A spread of the same extent is not present with the TKEB $\sqrt{A}$ relationship.

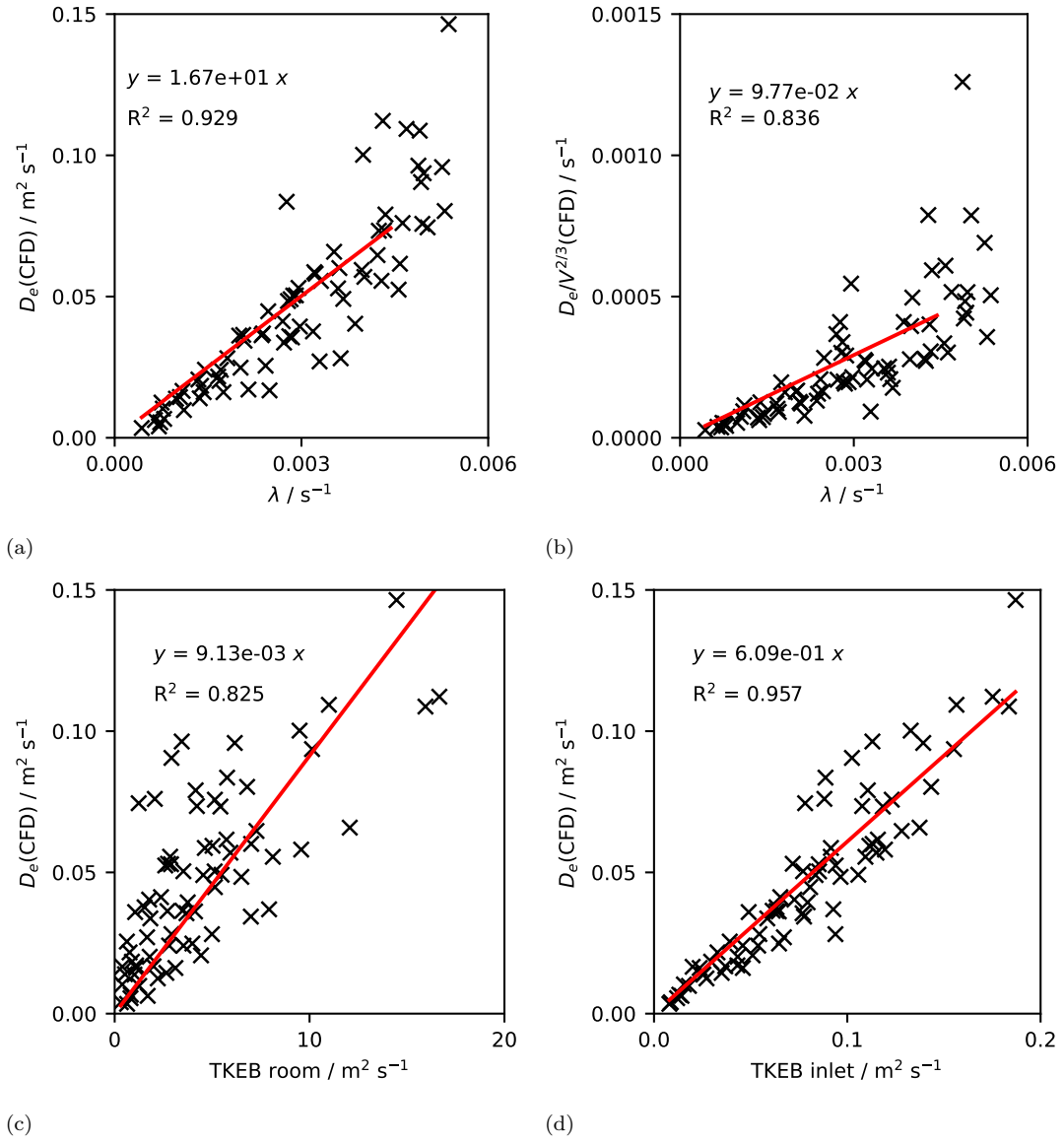

Figure 6.6: D_e or $D_e/V^{2/3}$, calculated from the CFD data, plotted against four possible methods: the ACR (a), the Cheng et al. (2011) relationship (b), the TKEB relationship with $L_{char} = H$ (c) and the TKEB relationship with $L_{char} = \sqrt{A}$ (d). The red line shows the linear regression line. Only data for the releases in the centre on the room is shown here.

6.4.1 Effect of release location and plane height

As stated previously, D_e was calculated by fitting the eddy diffusion model (Equation 6.4) independently over three planes at heights of 0.5 m, 1.0 m and 1.5 m. MB was calculated between the data for the planes at 1.5 m and 1.0 m and for the planes at 0.5 m and 1.0 m. For the planes at 1.5 m and 1.0 m, MB was 1.00. For the planes at 0.5 m and 1.0 m, MB was 0.95. Therefore, there was only a small decrease in D_e nearer to the floor.

The data from the three release locations: centre, mid-point and corner, is shown in Fig. 6.7. The steepest gradient of the linear regression line is for the releases in the corner of the room (1.15) and the shallowest is for releases in the centre of the room (0.61). The gradient for releases at the mid-point is slightly larger than that for centre releases.

The CFD derived diffusion coefficients for the corner releases compared to other release locations are most likely higher due to the type of ventilation used in the rooms. The square four-way diffusers on the ceiling produce jets which attach to the ceiling and then move down adjacent walls. Jets can also be forced downward where jets from two adjacent diffusers meet (Foat et al., 2017). This means that air flow close to walls or inter-diffuser boundaries (at the horizontal planes considered here) should be faster than flows at other locations. As the corner releases are always located close to a wall then they should always experience the higher air flow from the diffuser jet. It is assumed that the faster mixing for corner releases is caused by this effect.

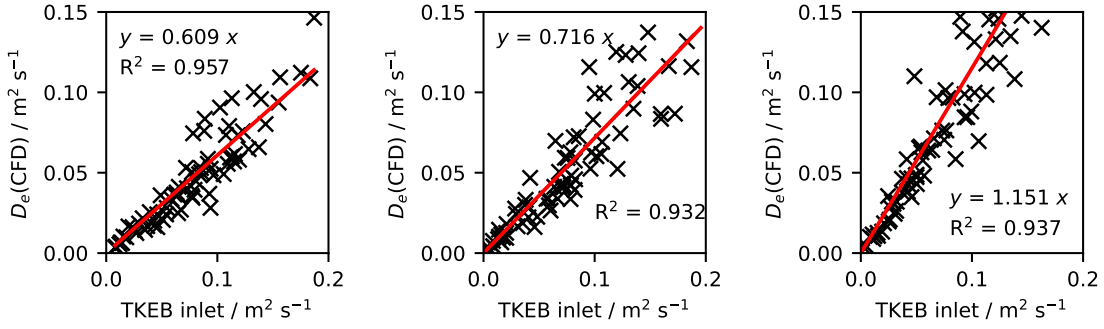

Figure 6.7: D_e, calculated from the CFD, plotted against the TKEB relationship, using Equation 6.15, for the three release locations: centre (left), mid-point (middle) and corner (right). The red line shows the linear regression line.

6.4.2 All data combined

CFD derived diffusion coefficients for every release location are plotted in Figure 6.8 along with the linear regression line, 95 % confidence intervals (CI) and prediction intervals (PI). The equation for the regression line is also shown.

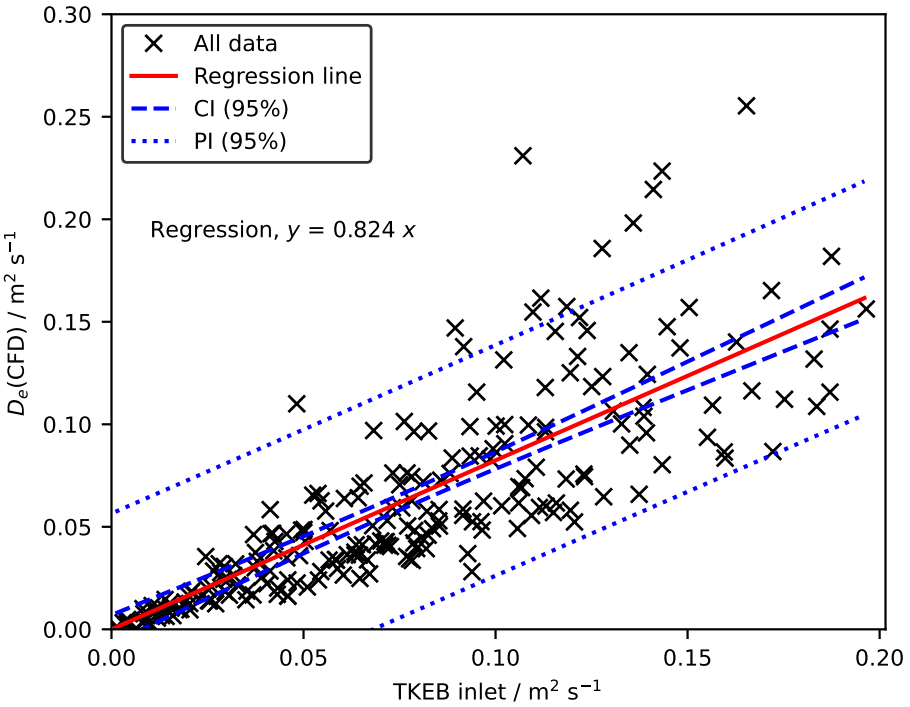

Figure 6.8: D_e, calculated from the CFD, plotted against the TKEB relationship, using Equation 6.15, for all release locations.

The equation for the linear regression line, which describes the TKEB relationship using $\sqrt{A}$ as the characteristic length, is given below. Straight line approximations to the upper and lower prediction interval lines are also given.

$$D_e(\text{upper PI}) = 0.827\frac{Q}{\sqrt[3]{V\,N^2}} + 0.0565\,\frac{\text{m}^2}{\text{s}}, \tag{6.16}$$

$$D_e(\text{regression}) = 0.824\frac{Q}{\sqrt[3]{V\,N^2}}, \tag{6.17}$$

$$D_e(\text{lower PI}) = 0.822\frac{Q}{\sqrt[3]{V\,N^2}} - 0.0565\,\frac{\text{m}^2}{\text{s}}. \tag{6.18}$$

The linear regression line equation shows that, based on the CFD data used here, a constant equal to 0.824 should be applied to the simplified TKEB relationship given in Equation 6.15. It is proposed that Equation 6.17 can be used to calculate D_e for use in an eddy diffusion model when only Q, V and N are known. Due to the spread of CFD derived diffusion coefficients around the regression line, Equations 6.16 and 6.18 can be used to calculate a possible range of value for D_e. As it has been suggested (Drivas et al., 1996) that the lower limit for D_e is $0.001\,\text{m}^2{\cdot}\text{s}^{-1}$ this bound should be applied when using these equation. In Section 6.4.3 the validity of using this approach is demonstrated through comparisons with experimental data.

To understand the error between the fitted eddy diffusion model and the CFD predictions, VG is plotted against D_e in Fig. 6.9 for the plane at 1 m.

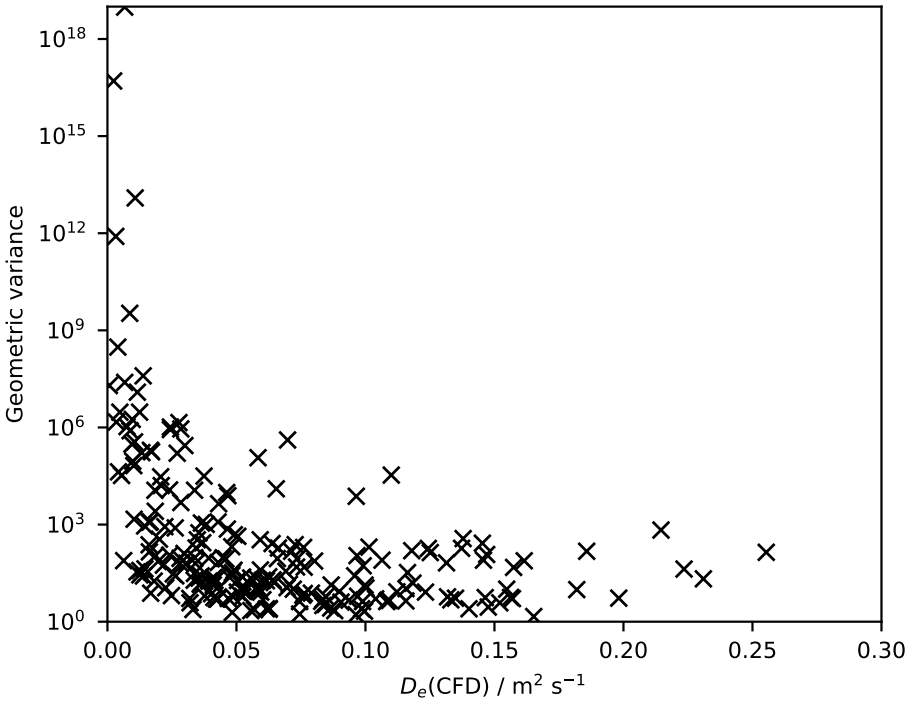

Figure 6.9: Geometric variance between each fitted diffusion model and the CFD concentration data.

Figure 6.9 shows that VG can be large, so the concentrations predicted by the fitted diffusion model can be widely scattered around the CFD data. This scatter increases as D_e decreases. For D_e <0.01 m^2·s^{-1}, VG is greater than 1000 in most cases. A VG of 1000 indicates a factor of 14 scatter (i.e. the predictions are on average a factor of 14 bigger or smaller than the observations). For D_e >0.05 m^2·s^{-1}, VG is less than 100 (indicating a factor of nine scatter) in 79 % of cases and less than 10 in 46 % of cases.

It should be noted that eddy diffusion models can be less accurate close to the source at short times, when the non-dimensional diffusion time, t_{ND}, is small (L_{diff} here is the distance from the source). Close to the source the concentration field will be more affected by local flow features, which eddy diffusion models are not designed to predict. When t_{ND} is small, a small error in the model can have a large effect on the concentration. The poor model performance when t_{ND} is small explains why VG tends to increase as D_e decreases in Fig. 6.9 (all models were run for 1500 s). Running the models that have smaller values of D_e (e.g. models with low air change rates) for longer should reduce VG.

The data from the eddy diffusion coefficient parameterisation is available as supplementary data with the paper by Foat et al. (2020).

6.4.3 Comparison with experimental and high-resolution model data

The TKEB relationship using $\sqrt{A}$ as the characteristic length has been compared to experimental and high-resolution model data using two methods. Firstly, the experimentally derived eddy diffusion coefficients of Cheng et al. (2011) and Shao et al. (2017) have been compared to the CFD derived coefficients and the TKEB relationship. Secondly, an eddy diffusion model, with D_e calculated using the TKEB relationship, has been used to predict gas concentrations in a number of scenarios and results have been compared to experimental or LES data.

6.4.3.1 Comparison with experimentally derived eddy diffusion coefficients

Cheng et al. (2011) conducted indoor dispersion experiments in two naturally ventilated residential rooms. They used a continuous gas release, measured concentrations at 30 or 37 locations and then averaged concentrations both temporally and radially. Ventilation of the building was via windows, which were opened by different amounts for each experiment. Shao et al. (2017) conducted a number of experiments in a bespoke test chamber. They used a continuous gas release and measured concentrations at two locations. The air was supplied to their room via a filter bank onto which four air diffusers were fitted. From both of these sets of experiments the authors calculated eddy diffusion coefficients.

In order to compare the data of Cheng et al. (2011) and Shao et al. (2017) to the TKEB relationship (Equation 6.17), Q, V and N are required. In both cases Q was calculated from the provided values for λ and V. V was used as provided, however, it is possible that a larger value for V could have been used with the Cheng et al. data as more than just a single room was being ventilated. N was set to 1 for the Shao et al. data and to 2 for the Cheng et al. data. In the Cheng et al. experiments, three windows were open, but it was assumed here that one of these was acting as an outflow. Therefore there is uncertainty in Q, V and N for the Cheng et al. experiments.

The eddy diffusion coefficients from Cheng et al. (2011) and Shao et al. (2017) are plotted alongside the CFD derived diffusion coefficients (from the automated CFD study) in Figure 6.10. The linear regression line from the CFD data, Equation 6.17, is also shown.

The experimental data in Figure 6.10 sits close to, or just above, the linear regression line. The Cheng et al. (2011) data generally follows the trend of the CFD data, the Shao et al. (2017) data deviates further from the linear regression line as D_e increases. This supports the validity of the TKEB relationship with $L_{char} = \sqrt{A}$ (Equation 6.17), but shows that for the set up used in the Shao et al. experiments, a steeper gradient may be more suitable. However, all the Shao et al. measured diffusion coefficients are, on average, within a factor of 2.0 of the values calculated by Equation 6.17. The Cheng

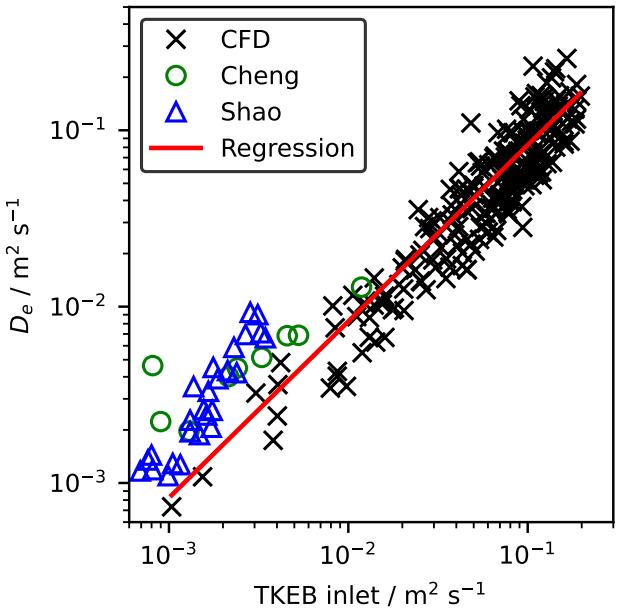

Figure 6.10: D_e plotted against the TKEB relationship with $L_{char} = \sqrt{A}$. Data from the CFD models and two experimental data sets are shown.

et al. data is on average within a factor of 2.1 of the regression line. Therefore, despite the different type of ventilation, the relationship derived from the CFD data provides a useful method to estimate D_e in naturally ventilated spaces.

It should be noted that Q, V and N for the experimental data could be different to the values chosen here and different values may affect the correlation of this data with the CFD derived model. It is also recognised that when applying the TKEB model, there may be some uncertainty over the values for Q, V and N in non-mechanically ventilated spaces.

6.4.3.2 Comparison with concentration time histories

An eddy diffusion model, with D_e calculated using the TKEB relationship, was used to predict gas concentrations in three scenarios, with the results compared with experimental or LES data. The first scenario was the same meeting room experiment as used in the CFD validation in Section 6.3.1. Although this experiment was used to validate the CFD methodology, the room was not used in the automated CFD study. The second scenario was an assembly hall, see Figure 6.11. The third was the LES model of the Nielsen (1990) test-case used in Chapter 3.

The assembly hall was approximately 1400 m^3 (maximum length, width and height of 29 m, 13 m, 5 m) and had a fresh air change rate, λ_f, of 3.8 h^{-1}, with no recirculation of air through the ventilation system. 14 slot type diffusers were located along the ceiling

and the four extract grilles were on one wall. The supply vents directed the air straight down into the hall. A section of the hall (on the right in the schematic in Figure 6.11) had a low ceiling and was poorly ventilated. It should be noted that more air was being extracted from the hall through the extract vents than was being supplied through the supply vents ($3.8\,\mathrm{h}^{-1}$ vs. $2.0\,\mathrm{h}^{-1}$). This means that air was also leaking into the room through other routes. For the purposes of the TKEB relationship, Q was set to the larger of the flow rates and N was set to the number of supply vents, as this is where bulk of the air entered the room.

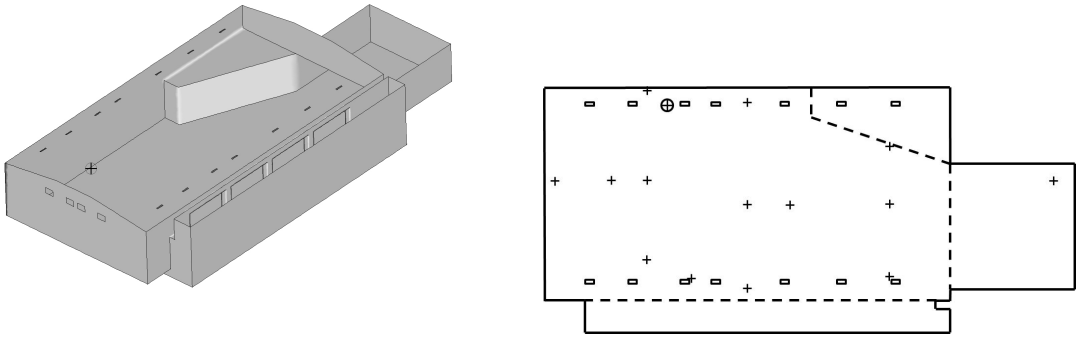

Figure 6.11: A CAD drawing of the assembly hall (left). A schematic showing the layout used in the experiment (right). The open rectangles indicate the supply vents, the crosses indicate the UVIC locations and the circle with a cross shows the tracer gas release location. The dashed lines indicate different sections of the room.

In the assembly hall experiment the tracer gas, propylene, was released on one side of the room as shown in Figure 6.11. $0.04\,\mathrm{m}^3$ of gas was released over approximately 20 s and the gas concentrations were monitored using 20 UVICs, which were positioned at a range of heights across the room.

An eddy diffusion model was used to predict the tracer gas transport from the two experiments. Both experiments had a gas release with a constant rate, $\dot{M}$ for a defined duration, t_{end}, so an eddy diffusion model was required which could represent this type of scenario.

A model for a release with an infinite duration, was used by Cheng et al. (2011) and Shao et al. (2017). This is reproduced below (Equation 6.19) making the dependence on t explicit.

$$C_{cont}(t) = \int_0^t \frac{\dot{M}\ \exp(-\lambda_f\ t)}{8(\pi\ D_e\ t)^{\frac{3}{2}}} r_x(t) r_y(t) r_z(t)\ dt \tag{6.19}$$

where C_{cont} is the concentration from a continuous release. Using Equation 6.19 as the basis and taking advantage of the superposition principle for linear systems, a solution for the concentration due to a finite duration release, C_{finite}, has been produced in Equation 6.20. This equation was solved using the mathmatics software tool Mathcad

V15.0 (Parametric Technology Corporation).

$$C_{finite}(t) = \begin{cases} C_{cont}(t) & (t \leq t_{end}) \\ C_{cont}(t) - C_{cont}(t - t_{end}) & (t > t_{end}) \end{cases} \tag{6.20}$$

The maximum, average and minimum concentrations for all monitoring locations are shown for both the model and the experiments in Figures[6] 6.12 and 6.13. For the meeting room the maximum, average and minimum concentrations were taken from seven monitors, for the assembly hall it was 20.

Eddy diffusion models were run using D_e calculated from the linear regression line for the TKEB relationship (Equation 6.17). Error metrics for the eddy diffusions models, calculated when the measured concentration was greater than $1\,\mathrm{mg{\cdot}m^{-3}}$, are reported in Tables 6.5 and 6.6. It should be noted that error metrics were calculated from data at all the monitor locations, not just for the maximum, average and minimum data shown in Figures 6.12 and 6.13. VG and MB are reported along with the fraction of concentration predictions within a factor of two of the measurements, FAC2 (Hanna et al., 2004), and the fraction of concentration predictions within a factor of five of the measurements, fraction of points within a factor of five (FAC5). A single-zone well-mixed model (Reinke and Keil, 2009) was also built of both scenarios for comparison.

In both scenarios the eddy diffusion model performed reasonably well. In the meeting room, more than 80 % of data points were within a factor of two of the experimental data. In the assembly hall, the model performance was lower, but still more than 88 % of data points were within a factor of five of the experimental data. The lowest concentrations in the assembly hall were under-predicted quite significantly at early times. This has resulted in a large geometric variance.

According to the error metrics, a better fit was achieved for both scenarios by using the upper 95 % PI equation to calculate D_e. The improved fit is also evident in the graph for the meeting room. In the assembly hall, however, the model's poor prediction of the lower concentrations has perhaps skewed the results when D_e was calculated using the linear regression equation. When using the upper 95 % PI equation the lower concentration predictions have improved but the predictions for the higher concentrations (as illustrated by the maximum and average curves) are worse.

[6]The graphs in figures 6.12 and 6.13 were plotted by Joe Drodge (DSTL) using eddy diffusion model data provided by the author. Joe also calculated the error metrics in Tables 6.5 and 6.6 using the same data.

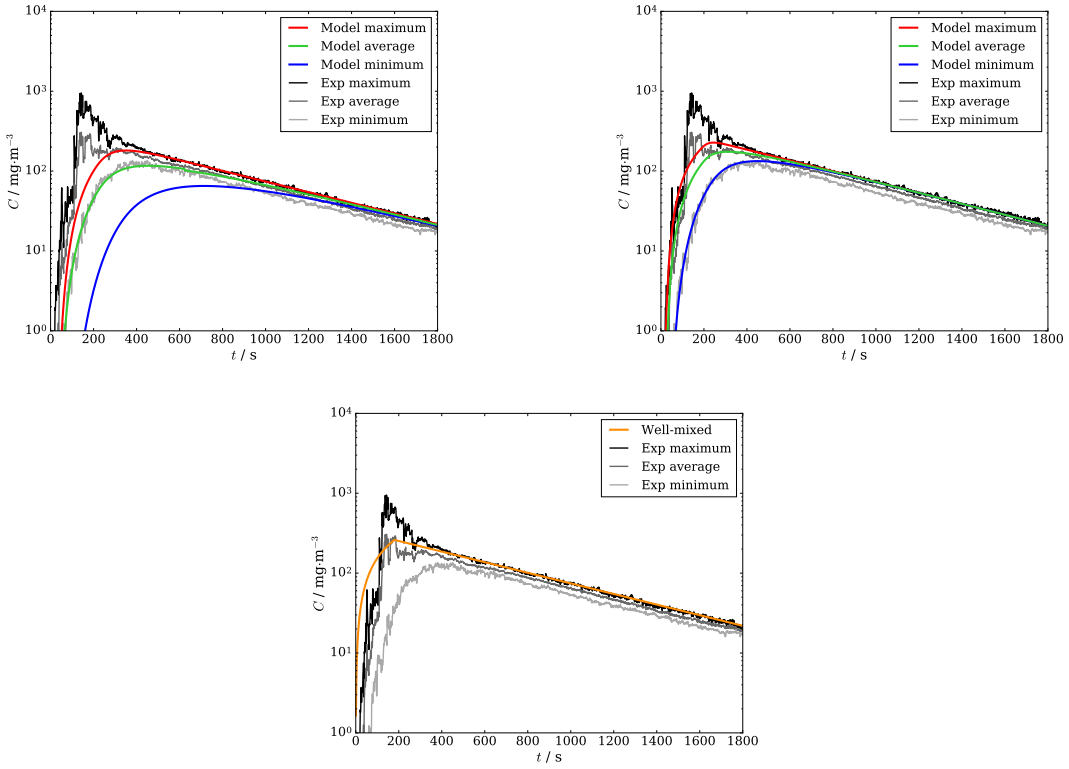

Figure 6.12: Maximum, average and minimum tracer concentrations in a meeting room compared to predictions from an eddy diffusion model and a well-mixed model. Calculating D_e using the linear regression line for the TKEB relationship, Equation 6.17 (upper left) and the upper 95 % PI for the TKEB relationship, Equation 6.16 (upper right). The results from a well-mixed model are shown (lower).

Model	TKEB eq.	D_e /m^2·s^{-1}	MB	VG	FAC2	FAC5
Eddy diffusion	Regression	0.033	1.50	4.10	0.80	0.90
Eddy diffusion	Upper PI	0.090	0.92	1.13	0.96	0.99
Well-mixed	–	–	0.73	1.64	0.89	0.95

Table 6.5: Error metrics for eddy diffusion and well-mixed model concentration predictions compared to experimental data for the meeting room scenario. The first column gives the transport model used, the second gives the TKEB equation or method used to calculate D_e.

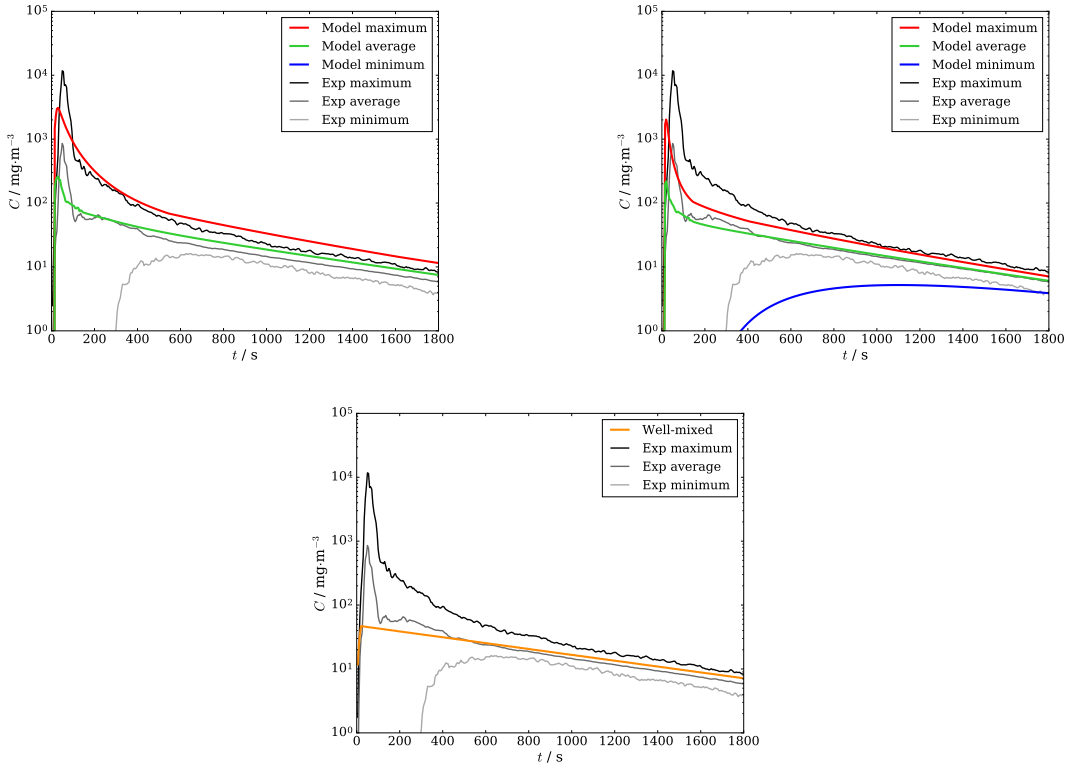

Figure 6.13: Maximum, average and minimum tracer concentrations in an assembly hall compared to predictions from an eddy diffusion model and a well-mixed model. Calculating D_e using the linear regression line for the TKEB relationship, Equation 6.17 (upper left) and the upper 95 % PI for the TKEB relationship, Equation 6.16 (upper right). The results from a well-mixed model are shown (lower).

Model	TKEB eq.	D_e /m^2·s^{-1}	MB	VG	FAC2	FAC5
Eddy diffusion	Regression	0.019	1.49	6644	0.65	0.88
Eddy diffusion	Upper PI	0.076	0.99	1.79	0.88	0.96
Well-mixed	–	–	0.88	1.46	0.89	0.97

Table 6.6: Error metrics for eddy diffusion and well-mixed model concentration predictions compared to experimental data for the assembly hall scenario. The first column gives the transport model used, the second gives the TKEB equation or method used to calculate D_e.

The faster mixing in the assembly hall compared to that given by the linear regression line relationship (i.e. as illustrated by the under-prediction of the lower concentrations) may be due to the type of supply vents present. These were slot vents which directed the air down into the room, as opposed to the four-way diffusers in the automated study (from which the linear regression relationship was derived), which directed the air along the ceiling. This could mean that more of the turbulent kinetic energy generated at the

inlet makes it into the lower parts of the room. In the meeting room experiment, the release was in the corner of the room so faster mixing would be expected (compared to the linear regression relationship), as discussed in Section 6.4.1.

The well-mixed model has performed well in comparison with the eddy diffusion models for both scenarios according to the error metrics. This is partly due to the type of tracer release used in both experiments. As a finite duration release was used in both scenarios the concentrations in the room tends towards a well-mixed condition with increasing time. However, it is clear in Figures 6.12 and 6.13 how a well-mixed modelling approach is not suitable for predicting concentrations at early times.

This comparison with the concentration time histories showed that the eddy diffusion model can perform well but the quality of the model is strongly dependent on the eddy diffusion coefficient, as would be expected. The TKEB relationship can be used to calculate the eddy diffusion coefficient, but a small error in D_e can have a large effect on the lowest concentrations in the room.

An eddy diffusion model will have particular utility when there is a continuous release in a ventilated room. Under this condition a concentration gradient will always exist in the space so the difference between the two modelling approaches should be larger. This type of scenario can be relevant to the study of longer term exposure to toxic material or the transport of vapour from explosives for detection purposes.

Another scenario where eddy diffusion models will have merit over well-mixed models is when the user is interested in concentrations or exposures soon after an instantaneous or short duration release, before the room becomes mixed. This period is often of interest when considering health effects from an overt release of a toxic material, as people are likely to evacuate the space by later times. However, as discussed in Section 6.4.2, care should be taken when applying an eddy diffusion model close to the source at short times. This is because close to the source the concentration field will be more affected by local flow features, which eddy diffusion models are not designed to predict.

To demonstrate how an eddy diffusion model performs when used to represent a continuous release, data from the LES model of the Nielsen (1990) test room, as described in Chapter 3, was used.

The data was for an explosive on the floor of the room and the LES model results had shown that this could be approximated to a constant release source. The release rate, $\dot{M}$, was taken directly from the CFD (Table 3.2) but could also be calculated using Equation 3.5 if the local friction velocity was known, or Equation 4.4 if u_τ was below the threshold given by Equation 4.5. The eddy diffusion coefficient was calculated using Equation 6.17, this gave $D_e = 0.044\,\mathrm{m^2{\cdot}s^{-1}}$.

The concentrations in the CFD and eddy diffusion model were calculated for the steady-state condition. The diffusion model for a continuous and constant release is given by Equation 6.19.

Normalised time-averaged concentrations predictions ($\bar{c}/c_0$) are shown along a vertical line from the centre of the source and from a horizontal line running along the mid-width of the domain at a height of 0.5 m.

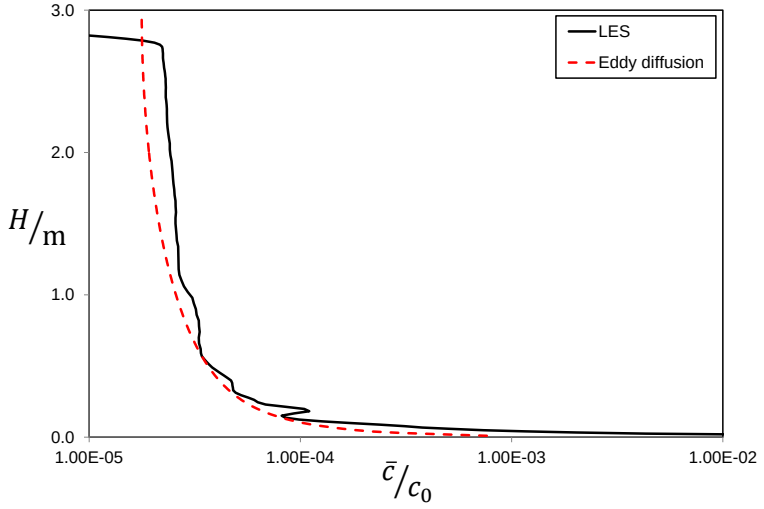

Figure 6.14: LES and eddy diffusion model predictions of normalised concentration on a vertical line from the centre of the source. Concentrations are plotted on a logarithmic scale.

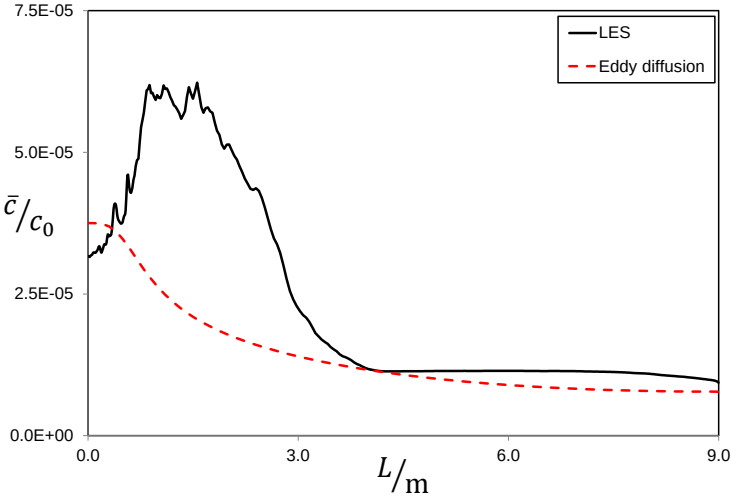

Figure 6.15: LES and eddy diffusion model predictions of normalised concentration on a horizontal line running along the mid-width of the domain at a height of 0.5 m. Concentrations are plotted on a linear scale.

The eddy diffusion model has performed very well in comparison to the LES model. In particular it has predicted a very similar vertical concentration profile. Even on the horizontal line, where the comparison is not as good, the eddy diffusion model still predicts the correct trend in the data and under-predicts the peak concentration by a factor of only 1.7. The linear regression line for the TKEB relationship has given a suitable eddy diffusion coefficient in this case.

The same comparison between the eddy diffusion model and the LES model was carried out for air change rates of $5\,\mathrm{h}^{-1}$ ($D_e = 0.021\,\mathrm{m}^2{\cdot}\mathrm{s}^{-1}$) and $0.5\,\mathrm{h}^{-1}$ ($D_e = 0.0021\,\mathrm{m}^2{\cdot}\mathrm{s}^{-1}$). The eddy diffusion model performed similarly well with the $5\,\mathrm{h}^{-1}$ case but performed badly with the $0.5\,\mathrm{h}^{-1}$ case. Better correlation with the $0.5\,\mathrm{h}^{-1}$ case close to the source was achieved when the molecular diffusion coefficient was used in place of the TKEB calculated eddy diffusion coefficient.

6.4.4 Discussion

The validity of the TKEB relationship has been demonstrated using an automated CFD modelling approach. The scenarios studied consisted of only a small subset of possible indoor environments. The rooms were isothermal, had mixing ventilation, were cuboidal in shape and contained no furniture. However, through comparison with experimental data generated in other types of rooms, broader applicability of the relationship has been shown. Other features that have not been considered here include the mixing induced by movement of people or machinery and strong sources of buoyancy. It should also be noted that the eddy diffusion method in general is only applicable when there is isotropic mixing on a large scale due to laminar and/or turbulent motion.

It should be noted that first-order upwind schemes were used for discretisation of all scalar terms in the CFD and a first-order implicit scheme was used for the transient scalar transport to ensure convergence in the automated analysis. It is known that first-order schemes can cause numerical diffusion. However, when a sub-set of the models from the automated study were re-run using all second-order discretisation schemes, the fitted D_e values reduced by only a small amount, approximately 20 % on average. Despite this effect being small, this additional uncertainty should be considered when interpreting the results of this study.

If the scenario being studied is for an instantaneous or short duration release and the modeller is interested in concentrations or exposures at longer times or in smaller rooms then a well-mixed model may be sufficient. If the modeller is interested in what happens at very early times, or close to the source, then a more highly resolved model such as CFD may be required. For instantaneous and short duration releases when the modeller is interested in what happens at intermediate times or in larger rooms, then an eddy diffusion model should give better results than a well-mixed model. The same is true for

continuous releases in ventilated rooms. Models such as that by Drescher et al. (1995) can be used to estimate when a room becomes well-mixed and to help guide when a particular model is required.

The eddy diffusion models applied here do not account for vapour sorption and it is shown in Chapter 5 that sorption can have a significant effect on vapour concentrations for low volatility explosives. One-way vapour sorption (i.e. a vapour sink only) could be included in the models in a simplistic global sense by adding another decay term to Equation 6.3. The decay term could be calculated if the mass transfer coefficient, a, could be estimated and if it is assumed that $C^* = 0$. Drivas et al. (1996) applied a similar approach for deposition of aerosol in their eddy diffusion model. Morrison and Nazaroff (2002) and Johansen (1991) described ways in which a can be estimated for rooms. It is recommended that the validity of including a global one-way sorption model is assessed.

Eddy diffusion models do not provide information on peak concentrations, such as those discussed in Chapters 3 and 4. As was shown, these can be significant for turbulent flow (instantaneous concentrations of >20 times the mean 0.1 m away from the source and >8 times the mean more than 1 m away). Ideally there would be a method to superimpose a spatially varying probability density function (PDF) for the fluctuating concentration onto the mean concentrations produced by the eddy diffusion model. However, as was discussed in Chapter 3, there is currently no evidence to support the extrapolation of the results from the Nielsen test-case study to other rooms.

An open source Python tool for indoor eddy diffusion modelling which includes the TKEB relationship is available at de Lisle (2020).

6.5 Eddy diffusion modelling conclusions and recommendations

Fast running mathematical models of indoor dispersion have application in a number of areas. In particular, eddy diffusion models, where the rate of transport is governed by the eddy diffusion coefficient, D_e, can be used to rapidly predict spatially resolved concentrations.

The following conclusions have been made:

- It has been shown that D_e can be predicted for isothermal rooms using the TKEB relationship which was originally proposed by Karlsson et al. (1994).
  - The relationship had previously been applied using the room height as the characteristic length (Drivas et al., 1996) but it has been demonstrated here

that $\sqrt{A}$ is a more appropriate variable, which means that D_e is dependent on Q, V and N only.

- An automated CFD approach was used to generate approximately 250 individual dispersion models which were then used to test the validity of the TKEB relationship and to calculate the model constants for the relationship.
  - It was shown that D_e was similar when calculated independently at three different heights.
  - The release location did, however, have an effect on D_e. Releases occurring in the corner of the room, where the air flow is consistently faster, generally resulted in a higher D_e than releases which were away from the walls.
- Eddy diffusion coefficients from two existing experimental data sets were compared to the coefficients derived from the CFD data and all data followed a similar trend.
- Using the TKEB relationship to calculate D_e, an eddy diffusion modelling approach was used to predict gas concentrations (from short duration releases) in two scenarios and predictions were compared to experimental data.
  - In both cases the eddy diffusion model performed well but it was out-performed by a simple well-mixed model. However, this was due to the type of scenario considered and the time period examined.
  - The same approach was applied to compare eddy diffusion model predictions to LES data for a continuous release scenario. In this case, the eddy diffusion model performed very well.
- The situations where an eddy diffusion model should have most merit over a well-mixed model are:
  - For instantaneous and short duration releases, when the modeller is interested in what happens at intermediate times in large rooms/spaces.
  - Continuous releases in ventilated rooms when a concentration gradient will be maintained.
- The TKEB relationship can be used to calculate D_e and the upper and lower 95 % PI equations (or the lower D_e limit of $0.001\,\mathrm{m^2{\cdot}s^{-1}}$ (Drivas et al., 1996)) can be used to understand the uncertainty.
- The TKEB relationship may not be suitable if the source imparts a large amount of energy to the room and, in the simplified form applied here, the relationship does not account for thermal effects.
- Eddy diffusion modelling could be used to support explosive detection activities. The fast running models could be used to support training activities or to predict

likely concentrations in operational settings. The vapour source in explosive detection scenarios is likely to be a continuous release so eddy diffusion models will have a significant advantage over well-mixed models.

It is recommended that the following work is undertaken:

- The eddy diffusion coefficient study should be extended to include rooms with a range of ventilation types and non-isothermal conditions. Naturally ventilated rooms would be of particular interest for explosive detection.
- The effects of people movement on the eddy diffusion coefficient could be considered, using methods such as that proposed by Mora and Gadgil (2002) or Mingotti et al. (2020) for example.
- If experimental data for continuous releases were available this may help to highlight the benefit that eddy diffusion modelling has over the well-mixed approach.
- The validity of including a global,one-way sorption model in an eddy diffusion model should be assessed.

Chapter 7

Conclusions and further work

Dogs remain the most effective method for the detection of explosives in many situations, yet the chemical signature they sense cannot easily be quantified experimentally. Air movement in indoor spaces can be complex due to large regions with no dominant flow direction and low mean velocities. Therefore, vapour released from an explosive indoors would be expected to result in a high degree of variability in concentration. To improve canine detection capability, specifically training equipment, training methods and concepts of use, the science of vapour signatures in enclosed spaces needs to be improved.

A LES model of vapour transport from a constant concentration surface source in a widely studied, isothermal, benchmark test room has been used to illustrate the complexity of indoor vapour fields and to assess how they may relate to the detection of explosives using dogs. This model was run with a range of air change rates to extend the applicability of the results.

Most of the materials of interest to explosive detection have low to very low vapour pressures indicating that they will have large partition coefficients. Therefore, the effect of vapour sorption onto or into surfaces could be significant. A new spatially resolved sorption/permeation modelling capability was validated using a set of increasingly complex experiments. The effect of sorption on vapour concentrations in the benchmark test room was then considered.

Even with all of the complexity of indoor air flow, advective transport indoors can often be represented by a simple diffusion model. This approach, called eddy diffusion modelling, can be applied when there is isotropic mixing on a large scale (i.e. room scale) due to laminar and/or turbulent motion. The single parameter that governs mixing in these models is the eddy diffusion coefficient. A novel automated computational fluid dynamics tool was used to calculate the eddy diffusion coefficient in a range of isothermal, mechanically ventilated rooms and available relationships for the diffusion coefficient were tested.

The main conclusion of this PhD are given in the following sections.

7.1 The complex vapour signature in an indoor space

- The air flow in the benchmark test-case room was turbulent for Reynolds numbers ≥ 1230, based on the height of the inlet. At an inlet height Reynolds number of 1230, *Re* based on the inlet area was 5180 and the room ACR was $2.5\,\mathrm{h}^{-1}$. The air flow was laminar when the inlet height $Re = 245$. Without further work it is difficult to conclude which of these three parameters is the best indicator of turbulent flow in a room in general.

- Apart from a few minor variations, the air flow in the room appeared to be Reynolds number independent for Re ≥ 1230.

- It was shown that two simple models, one controlled by the friction velocity and the other by molecular diffusion, can be used to predict the vapour flux from a constant concentration area vapour source.

- Due to the low volatility of some compounds of interest and the diluting effect of the fresh air in the room, the time averaged vapour concentrations present in the bulk of the benchmark test room may be extremely low, whereas the peak concentration can be much greater than the mean.

  - Near the source, the concentration fluctuates significantly but the amplitude of these fluctuations was shown to be dependent on the location of the source, and the local turbulent flow field.
  - When the air flow was turbulent it was shown that instantaneous concentrations of greater than 20 times the mean were predicted 0.1 m away, and greater than 8 times the mean more than 1 m away, for a square area source with side length of 0.144 m.
  - It was also shown that fluctuations in the concentration do occur when the air flow was laminar but they were of the order of 0.5τ.
  - When the air flow was turbulent, a dog should be able to differentiate the concentration fluctuations, as the integral time scales for concentration were well above reported dog sniffing time scales.

- The vapour field did not scale linearly with the surface area of the source, for the modelled source sizes. This is perhaps not surprising given the very low speed of airflow in the room and the relatively large area size of the sources.

- The source size did not have a significant effect on the instantaneous and RMS concentrations, relative to the local time-averaged concentration, apart from close to the source. Therefore, ten times the surface area of the source material would

not produce ten times the vapour, but may produce the same relative RMS and relative instantaneous concentration field.

- Based on the ways in which animals are known to use air- or water-borne chemicals to locate a source, it is not clear whether there is sufficient information present in large parts of the test room for dogs to be able to achieve this after they have detected the vapour.
  - It may be necessary to use a structured or random search pattern that enables a detection dog to encounter sufficiently high concentrations or gradients (in the mean or RMS field) close to the source.
- For the particular room modelled, a dog is perhaps more likely to be able to detect the vapour when the air flow is laminar as higher concentrations build up near the source. However, if a dog was searching in a room with turbulent air flow for long enough they may chance upon one of the fluctuating high concentration peaks.
- Dog handlers should be advised to spend more time searching a room if the air flow is turbulent, whereas a single pass around the room may suffice if the air flow is laminar. Without information indicating otherwise, they could assume that air flow in the room is laminar if the air change rate is below $0.5\,\mathrm{h}^{-1}$.

7.2 The effects of vapour sorption

- It has been shown that absorption of EGDN in the test room had little effect on the well-mixed concentration but could have a significant effect on concentrations close to the absorbing surface within the first hour.
- TNT absorption had a greater effect on the well-mixed concentration, and for the case examined, would take more than 1000 h to reach the equilibrium concentration.
- Using CFD and well-mixed modelling the following were shown to increase the time taken to reach concentration equilibrium: decreasing the room flow rate, increasing the partition coefficient or increasing the solid phase diffusion coefficient.
- When planning training scenarios for detection dogs, vapour sorption should be considered for most explosives. The CFD sorption and permeation model could be used to model the specific scenario if required input parameters were available.

7.3 Eddy diffusion modelling for vapour dispersion indoors

- It has been shown that the eddy diffusion coefficient can be predicted for isothermal rooms using a TKEB relationship.

  - The relationship had previously been applied using the room height as the characteristic length but it has been demonstrated here that the square root of the inlet area is a more appropriate variable. This means that the eddy diffusion coefficient is only dependent on the air flow rate, the room volume and the number of supply vents.

- Using the TKEB relationship to calculate the eddy diffusion coefficient, an eddy diffusion modelling approach was used to predict gas concentrations (from short duration releases) in two scenarios and predictions were compared to experimental data.

  - In both cases the eddy diffusion model performed well but it was out-performed by a simple well-mixed model. However, this was due to the type of scenario considered and the time period examined.

- The TKEB relationship can be used to calculate the eddy diffusion coefficient. The upper and lower 95 % PI equations (or the lower eddy diffusion coefficient limit of $0.001\,\mathrm{m^2{\cdot}s^{-1}}$) can be used to understand the uncertainty.

- Eddy diffusion modelling could be used to support explosive detection activities. The fast running models could be used to support training activities or to predict likely concentrations in operational settings. The vapour source in explosive detection scenarios is likely to be a continuous release so eddy diffusion models will have a significant advantage over well-mixed models.

7.4 Further work

It is proposed that the following work is undertaken.

7.4.1 The complex vapour signature in an indoor space

- The LES modelling methods applied to the benchmark test-case are applied to a range of room types, including various mechanical ventilation configurations, naturally ventilated rooms and various room shapes. This should be done to see whether the conclusions can be applied more generally.

- Work is undertaken to reduce the LES model run-time.

  - Using the results of the current simulations it may be possible to use the standard Smagorinsky instead of the dynamic model (the volume averaged value for $\sqrt{C_{DS}}$ in the current model was 0.14) and achieve similar results.
  - It may also be possible to reduce the mesh resolution near some of the walls, away from the source regions, without having a negative effect on the results.

  - The model may run quicker in a different CFD code such as OpenFOAM®.

- A laminar model is used to predict the air flow in the benchmark test-case for ACRs of $0.5\,\mathrm{h}^{-1}$ and $2.5\,\mathrm{h}^{-1}$. This should be carried out with both the same mesh used for the LES study and a slightly coarser mesh. The results of this should be compared to the prediction from the LES model.
- Further modelling or experimental work is carried out to try to find the optimum indicator for turbulent air flow in a room.
- The room and turbulence time scales are explored further to see whether a more general relationship between them can be found.

7.4.2 The effects of vapour sorption

- The permeation model is extended to include 3D diffusion in the solid. This may give more accurate results in some situations but might require non-isotropic diffusion coefficients to be measured.
- Determine whether the stability of the sorption/permeation UDF can be improved through the use of adaptive time-stepping to automatically increase the time step size as the simulation progresses, or by using an implicit scheme rather than the current explicit scheme.

7.4.3 Eddy diffusion modelling for indoor dispersion

- The eddy diffusion coefficient study should be extended to include rooms with a range of ventilation types and non-isothermal conditions. Naturally ventilated rooms would be of particular interest for detection of explosives.
- The effects of people movement on the eddy diffusion coefficient could be considered, using methods such as that proposed by Mora and Gadgil (2002) or Mingotti et al. (2020) for example.
- If experimental data for continuous releases were available this may help to highlight the benefit that eddy diffusion modelling has over the well-mixed approach.
- The validity of including a global, one-way sorption model in an eddy diffusion model should be assessed.

Appendix A

Vapour emission

A.1 Acronyms for explosives

This table gives acronyms for some explosives, compounds found in explosives and explosive precursors.

Acronym	Full name
2,4-DNT	2,4-dinitrotoluene
2,6-DNT	2,6-dinitrotoluene
AN	Ammonium nitrate
DADP	Diacetone diperoxide
EGDN	Ethylene glycol dinitrate
HP100	100 % hydrogen peroxide
NG	Nitroglycerin
NM	Nitromethane
PETN	Pentaerythritol tetranitrate
P acid	2,4,6-trinitrophenol
p-MNT	P-nitrotoluene
RDX	Cyclotrimethylene trinitramine
S acid	2,4,6-trinitroresorcinol
TATP	Triacetone triperoxide
Tetryl	N-methyl-n,2,4,6-tetranitroaniline
TNA	2,4,6-trinitroaniline
TNB	1,3,5-trinitrobenzene
TNC	2,4,6-trinitro-m-cresol
TNM	2,4,6-trinitromesitylene
TNT	2,4,6-trinitrotoluene
TNX	2,4,6-trinitro-m-xylene
UN	Urea nitrate
EH	2-ethyl-1-hexanol
2NT	2-nitrotoluene
4NT	4-nitrotoluene
HP100	Hydrogen peroxide. The number gives the percent of HP in water
DMNB	2,3-dimethyl-2,3-dinitrobutane

Table A.1: Acronyms for some explosives, compounds found in explosives and explosive precursors.

A.2 Constituent components of TNT

TNT is a yellow coloured solid and comes in either flake or cast forms. A number of impurities can form during the manufacturing process. Leggett et al. (1977) surveyed eight military TNT samples and the average make-up of the constituent components is given in Table A.2. Leggett et al. included data for both US military and foreign samples.

Figure A.1: A sample of cast TNT.

Vapour phase concentrations for TNT were given by both Leggett et al. (1977) and Murrman and Nakano (1971).

Component	MW /g·mol^{-1}	**Solid phase** /%	**Vapour phase** P_n /Pa
2,4,5 TNT	227.13	0.068	
2,3,4 TNT	227.13	0.203	
2,6 DNT	182.13	0.003	1.01×10^{-4}
2,5 DNT	182.13	0.004	4.05×10^{-4}
2,4 DNT	182.13	0.077	2.68×10^{-3}
2,3 & 3,5 DNT	182.13	0.018	4.19×10^{-4}
3,4 DNT	182.13	0.002	
Unknown 1	-	0.014	
Unknown 2	-	0.021	
Unknown 3	-	0.113	
Unknown 4	-	0.036	
Unknown 5	-	0.277	
2,4,6 TNT	227.13	99.204	1.59×10^{-4}

Table A.2: Average solid (percentage by weight) and vapour phase constituent components of military grade TNT (Leggett et al., 1977). P_n is the partial pressure at 20 °C and MW is the molecular weight.

The density of TNT crystals are 1654 kg·m^{-3} (Meyer et al., 2007).

A.3 Molecular diffusion coefficient

The molecular diffusion coefficient for a vapour in air is important for both the vapour production rate as described in Section 4.3.2 and also for the broader vapour transport.

The molecular diffusion coefficients of explosive vapours in air can be estimated from their molecular weights and other parameters using a number of different method as described in Poling et al. (2007); Guo (2002). One method is given by the following (Poling et al., 2007).

$$D_m = \frac{0.00143 T^{\frac{7}{4}}}{P\, MW_{ab}^{\frac{1}{2}} \left[\Sigma_{v-a}^{\frac{1}{3}} + \Sigma_{v-b}^{\frac{1}{3}}\right]^2}, \tag{A.1}$$

where MW_{ab} [kg·mol^{-1}] is given by Equation A.2 and Σ_{v-a} and Σ_{v-b} are the atomic diffusion volumes of molecule a and b respectively. The atomic diffusion volume can be calculated from tables which provide the volume increments for different atoms and simple molecules, as given by Poling et al. (2007).

$$MW_{ab} = 2\left[\frac{1}{MW_a} + \frac{1}{MW_b}\right]^{-1}, \tag{A.2}$$

where MW_a and MW_b [g·mol^{-1}] are the molecular weights of component a and component b.

Phelan and Webb (1997) gave measured diffusion coefficients for TNT and DNT in air at 27 °C of 4.5×10^{-6} m^2·s^{-1} and 4.8×10^{-6} m^2·s^{-1} respectively. The model described above gives diffusivities of approximately 6.7×10^{-6} m^2·s^{-1} and 7.1×10^{-6} m^2·s^{-1} for TNT and DNT respectively. Based on this limited data, the model prediction is within a factor of 1.5.

A.4 Diffusion limited vapour flux

As discussed in Chapter 4, the diffusion limited vapour flux model of Gershanik and Zeiri (2010) can be used to calculate the flux from a relatively small source (hemisphere, flat disc or flat square) in slowly moving air.

Combining and rearranging Equations 3.3, 3.4 and 4.4 gives $Sh = \frac{8}{\pi}$ for a flat disc when the rate is governed by diffusion only (and when $C_{ambient} = 0$) and $L = 2R$. Similarly, combining Equations 3.3, 3.4 and 4.3 for a hemisphere, gives $Sh = 2$.

Gershanik and Zeiri (2010) stated that for a small hemispherical sources, a significant proportion of the change in concentration is contained within a small distance from the

source. The concentration reduced by 90 % at a distance of $10R$. For small particles of explosive this region will be small and therefore it is likely to be contained within the viscous sub-layer of a boundary layer[1]. From this Gershanik and Zeiri concluded that air flow further from the source is unlikely to have much effect on the sublimation flux.

The equations presented in Section 4.3.2 are for an equilibrium sublimation condition which occurs when the time is infinite, at which point $C(r) = C_0 \frac{R}{r}$ (Equation 4.2). The diffusion limited sublimation rate is controlled by the concentration gradient and so for small times, the gradients will be larger and the rate higher. A modelling study was conducted to see how long it would take for the equilibrium condition to be reached. For the study, diffusion from a hemisphere into an unbounded space was modelled. Equation A.3 gives the concentration for a sphere in an infinite medium or a hemisphere in a semi-infinite medium, where the surface of the sphere is fixed at a concentration, C_0, for $r \geq R$ (Coffey, 2010).

$$C = C_0 \frac{R}{r} \operatorname{erfc}\left(\frac{r-R}{2\sqrt{D\,t}}\right). \tag{A.3}$$

This can be multiplied by the surface area and integrated between the hemisphere radius, R, and infinity to give the total mass of vapour released from a hemisphere.

$$M = \int_R^\infty C_0 \frac{R}{r} \operatorname{erfc}\left(\frac{r-R}{2\sqrt{D\,t}}\right) A\, dr, \tag{A.4}$$

where the surface area, A, is $2\pi R^2$ for a hemisphere. This can then be differentiated with respect to t to give the time dependent sublimation rate. This can be achieved by differentiating only the complementary error function term, as this is the only term which is a function of t. This symbolic differentiation was carried out by using Mathcad V15.0.

$$\frac{dM}{dt} = \int_R^\infty C_0 \frac{R}{r} \left(\frac{1}{2\sqrt{\pi}} e^{\frac{-1}{4}\frac{(r-R)^2}{D\,t}} \frac{r-R}{(D\,t)^{\frac{3}{2}}} D\right) A\, dr. \tag{A.5}$$

Models were run to calculate the time and t_{ND}, at which the unsteady sublimation rate, given by Equation A.5, drops to an arbitrary 101% of the steady state rate, which is given by Equation 4.3. $t_{ND} = \frac{t}{L^2\,D}$ and in this case, t is the time and L is the hemisphere radius.

A hemisphere with the same area as the large source used in Chapter 4 has $R = 0.057$ m. If the diffusion coefficient is equal to D_m for TNT i.e. $5.6 \times 10^{-6}\,\mathrm{m^2{\cdot}s^{-1}}$ (Gershanik and Zeiri, 2010), then it will take almost 2 million seconds to reach 101% of the steady state

[1]For the indoor air LES modelled discussed in Chapter 3 (with an ACR = $10.2\,\mathrm{h^{-1}}$), the viscous sub-layer on the floor of the room was approximately 10 mm deep. This is assuming that the sub-layer ends when the non-dimensional distance from the wall, $y^+ = 5$.

rate. If the diffusion coefficient is equal to D_e for the test-case room i.e. $0.044\,\mathrm{m^2{\cdot}s^{-1}}$ (see Section 6.4.3.2), then it will take only 239 s to reach 101% of the steady state rate. In both cases, $t_{ND} = 3183$.

A.4.1 Sublimation flux data

Phelan and Patton (2004); Gershanik and Zeiri (2010); Mu et al. (2003) provided data on sublimation rates measured using a range of techniques such as quartz crystal microbalance (QCM) and thermogravimetric analysis. They were measured on small deposited samples with diameters of less than 1 cm and thicknesses of the order of micrometers or tens of micrometers. Some explosives deposited as continuous layers while others formed discrete crystals.

The sublimation rates in air given by Mu et al. (2003) (as reported by Phelan and Patton (2004)) for a layer of TNT, deposited onto a QCM, at 25 °C and 30 °C were $0.0248\,\mathrm{ng{\cdot}cm^{-2}{\cdot}s^{-1}}$ and $0.0496\,\mathrm{ng{\cdot}cm^{-2}{\cdot}s^{-1}}$ respectively. The layer having a diameter of 6 mm gave a total sublimation rate of $7.01 \times 10^{-3}\,\mathrm{ng{\cdot}s^{-1}}$ at 25 °C.

The vapour pressure concentration, C_0, of TNT at 25 °C is $7.06 \times 10^{-8}\,\mathrm{kg{\cdot}m^{-3}}$ (calculated from vapour pressure data from Gongwer (2005)) and if the diffusion coefficient is taken to be $4.47 \times 10^{-6}\,\mathrm{m^2{\cdot}s^{-1}}$ (Phelan and Webb, 1997), Equation 4.4 gives a value of $3.79 \times 10^{-3}\,\mathrm{ng{\cdot}s^{-1}}$, which is within a factor of two of the empirical data of Mu et al. (2003) given above.

Appendix B

Supporting data for the indoor vapour transport test-case

This appendix shows the results of various sensitivity test of the LES model used to simulate the flow in the Nielsen test room (Nielsen, 1990), as described in Chapter 3.

Figures B.1 and B.2 show the effect of refining the mesh around the inlet and the shear layer on the velocity profiles. This sensitivity test was conducted on a earlier version of the model i.e. when the model was run without the precursor simulation, with flat (constant) velocity, TKE and dissipation rate profiles applied directly to the start of the inlet channel. However, it is assumed that the findings can be applied to the model with the precursor simulation.

Figures B.3 and B.4 show the effect of using laminar inflow condition or turbulent inflow on the velocity profiles. The turbulent inflow was applied using the vortex method, which is implemented in Fluent according to Mathey et al. (2006).

Figures B.5 to B.12 shows the effect of changing Δt from 0.01 s to 0.005 s on the velocity profiles, concentration profiles and probability histograms of relative instantaneous concentrations. These models were also run without the precursor simulation.

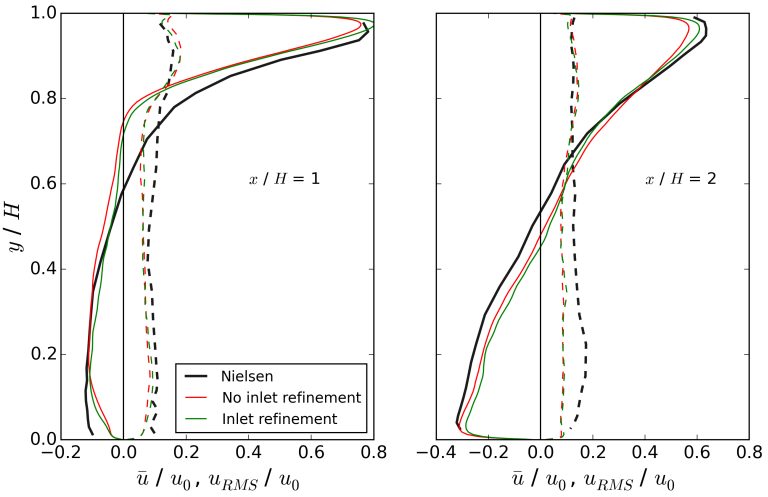

Figure B.1: $\overline{u}$ / u_0 and u_{RMS} / u_0 against y / H on vertical lines on the centre plane at x / $H = 1$ (left graph) and x / $H = 2$ (right graph) for the mesh with no inlet and shear layer refinement and the mesh with inlet and shear layer refinement compared against the experimental data of Nielsen (1990).

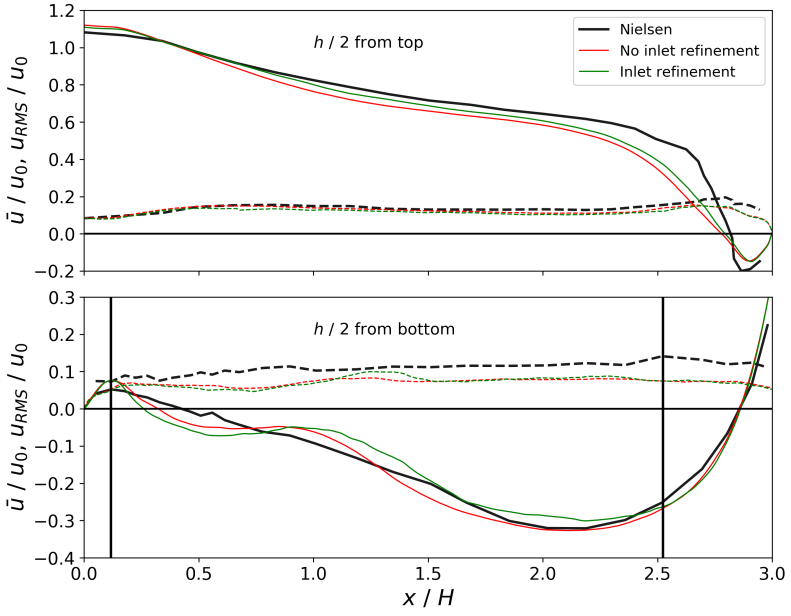

Figure B.2: $\overline{u}$ / u_0 and u_{RMS} / u_0 against x / H on horizontal lines on the centre plane at a distance of H_{inlet} / 2 from the top wall (upper graph) and H_{inlet} / 2 from the bottom wall (lower graph) for the mesh with no inlet and shear layer refinement and the mesh with inlet and shear layer refinement compared against the experimental data of Nielsen (1990). The vertical lines show the locations of the source centres.

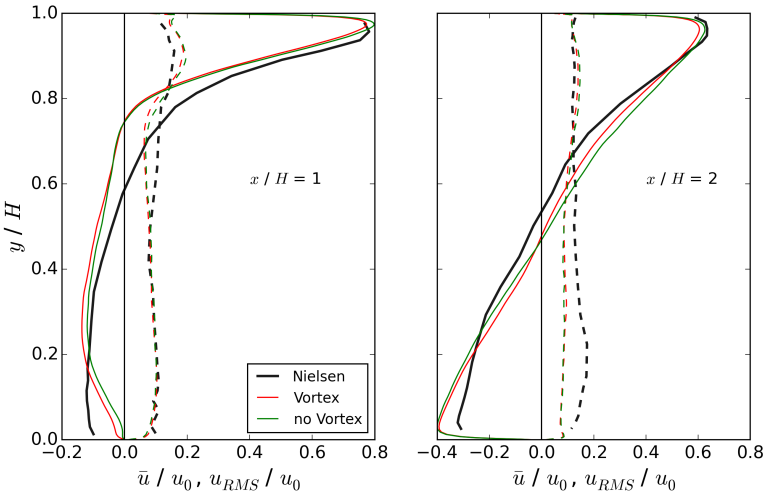

Figure B.3: $\overline{u}$ / u_0 and u_{RMS} / u_0 against y / H on vertical lines on the centre plane at x / H = 1 (left graph) and x / H = 2 (right graph) with and without the vortex method to generate turbulent inflow conditions, compared against the experimental data of Nielsen (1990).

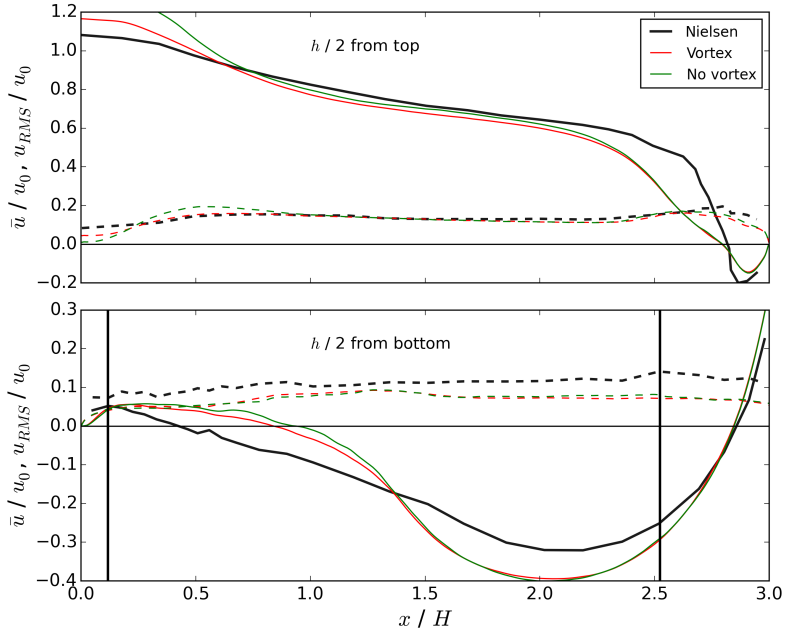

Figure B.4: $\overline{u}$ / u_0 and u_{RMS} / u_0 against x / H on horizontal lines on the centre plane at a distance of H_{inlet} / 2 from the top wall (upper graph) and H_{inlet} / 2 from the bottom wall (lower graph) with and without the vortex method to generate turbulent inflow conditions, compared against the experimental data of Nielsen (1990). The vertical lines show the locations of the source centres.

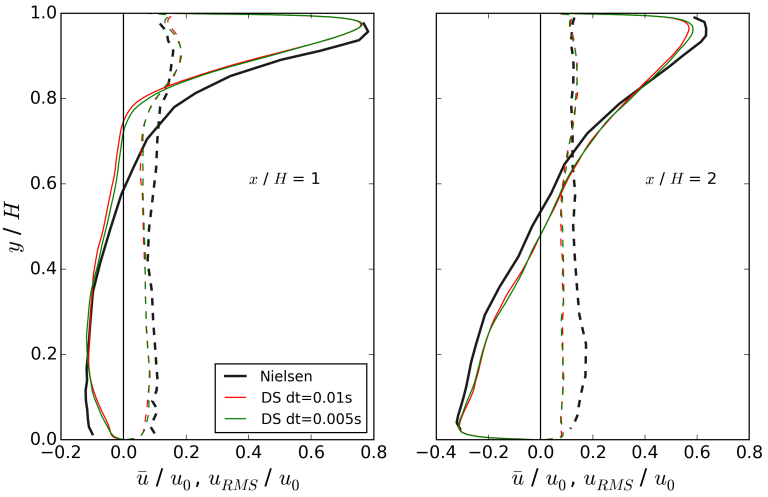

Figure B.5: $\overline{u}$ / u_0 and u_{RMS} / u_0 against y / H on vertical lines on the centre plane at x / $H = 1$ (left graph) and x / H = 2 (right graph) with $\Delta t = 0.01$ s and 0.005 s, compared against the experimental data of Nielsen (1990).

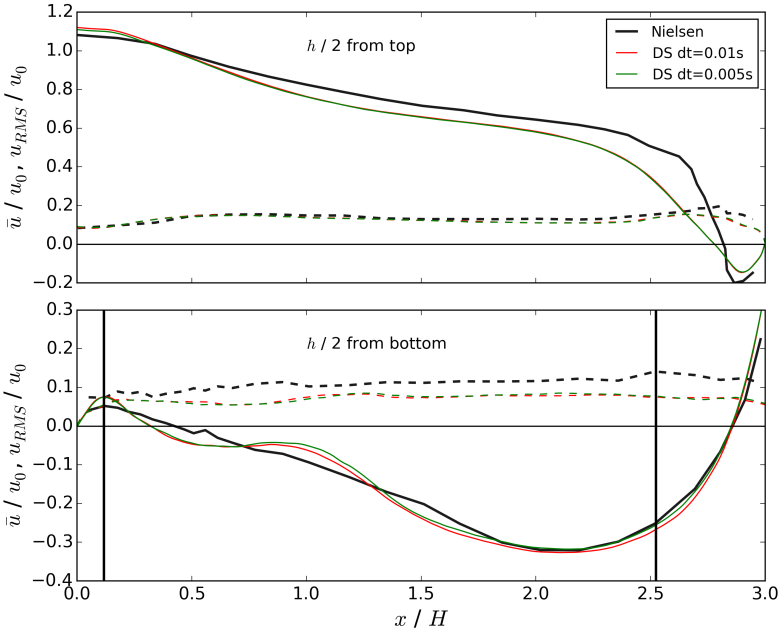

Figure B.6: $\overline{u}$ / u_0 and u_{RMS} / u_0 against x / H on horizontal lines on the centre plane at a distance of H_{inlet} / 2 from the top wall (upper graph) and H_{inlet} / 2 from the bottom wall (lower graph) with $\Delta t = 0.01$ s and 0.005 s, compared against the experimental data of Nielsen (1990). The vertical lines show the locations of the source centres.

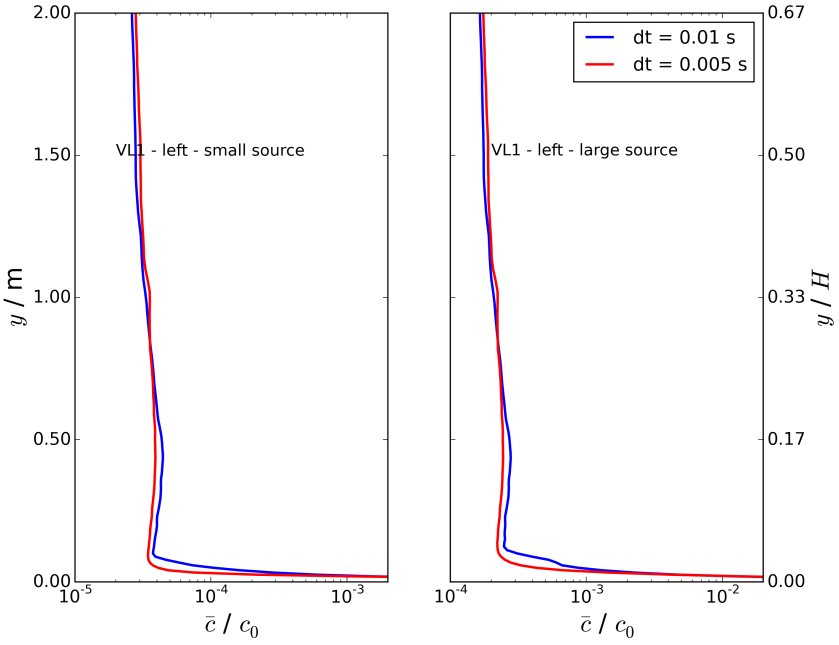

Figure B.7: $\bar{c}$ / c_0 along vertical line VL1, for the large and small left source, with Δt = 0.01 s and 0.005 s. Only data up to y = 2.0 m (or y / H = 0.66) is shown.

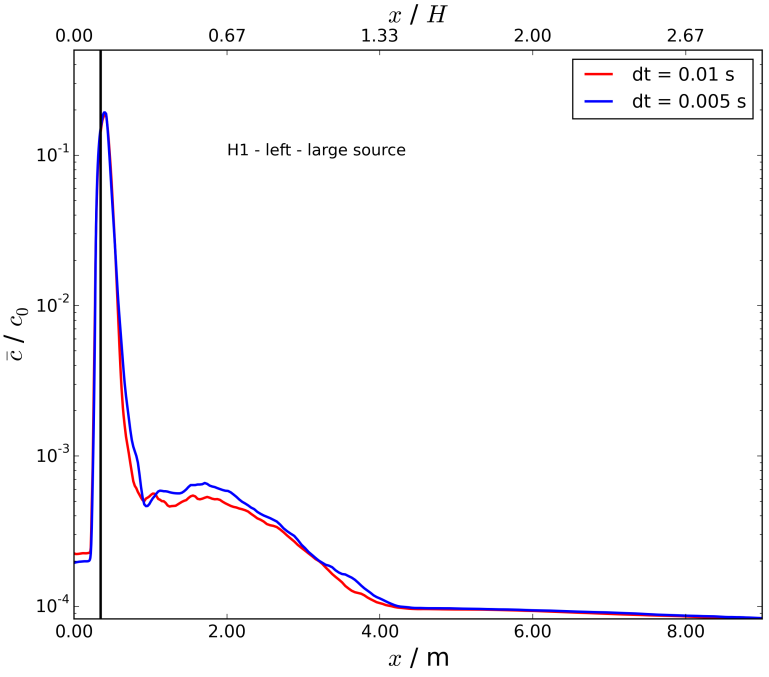

Figure B.8: $\bar{c}$ / c_0 along horizontal line H1, for the large left source, with Δt = 0.01 s and 0.005 s.

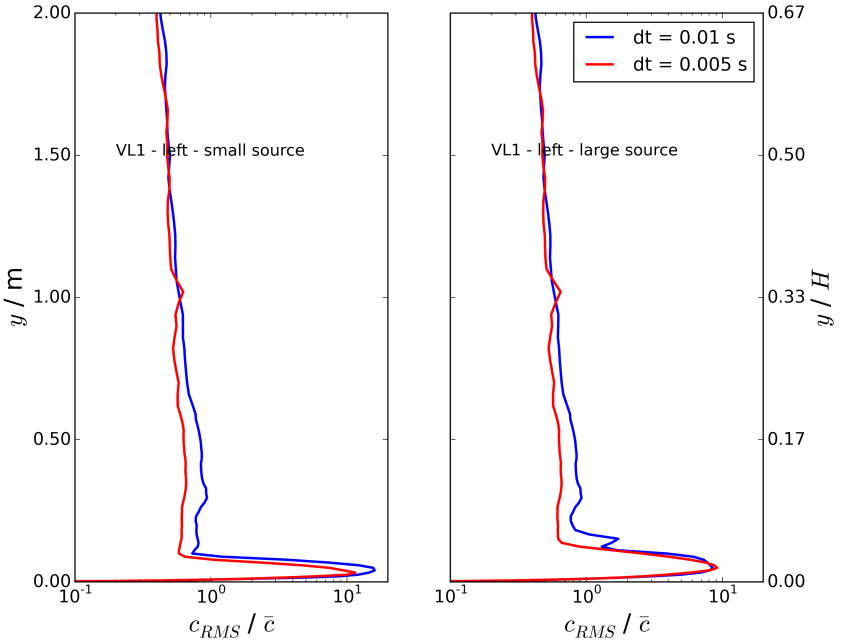

Figure B.9: c_{RMS} / $\bar{c}$ along vertical line VL1, for the large and small left source, with Δt = 0.01 s and 0.005 s. Only data up to y = 2.0 m (or y / H = 0.66) is shown.

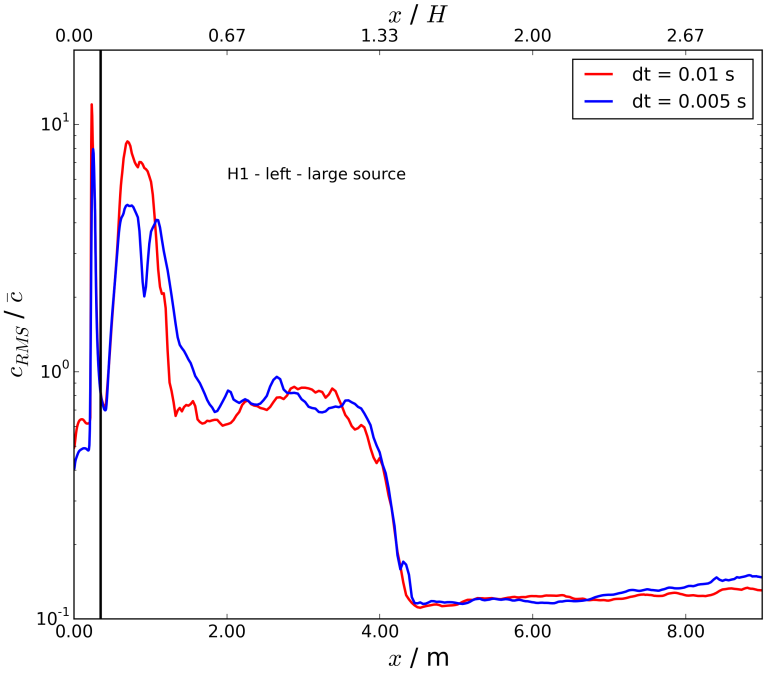

Figure B.10: c_{RMS} / $\bar{c}$ along horizontal line H1, for the large left source, with Δt = 0.01 s and 0.005 s.

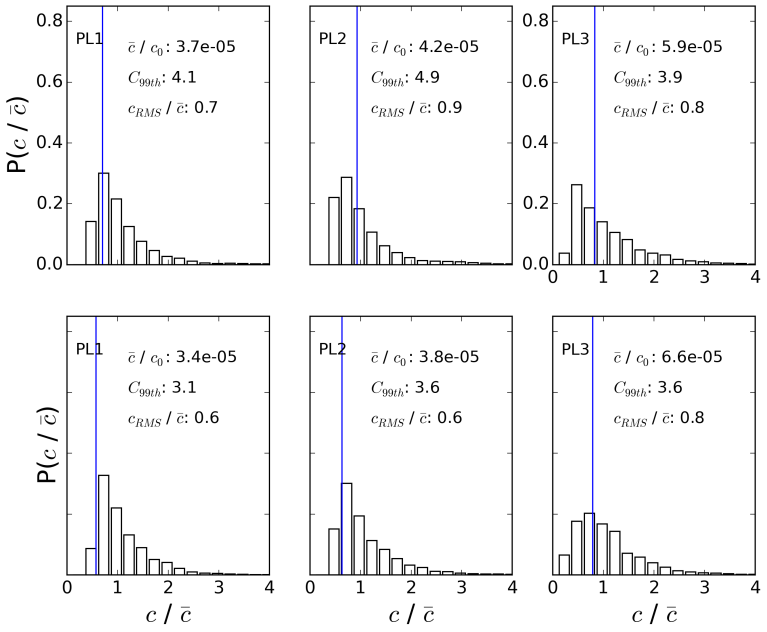

Figure B.11: The probability of c / $\bar{c}$ for the left small source at points PL1, PL2 and PL3. The upper graphs show result from the model with the Δt = 0.01 s, the lower graphs = 0.005 s. The vertical line shows c_{RMS} / $\bar{c}$. The bin width = 0.25.

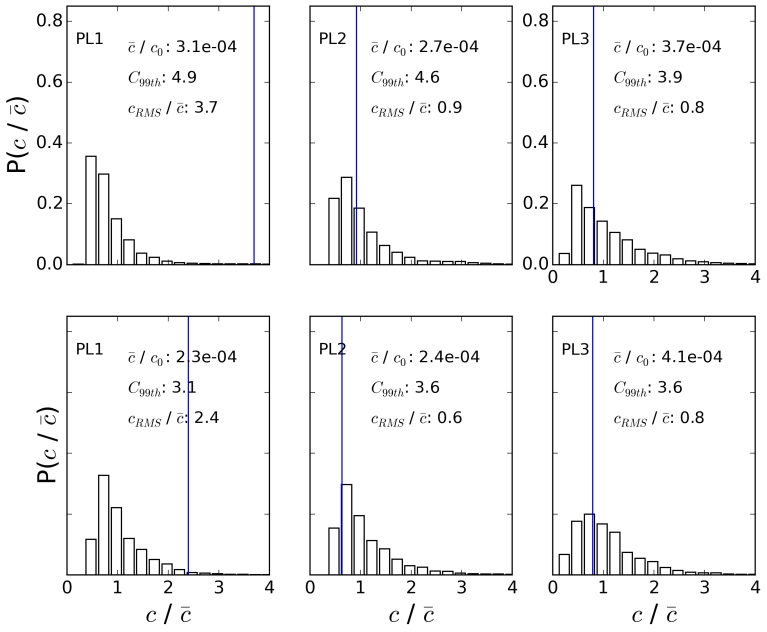

Figure B.12: The probability of c / $\bar{c}$ for the left large source at points PL1, PL2 and PL3. The upper graphs show result from the model with the Δt = 0.01 s, the lower graphs = 0.005 s. The vertical line shows c_{RMS} / $\bar{c}$. The bin width = 0.25.

Appendix C

State-space model

A state-space model was used in Chapter 2.3 to predict the concentration in a room, taking account of losses due to vapour sorption/permeation.

A diagram of the processes being modelled is shown in Figure 5.17 in Chapter 2.3. The governing equations for the model are shown below and are based on Parker and Bowman (2011) and Parker et al. (2014a).

The equation for rate of change in concentration, $\dot{\boldsymbol{C}}$ [kg·m^{-3}·s^{-1}], in the room and permeation layers is

$$\dot{\boldsymbol{C}} = \boldsymbol{A_{ss}}\boldsymbol{C} + \boldsymbol{B}\boldsymbol{u_{ss}}, \tag{C.1}$$

where the state vector, $\boldsymbol{C}$, is given by

$$\boldsymbol{C} = \begin{bmatrix} C_1 \\ C_2 \\ \vdots \\ C_n \end{bmatrix}, \tag{C.2}$$

where C_i is the concentration [kg·m^{-3}] in zone i and $\dot{\boldsymbol{C}}$ is given by

$$\dot{\boldsymbol{C}} = \begin{bmatrix} \frac{dC_1}{dt} \\ \frac{dC_2}{dt} \\ \vdots \\ \frac{dC_n}{dt} \end{bmatrix}. \tag{C.3}$$

$\boldsymbol{A_{ss}}$ [s^{-1}] is an n by n matrix where

$$\boldsymbol{A_{ss}} = \boldsymbol{V}^{-1}\boldsymbol{Q}. \tag{C.4}$$

$\boldsymbol{V}$ is a diagonal matrix where $V_{i,i} = V_i$, V_i is the volume of zone i [m^3] and $V_{i,j} = 0$ for $i \neq j$. $\boldsymbol{Q}$ is an n by n matrix which describes the flow (or movement of vapour) between zones and has unit of [$m^3 \cdot s^{-1}$]. $Q_{i,i}$ represents the flows out of zone i, $Q_{i,j}$ represent the flow from zone j into zone i.

$$\boldsymbol{Q} = \begin{bmatrix} -Q_{1,1} & Q_{1,2} & \dots & Q_{1,n} \\ Q_{2,1} & -Q_{2,2} & \ddots & \vdots \\ \vdots & \ddots & \ddots & Q_{n-1,n} \\ Q_{n,1} & \dots & Q_{n,n-1} & -Q_{n,n} \end{bmatrix}. \tag{C.5}$$

From the diagram in Figure 5.17, $Q_{1,1} = Q_{0,1} + aA$, $Q_{1,2} = \frac{aA}{K_{ab}}$, $Q_{1,3} = 0$, $Q_{2,1} = aA$, $Q_{2,2} = \left(\frac{aA}{K_{ab}} + \frac{DA}{d_{layer2,3}}\right)$ etc.

The $\boldsymbol{B u_{ss}}$ term in Equation C.1 represents inputs into the system. $\boldsymbol{B}$ is a diagonal matrix and equals $\boldsymbol{V}^{-1}$. $\boldsymbol{u_{ss}}$ [$kg \cdot s^{-1}$] is a vector which represents the sources in each zone and in this case, $u_{ss1} = \dot{M}_1$ and all the other elements are zero.

The analytical solution to Equation C.1 for a constant flow rate and a continuous and constant source is given by (Parker et al., 2014a)

$$C(t) = -(\boldsymbol{I} - e^{\boldsymbol{A}t})\boldsymbol{A}^{-1}\boldsymbol{B u_{ss}}, \tag{C.6}$$

where $\boldsymbol{I}$ is an n by n identity matrix. Equation C.6 is solved directly at the required time point using methods described in Parker et al. (2014b).

Appendix D

Comparison between a state-space and CFD model

To build confidence in the state-space approach used to model sorption and permeation (see 5.4.1.2), the predictions from a state-space model were compared to those from a CFD model. For the comparison a simple geometry was used where mixing of the vapour was maximised through the use of a high air change rate and a large molecular diffusion coefficient. The geometry, shown in Figure D.1 was a 1 m cube which was meshed with only 8800 cells so that it could easily be run for long simulation times.

The geometry had an inlet in the top right corner with two extracts low down to promote mixing. The flow rate, Q_f was $8.16 \times 10^{-3}\,\mathrm{m^3{\cdot}s^{-1}}$, which gives an air change rate of $29.4\,\mathrm{h^{-1}}$. The molecular diffusion coefficient $D_m = 1 \times 10^{-3}\,\mathrm{m^2{\cdot}s^{-1}}$. The top half of one of the walls was defined as a vapour source and was given a fixed concentration boundary condition. The floor was a permeable surface, for which $d_{total} = 0.0065$ m, $n_{layer} = 100$, $D_{solid} = 1 \times 10^{-11}\,\mathrm{m^2{\cdot}s^{-1}}$ and $K_{ab} = 5000$.

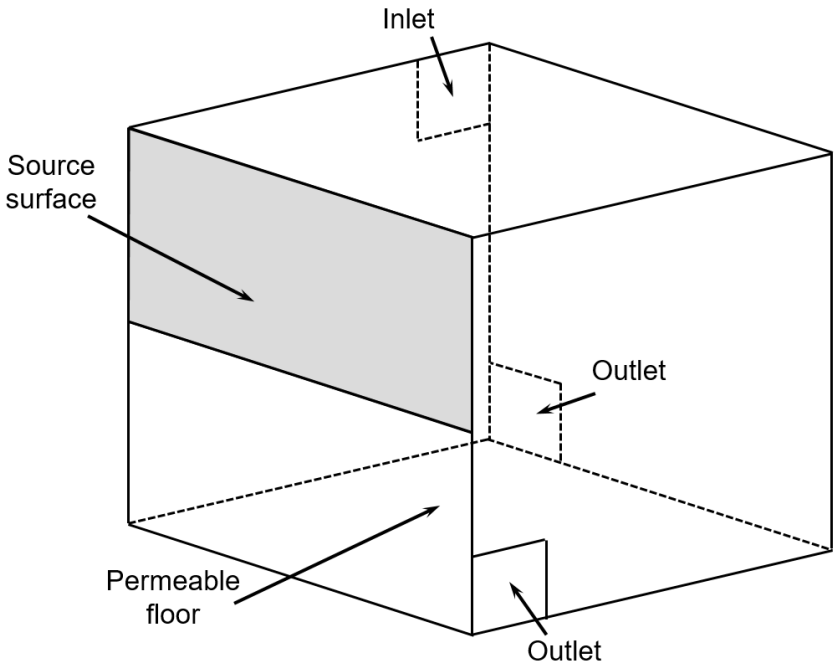

Figure D.1: The geometry used to compare the state-space approach for sorption/permeation to CFD. The hidden lines are dashed.

Figure D.2 shows the concentration in the air from both the CFD and state-space model. For the CFD, the average concentration across the air volume is shown. When the state-space model was run with the same flow rate as the CFD model it under-predicted the concentration. When it was run with a flow rate of $2.00 \times 10^{-2}\,\mathrm{m^3{\cdot}s^{-1}}$ (a factor of 2.5 higher) the predictions were much closer to the CFD. This suggests that even with the high air change rate and molecular diffusion coefficient the space is not completely well-mixed. Investigation of the flow pattern indicated that short-circuiting between the inlet and outlets has resulted in faster mixing in parts of the room compared to a well-mixed condition.

For times larger than approximately 25 min, the state-space model predictions for C / C_{equil}, when $Q_f = 8.16 \times 10^{-3}\,\mathrm{m^3{\cdot}s^{-1}}$, were only 2 % smaller than the CFD predictions.

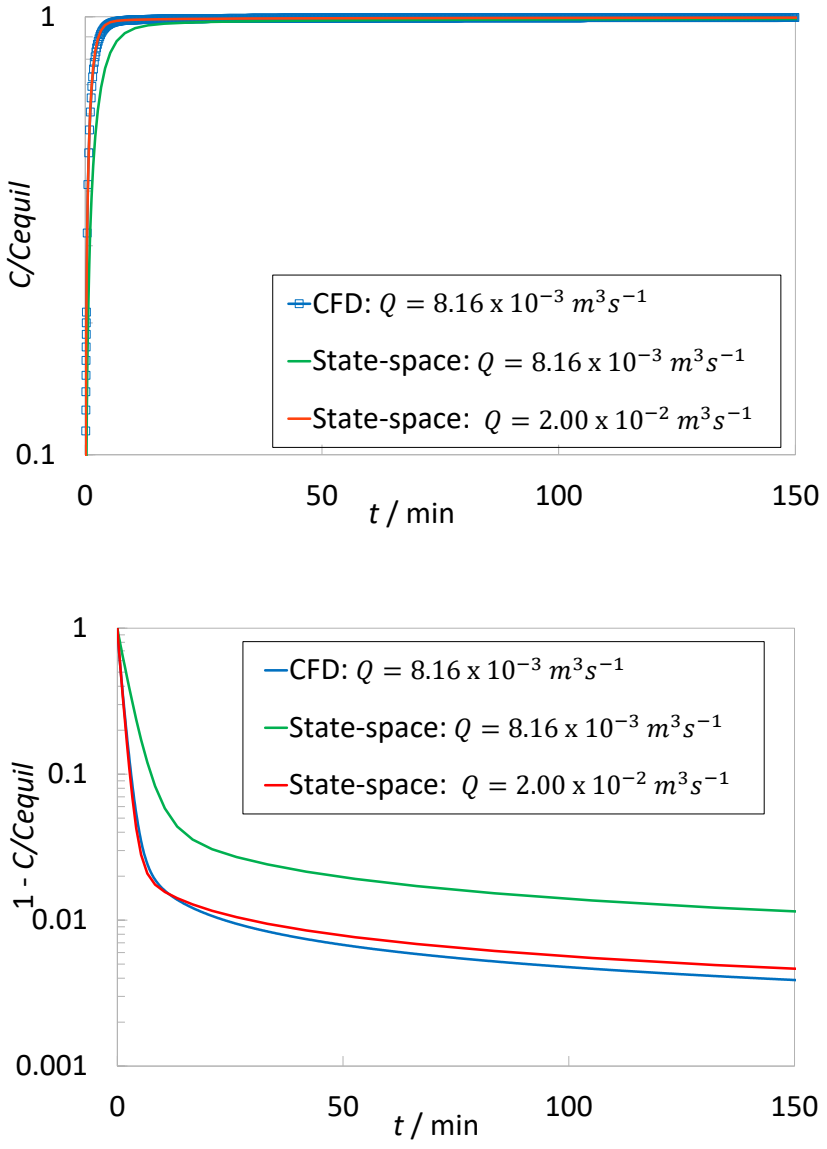

Figure D.2: CFD predictions for C / C_{equil} (upper) and 1 - C / C_{equil} (lower) for the CFD and state-space model.

Appendix E

Investigating a selection of mixing times

The automated CFD process used to parameterise the eddy diffusion coefficient, as discussed in Chapter 6 was originally demonstrated by studying pollutant mixing times in mechanically ventilated, isothermal rooms. The work is described in full in Foat et al. (2017) and is summarised below.

Three analytical mixing time models, including a novel jet transit based approach, were selected for comparison with CFD predictions for a wide range of cuboidal rooms with ceiling ventilation. The jet transit approach to pollutant mixing times uses the time it takes for a jet of air to move from a ceiling diffuser to a horizontal plane on interest in the room. The two other mixing models were the mechanical power model of Drescher et al. (1995) and a simple characteristic time model where the characteristic time, $\tau = 1 / \lambda$. Three different mixing time metrics were calculated from the CFD for comparison with the analytical models, one of the metric, t_{95-5}, is described below.

If the range of concentrations within the room is described by a distribution, then a useful measure of mixing is given by the difference between the time when only the highest concentrations (the 95th percentile value) have crossed a threshold concentration and when all but the lowest have (the 5th percentile value). This time is referred to as t_{95-5} and is indicative of the time between the first people and the last people in a room being exposed to a threshold concentration. The threshold was defined as a fraction of the maximum concentration reached in a well-mixed room of the same size and flow rate.

The modelled rooms were similar to those described in Section 6.3.2. They were a set of isothermal rooms which were cuboid in shape and contained no furniture. They were served by mixing ventilation with no recirculation, with air supplied via supply and extract vents (square four-way diffuser) located in the ceiling. The room volume and

shape, the air change rate and vent layout were varied across the parameter space shown in Table E.1 using a Sobol sequence space filling algorithm.

Parameters	**Symbol**	**Ranges**
Room volume	V	$50\,\mathrm{m}^3$ - $5000\,\mathrm{m}^3$
Floor aspect ratio	L / W	1 - 3
Height / (floor area)$^{1/2}$	H / $(LW)^{1/2}$	0.1 - 1.5
Air change rate	λ	$0.5\,\mathrm{h}^{-1}$ - $20\,\mathrm{h}^{-1}$

Table E.1: Experimental design space.

The main difference between the automated CFD scenario discussed in Chapter 6 and that used here is that the pollutant was released into each room via the ventilation system for a short duration. The release mass was defined as the amount of material required to achieve a specific concentration in a well-mixed room of the same size and flow rate.

The CFD method (using the k-ω SST turbulence model) was validated using a tracer experiment in the meeting room described in 6.3.1. In this case, the tracer gas was released over a period of 180 s, just upstream of the HVAC air handling unit. The results of the validation are shown in Figure E.1.

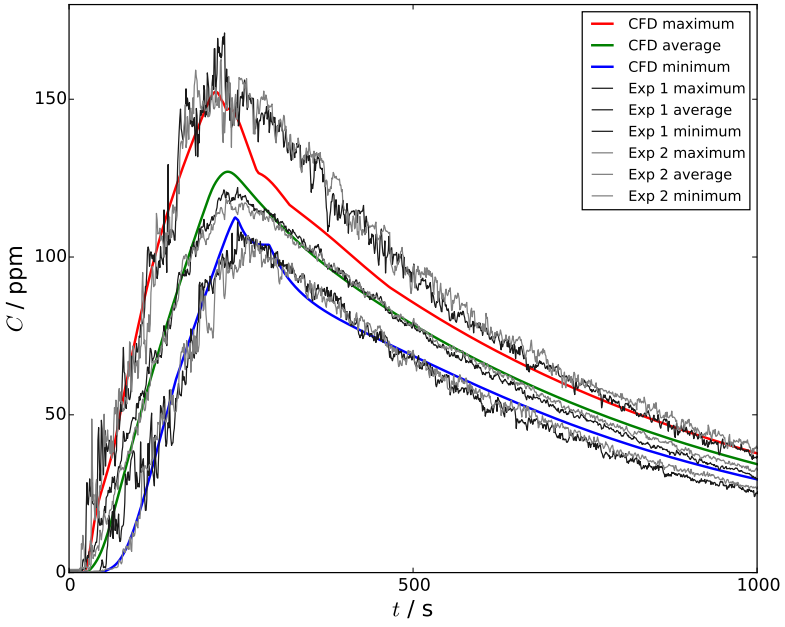

Figure E.1: Maximum, average and minimum tracer concentrations in parts per million (ppm) across nine measurement locations from two experiments compared to predictions from the CFD model.

The key results of the study are shown in Figure E.2. This figure shows the mixing time metrics, t_{95-5}, as calculated from each of the automated CFD models, plotted against the mixing time calculated by either: the jet transit model $t_{transitAR}$ or the mechanical power model $t_{mixCell}$ Drescher et al. (1995). Also shown is t_{95-5} plotted against τ. This figure shows that, based on R^2, t_{95-5} was best represented by the characteristic time model.

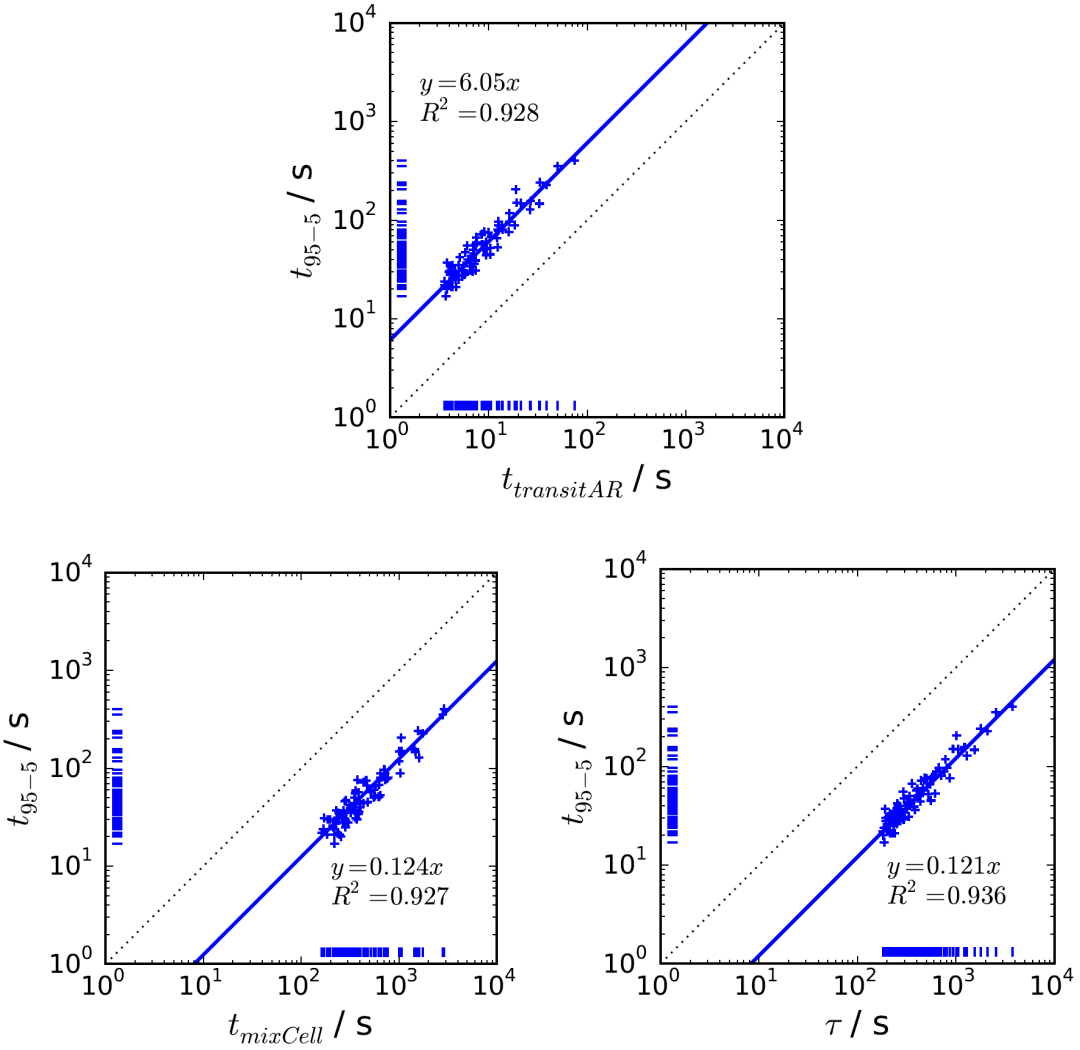

Figure E.2: t_{95-5} plotted against $t_{transitAR}$, $t_{mixCell}$ and τ. Each cross represents the prediction from an individual CFD model. The solid lines are linear regressions with the gradients of the lines and the R^2 values given. The dotted line shows a 1:1 gradient. Values are shown as ticks on the axes to indicate the distribution of values

Additional results, analysis and discussion are given in Foat et al. (2017).

References

Abdilghanie, A. M., Collins, L. R., and Caughey, D. A. (2009). Comparison of turbulence modeling strategies for indoor flows. *Journal of Fluids Engineering*, 131(5):051402.

Acevedo-Bolton, V., K-C, C., Jiang, R.-T., Ott, W., Klepeis, N., and Hildemann, L. (2012). Measurement of the proximity effect for indoor air pollutant sources in two homes. *Journal of Environmental Monitoring*, 14(1):94–104.

Aernecke, M. (2014). Ultra-sensitive real-time vapor detection for characterizing canine training aids. In *2014 Canine S&T Workshop*.

ARID (2004). UVIC MkII User's manual. ARID Ltd.

ASHRAE (2001). *ASHRAE Handbook of fundamentals*. American Society of Heating, Refrigeration and Air-Conditioning Engineers, Atlanta, GA.

Atema, J. (1996). Eddy chemotaxis and odor landscapes: exploration of nature with animal sensors. *Biological Bulletin*, 191(1):129–138.

Awbi, H. (2003). *Ventilation of buildings*. Spon Press, New York.

Baughman, A., Gadgil, A., and Nazaroff, W. (1994). Mixing of a point source pollutant by natural convection flow within a room. *Indoor air*, 4(2):114–122.

Bigger, R. (2008). Chemical vapor plume detection using the Schlieren optical method. Master's thesis, The Pennsylvania State University.

Boppana, V., Xie, Z.-T., and Castro, I. (2010). Large-eddy simulation of dispersion from surface sources in arrays of obstacles. *Boundary-layer meteorology*, 135(3):433–454.

Boppana, V., Xie, Z.-T., and Castro, I. (2012). Large-eddy simulation of dispersion from line sources in a turbulent channel flow. *Flow, turbulence and combustion*, 88(3):311–342.

Byrd, R., Lu, P., Nocedal, J., and Zhu, C. (1995). A limited memory algorithm for bound constrained optimization. *SIAM J. Sci. Comput.*, 16(5):1190–1208.

Chen, Q. (1995). Comparison of different k-ε models for indoor air flow computations. *Numerical Heat Transfer, Part B Fundamentals*, 28(3):353–369.

Chen, Q. (1996). Prediction of room air motion by Reynolds-stress models. *Building and Environment*, 31(3):233–244.

Chen, Q. and Srebric, J. (2002). A procedure for verification, validation, and reporting of indoor environment cfd analyses. *HVAC&R Research*, 8(2):201–216.

Cheng, K.-C., Acevedo-Bolton, V., Jiang, R.-T., Klepeis, N., Ott, W., Fringer, O., and Hildemann, L. (2011). Modeling exposure close to air pollution sources in naturally ventilated residences: Association of turbulent diffusion coefficient with air change rate. *Environmental Science and Technology*, 45:4016–4022.

Cherdron, W., Durst, F., and Whitelaw, J. H. (1978). Asymmetric flows and instabilities in symmetric ducts with sudden expansions. *Journal of Fluid Mechanics*, 84(01):13–31.

Choi, J.-I. and Edwards, J. (2008). Large eddy simulation and zonal modeling of human-induced contaminant transport. *Indoor air*, 18(3):233–249.

Choi, J.-I. and Edwards, J. (2012). Large-eddy simulation of human-induced contaminant transport in room compartments. *Indoor Air*, 22:77–87.

Clark, M., Aernecke, M., Gregory, K., Hardy, D., and Kunz, R. (2010). Sensing impacts of the fate of trace explosives signatures under environmental conditions. Technical report, Edgewood Chemical Biological Center.

Clausen, P., Liu, Z., Xu, Y., Kofoed-Sorensen, V., and Little, J. (2010). Influence of air flow rate on emission of DEHP from vinyl flooring in the emission cell flec: Measurements and CFD simulation. *Atmospheric Environment*, 44(23):2760–2766.

Coffey, C. (2010). Classified title. Technical Report DSTL/TR39624, Dstl.

Cooper, D. and Horowitz, M. (1986). Exposures from indoor powder release: models and experiments. *Am. Ind. Hyg. Assoc. J.*, 47(4):214–218.

Cortes, I. and Nielsen, P. (2010). Analysis of the IEA 2D test. 2D, 3D, steady or unsteady airflow? Technical Report DCE Technical Reports, No. 106, Aalborg: Department of Civil Engineering, Aalborg University.

Cragin, J. and Leggett, D. (2003). Diffusion and flux of explosive related compounds in plastic mine surrogates. Technical Report 20040329 078, ERDC - Cold regions research and engineering laboratory.

Crank (1979). *Mathematics of Diffusion*. Oxford University Press, UK.

Craven, B., Paterson, E., and Settles, G. (2010). The fluid dynamics of canine olfaction: unique nasal airflow patterns as an explanation of macrosmia. *Journal of the Royal Society Interface*, 7:933–943.

Crimaldi, J. and Koseff, J. (2001). High resolution measurement of the spatial and temporal scalar structure of a turbulent plume. *Experiments in Fluids*, 31:90–102.

Cussler, E. (2009). *Diffusion - Mass transfer in fluid systems*. Cambridge University Press, Cambridge, UK.

Danberg, J. (2008). Evaporation into couette flow. Technical Report ECBC-CR-092, Edgewood Chemical Biological Center.

Davidson, L. and Nielsen, P. (1996). Large eddy simulation of the flow in a three-dimensional ventilated room. Technical Report No. 59, Vol. R9651, Aalborg: Dept of Building Technology and Structural Engineering.

Davidson, L., Nielsen, P., and Topp, C. (2000). Low-Reynolds number effects in ventilated rooms: a numerical study. Technical Report No. 121, Vol. R0046, Aalborg Univerisy.

de Lisle, J. (2020). Rapid indoor dispersion tool. `https://github.com/riskaware-ltd/ridt`. Accessed: 12/01/21.

Demou, E., Hellweg, S., Wilson, M., Hammond, S., and Mckone, T. (2009). Evaluating indoor exposure modeling alternatives for LCA: A case study in the vehicle repair industry. *Environ. Sci. Technol.*, 43(15):5804–5810.

Deng, B. and Kim, C. N. (2007). CFD simulation of VOCs concentrations in a resident building with new carpet under different ventilation strategies. *Building and Environment*, 42(1):297–303.

Donovan, E., Donovan, B., Sahmel, J., Scott, P., and Paustenbach, D. (2011). Evaluation of bystander exposures to asbestos in occupational settings: a review of the literature and application of a simple eddy diffusion model. *Crit. Rev. Toxicol.*, 41(1):50–72.

Drescher, A., Lobascio, C., Gadgil, A., and Nazarofif, W. (1995). Mixing of a point-source indoor pollutant by forced convection. *Indoor Air*, 5(3):204–214.

Drivas, P., Valberg, P., Murphy, B., and Wilson, R. (1996). Modeling indoor air exposure from short-term point source releases. *Indoor air*, 6:271–277.

Drodge, J., Foat, T., Nally, J., and Parker, S. (2019). Eddy diffusion modelling - a tool for rapid spatially resolved indoor hazard assessment. Poster presented at the DTRA CBD S&T conference 2019.

Drolet, D. and Armstrong, T. (2018). Ih mod 2.0. ms excel workbook of deterministic and monte carlo simulation mathematical models to estimate airborne concentrations of chemicals. `https://www.aiha.org/public-resources/consumer-resources/topics-of-interest/ih-apps-tools`. Accessed: 30/09/19.

Eisenhauer, J. (2003). Regression through the origin. *Teach. Stat.*, 25(3):76–80.

Elhadidi, B. and Khalifa, H. (2013). Comparison of coarse grid lattice Boltzmann and Navier Stokes for real time flow simulations in rooms. *Building Simulation*, 6(2):183–194.

Endregard, M., Reif, B. A. P., Vik, T., and Busmundrud, O. (2010). Consequence assessment of indoor dispersion of sarin - a hypothetical scenario. *Journal of hazardous materials*, 176(1):381–388.

Ewing, R. G., Waltman, M. J., Atkinson, D. A., Grate, J. W., and Hotchkiss, P. J. (2013). The vapor pressures of explosives. *Trends in Analytical Chemistry*, 42.

Fackrell, J. and Robins, A. (1982). Concentration fluctuations and fluxes in plumes from point sources in a turbulent boundary layer. *Journal of Fluid Mechanics*, 117(1):26.

Feigley, C., Bennett, J., Lee, E., and Khan, J. (2002). Improving the use of mixing factors for dilution ventilation design. *Appl. Occup. Environ. Hyg.*, 17(5):333–343.

Fernandez de la Mora, G. and Fernandez de la Mora, J. (2013). AIP-MS detection of low volatility explosive species in the gas phase for cargo screening. In *4th Annual Workshop on Trace Explosives Detection.*

Ferri, G., Caselli, E., Mattoli, V., Mondini, A., and Dario, B. M. P. (2009). Spiral: A novel biologically-inspired algorithm for gas/odor source localization in an indoor environment with no strong airflow. *Robotics and Autonomous Systems*, 57(4):393–402.

Finkelstein, W., Melikov, A., Sefker, T., and Langkilde, G. (1996). Laser doppler measurement of airflow characteristics in rooms with mechanical ventilation. *Indoor Air 96. Proceedings of the 7th international conference on indoor air quality and climate.*

Fischer, H., List, E., Koh, R., Imberger, J., and Brooks, N. (1979). *Mixing in inland and coastal waters.* Academic Press, UK.

Foat, T. (2014). Using fluid dynamics to aid canine detection of vapour. Paper presented at the 2014 Canine S&T workshop, North Carolina, USA.

Foat, T. (2015). Understanding vapour plume structure in indoor environments for the detection of explosives. Paper presented at the 68th Annual Meeting of the APS Division of Fluid Dynamics, Massachusetts, USA.

Foat, T. (2016). Understanding vapour production and transport in indoor environments for the detection of explosives. Presentation given to the Aerodynamics and Flight Mechanics Group at Southampton University, Hampshire, UK.

Foat, T. (2017). Can the unsteady vapour plume from explosives be exploited for canine search indoors? Presentation given at the 2017 International Defence and Security Canine Conference, Cirencester, UK.

Foat, T. (2019). Modelling vapour transport in indoor environments for improved detection of explosives using dogs. Presentation given to the Aerodynamics and Flight Mechanics Group at Southampton University, Hampshire, UK.

Foat, T., Drodge, J., Charleson, A., Whatmore, B., Pownall, S., Glover, P., Nally, J., Parker, S., Khan, C., and Marr, A. (2021). Predicting vapour transport from semi-volatile organic compounds concealed within permeable packaging. *International Journal of Heat and Mass Transfer*.

Foat, T., Drodge, J., Nally, J., and Parker, S. (2020). A relationship for the diffusion coefficient in eddy diffusion based indoor dispersion modelling. *Building and Environment*, 169.

Foat, T., Nally, J., and Parker, S. (2017). Investigating a selection of mixing times for transient pollutants in mechanically ventilated, isothermal rooms using automated computational fluid dynamics analysis. *Building and Environment*, 118:313–322.

Foat, T., Parker, S., Castro, I., and Xie, Z.-T. (2018). Numerical investigation into the structure of scalar plumes in a simple room. *Journal of Wind Engineering & Industrial Aerodynamics*, 175:252–263.

Gan, G. and Awbi, H. (1994). Numerical simulation of the indoor environment. *Building and Environment*, 29(4):449–459.

Gaskell, P. and Lau, A. (1988). Curvature-compensated convective transport: Smart, a new boundedness-preserving transport algorithm. *International journal for numerical methods in fluids*, 8(6):617–641.

Germano, M., Piomello, U., Moin, P., and Cabot, W. (1991). A dynamic subgrid-scale eddy viscosity model. *Physics of Fluids A*, 3:1760–1765.

Gershanik, A. and Zeiri, Y. (2010). Sublimation rate of tnt microcrystals in air. *Journal Physical Chemistry*, 114.

Gershanik, A. and Zeiri, Y. (2012). Sublimation rate of energetic materials in air: RDX and PETN. *Propellants Explosives, Pyrotechnics*, 37:207–214.

Glauert, M. (1956). The wall jet. *Journal of Fluid Mechanics*, 1(6):625–643.

Goldfarb, J. and Suuberg, E. (2010). Raoult's law and its application to sublimation vapor pressures of mixtures of polycyclic aromatic hydrocarbons. *Environmental Engineering Science*, 25.

Gongwer, P. (2005). Vapor pressure data base for explosives and related compounds. Technical Report DHS/TSA/TSL-06/40, DHS.

Goss, K. and Schwarzenbach, R. (1998). Gas/solid and gas/liquid partitioning of organic compounds: Critical evaluation of the interpretation of equilibrium constants. *Environmental Science and Technology*, 32.

Griffy, T. (1992). *A Model of Explosive Vapor Concentration II, in Proceedings of the Fourth International Symposium on the Analysis and Detection of Explosives*. Kluwer-Academic, New York.

Guo, Z. (2002). Review of indoor emission source models. part 2. parameter estimation. *Environmental Pollution*, 120:551–564.

Guo, Z. (2013). A framework for modelling non-steady-state concentrations of semivolatile organic compounds indoors–i: Emissions from diffusional sources and sorption by interior surfaces. *Indoor and Built Environment*, 22(4):685–700.

Han, M., Ooka, R., and Kikumoto, H. (2019). Lattice boltzmann method-based large-eddy simulation of indoor isothermal airflow. *International Journal of Heat and Mass Transfer*, 130:700–709.

Hanna, S., Hansen, O., and Dharmavaram, S. (2004). FLACS CFD air quality model performance evaluation with Kit Fox, MUST, Prairie Grass, and EMU observations. *Atmos. Environ.*, 38(28):4675–4687.

Hargather, M., Staymates, M., Madalis, M., Smith, D., and Settles, G. (2011). The internal aerodynamics of cargo containers for trace chemical sampling and detection. *IEEE Sensors Journal*, 11(5):1184–1193.

Hobbs, J. and Conde, E. (1993). Analysis of airflows in personnel screening booths. In *Advances in Analysis and Detection of Explosives*, pages 437–453.

ICON (2017). IconCFD 3.3 Technical User Guide.

Incropera, F. and De Witt, D. (1990). *Fundamentals of heat and mass transfer*. Wiley.

Jayatilleke, C. (1966). *The influence of Prandtl number and surface roughness on the resistance of the laminar sub-layer to momentum and heat transfer*. PhD thesis, University of London.

Jayjock, M., Chaisson, C., Arnold, S., and Dederick, E. (2007). Modeling framework for human exposure assessment. *J. Expo. Sci. Env. Epid.*, 17:S81–S89.

Jiang, J. (2007). *Experimental and numerical study of air flows in a full scale room*. PhD thesis, University of Illinois.

Jiji, L. (2009). *Heat convection*, chapter 2. Springer-Verlag, Berlin, Germany, 2nd edition.

Johansen, S. (1991). The deposition of particles on vertical walls. *International journal of multiphase flow*, 17(3):355–376.

Jørgensen, R., Dokka, T., and Bjørseth, O. (2000). Introduction of a sink-diffusion model to describe the interaction between volatile organic compounds (VOCs) and material surfaces. *Indoor Air*, 10(1):27–38.

Joubert, P., Sandu, A., Beghein, C., and Allard, F. (1996). Numerical study of the influence of inlet boundary conditions on the air movement in a ventilated enclosure. *Proceedings of 5th International Conference on Air Distribution in Rooms (ROOMVENT), Yokohama, Japan.*

Kader, B. (1981). Temperature and concentration profiles in fully turbulent boundary layers. *International Journal of Heat and Mass Transfer*, 24:1541–1544.

Kandzia, C. and Mueller, D. (2016). Flow structures and Reynolds number effects in a simplified ventilated room experiment. *International Journal of Ventilation*, 15(1):31–44.

Karlsson, E. and Huber, U. (1996). Influence of desorption on the indoor concentration of toxic gases. *Journal of Hazardous Materials*, 49:15–27.

Karlsson, E., Sjöstedt, A., and Håkansson, S. (1994). Can weak turbulence give high concentrations of carbon dioxide in baby cribs? *Atmos. Environ.*, 28(7):1297–1300.

Keil, C. (2015). Experimental measurements of near-source exposure modeling parameters. *Journal of occupational and environmental hygiene*, 12(10):692–698.

Khan, M., Delbosc, N., Noakes, C., and Summers, J. (2015). Real-time flow simulation of indoor environments using lattice Boltzmann method. *Build. Simul.*, 8(4):405–414.

Knight, K., Debus, K., Berkoe, J., and Dasey, T. (2005). Practical application of the les method to mixing in large indoor spaces. In *ASME International Mechanical Engineering Congress and Exposition*, volume 42193, pages 587–594.

Koehl, M. (2006). The fluid mechanics of arthropod sniffing in turbulent odor plumes. *Chemical Senses*, 31:93–105.

Kovanen, K., Seppänen, O., Sirén, K., and Majanen, A. (1989). Turbulent air flow measurements in ventilated spaces. *Environment International*, 15(1-6):621–626.

Kunz, R. R., Gregory, K. E., Aernecke, M. J., Clark, M. L., Ostrinskaya, A., and III, A. W. F. (2012). Fate dynamics of environmentally exposed explosive traces. *The Journal of Physical Chemistry A*, 116:3611–3624.

Launder, B., Reece, G., and Rodi, W. (1975). Progress in the development of a Reynolds-stress turbulence closure. *Journal of fluid mechanics*, 68(3):537–566.

Launder, B. E. and Spalding, D. B. (1972). *Lectures in Mathematical Models of Turbulence*. Academic Press, London, England.

Lawson, M. J., Craven, B. A., Paterson, E. G., and Settles, G. S. (2012). A computational study of odorant transport and deposition in the canine nasal cavity: Implications for olfaction. *Chemical Senses*, 37(6):553–566.

Le Dreau, J., Heiselberg, P., and Nielsen, P. (2012). Simulation with different turbulence models in an annex 20 benchmark test using STAR-CCM+. Technical Report 147, Department of Civil Engineering, Aalborg University.

Leggett, D., Jenkins, T., and Murrmann, R. (1977). Composition of vapors evolved from military tnt as influenced by temperature, solid composition, age and source. Technical Report SR 77-16, Cold regions research and engineering laboratory.

Leonard, B. (1991). The ULTIMATE conservative difference scheme applied to unsteady one-dimensional advection. *Computer Methods in Applied Mechanics and Engineering*, 88:17–74.

Li, Y. and Nielsen, P. (2011). CFD and ventilation research. *Indoor Air*, 21:442–453.

Liang, Y. and Xu, Y. (2014). Improved method for measuring and characterizing phthalate emissions from building materials and its application to exposure assessment. *Environmental science & technology*, 48(8):4475–4484.

Lilly, D. K. (1992). A proposed modification of the germano subgrid-scale closure model. *Physics of Fluids*, 4:633–635.

Little, J. C., Weschler, C. J., Nazaroff, W. W., Liu, Z., and Cohen Hubal, E. A. (2012). Rapid methods to estimate potential exposure to semivolatile organic compounds in the indoor environment. *Environmental science & technology*, 46(20):11171–11178.

Liu, C.-H. and Barth, M. (2002). Large-eddy simulation of flow and scalar transport in a modeled street canyon. *Journal of Applied Meteorology*, 41(6):660–673.

Liu, Z., Yea, W., and Little, J. (2013). Predicting emissions of volatile and semivolatile organic compounds from building materials: A review. *Building and Environment*, 64:7–25.

Lovestead, T. and Bruno, T. (2010). Trace headspace sampling for quantitative analysis of explosives with cryoadsorption on short alumina porous layer open tubular columns. *Anal. Chem.*, 82:5621–5627.

Mao, Y.-F., Li, Z., He, Y.-L., and Tao, W.-Q. (2016). CFD analysis of SVOC mass transfer in different chambers. *International Journal of Heat and Mass Transfer*, 99:613 – 621.

Mao, Y.-F., Li, Z., Zhang, Y.-P., He, Y.-L., and Tao, W.-Q. (2018). A review of mass-transfer models and mechanistic studies of semi-volatile organic compounds in indoor environments. *Indoor and Built Environment*, 27(10):1307–1321.

Mathey, F., Cokljat, D., Bertoglio, J., and Sergent, E. (2006). Assessment of the vortex method for large eddy simulation inlet conditions. *Progress in Computational Fluid Dynamics, An International Journal*, 6(1-3):58–67.

Matthews, T., Thompson, C., Wilson, D., Hawthorne, A., and Mage, D. (1989). Air velocities inside domestic environments: an important parameter in the study of indoor air quality and climate. *Environment International*, 15(1-6):545–550.

Mazzaro, R., Mariani, V., and Mendonca, K. (2010). Performance of rsm turbulence model in predicting the airflow in a ventilated room. *Proceedings of ENCIT 2010. 13th Brazilian Congress of Thermal Sciences and Engineering.*

Megri, A. and Haghighat, F. (2007). Zonal modeling for simulating indoor environment of buildings: Review, recent developments, and applications. *HVAC&R Res.*, 13(6):887–905.

Mentor, F. (1994). Two-equation eddy-viscosity turbulence models for engineering applications. *AIAA Journal*, 32:1598–1605.

Meyer, R., Kohler, J., and Homburg, A. (2007). *Explosives*. Wiley-VCH, Weinheim, Germany, 6th edition.

Mills, A. (1995). *Heat and mass transfer*, chapter 4. Irwin, USA, 1st edition.

Mingotti, N., Wood, R., Noakes, C., and Woods, A. (2020). The mixing of airborne contaminants by the repeated passage of people along a corridor. *Journal of Fluid Mechanics*, 903.

Mora, L. and Gadgil, A. (2002). Theoretical study of pollutant mixing in rooms induced by occupancy. *Proceedings of the Room Vent 2002 Conference, Copenhagen, Denmark.*

Morrison, G. and Nazaroff, W. (2002). The rate of ozone uptake on carpet: mathematical modeling. *Atmospheric Environment*, 36(11):1749–1756.

Mu, R., Ueda, A., Liu, Y., Wu, M., Henderson, D., Lareau, R., and Chamberlain, R. (2003). Effects of interfacial interaction potential on the sublimation rates of tnt films on a silica surface examined by qcm and afm techniques. *Surface Science*, 530.

Muller, D. and Davidson, L. (2000). Comparison of different subgrid turbulence models and boundary conditions for large-eddy-simulation of room air flows. In awbi, H., editor, *Air distribution in rooms - ventilation of health and sustainable environment*, volume 1, pages 301–306, Amsterdam. Elsevier Science Ltd.

Murakami, S. and Kato, S. (1989). Numerical and experimental study on room airflow - 3-d predictions using the k-ϵ turbulence model. *Building and Environment*, 24(1):85–97.

Murakami, S., Kato, S., Ito, K., and Zhu, Q. (2003). Modeling and CFD prediction for diffusion and adsorption within room with various adsorption isotherms. *Indoor Air*, 13:20–27.

Murakami, S., Mochida, A., and Matsui, K. (1995). Large eddy simulation of non-isothermal room airflow, comparison between standard and dynamic type of smagorinsky model. *SEISAN-KENKYU, Journal of Institute of Industrial Science, University of Tokyo*, 47(2):7–12.

Muralidharan, G., Wig, A., Pinnaduwage, L., Hedden, D., Thundat, T., and Lareau, R. T. (2003). Adsorption–desorption characteristics of explosive vapors investigated with microcantilevers. *Ultramicroscopy*, 97(1-4):433–439.

Murray, D. and Burmaster, D. (1995). Residential air exchange rates in the united states: Empirical and estimated parametric distributions by season and climatic region. *Risk Analysis*, 15(4).

Murrman, R. and Nakano, Y. (1971). Influence of soil on detection of buried explosives and tunnels by trace gas analysis. Technical Report RR 288/AD 727667, U.S. Army Corps of Engineers, Cold Regions Research and Engineering Laboratory.

Nally, J., Parker, S., and Hindmarsh, C. (2009). Predictive modelling to assess low level hazards due to toxic chemical vapours. Technical Report DSTL/PS31882, Dstl.

Nehorai, A. (1995). Detection and localization of vapour-emitting sources. *IEEE T. Signal Proces.*, 43(1):243–253.

Nicas, M. (1996). Estimating exposure intensity in an imperfectly mixed room. *Am. Ind. Hyg. Assoc. J.*, 57(6):542–550.

Nicas, M. (2001). Modeling turbulent diffusion and advection of indoor air contaminants by Markov chains. *Am. Ind. Hyg. Assoc. J.*, 62(2):149–158.

Nicas, M. (2009). Turbulent eddy diffusion models. In Kiel, C. B., Simmons, C. E., and Anthony, T. R., editors, *Mathematical Models for Estimating Occupational Exposure to Chemicals*, chapter 7, pages 53–65. American Industrial Hygiene Association.

Nicklin, S. (2015). Personal communication. 2015-10-05.

Nielsen, P. (1973). Berechnung der luftbewegung in einem zwangsbelüfteten raum. *GI-Gesundheits Ingenieur*.

Nielsen, P. (1981). Contaminant distribution in industrial areas with forced ventilation and two-dimensional flow. In IIR-Joint Meeting Aalborg: Institut for Bygningsteknik, Aalborg Universitet.

Nielsen, P. (1988). Numerical predictions of air distribution in rooms - status and potentials: status and potentials. Technical Report Indoor Environmental Technology, No. 5, Vol. R8823, Aalborg: Dept. of Building Technology and Structural Engineering, Aalborg University.

Nielsen, P. (1990). Specification of a two-dimensional test case: (IEA). Technical Report Gui serie: No. 8, Vol. R9040, Aalborg: Institute for Bygningsteknik, Aalborg Universitet.

Nielsen, P. (1992). Air distribution systems: Room air movement and ventilation effectiveness. Technical Report Indoor Environmental Technology: No. 25, Vol R9250, Aalborg University.

Nielsen, P. (2015). Fifty years of CFD for room air distribution. *Building and Environment*, 91:78–90.

Nielsen, P., Filholm, V., Topp, C., and Davidson, L. (2000). Model experiments with low Reynolds number effects in a ventilated room. Technical Report Indoor Environmental Engineering: No. 119, Vol R0044, Aalborg University.

Nielsen, P., Rong, L., and Cortes, I. (2010). The IEA annex 20 two-dimensional benchmark test for CFD predictions. 10th Rehva World Congress: Sustainable Energy Use in Buildings.

Ong, T.-H., T, M., Geurtsen, G., Kelley, J., Ostrinskaya, A., and Kunz, R. (2017). Use of mass spectrometric vapor analysis to improve canine explosive detection efficiency. *Analytical Chemistry*, 89:6482–6490.

Orszag, S., Yakhot, V., Flannery, W., Boysan, F., Choudhury, D., Maruzewski, J., and Patel, B. (1993). Renormalization group modeling and turbulence simulations. *In International Conference on Near-Wall Turbulent Flows, Tempe, Arizona,*.

Ostmark, H., Wallin, S., and Ang, H. (2012). Vapor pressure of explosives: A critical review. *Propellants Explos. Pyrotech.*, 37:12–23.

Parker, S. and Bowman, V. (2011). State-space methods for calculating concentration dynamics in multizone buildings. *Building and Environment*, 46(8):1567–1577.

Parker, S., Coffey, C., Gravesen, J., Kirkpatrick, J., Ratcliffe, K., Lingard, B., and Nally, J. (2014a). Contaminant ingress into multizone buildings: An analytical state-space approach. *Building Simulation*, 7(1):57–71.

Parker, S., Lorenzetti, D., and Sohn, M. (2014b). Implementing state-space methods for multizone contaminant transport. *Building and Environment*, 71:131–139.

Patankar, S. and Spalding, D. (1972). A calculation procedure for heat, mass and momentum transfer in three-dimensional parabolic flows. *Int. J. Heat. Mass Tran.*, 15.

Pedersen, J. and Meyer, K. (2000). POD analysis of flow structures in a scale model of a ventilated room. *Experiments in fluids*, 33:940–949.

Phelan, J. and Patton, R. (2004). Sublimation rates of explosive materials - method development and initial results. Technical Report SAND2004-4525, Sandia National Laboratories.

Phelan, J. and Webb, S. (1997). Environmental fate and transport of chemical signatures from buried landmines-screening model formulation and initial simulations. Technical Report SAND97-1426, Sandia National Laboratories.

Pinnaduwage, L. A., Gehl, A., Hedden, D. L., Muralidharan, G., Thundat, T., Lareau, R. T., Sulchek, T., Manning, L., Rogers, B., Jones, M., and Adams, J. D. (2003). Explosives: A microsensor for trinitrotoluene vapour. *Nature*, 425:474–474.

Pinnaduwage, L. A., Yi, D., Tian, F., Thundat, T., and Lareau, R. (2004). Adsorption of trinitrotoluene on uncoated silicon microcantilever surfaces. *Langmuir*, 20:2690–2694.

Poling, B., Prausnitz, J., and O.Connell, J. (2007). *Diffusion coefficients, In: The properties of gases and liquids*. McGraw Hill, Singapore.

Pope, S. (2004). Ten questions concerning the large-eddy simulation of turbulent flows. *New journal of Physics*, 6(1):35.

Porritt, F., Mansson, R., Berry, A., Cook, N., Sibbald, N., and Nicklin, S. (2015). Validation of a short odour discrimination test for working dogs. *Applied Animal Behaviour Science*, 165:133–142.

Posner, J., Buchanan, C., and Dunn-Rankin, D. (2003). Measurement and prediction of indoor air flow in a model room. *Energy and buildings*, 35(5):515–526.

Pulat, E. and Nielsen, P. (2015). Numerical simulation of turbulent airflow in a ventilated room: Inlet turbulence parameters and solution multiplicity. *Energy and Buildings*, 93:227–235.

Rajaratnam, N. (1976). *Turbulent jets*, volume 5. Elsevier.

Reinke, P. and Keil, C. (2009). Well-mixed box models. In Kiel, C. B., Simmons, C. E., and Anthony, T. R., editors, *Mathematical Models for Estimating Occupational Exposure to Chemicals*, chapter 4, pages 23–31. American Industrial Hygiene Association.

Restivo, A. (1979). *Turbulent flow in ventilated rooms*. PhD thesis, University of London.

Rong, L. and Nielsen, P. (2008). Simulation with different turbulence models in an annex 20 room benchmark test using Ansys CFX 11.0. Technical Report ISSN 1901-726X, Aalborg University.

Said, M., Jouini, D., and E.G.Plett (1993). Influence of turbulence parameters at supply inlet on room air diffusion. *Proceedings of ASME Winter Meeting, New Orleans, Louisiana, USA*. Paper 93-WA/HT-67.

Scheff, P., Friedman, R., Franke, J., Conroy, L., and Wadden, R. (1992). Source activity modeling of freon emissions from open-top vapor degreasers. *Appl. Occup. Hyg.*, 7(2):127–134.

Settles, G. (2005). Sniffers: Fluid-dynamic sampling for olfactory trace detection in nature and homeland security - the 2004 Freeman Scholar Lecture. *Journal of Fluids Engineering*, 128:189–218.

Shade, W. and Jayjock, M. (1997). Monte carlo uncertainty analysis of a diffusion model for the assessment of halogen gas exposure during dosing of brominators. *American Industrial Hygiene Association Journal*, 58(6):418–424.

Shao, Y., Ramachandran, S., Arnold, S., and Ramachandran, G. (2017). Turbulent eddy diffusion models in exposure assessment-determination of the eddy diffusion coefficient. *J. Occup. Environ. Hyg.*, 14(3):195–206.

Shi, S. and Zhao, B. (2014). Modeled exposure assessment via inhalation and dermal pathways to airborne semivolatile organic compounds (SVOCs) in residences. *Environmental science & technology*, 48(10):5691–5699.

Shih, T.-H., Liou, W., Shabbir, A., and Zhu, Z. Y. J. (1995). A new k-ϵ eddy viscosity model for high Reynolds number turbulent flows. *Computers & Fluids*, 24(3):227–238.

Singer, B., Hodges, A., Destaillats, H., Hotchi, T., Revzan, K., and Sectro, R. (2005). Indoor sorption of surrogates for sarin and related nerve agents. *Environmental Science and Technology*, 39(9).

Singer, B., Revzan, K., Hotchi, T., Hodgson, A., and Brown, N. (2004). Sorption of organic gases in a furnished room. *Atmospheric Environment*, 38(16):2483–2494.

Smagorinsky, J. (1963). General circulation experiments with the primitive equations. 1. the basic experiment. *Monthly Weather Review*, 91:99–164.

Sobol, I. (1967). Distribution of points in a cube and approximate evaluation of integrals. *USSR Comp. Math. Math. Phys.*, 7:86–112.

Sorensen, D. and Weschler, C. (2002). Modeling-gas phase reactions in indoor environments using computational fluid dynamics. *Atmospheric Environment*, 36(1):9–18.

Srebric, J. and Chen, Q. (2002). Simplified numerical models for complex air supply diffusers. *Hvac&R Research*, 8(3):277–294.

Susin, R., Lindner, G., Mariani, V., and Mendonca, K. (2009). Evaluating the influence of the width of inlet slot on the prediction of indoor airflow: Comparison with experimental data. *Building and Environment*, 44(5):971–986.

Tabor, G. and Baba-Ahmadi, M. (2010). Inlet conditions for large eddy simulation: A review. *Computers & Fluids*, 39(4):553–567.

Thysen, J.-H. (2015). *CFD analysis of the mixing in an enclosure under time-periodic inlet conditions*. PhD thesis, Eindhoven University of Technology.

Tominaga, Y. (2015). Flow around a high-rise building using steady and unsteady RANS CFD: Effect of large-scale fluctuations on the velocity statistics. *Journal of Wind Engineering and Industrial Aerodynamics*, 142:93–103.

Tominaga, Y. and Stathopoulos, T. (2007). Turbulent schmidt numbers for CFD analysis with various types of flowfield. *Atmos. Environ.*, 41:8091–8099.

Topp, C. (1999). *Diffusion and evaporation-controlled emission in ventilated rooms*. PhD thesis, Aalborg University, The Faculty of Engineering and Science, Department of Building Technology and Structural Engineering.

Topp, C., Nielsen, P., and Davidson, L. (2000). Room airflows with low Reynolds number effects. Technical Report Indoor Environmental Engineering: No. 107, Vol R0030, Aalborg University.

Trox (2018). Ceiling diffusers type ADT. `https://www.troxuk.co.uk/ceiling-diffusers/type-adt-995f6e2818a938ff`. Accessed: 25/07/18.

Tung, Y., amd D.O. Henderson, R. M., and Curby, W. (1997). Diffusion kinetics of TNT in acrylonitrile butadiene rubber via FT-IR/ATR spectroscopy. *applied spectroscopy*, 51(2).

van Hooff, T. and Blocken, B. (2017). Low-Reynolds number mixing ventilation flows: Impact of physical and numerical diffusion on flow and dispersion. *Building Simulation*, 10(4):589–606.

van Hooff, T., Blocken, B., Carmeliet, T., Carmeliet, J., and van Heijst, G. (2012a). PIV measurements and analysis of transitional flow in a reduced-scale model: ventilation by a free plane jet with coanda effect. *Building and Environment*, 56:301–313.

van Hooff, T., Blocken, B., Defraeye, T., Carmeliet, J., and van Heijst, G. (2012b). PIV measurements of a plane wall jet in a confined space at transitional slot Reynolds numbers. *Experiments in Fluids*, 53(2):499–517.

van Hooff, T., Blocken, B., Gousseau, P., and van Heijst, G. (2014). Counter-gradient diffusion in a slot-ventilated enclosure assessed by LES and RANS. *Computers & Fluids*, 96:63–75.

van Hooff, T., Blocken, B., and Tominaga, Y. (2017). On the accuracy of CFD simulations of cross-ventilation flows for a generic isolated building: comparison of RANS, LES and experiments. *Building and Environment*, 114:148–165.

van Hooff, T., Blocken, B., and van Heijst, G. (2013). On the suitability of steady RANS CFD for forced mixing ventilation at transitional slot Reynolds numbers. *Indoor air*, 23:236–249.

Van Leer, B. (1979). Towards the ultimate conservative difference scheme. V. a second-order sequel to Godunov's method. *Journal of computational Physics*, 32(1):101–136.

Venetsanos, A., Papanikolaou, E., Delichatsios, M., Garcia, J., Hansen, O., Heitsch, M., Huser, A., Jahn, W., Jordan, T., Lacome, J.-M., Ledin, H., Makarov, D., Middha, P., Studer, E., Tchouvelev, A., Teodorczyk, A., Verbecke, F., and Van der Voort, M. (2000). An inter-comparison exercise on the capabilities of CFD models to predict the short and long term distribution and mixing of hydrogen in a garage. *International journal of hydrogen energy*, 34:5912–5923.

Vickers, N. (2000). Mechanisms of animal navigation in odor plumes. *The Biological Bulletin*, 198(2):203–212.

Voigt, L. (2001). *Navier-Stokes simulation of airflow in rooms and around a human body*. PhD thesis, University of Denmark.

Voigt, L. (2005). Evaluating turbulence models for 3-d flows in enclosure by topology. In *Montreal Canada: Ninth International IBPSA Conference*.

Walker, D. B., Walker, J. C., Cavnar, P. J., Taylor, J. L., Pickel, D. H., Hall, S. B., and Suarez, J. C. (2006). Naturalistic quantification of canine olfactory sensitivity. *Applied Animal Behaviour Science*, 97:241–254.

Wang, H. and Zhai, Z. (2012). Application of coarse-grid computational fluid dynamics on indoor environment modeling: Optimizing the trade-off between grid resolution and simulation accuracy. *HVAC&R Research*, 18(5):915–933.

Wang, M. and Chen, Q. (2010). On a hybrid RANS/LES approach for indoor airflow modeling. *HVAC&R Research*, 16(6):731–747.

Wang, Y., Deng, B., and Kim, C. (2012). Transient characteristics of VOCs removal by an air cleaner in association with a humidifier combined with different ventilation strategies in an office. *Indoor and Built Environment*, 21(1):71–78.

Weissburg, M. (2000). The fluid dynamical context of chemosensory behavior. *The Biological Bulletin*, 198(2):188–202.

Weschler, C. and Nazaroff, W. (2008). Semivolatile organic compounds in indoor environments. *Atmospheric Environment*, 42:9018–9040.

Wilcox, D. C. (1998). *Turbulence Modeling for CFD*. DCW Industries, Inc., La Canada, California.

Wolfshtein, M. (1969). The velocity and temperature distribution in one-dimensional flow with turbulence augmentation and pressure gradient. *International Journal of Heat and Mass Transfer*, 12(3):301–318.

Xie, Z.-T. and Castro, I. (2008). Efficient generation of inflow conditions for large eddy simulation of street-scale flows. *Flow Turbulence and Combustion*, 81:449–470.

Xie, Z.-T. and Castro, I. (2009). Large-eddy simulation for flow and dispersion in urban streets. *Atmospheric Environment*, 43(13):2174–2185.

Xie, Z.-T., Hayden, P., Robins, A., and Voke, P. (2007). Modelling extreme concentrations from a source in a turbulent flow over a rough wall. *Atmospheric Environment*, 41(16):3395–3406.

Xiong, J., Liu, C., and Zhang, Y. (2012). A general analytical model for formaldehyde and voc emission/sorption in single-layer building materials and its application in determining the characteristic parameters. *Atmospheric environment*, 47:288–294.

Yang, X. and Chen, Q. (2001). A coupled airflow and source/sink model for simulating indoor voc exposures. *Indoor Air*, 11(4):257–269.

Yang, Y., Feng, Q., Cai, H., Xu, J., Li, F., Deng, Z., Yan, C., and Li, X. (2019). Experimental study on three single-robot active olfaction algorithms for locating contaminant sources in indoor environments with no strong airflow. *Building and Environment*, 155:320–333.

Zhai, J., Zhang, Z., Zhang, W., and Chen, Q. (2007). Evaluation of various turbulence models in predicting airflow and turbulence in enclosed environments by CFD: Part-1: Summary of prevalent turbulence models. *HVAC&R Research*, 13:853–870.

Zhang, Q. and Zhang, G. (2007). Study on TVOCs concentration distribution and evaluation of inhaled air quality under a re-circulated ventilation system. *Building and environment*, 42(3):1110–1118.

Zhang, W. and Chen, Q. (2000). Large eddy simulation of indoor airflow with a filtered dynamic subgrid scale model. *International Journal of Heat and Mass Transfer*, 43(17):3219–3231.

Zhang, Y., Xiong, J., Mo, J., Gong, M., and Cao, J. (2016). Understanding and controlling airborne organic compounds in the indoor environment: mass transfer analysis and applications. *Indoor air*, 26(1):39–60.

Zhang, Z., Zhang, W., Zhai, Z., and Chen, Q. (2007). Evaluation of various turbulence models in predicting airflow and turbulence in enclosed environments by CFD: Part-2: Comparison with experimental data from literature. *HVAC&R Research*, 13:871–886.

Zhou, G. (1999). *Human perception of air movement. Impact of frequency and airflow direction on draught sensation.* PhD thesis, Technical University of Denmark.

Zhou, Y., Long, X., and Wei, X. (2011). Theoretical study on the diffusive transport of 2,4,6-trinitrotoluene in polymer-bonded explosive. *Journal of molecular modelling*, 17:3015–3019.

Zhu, W. and Chen, Q. (2009). Real-time or faster-than-real-time simulation of airflow in buildings. *Indoor Air*, 19:33–44.

Zontek, T., Hollenbeck, S., Jankovic, J., and Ogle, B. (2019). Modeling particle emissions from three-dimensional printing with acrylonitrile-butadiene-styrene polymer filament. *Environ. Sci. Technol.*, 53(16):9656–9663.

Zuo, W. and Chen, Q. (2010). Fast and informative flow simulations in a building by using fast fluid dynamics model on graphics processing unit. *Build. Environ.*, 45(3):747–757.